ULTRASONIC DIFFRACTION EFFECTS ON PERIODIC SURFACES

A Thesis
Presented to
The Academic Faculty

by

Sarah W. Herbison

In Partial Fulfillment
of the Requirements for the Degree
Doctor of Philosophy in the
George W. Woodruff School of Mechanical Engineering

Georgia Institute of Technology
August 2011

ULTRASONIC DIFFRACTION EFFECTS ON PERIODIC SURFACES

Approved by:

Dr. Nico F. Declercq, Advisor
School of Mechanical Engineering
Georgia Institute of Technology

Dr. Yves H. Berthelot
School of Mechanical Engineering
Georgia Institute of Technology

Dr. Abdallah Ougazzaden
School of Electrical and Computer Engineering
Georgia Institute of Technology

Dr. Karim Sabra
School of Mechanical Engineering
Georgia Institute of Technology

Dr. Massimo Ruzzene
School of Aerospace Engineering
Georgia Institute of Technology

Date Approved: 24 June 2011

ACKNOWLEDGEMENTS

There are so many people and organizations that are deserving of recognition for their roles in making this thesis happen. I can only hope to thank some of them here.

First, I should thank my thesis advisor Nico Declercq. I have always appreciated his intellectual curiosity and support in this endeavor. I also know that he goes to great lengths to maintain a congenial atmosphere in our lab, and I think that is a special thing. Also deserving of many thanks is Yves Berthelot, not only for his service as a member of my committee but also for his role as President and tireless supporter of Georgia Tech Lorraine (GTL). I would also like to express my gratitude to Abdallah Ougazzaden for his dedication to the success of the GT-CNRS UMI 2958 Laboratory (UMI) as its Director. My committee members Massimo Ruzzene and Karim Sabra also deserve recognition and thanks for their insights on my work as well as their flexibility in working with me on this trans-Atlantic effort.

The Woodruff School of Mechanical Engineering generously provided me with the opportunity to be a teaching assistant for many semesters while I was in Atlanta as well as with the chance to be a course instructor during one summer term in Metz. Georgia Tech provided me with a President's Fellowship for which I am very thankful. I also received support from the Acoustical Society of America, the National Center for Physical Acoustics, and the UMI to attend various conferences and events. I was incredibly fortunate to have attended was the First International Workshop on Phononic Crystals, and this was only made possible with the support of the UMI and Abdallah Ougazzaden, Ali Adibi, and Abdelkrim Khelif in particular.

The research that was performed in Metz, France, was funded through a *Bourse de Doctorat pour Ingénieurs* (BDI) with financial support from the French *Centre*

National de Recherche Scientifique (CNRS), the *Conseil Régional de Lorraine*, and Georgia Tech Lorraine. The sample that was studied in Chapter 3 was generously provided by Arcelor-Mittal. The experimental studies presented in Chapter 4 would not have been possible without the generosity of the late Mack Breazeale of The University of Mississippi, who loaned us the original corrugated brass sample that he used in the first observation of an ultrasonic backward beam displacement in 1976. The transmission experiments were performed in cooperation with John Vander Weide, who was always a source of optimism in the lab. The work on phononic crystals in Chapter 5 was performed under Grant ANR-09-BLAN-0167-01 through the *Agence National de la Recherche*. I found our discussions with Vincent Laude very valuable, and I enjoyed working with Rayisa Moiseyenko during our week in Metz together.

I also wish to thank Jean-Jacques Michel for the tech support that he has provided over the years in Metz. He has gone above and beyond the call of duty on multiple occasions, and he showed amazing patience with me while rescuing the contents of my hard drive. I back up my data now, I really do! I'd also like to thank him for not laughing too hard the time a cup of coffee met my laptop.

I would like to thank all the staff of GTL for their dedication to making GTL successful (and for not laughing at me stumbling over the pronunciation of French r's and u's). It has been a pleasure getting to know them over the years. I would like to thank Josyane Roschitz in particular for helping me not only arrive in France but stay there. On the other side of the Atlantic there is Glenda Johnson, who I cannot thank enough for helping me (along with 700+ other grad students!) through the all the required paperwork.

I'd like to thank my fellow (current and former) lab mates Peter McKeon, Satyanarayan, Jingfei Liu, Ebrahim Lamkanfi, and John Vander Weide for being the kind of colleagues that I can also call friends. You were ever-willing to help out with adjustments to experiments and you were always excellent sounding-boards for ideas. I

want to acknowledge Peter in particular for his contribution of the Disperse simulations that appear in Chapter 2. James Hall was also a great addition to our lab who we were lucky to have had even for one semester.

Now that I've thanked everyone who helped me get the work done, I'd like to thank those who kept me sane while I was doing it! First I'd like to thank all my fellow students who have made up the PhD community at GTL over the years. I couldn't have done this without you all! I think that the camaraderie of our group is one of the greatest strengths of GTL, and it is something that I already miss very much. The atmosphere even carried over to Atlanta, where Peter Bonnano very kindly assisted with the refreshments at my proposal and where I was happy to aid Damien Rontani with certain peculiarities of American culture. I would also like to thank Vinod Ravindran, who is a good friend even though one of his favorite pastimes is making jokes about Texas.

I also sincerely appreciate the friendship and guidance of former ME students Mike and Tanya Haberman, Maria-Isabel Carnasciali, and Beth Douglas Kelly, who was a wonderful roommate in Atlanta. For their kindness and hospitality, I would like to thank Alex Mychkovsky, Susan and David Swafford (especially in the face of busted pipes, waterfalls in apartments, and landlords that say you can go without showering for a few days), Janice and Jeramy Dickerson, Maria and Rocky Dunlap, and Alex and John Vander Weide. You are all amazing!

I also want to thank Frances Baxter, since having her come into my life during my last year in France means more to me than I can say. Fran, I think I just about heard angels singing the first time I met you at GTL!

Upon my return to Texas, Carolyn and Dennis Agnelly provided not only good walking company but valuable career-related discussions. I value their friendship very much. They also provided me many morning lattes that made the writing of this thesis possible. And yes, it is thanks to Carolyn that there is a Starbucks in the

Houston area that has the deliciousness that is the Pumpkin Spice Latte until March, and no, we won't tell you where it is.

Three women who have been dear friends for many years and have always been supportive and reassuring are Andrea Velicevich, Tran Vuong, and Georgina Goodnight. It would take me far more pages than I have here to express my gratitude to my parents Kathryn Herbison and Matt Herbison for the incredible generosity and patience they have shown me, not only during the last few months while I completed the writing of this thesis but throughout the years. My siblings Matt and Alicia have not only laughed at me but with me. No, Matt, one does not need to wear an orange vest while snail-hunting, and I am someone who would know. You are both brilliant.

Finalement, je voudrais remercier "ma famille française", et plus particulièrement Francine Coppin, d'avoir accepté cette Américaine. Vous m'avez montré une vue de la France qui n'est pas accessible aux touristes et tous mes plus beaux souvenirs de France, c'est à vous que je les dois. Votre soutien et votre confiance en moi (et cela va sans dire, votre confiture de groseille) étaient indispensables pour mener à bien cette thèse. And most of all, I want to thank Antoine. You were not only the source of my brightest days but you were there for me during the darkest ones, and I am more than grateful for that. I couldn't have done this without you!

TABLE OF CONTENTS

LIST OF TABLES

LIST OF FIGURES

SUMMARY

Although the study of the interaction of acoustic and elastic waves with periodic surfaces and structures has a rich history dating back to Lord Rayleigh, it has recently been attracting new research efforts due to its value in the study of phononic crystals and in methods for ultrasonic non-destructive evaluation (NDE). The objective of the research described in this thesis is to provide new numerical and experimental tools capable of capturing important features that occur due to the diffraction of ultrasound on periodic solid surfaces. These improved predicting capabilities should be useful for the design of advanced NDE techniques and devices.

This thesis is divided into four main parts. First, the Rayleigh-Fourier (R-F) method will be used to simulate diffracted fields generated by structures containing multiple periodic surfaces and/or multiple solid layers. Because theoretical simulations such as those performed with the R-F method are often restricted to the case of ideal periodic surfaces having perfect periodicities rather than real surfaces with imperfect periodicities that would more likely be encountered in practice, the second part of this thesis examines diffraction effects and compares ultrasonic NDE techniques for surfaces with imperfect periodicities. The third portion of this thesis focuses on one unusual phenomenon that has been observed on periodic surfaces, namely the lateral backward displacement of a bounded ultrasonic beam along the surface. This effect is currently understood to occur due to backward propagating surface waves that result from diffraction and mode conversion on the surface. However, this phenomenon has only been observed for time-harmonic waves in reflection. Since ultrasonic NDE methods often employ pulses, this phenomenon will be studied experimentally for the case of ultrasonic pulses in reflection as well as in transmission. The fourth and final

part of this thesis describes the diffraction of bulk ultrasonic waves that can occur on the surfaces of phononic crystals. A thorough understanding of this diffraction is required in order for the transition to be made from studies of infinite phononic crystals to the application of finite-size phononic crystals in actual devices.

CHAPTER I

INTRODUCTION

The study of wave scattering on periodic surfaces dates back to Rayleigh's classic work in *The Theory of Sound* [1, 2] and this subject has been capturing the attention of scientists and engineers for over 100 years. Even though research in this area has a rich history, acoustic and elastic wave scattering on periodic surfaces and structures continues to attract new research efforts. This has been seen especially in the last decade due to the growing interest in sonic and phononic crystals [3].

This thesis is concentrated on one particular aspect of acoustic and elastic wave interaction with periodic structures, namely the diffraction that occurs on periodic surfaces in the ultrasonic regime. Periodicity of a surface can exist for many reasons, including a material's surface preparation, grain structure, lamination, or fiber reinforcement, among others [4]. The diverse origins of surface periodicity explain why wave interaction and diffraction effects occurring on periodic surfaces play important roles in diverse areas of acoustics, from architectural [5, 6] to underwater acoustics [7, 8, 9]. Applications of periodic surfaces within the field of ultrasonics include techniques such as ultrasonic diffraction grating spectroscopy [10] as well as devices to convert bulk waves into surface waves and vice-versa [11, 12]. In particular, it is periodic surfaces' ability to generate surface waves that gives them significance in the field of ultrasonic non-destructive evaluation (NDE).

Four topics concerning ultrasonic diffraction effects on periodic surfaces, especially as they relate to ultrasonic non-destructive evaluation (NDE) and the study of phononic crystals, will be covered by this thesis. Chapter 2 will cover the use of the Rayleigh-Fourier method for the simulation of ultrasonic diffraction on periodic surfaces. Periodic surfaces function as acoustic diffraction gratings, generating diffracted modes that propagate in different discrete directions as determined by the classical grating equation [13]. Although diffraction gratings have been thoroughly studied in optics [14], relatively little attention has been paid to them in acoustics. Several lessons can be learned from the optical community, and one of these is that theoretical and numerical techniques for treating diffraction on a periodic surface can generally only accommodate cases that involve perfect periodicities [13]. Any "real" surface that exhibits a periodic surface texture is, however, unlikely to exhibit a perfect periodicity. Therefore, Chapter 3 is devoted to the experimental investigation of ultrasonic techniques that incorporate surface diffraction for the evaluation of a thin plate with imperfectly periodic surface textures. Because ultrasonic NDE techniques and the techniques employed in Chapter 3 generally employ pulses, Chapter 4 will investigate one unusual phenomenon, namely the lateral backward displacement of an ultrasonic beam, using pulsed ultrasound. This backward beam displacement can be attributed to the diffraction that occurs on periodic surfaces, and it has only been observed in the past for time-harmonic waves. Finally, because the renewed interest in periodic surfaces and structures is currently being driven by the study of phononic crystals, Chapter 5 is dedicated to experiments to study the diffraction of bulk ultrasonic waves that occurs on the surfaces of a two-dimensional phononic crystal. Because these chapters are somewhat distinct, each chapter contains its own introductory section.

This introductory chapter, then, is intended to give a general introduction to ultrasonic diffraction on periodic surfaces, and it is divided into four sections. First, a brief introduction to ultrasonic non-destructive testing and evaluation (NDT&E) will be presented. Next, a brief introduction to the most common types of elastic surface and guided waves will be given because these waves play an important role in ultrasonic NDT&E. The link between diffraction on periodic surfaces and surface wave generation will also be explained. The third section contains a chronological history of the study of ultrasonic diffraction effects on periodic surfaces in order to explain what exactly is meant by the term "diffraction effects" and to show the directions the field has taken in the past and where it may go in the future. The fourth and final section will present additional motivation for the research described by this thesis as well as its objectives.

1.1 Brief introduction to ultrasonic non-destructive evaluation (NDE)

Two terms that are often used interchangeably are *non-destructive testing* (NDT) and *non-destructive evaluation* (NDE). Generally, NDT would be defined as testing that is used to examine an object that does not affect its future usefulness [15]. It can include the examination of a material or object in order to detect imperfections at the time of manufacture or those that may occur over time (fatigue cracks or corrosion, for instance). These imperfections or defects may be internal or external. NDT can also be used to determine characteristics of a material or object, such as its geometry, structure, composition, or other properties, all without affecting its future usefulness. Because NDT can be performed without compromising a product's final use, it can be used as part of a cost-effective quality control strategy.

Different methods of NDT exist. Several examples of testing methods that can be considered non-destructive include visual/optical inspection, radiography, magnetic particle testing, liquid penetrant testing, and electromagnetic testing [16]. NDT methods that involve acoustic/elastic waves include acoustic emission testing as well as ultrasonic inspection [17, 18]. Examples of materials or parts that may be inspected include railroad track, aircraft components, highway bridges, storage tanks, and pipelines. In all of these examples, an undetected defect could grow over time and ultimately result in mechanical failure and potentially catastrophic consequences.

Although very similar to NDT, NDE refers to techniques and measurements that are more quantitative in nature. NDE techniques can be used not only to locate defects in a material or part, but they might also be used to characterize the defect by measuring its size, shape, or orientation [19].

In general, ultrasonic NDT&E involves the use of ultrasonic transducers, and because the field is well-developed, many different types are available commercially. Some examples include contact, immersion, and air-coupled transducers, and these emit ultrasonic beams that may be focused or unfocused. The transducers used in this thesis research are commercially available immersion transducers (designed for use underwater), and they have been used in combination with an ultrasonic scanner. This scanning equipment includes a pulser/receiver to send and receive electrical pulses to and from the transducers, data acquisition cards to acquire the waveforms generated and detected by the transducers, software to analyze those waveforms, and a robot to automate any motion of the transducers.

It is an electrical pulse from the pulser/receiver that causes a transducer to generate an ultrasonic pulse. This emitted pulse then propagates through a medium (which in the case of this thesis is water, but the medium could be air in the case of air-coupled transducers or a solid material in the case of contact transducers) until it encounters some type of material discontinuity, which could be the edge of a material or part, or a crack or defect. Whenever the pulse encounters a discontinuity, part of its energy will be reflected, and this energy can be potentially captured by the emitting transducer which can receive ultrasonic signals in addition to sending them. This scenario is often referred to as *pulse-echo* since the same transducer is used to send the pulse as well as receive any echoes from material discontinuities or flaws. Based on the time-of-flight between the initial pulse and any received echo, the distance to the discontinuity (source of the reflection) can be determined if the wave propagation speeds in the media involved are known. Figure 1.1 shows a pulse-echo

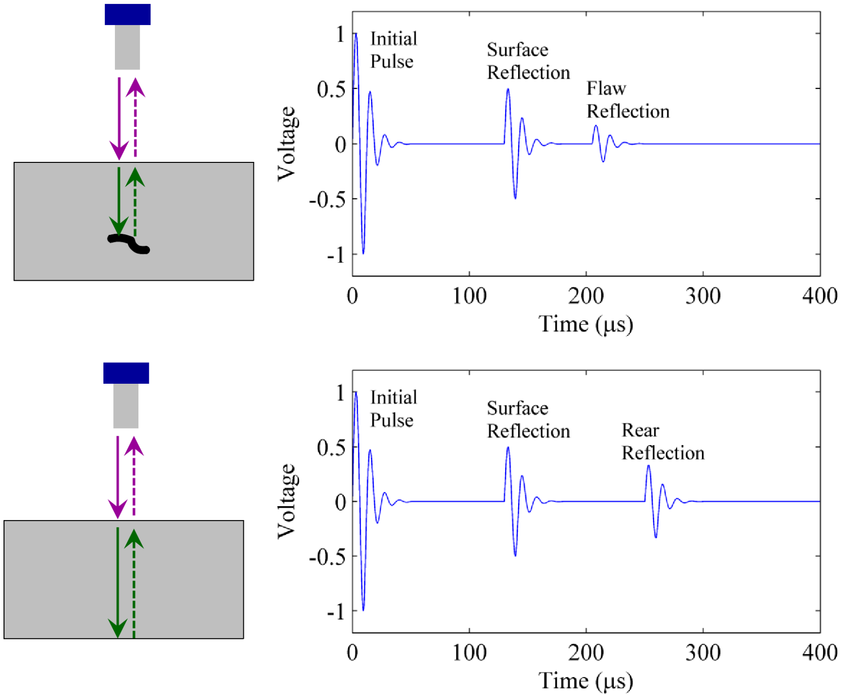

Figure 1.1: Diagram of pulse-echo transducer configuration along with sample waveforms.

configuration along with sample waveforms that might be observed due to surface and flaw reflections. Another possibility is that a second transducer can be used as a receiver, and this transducer can capture emitted waves that interact with a material sample but do not return to the emitter. This arrangement may be referred to as *pitch-catch*. The pitch-catch arrangement is particularly useful for the measurement of diffracted fields as shown in Figure 1.2. Another arrangement that is possible has the receiving transducer directly facing the emitting transducer with a sample placed between them. The receiver captures sound that has propagated through the sample, and the term *through-transmission* may be used to refer to this configuration. All of these terms regarding transducer configurations are used commonly throughout the ultrasonic literature, but they are introduced here as well since this thesis will employ all three of these transducer arrangements.

Additional terms related to ultrasonic NDT&E that may be seen in this thesis

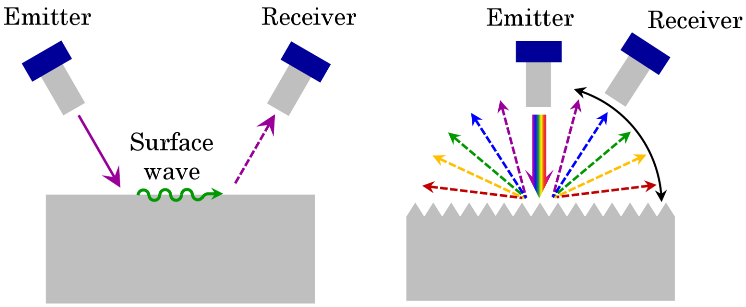

Figure 1.2: Diagram of pitch-catch transducer configuration. (Left) Transducers used to generate and receive a (leaky) surface wave. (Right) Emitter used to generate a pulse incident on a periodic surface and receiver rotated through diffracted field.

include *A-scan*, which just refers to a waveform (often pulse-echo) obtained at a single location on a material. The term *B-scan* is used when the transducer (or transducer pair in the case of through-transmission) is translated linearly along a material. Waveforms (or waveform properties, such as maximum amplitude) are then stored for specific locations along the scan. The term *C-scan* is used when the transducer(s) is moved such that it covers a two-dimensional area on a sample. Like the case of a B-scan, waveforms or specific waveform properties can be acquired and stored for discrete locations. These three types of scans are depicted graphically in Figure 1.3. There also exists a *polar scan* that is only encountered in NDE. In this case, a transducer is rotated about a sample's surface in two angular directions. The ultrasonic scanner at Georgia Tech Lorraine that was employed for this thesis research is capable of A-, B-, C-, and polar scans, and it is therefore referred to as the "polar/C-scan" equipment.

1.2 Surface and guided waves in ultrasonic NDE

Surface waves are particularly useful tools in ultrasonic NDE since they can often be used to detect surface or near-surface defects and can propagate long distances [20]. Surface waves can be considered a subset of guided waves, since their propagation is confined to a surface and is therefore guided. In general, however, the term *guided*

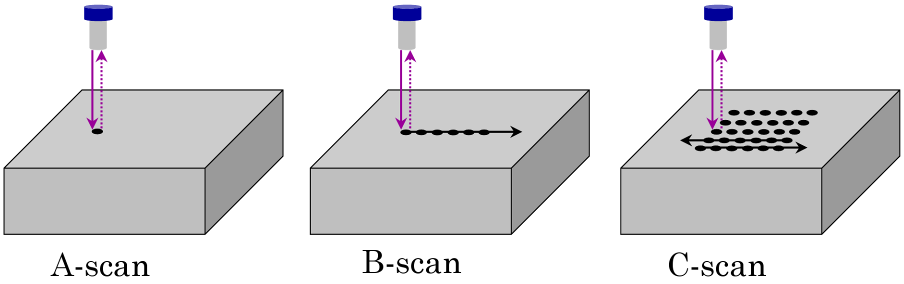

Figure 1.3: Diagram of pulse-echo A-, B-, and C-scans. Discrete measurement points indicated and scan paths shown with black arrows along sample surface. Measurement positions not necessarily to scale with transducer size.

waves generally applies to waves that are propagating in "waveguide-like" structures or objects such as thin plates or cylindrical shells whereas *surface waves* exist on "thick" solids (i.e. solids that can be considered thick when compared to wavelength). Sometimes surface and guided waves may be referred to as *interface waves* since they require the presence of one or more interfaces to propagate. These distinctions in terminology, however, vary across the disciplines in which these waves are studied.

Surface and guided waves are, in general, neither purely longitudinal nor purely shear, but exhibit particle displacements that are a combination of these two polarizations. One of the main differences between surface and guided waves is that surface waves (at least on isotropic and homogeneous media) are not dispersive, but guided waves such as Lamb modes on a thin plate (even if the plate is made of an isotropic and homogeneous material) are dispersive and their velocity will vary with frequency and plate thickness.

There are usually several different types of surface or guided waves that can exist on a given structure, depending on the nature of the materials and interfaces involved [21]. The following chapters of this thesis will mention four types of waves that require the presence of at least one interface in order to propagate, namely Rayleigh, Scholte-Stoneley, Stoneley, and Lamb waves. The Rayleigh and Scholte-Stoneley waves will be discussed in the context of fluid-solid interfaces, and the Stoneley wave in the case of an interface between two solids. For the study of thin plates, Lamb wave generation must be considered.

Rayleigh and Lamb waves [22] are commonly encountered in ultrasonics [23], and although Stoneley [24] waves are more commonly encountered in geophysics, they have been investigated in ultrasonics as well [25, 26]. Scholte-Stoneley waves [27] are less commonly studied, but they play an important role in diffraction on periodic surfaces.

1.2.1 Rayleigh waves

The Rayleigh wave, first predicted theoretically by Lord Rayleigh [28], is a wave that exists on the surface of a semi-infinite isotropic elastic solid having stress-free boundary conditions (i.e. a solid-vacuum interface). The particle motion is elliptical since the wave is a type of coupling between longitudinal and shear waves in the solid, and it propagates undamped along the surface. The wave experiences an exponential decay in amplitude with distance from the surface, meaning that its energy is truly confined to the surface. There is a tremendous body of literature that exists on Rayleigh waves, especially since they have proven useful in the detection of surface cracks in ultrasonic NDE. The speed of the Rayleigh wave on a solid can be determined from the "Rayleigh equation" [21, 22, 29, 30], and the result is that its velocity is generally slightly lower than the shear wave speed in the solid material. This velocity is constant with frequency, as the wave is non-dispersive [31].

For the case of a fluid-solid interface (water-solid being commonly encountered in ultrasonics), the boundary conditions at the surface are slightly different. The surface of the solid is no longer considered stress-free was it is in the strict definition of the Rayleigh wave. Now, normal stresses and normal particle displacements are continuous, but the tangential stress vanishes in the fluid at the interface [21]. The secular equation that can be solved for the wave speed(s) along the surface tends to the Rayleigh equation mentioned above as the density of the fluid becomes negligible compared to the density of the solid. One of the roots of the equation corresponds to the “generalized Rayleigh wave” on the surface. Its velocity is slightly less than what the true Rayleigh wave speed would be on the solid (that is to say if the solid did experience the stress-free boundary condition), and it tends towards the true Rayleigh wave speed as the density of the fluid tends to zero. This wave decays as it propagates along the surface because it will “leak” energy into the fluid. Therefore, the term “leaky Rayleigh wave” or even just “Rayleigh wave” (even though it is understood that it is not one in the strictest sense) may also be used for this wave.

There are multiple methods of generating Rayleigh waves [19, 22], and one of these methods involves aiming a sound beam (perhaps through a fluid medium or with the use of a solid wedge) upon the solid surface at the “Rayleigh angle” [22, 32, 33] so the incident wave is phase-matched to the Rayleigh wave along the surface. The principle of phase-matching is so important in acoustic and elastic wave behavior that it will now be discussed before the other types of surface and guided waves are presented.

1.2.2 Surface wave generation: phase matching and Snell’s law

Phase-matching (which may also be called trace velocity matching) can be expressed in the form of Snell’s law which is shown in Equation 1.1 and depicted graphically in Figure 1.4.

$$\frac{c_1}{\sin\theta_1} = \frac{c_2}{\sin\theta_2} \tag{1.1}$$

Figure 1.4 shows a wave incident upon an interface between two media. The wave originates in the upper medium with sound speed c_1 and is transmitted into the lower medium where its speed will be c_2. The term *phase-matching* refers to the fact that the phases of the incident wave and transmitted wave (or their trace wavelengths λ_{tr}) must match along the interface separating the two media. This can be seen in the figure where the colored bands represent wavefronts which are perpendicular to the

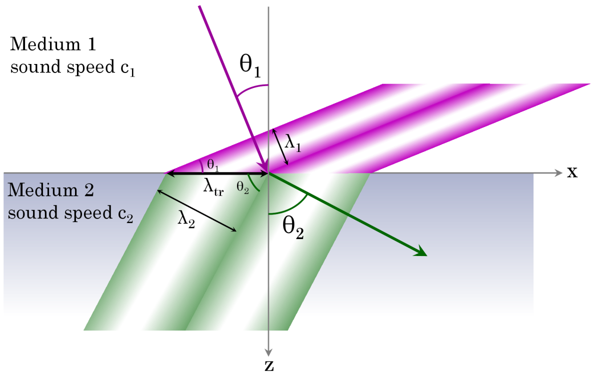

Figure 1.4: Illustration of phase-matching and Snell's Law. Phases of incident and transmitted waves match along the interface. Wavefronts depicted as shaded bands perpendicular to directions of propagation.

directions of propagation of the incident and transmitted waves. Mathematically this can be expressed as $\lambda_{tr} = \frac{\lambda_1}{\sin\theta_1} = \frac{\lambda_2}{\sin\theta_2}$ where λ_1 and λ_2 denote the wavelengths in each medium, respectively. For a wave with frequency f (so that $c = \lambda f$) this expression is equivalent to $\frac{c_1}{\sin\theta_1} = \frac{c_2}{\sin\theta_2}$, the most commonly encountered form of Snell's law. (Another way to express Snell's law is to say that the components of the incident and transmitted wave vectors along the x-direction as shown in Figure 1.4 must be equal. This statement will become more meaningful in Chapter 2 of this thesis.)

Clearly Figure 1.4 shows a simplified situation designed for the purposes of demonstrating phase-matching. For example, if the two media are fluids and therefore only support longitudinal waves, the incident and transmitted waves would propagate at each medium's respective wave speed as shown. However, if either medium is an isotropic solid, both longitudinal wave and shear wave speeds may be involved since mode conversion can occur between the two polarizations. In any case, mode conversion between longitudinal and shear waves and between these bulk waves and surface waves still involves phase-matching so c_1 and c_2 can be thought of as belonging to any bulk or surface wave.

To apply the phase-matching principle to the generation of Rayleigh or other surface waves, the variable substitutions $\sin\theta_2 = 1$ and $c_2 = c_{surf}$ are made in Equation 1.1 since the "transmitted" wave is the surface wave that propagates at c_{surf}. This results in the expression $\sin\theta_{surf} = \frac{c_1}{c_{surf}}$ [34]. The angle θ_{surf} is the angle at which sound must be incident from Medium 1 in order to generate a surface wave along the positive x-direction that will propagate with speed c_{surf}. To generate a Rayleigh wave along a liquid-solid interface using waves incident from the liquid (which have speed c), the expression becomes $\sin\theta_R = \frac{c}{c_R}$ where c_R is the Rayleigh wave speed and θ_R is the angle known as the *Rayleigh angle.*

1.2.3 Scholte-Stoneley waves

This discussion on the generation of Rayleigh waves leads to the second type of surface wave that can exist on a fluid-solid interface, the Scholte-Stoneley wave. Generating this type of wave is not as straight-forward a process as in the case of the Rayleigh wave.

An additional solution to the secular equation for the fluid-solid interface mentioned in the case of the Rayleigh wave belongs to a wave with a velocity less than the velocity of sound in the fluid. (If the longitudinal and shear wave speeds in the solid can be denoted by c_{long} and c_{shear}, respectively, and the velocity of sound in the fluid by c, then in general, $c < c_{shear} < c_{long}$). This wave is the Scholte-Stoneley wave. Referring to this wave by the name "Scholte-Stoneley" is consistent with several other references [35, 36]. However, it should be noted that this wave is sometimes referred to as a Scholte wave [37], a Stoneley wave [21, 30], or even a "pseudo-Stoneley" wave [27]. These naming conventions are explained by the fact that the first examination of the possibility of waves existing at the interface of two solids is attributed to Stoneley [24], but it was Scholte who considered the case where one of the media is a fluid [38].

The Scholte-Stoneley wave is a surface wave that propagates without attenuation along the surface since its speed is lower than the speed of sound in the fluid, and it has no counterpart in the solid-vacuum interface case since most of the energy of the Scholte-Stoneley wave remains in the fluid (as long as the density of the fluid is much lower than the density of the solid) [21, 39]. Generation of Scholte-Stoneley waves has proven more difficult [39] than the generation of Rayleigh waves since based on Snell's law, it is clear that no phase-matching can occur between bulk waves and Scholte-Stoneley waves, at least on a smooth surface. (If c_{SSt} is used to denote the Scholte-Stoneley wave velocity and θ_{SSt} to denote the incident angle necessary to generate the wave, it is clear in the expression $\sin\theta_{SSt} = \frac{c}{c_{SSt}}$ derived from phase-matching conditions that the argument of the sin would be greater than 1.)

Some methods that have been proposed to bypass this phase-matching breakdown include a liquid wedge technique [40] and the conversion of Rayleigh waves along a partially submerged solid [27]. However, the diffraction and mode conversion that occurs on periodic surfaces represents a more convenient method for the generation of these waves [41, 42]. Because diffraction and mode conversion presents a coupling between bulk waves and Scholte-Stoneley waves, the term "leaky" will be applied in this case [43], and these waves will be investigated further in Chapter 4 of this thesis.

1.2.4 Stoneley waves

As mentioned above, waves that propagate at the interface of two solids are generally termed *Stoneley waves.* These waves were first considered theoretically by Stoneley in the context of geophysics [24]. He considered the problem of elastic wave propagation at the interface between two isotropic solids with different elastic constants where the boundary conditions across the interface consist of continuity of particle displacement and continuity of stress.

Since Stoneley waves requires the presence of a second medium (as opposed to the true Rayleigh wave), these waves may be more properly referred to as *interface* *waves* rather than surface waves. It is important to note that strict conditions on elastic constants govern the material pairs for which Stoneley waves can exist [44, 45]. Broadly speaking, the shear wave speeds of the two solids must be nearly equal in order for a Stoneley wave to exist. The speed of the Stoneley wave is then in between the fastest Rayleigh wave speed and slowest shear wave speed for the two media [45]. (For Rayleigh waves, $v_R < v_{shear}$ and for Stoneley waves, $v_R|_{fastest} < v_{St} < v_{shear}|_{slowest}$.) Like the Rayleigh and Scholte-Stoneley waves already discussed, the particle displacements are two-dimensional (i.e. they consist of both longitudinal and shear components) and elliptical in nature, and the wave decays rapidly with distance from the interface.

Although Stoneley waves have been of more interest in geophysics than in ultrasonics, there has been some interest in Stoneley wave applications in ultrasonics. Some examples include the possibility of employing them in signal processing devices in harsh environments [26] and in NDE of material bonds and laminated structures [46]. Ultrasonic Stoneley waves have been generated by the conversion of Rayleigh waves [26, 46] on a surface and with a wedge technique to phase-match bulk waves to Stoneley waves [47]. However, if the interface between the two solids is periodic, diffraction and mode conversion of bulk waves incident from one of the solid media may present another method of generating Stoneley waves.

1.2.5 Lamb waves

Pure surface waves such as Rayleigh and Scholte-Stoneley waves cannot exist on thin plates unless their wavelengths are sufficiently small compared to the plate thickness. When the thickness of the plate is on the order of a wavelength for the wave frequencies considered, the multiple reflections and interference patterns of longitudinal and shear waves within the plate result in *Lamb waves* which propagate along the plate [22, 48].

Just as the Rayleigh wave is strictly defined as existing on a solid-vacuum interface, so Lamb waves are strictly defined as modes of vibration for a homogeneous and isotropic thin plate in a vacuum [22]. Despite this strict definition, one can also refer to "leaky" Lamb waves that can exist on fluid-loaded plate just as leaky Rayleigh waves can exist on a fluid-loaded solid surface [49]. An infinite number of Lamb modes exist, but they can be classified as being either symmetric or antisymmetric, depending on the symmetry of the particle motion with respect to the plane of the plate that passes through its neutral axis. Lamb waves are dispersive, and dispersion curves can be calculated that show phase and group velocity as a function of the product of frequency and plate thickness fd for various modes [29].

Much like Rayleigh waves, there has been intense and long-standing interest in the investigation in both the theory and application of Lamb waves, see for example Refs. [23] and [50], especially for NDE of structures that possess thin plate-like features. Lamb waves are of interest in the study of diffraction on periodic surfaces in the event that a diffracted mode generated along the surface may couple to a Lamb mode [51].

1.3 History of ultrasonic diffraction effects on periodic surfaces

Although the study of diffraction on periodic surfaces was initiated by Lord Rayleigh [1], studies within the ultrasonic regime really began to occur in the late 1970's and early 1980's, most likely due to a general increase in research interest in ultrasonics and due to the increased availability of computational power to perform numerical calculations. Therefore, this discussion of the history of ultrasonic diffraction effects on periodic surfaces will begin with this generation of researchers.

As discussed in the previous section, phase-matching considerations are one way in which periodic surfaces differ from smooth surfaces. One additional significant difference between periodic surfaces and smooth surfaces is that certain unique features occur in the reflection and transmission spectra obtained from periodic surfaces that do not appear in the spectra resulting from smooth surfaces. In particular, sharp discontinuities occur at certain frequencies in the spectra obtained from periodic surfaces. These discontinuities were first observed experimentally in ultrasonics by Jungman et al. [4] in the early 1980's and were interpreted as being due to mode conversion between bulk and surface waves along the surface. They were named Wood anomalies in reference to the analogous optical phenomena introduced by Wood [52]. Although the classical grating equation successfully described the relationship between surface periodicity, surface wave velocities, and frequency positions of the anomalies, no other theoretical treatment was available at the time that could predict the occurrence of these anomalies in the spectra.

However, it was soon discovered by Claeys and Leroy [53] that the Rayleigh-Fourier method for modeling diffraction on periodic surfaces could accurately predict ultrasonic reflection and transmission spectra obtained from periodic liquid-solid interfaces [4, 54]. Anomalies in the spectra were attributed to the generation of Rayleigh or Scholte-Stoneley waves as a result of diffraction and mode conversion on the surface [55]. As discussed in the previous section, methods to generate Rayleigh waves on most solid surfaces are well known, but phase-matching considerations generally prevent coupling between bulk waves and Scholte-Stoneley waves on smooth surfaces. Therefore, the diffraction parallel to the surface and consequent mode conversion on periodic surfaces that can result in Scholte-Stoneley wave generation became recognized as a potential technique to generate this type of wave in situations where it is not possible otherwise.

Although the Rayleigh-Fourier (R-F) method was developed to model diffraction spectra resulting from known periodic profiles, Jungman et al. [41] hypothesized that the inverse problem could be addressed, namely the determination of a profile's geometric characteristics (periodicity and height) from experimentally determined spectra, a type of ultrasonic NDE for periodic surfaces. It was shown that the value of a surface's periodicity can be determined from the frequencies of the Wood anomalies in its spectra if the velocities of the surface waves responsible for the appearance of those anomalies are known [56]. Simulations were also performed for periodic surfaces with identical periodicities but different profile heights, and it was shown that the depth of the Wood anomalies increased with profile height [41]. The inspection of periodic surfaces has been attempted using not only reflection and transmission spectra, but also using backscatter that is generated at specific (Bragg) angles [57], and the R-F method can be used to calculate the theoretical amplitude of this backscatter as a function of a surface's profile and material properties. Unfortunately, theoretical techniques such as the Rayleigh-Fourier method can generally only accommodate surfaces having perfect periodicities [13]. "Real" periodic surfaces with imperfect periodicities, however, are more likely to be encountered in practice. Therefore, due to the limitations of theoretical techniques such as the R-F method, experimental investigations of diffraction effects such as Wood anomalies on such surfaces are preferable.

The R-F method was originally developed to accommodate time-harmonic homogeneous plane waves, but it was eventually extended to accommodate inhomogeneous waves [51, 58]. When combined with a theoretical decomposition of an ultrasonic bounded beam in terms of inhomogeneous waves [59], the diffraction resulting from a bounded beam instead of a plane wave of infinite extent was able to be simulated. This new simulation technique was able to address a phenomenon that had been observed by Breazeale and Torbett [60] almost 30 years earlier in the late 1970's, namely a lateral backward displacement of an ultrasonic beam in reflection from a periodically corrugated water-brass interface. Breazeale and Torbett hypothesized that the backward displacement was caused by a backward propagating surface wave in a manner analogous to the forward Schoch displacement that occurs as a result of Rayleigh wave generation [61, 62], but they could not identify the type of surface wave responsible for the displacement. By simulating bounded beam diffraction on a periodic surface, Declercq et al. [63] were able to attribute the phenomenon to the generation of a backward propagating leaky Scholte-Stoneley wave [43].

To summarize this history, the Rayleigh-Fourier method has successfully been used to theoretically predict diffraction effects including Wood anomalies and Scholte-Stoneley wave generation on periodically corrugated surfaces. Wood anomalies have been used to determine geometric parameters of a periodic surface, and Scholte-Stoneley waves can potentially be used for the detection of surface defects, making both of these diffraction effects relevant to ultrasonic NDE. These effects may also occur on surfaces having imperfect periodicities that cannot be modeled using techniques such as the R-F method.

1.4 Research motivation and objectives

In addition to the studies mentioned in the previous section, the study of periodic surfaces has also increased recently in a number of different application areas. Surface acoustic waves on periodic fluid-fluid interfaces have been investigated in their theoretical ability to assist in the collimation of sound [64]. Research in ultrasonic NDE applications for periodic surfaces has also increased in recent years. One example is the study of Lamb wave propagation in corrugated plates (waveguides) with application in the NDE of non-planar surfaces [65]. The characterization of periodically rough surfaces has also recently received attention due to the role they play in adhesive bond quality [66]. The diffraction occurring on periodic surfaces has been studied in the industrial context of the development of acoustic monitoring systems for heat exchangers consisting of tube bundles [67] as well as in the framework of the development of real-time ultrasonic inspection systems for machined part surfaces [68]. Periodically rough claddings on thick plates and pipes used to reduce corrosion that are often found in the nuclear power industry are also a current area of study [69].

The applications for periodic surfaces currently observed and envisioned for the future are numerous and diverse, and they are the driving force behind the continued study of acoustic and elastic wave interaction with such surfaces. However, according to Beckmann there are at least two other reasons why scattering on periodic surfaces merits close attention [70]. The first is that the results obtained are general enough to give some indication of the global behavior of rough surfaces, and the second is that if a surface is to be manufactured with the specific aim of preventing specular reflection or preventing scattering in a certain direction, it would be easier to make the roughness periodic than to make it random with some prescribed probability distribution.

As stated earlier, the research presented in this thesis is focused on one particular aspect of acoustic and elastic wave interaction with periodic surfaces, namely the diffraction that results from the surface periodicity. In particular, the objective of this thesis research is to advance the current state of knowledge of acoustic and elastic wave diffraction that occurs on periodic surfaces using both theoretical and experimental methods and increase potential applications for diffraction effects in ultrasonic NDE methods and contribute to the body of knowledge on phononic crystals. The first step in meeting this objective leads to Chapter 2 of this thesis, where the Rayleigh-Fourier method will be applied to simulate ultrasonic diffraction on structures containing multiple periodic surfaces and multiple solid materials.

CHAPTER II

THE RAYLEIGH-FOURIER METHOD FOR THE SIMULATION OF ULTRASONIC DIFFRACTION ON PERIODIC SURFACES

2.1 Introduction to the Rayleigh-Fourier method

The study of wave diffraction on periodic surfaces can be traced back to Lord Rayleigh who first considered the problem of determining the reflected field generated by a time-harmonic plane wave normally incident on a surface having a sinusoidal roughness [1, 2, 71]. Since then, much effort has been focused in both acoustics and optics towards the development of theoretical techniques to describe and predict the scattering (diffraction) that occurs on periodic surfaces.

Although multiple theoretical techniques exist, Rayleigh's approach to the problem has proven to be so useful that it still attracts discussion and research efforts over 100 years after Rayleigh's first work [72]. Methods that rely in some form on his approach are often termed "Rayleigh methods" but the particular Rayleigh method used in this thesis, the so-called "Rayleigh-Fourier" method, stands apart since it is straight-forward and requires a relatively short computational time compared to other methods [13, 58]. This method carries the names of Rayleigh and Fourier since it relies on the plane wave expansion series first used by Rayleigh which is followed by the use of Fourier coefficients to handle the periodicity of the surface. Although the method has sometimes appeared in the literature under different names, the "Rayleigh decomposition" [43] for example, the use of the name "Rayleigh-Fourier" helps distinguish the method from other Rayleigh methods [73].

A fundamental distinction should be made between the Rayleigh-Fourier method and Kirchoff theory that is often used to treat scattering from randomly rough surfaces [70, 71]. Whereas Kirchoff theory provides an approximation to the wave field on the scattering surface that can then be used in an integral formula to calculate the scattered field at a distance, the Rayleigh-Fourier (R-F) method functions in an inverse manner.

In the R-F method, a known form for the scattered field at a distance from the surface is assumed, namely a series expansion of plane waves with wave vectors that are determined from the classical grating equation. The series expansion coefficients are then obtained by satisfying the boundary conditions on the periodic surface. One particular advantage of the R-F method is that the coefficients of the plane wave series can be interpreted as reflection or transmission coefficients, or amplitudes of the individual modes that make up the reflected field. This is in contrast to other methods where the physical interpretation of the coefficients is not straight-forward [70].

2.1.1 Description of the problem

The physical problem of acoustic and elastic wave scattering from a single periodic surface can be defined as follows [13]. An acoustic or elastic wave with wavelength λ_i is incident at angle θ_i on a periodic interface that separates two semi-infinite media as shown in Figure 2.1. Although the periodic surface shown in Figure 2.1 happens to have a sawtooth profile (for ease of illustration), it is possible to treat other surface profiles with the method. In general, the boundary needs to be described by $z = f(x)$ where $f(x) = f(x + \Lambda)$ and Λ is the periodicity of the surface. Due to the surface periodicity, the scattered field will be concentrated in certain directions, or diffraction orders, with the specular reflection representing diffraction of order zero. The goal is to determine the distribution of the diffracted field amongst the orders. In the study of optical diffraction gratings, this distribution may be referred to as diffraction efficiency.

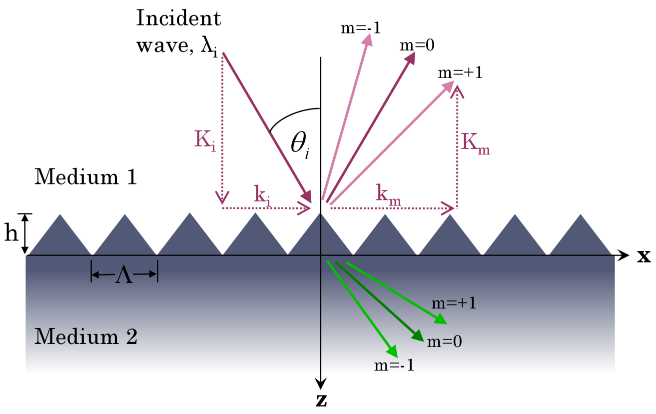

Figure 2.1: Diagram of diffraction on a periodic surface.

The directions of the diffraction orders are determined by the classical grating equation shown in Equation 2.1. In this expression, k_i is the component of the incident wave vector along the surface as shown in Figure 2.1, m is the integer identifing the diffraction order, and k_m is the component of the wave vector along the surface for diffraction order m. The x- and z-components of the wave vectors are related through Equation 2.2 where ω is the angular frequency $(2\pi f)$ of the wave, v is the wave speed for the type of wave being considered, and k and K signify the components of the wave vectors parallel to and perpendicular to the surface, respectively.

$$k_m = k_i + \frac{2\pi}{\Lambda}m \tag{2.1}$$

$$\left(\frac{\omega}{v}\right)^2 = k^2 + K^2 \tag{2.2}$$

For the case shown in Figure 2.1, if "Medium 1" is a fluid, then both $k_i^2 + K_i^2$ and $k_m^2 + K_m^2$ will be equal to $\left(\frac{\omega}{v_1}\right)^2$ where v_1 is the longitudinal wave speed in the fluid. (Throughout this chapter and in Appendices A-E, variables employing a lower-case k will be used to signify wave vector components parallel to the surface, and variables employing an upper-case K will refer to wave vector components perpendicular to the surface. However, in Section 2.1.4 when the variable $\vec{k}$ appears, it will refer to the wave vector itself with magnitude $\frac{\omega}{v}$ and x- and z- components k and K, respectively.)

2.1.2 The classical grating equation

Before continuing, it is appropriate to briefly discuss the classical grating equation that has just been introduced. In this chapter, surfaces that consist of a periodic series of grooves are being considered. These surfaces function as acoustic diffraction gratings so the behavior of the waves that are incident on the surfaces can be described by the so-called classical grating equation. The equation can take several different forms, one of which is Equation 2.1.

When sound is incident on a periodically corrugated surface, each one of the grooves on the surface becomes a small source of reflected and/or transmitted sound. Therefore, for a given periodicity value, there exists a unique set of angles where the sound scattered from all the grooves is in phase (i.e. does not experience destructive interference). Figure 2.2 shows a plane wave incident on a grating surface at an angle θ_i with respect to the normal to the surface (grating normal). The geometric path length difference between the sound reflected by adjacent grooves in direction θ_m is equal to $\Lambda \sin\theta_i - \Lambda \sin\theta_m$ where Λ is equal to the groove periodicity and angle θ_m is the angle of diffraction. When this path length difference is equal to the wavelength λ or an integer multiple m of the wavelength, constructive interference will occur. At all other angles, destructive interference will occur. Thus, the well-known ability of gratings to diffract the incident wave into clearly identifiable directions can be expressed by Equation 2.3. This equation can be transformed into Equation 2.1 through straight-forward algebra.

$$\Lambda \sin\theta_m - \Lambda \sin\theta_i = m\lambda \tag{2.3}$$

2.1.3 Assumptions

Several natural assumptions have been made in the formulation of the problem so that it can be treated using the Rayleigh-Fourier method. The incident wave is considered to be a time-harmonic plane wave. Using a wave of a single frequency is acceptable

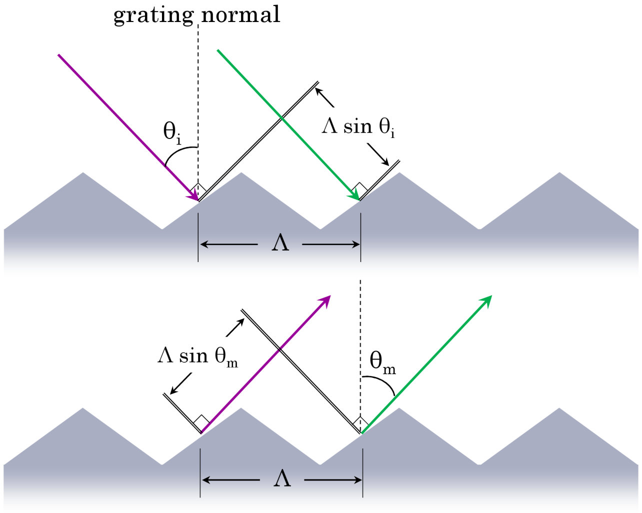

Figure 2.2: Diagram showing path length difference between sound reflected off adjacent grooves on a periodically corrugated surface.

within the regime of linear acoustics since a sound pulse containing many spectral components will be diffracted as a linear superposition of those components. The use of an infinite plane wave is generally acceptable for as long as the beam width exceeds many wavelengths, the finite width of the beam can be neglected. Prior studies have shown that results from simulations performed using infinite plane waves correspond well with experimental results obtained using bounded beams [54]. There are some exceptions to this, however, such as in the simulation of certain effects that are clearly beam-width dependent, such as lateral beam displacements along the surface [43, 74].

The material properties of the media (density and Lamé constants or wave speeds) are considered to be known and the media are assumed to be homogeneous and isotropic. The corrugated surface is considered to be infinitely long and perfectly periodic. The direction of incidence is considered to be perpendicular to the grooves, so that if the grooves exist along the y-direction of the x-y plane (the y-axis would be directed out of the page for the coordinate axes shown in Figure 2.1), the direction of propagation of the incident wave is confined to the x-z plane. For a fluid medium, the incident wave is longitudinal whereas for a solid medium, the incident wave may have one of three polarizations: longitudinal, vertical shear, or horizontal shear. For both the longitudinal and vertical shear polarizations, the particle motion is confined within the x-z plane whereas for the horizontal shear polarization, the particle motion is confined to the y-direction. In general, we can expect mode conversion to occur between longitudinal and vertical shear wave polarizations whenever a solid medium is present, but horizontal shear waves can exist only if waves of this polarization are initially incident on the surface [75].

One important aspect of the Rayleigh-Fourier method, or any method based on the plane wave series first used by Rayleigh, remains to be discussed. The assumed series expansions for the diffracted fields satisfy certain radiation conditions, namely that only one incident wave carries energy towards the surface. Therefore, all the reflected and transmitted diffraction orders are evanescent or propagating *away* from the interface. (The z-components of the diffracted wave vectors, calculated from Equation 2.2, are always chosen so that they propagate away from the interface.) Although these series expansions are valid outside the corrugated region (above the line that connects the highest points of the grooves and below the line that connects the lowest points), the assumption that they are valid within the corrugated region and can be used to satisfy the boundary conditions at the surface has been a subject of debate for over 50 years [12, 76].

The use of only outgoing waves has come to be known as the "Rayleigh hypothesis" and it was first criticized by Lippmann [77] in 1953, who argued based on intuition that, especially for very rough corrugations, one must also consider waves traveling towards the surface. The essence of the Rayleigh hypothesis is that the far-field solution to the problem can beused to satisfy the boundary conditions in the near-field. Although the R-F method is based on this long-debated hypothesis, the method is generally accepted to be valid in its description of diffraction phenomena that occur when the incident wavelength λ_i is on the order of the surface periodicity $\lambda_i \approx \Lambda$ and much larger than the height of the surface corrugation ($max\,|f(x)| \ll \lambda_i$) [58, 78].

2.1.4 Theoretical development

The solution to the diffraction problem must satisfy the wave equation (equation of motion) within the bulk of each medium, and it must also satisfy the boundary conditions at the periodic surface. Therefore, solution forms for the wave fields in the media that satisfy the wave equation are assumed first, and these forms are then used to satisfy the boundary conditions at the surface.

The derivation of the equation of motion for an infinite elastic solid has been covered in many textbooks [29, 30, 79] so it will not be repeated here. The final form of the equation for particle displacement in vector form $\vec{u}$ within a homogeneous infinite elastic solid medium can be expressed as

$$\rho \frac{\partial^2 \vec{u}}{\partial t^2} = (\lambda + \mu)\nabla\left(\nabla \cdot \vec{u}\right) + \mu \nabla^2 \vec{u} \tag{2.4}$$

where ρ is density, λ and μ are the Lamé constants, and t is time. By assuming the solution to be a homogeneous plane wave (where the wavefront is of infinite extent normal to the direction of propagation and all displacements are uniform over the wavefront at a given instant in time), two bulk wave solutions are possible [80]. These correspond to a longitudinal wave, where the particle displacement is along the direction of propagation, and a shear wave, where the particle displacement is normal to the direction of propagation. (An ideal fluid medium can be considered to be a special case of the above equation where $\mu = 0$, and the only bulk wave that can exist is longtudinal in nature.)

The particle displacement resulting from these solutions can be conveniently expressed in terms of derivatives of potential functions. In particular, the Helmholtz decomposition can be used so that $\vec{u} = \nabla\varphi + \nabla \times \vec{\psi}$ where $\nabla \cdot \vec{\psi} = 0$ [29, 79]. In this formulation, $\varphi(\vec{x}, t)$ is a scalar potential for the longitudinal wave and $\vec{\psi}(\vec{x}, t)$ is a vector potential for the shear wave. The vector field $\vec{u}$ will satisfy the wave equation as long as φ and $\vec{\psi}$ are solutions to wave equations where the bulk wave speeds correspond to the longitudinal wave speed v_l and shear wave speed v_s, respectively [79], as shown in Equation 2.5. In Equation 2.5, the longitudinal and shear wave speeds are given as a function of the Lamé constants λ and μ and the density ρ for the material.

$$\begin{aligned} \nabla^2\varphi &= \frac{1}{v_l^2}\frac{\partial^2\varphi}{\partial^2 t} \quad \text{where } v_l &= \sqrt{\frac{\lambda+2\mu}{\rho}} \\ \nabla^2\vec{\psi} &= \frac{1}{v_s^2}\frac{\partial^2\vec{\psi}}{\partial^2 t} \quad \text{where } v_s &= \sqrt{\frac{\mu}{\rho}} \end{aligned} \tag{2.5}$$

The diffraction problem as it has been framed in Figure 2.1 can be considered to exist in two-dimensions. In this case, all waves would be restricted to existence in the x-z plane, and the shear waves can be considered to exist in two polarizations, namely vertical and horizontal. Both types of shear waves have their propagation direction within the x-z plane, but their particle displacements are not necessarily confined to the plane as well. The vertical shear waves do consist of particle displacement restricted to the x-z plane, but the horizontal shear waves have their particle displacement confined to the y-direction perpendicular to the x-z plane so they would not be considered in the problem. This is possible since the propagation of these two types of shear waves is independent.

If a solid medium is considered in the diffraction problem as it has been defined, longitudinal waves (with particle displacement occurring along the x- and z-directions) incident on a periodic surface can experience mode conversion to vertical shear waves but they will not transform into horizontal shear waves. Likewise, vertical shear waves can experience mode conversion to longitudinal waves, but not horizontal shear waves. Therefore, several implementations of the Rayleigh-Fourier method [51, 54, 81] have considered only "vertical" waves, defined as being waves with particle displacement in the x-z plane only, i.e. longitudinal and vertical shear waves. This results in the shear waves being represented by the vector function $\vec{\psi} = \psi\vec{e_y}$ (where $\vec{e_y}$ is a unit vector in the y-direction) so that the vector $\nabla \times \vec{\psi}$ will have components in the x-and z-directions only. For the case when only "vertical waves" are considered, the potential functions are assumed to be those shown in Equations 2.6 and 2.7.

$$\varphi = A_L \, e^{i(\vec{k}\cdot\vec{x}-\omega t)} \tag{2.6}$$

$$\vec{\psi} = \psi \vec{e_y} = \begin{bmatrix} 0 \\ A_S \, e^{i(\vec{k}\cdot\vec{x}-\omega t)} \\ 0 \end{bmatrix} \tag{2.7}$$

In these equations, A_L and A_S represent amplitude and $e^{i(\vec{k}\cdot\vec{x}-\omega t)}$ is the complex exponential form of expressing the plane waves. Since the wave vector $\vec{k}$ has only the components k and K in the x- and z- directions, respectively, these potential functions result in the longitudinal and shear displacement vectors $\vec{u_L}$ and $\vec{u_S}$ shown in Equation 2.8.

$$\vec{u_L} = \nabla\varphi = \begin{bmatrix} ik\varphi \\ 0 \\ iK\varphi \end{bmatrix} \text{ and } \vec{u_S} = \nabla \times \vec{\psi} = \begin{bmatrix} -iK\psi \\ 0 \\ ik\psi \end{bmatrix} \tag{2.8}$$

If horizontal shear waves are to be included in the problem as well, an alternate but equivalent formulation can be used where the particle displacement for the shear waves is expressed directly in vector form [75]. This is the approach that will be employed in this thesis. Therefore, the displacement vector used to represent shear waves is instead

$$\vec{u_S} = \begin{bmatrix} P_x A_S \, e^{\vec{k}\cdot\vec{x}-\omega t} \\ P_y A_S \, e^{\vec{k}\cdot\vec{x}-\omega t} \\ P_z A_S \, e^{\vec{k}\cdot\vec{x}-\omega t} \end{bmatrix} \tag{2.9}$$

where P_x, P_y, and P_z are polarization factors that determine the polarization of the shear wave. (For a vertical wave, $P_y = 0$, and for a horizontal wave, $P_x = P_z = 0$.) It is then necessary to explicitly state that the shear wave direction of propagation is perpendicular to its particle displacement, and this can be accomplished by requiring that $\vec{k} \cdot \vec{u_S} = 0$ so then $kP_x + KP_z = 0$.

Once the solution form has been chosen in terms of longitudinal and shear waves, the plane wave expansion that is attributed to Rayleigh can be constructed. For the medium containing the incident wave, the field will consist of the incident wave along with the specular reflection (diffraction of order zero) and an infinite series of propagating and evanescent plane waves for the other diffraction orders. For example, if "Medium 1" in Figure 2.1 is a fluid, the particle velocity for the entire field in the medium, $\vec{u}^{\mathbf{1}}$ where the superscript 1 designates the medium, would be expressed as

$$\vec{u}^{\mathbf{1}} = \nabla\varphi_i + \nabla\varphi_R \ . \tag{2.10}$$

Here, φ_i is the potential function for the incident wave, and φ_R is the potential for the series of diffracted waves. They can each be expressed as

$$\begin{gathered} \varphi_i = A_i e^{i(k_i x + K_i z)} \\ \varphi_R = \sum_{m=-\infty}^{\infty} \varphi_{Rm} = \sum_{m=-\infty}^{\infty} R_m e^{i(k_m x + K_{Rm} z)} \ . \end{gathered} \tag{2.11}$$

In the potential φ_i, A_i represents the amplitude of the wave, and k_i and K_i are the components of the wave vector in the x- and z-directions as previously discussed. The potential φ_R consists of the sum of the potentials φ_{Rm} associated with each reflected diffracted order m. For each order, the wave vector component k_m is computed from the grating equation and the corresponding K_{Rm} can then be found from Equation 2.2. The series expansion coefficients R_m are unknown, and it is through fulfilling the boundary conditions on the surface that they can be obtained. Because a time-harmonic wave is assumed, there is an $e^{-i\omega t}$ dependence that is implied in the expressions of Equation 2.11 (i.e. the full expressions have the form $e^{i(\vec{k}\cdot\vec{x}-\omega t)}$).

If one of the media in the problem is a solid, a series expansion consisting of diffracted shear modes must be included in addition to the diffracted longitudinal modes for that medium, even if the incident wave is longitudinal. This is due to the mode conversion that may occur at the interface. Likewise, if the incident wave is shear, longitudinal diffracted modes must be considered in addition to the shear modes.

For the problem shown in Figure 2.1, the transmitted field in “Medium 2” will consist of propagating and evanescent diffraction orders: longitudinal if the medium is a liquid, and longitudinal and shear for the case of a solid. The term propagating refers to orders for which both components of the wave vector, k_m and K_m, are real. Evanescent modes are those which have a real k_m calculated from the grating equation, but have an imaginary K_m determined from Equation 2.2.

Once expressions for the velocity fields in the media are constructed, they can be used to derive expressions for stresses and strains in the media according to linear elasticity theory. The components ϵ_{ij} of the small strain tensor can be expressed according to Equation 2.12 where $\vec{u}$ is the particle displacement vector having components u_i, u_j, and u_k and the position vector $\vec{x}$ has components x_i, x_j, and x_k.

$$\epsilon_{ij} = \frac{1}{2}\left[\frac{\partial u_i}{\partial x_j} + \frac{\partial u_j}{\partial x_i}\right] \tag{2.12}$$

Because the materials in the diffraction problem are considered to be linearly elastic, the strain tensor and the stress tensor will be linearly related according to Hooke’s law. Because the media are also considered to be homogeneous and isotropic, Hooke’s law for the stress tensor components T_{ij} ultimately reduces to Equation 2.13.

$$T_{ij} = \sum_k \lambda \epsilon_{kk}\delta_{ij} + 2\mu\epsilon_{ij} \tag{2.13}$$

In Equation 2.13, λ and μ represent the Lamé constants for the material, and δ_{ij} is the Kronecker delta. The expressions for stresses and strains that ultimately result from Equations 2.12 and 2.13 can then be substituted into boundary conditions that are appropriate for the interface being considered. The boundary conditions that must be satisfied depend on the nature of the interface (liquid-solid, solid-solid, etc.) but they generally involve continuity of particle displacement and continuity of stress.

For example, for a liquid-solid interface, continuity of normal particle displacement provides the first boundary condition, and the two remaining boundary conditions would be obtained through applying continuity of stress at the interface, with shear stress vanishing in the liquid. The continuity of normal particle displacement can be expressed through Equation 2.14 where the function $h(x, z) = f(x) - z = 0$ is used to represent the surface profile and the superscripts 1 and 2 are used to designate the media separated by the periodic boundary. The particle displacement vectors $\vec{u}^1$ and $\vec{u}^2$ represent the total displacement in the materials (i.e. the sum of any incident wave and any diffracted wave fields). The continuity of stress at the boundary is given by Equation 2.15. Although Equations 2.12 through 2.15 have been expressed using indicial notation, it is straightforward to convert these indicies to the x-,y-, and z-directions in which the diffraction problem has been framed.

$$\vec{u}^1 \cdot \nabla h = \vec{u}^2 \cdot \nabla h \tag{2.14}$$

$$\sum_{j=1}^{3} T^1_{ij} \left(\nabla h\right)_j = \sum_{j=1}^{3} T^2_{ij} \left(\nabla h\right)_j \tag{2.15}$$

To continue with the example of a liquid-solid interface, when a potential representation is used for the diffracted shear fields generated, three sets of series expansion coefficients are unknown (longitudinal in the liquid, and longitudinal and shear in the solid), and three boundary conditions to solve for these coefficients are obtained (one from the continuity of normal particle displacement and two from the continuity of stress). When using a direct displacement representation for the shear waves, however, one set of diffracted shear waves requires two series expansions (one for P_x and the other for P_z) so an additional boundary condition must be obtained by requiring that the direction of shear wave propagation be normal to the particle displacement as previously discussed. Regardless of the type of representation that is employed, the number of boundary conditions must match the number of unknown series expansions used to represent the diffracted fields in order to obtain the solution.

To solve for the series expansion coefficients that eventually appear in the boundary condition equations, the equations are expanded in Fourier series over one period of the surface corrugation, from 0 to Λ. The series expansion coefficients can then be determined by equating the resulting Fourier coefficients. Although the plane wave series used to represent the reflected and transmitted fields are technically infinite, a truncation to a finite number of modes must be performed so that the system can be solved numerically. Truncation to an order of 8 has been chosen based on the error calculations found in Refs. [54] and [55]. The end result is a linear system of the form $[A]\,\vec{x} = \vec{b}$ that can be solved for $\vec{x}$, the vector containing the unknown series expansion coefficients. If this linear system is evaluated for many frequencies, the resulting series coefficients for a particular order can be plotted as a function of frequency, which can be interpreted as a reflection or transmission spectrum for that order.

2.2 Prior applications of the Rayleigh-Fourier method

When Lord Rayleigh first considered the diffraction of sound from a periodic surface [1], he examined a case where the surface was perfectly reflecting, and for many years thereafter, the Rayleigh-Fourier method was used to treat diffraction occurring only on surfaces that were completely impenetrable to sound, either by being perfectly rigid or pressure-release [8, 82]. The treatment of cases where the second medium can support the transmission of waves is more complicated, and the R-F method was first used to address such a case in the early 1980's by Claeys and Leroy [53, 54] when they studied the diffraction occurring at liquid-solid interfaces. The R-F method was also examined for fluid-solid interfaces by Berman and Perkins [73]. It was later extended by Mampaert and Leroy [55] to accommodate incident waves originating in the solid and by Briers et al. [51, 58, 83] to accommodate incident inhomogeneous waves. Thin plates with a single surface corrugated have also been studied using the R-F method [51, 58, 81], and the method has also been extended by Declercq et

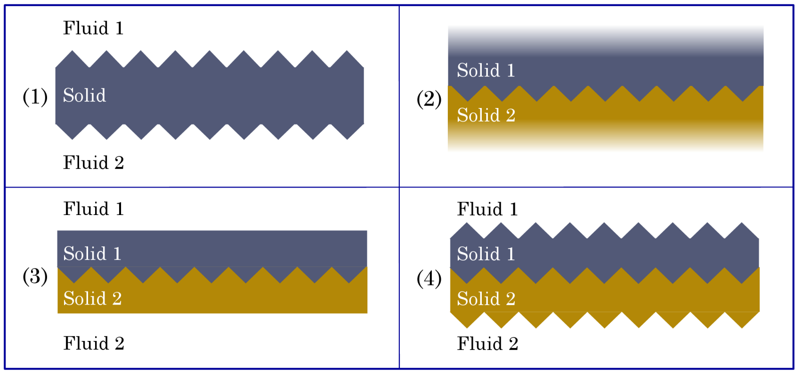

Figure 2.3: Four cases to treat with the Rayleigh-Fourier method.

al. [75] to study horizontal shear waves.

The following chapter sections will address the extension of the R-F method to four cases that have not yet been examined using the method, namely (1) a fluid-loaded-plate with both sides periodic, (2) a periodic interface separating two semi-infinite solid media, (3) a fluid-loaded plate consisting of two solids separated by a periodic interface, and (4) a fluid-loaded plate consisting of two solid layers where all surfaces are periodic. These cases are shown in Figure 2.3.

Before performing the theoretical derivations for these four new cases, it was desired to apply the R-F method with the direct displacement representation of the shear waves to the case of a fluid-loaded plate with one side periodic. This case has been treated before in the literature [51, 58] but only with a potential representation for the shear waves. A diagram of the diffracted fields present, along with the creation of the displacement fields and the derivation of the boundary conditions for the linear system $[A]\,\vec{x} = \vec{b}$ can be found in Appendix A.

A brass plate with an average thickness of 2 mm is considered immersed in water with a wave normally incident from the water upon the plate's periodic side. The periodic profile is considered to be sawtooth with its periodicity Λ equal to 2.2 mm and the peak-to-peak height h equal to 50 µm. Densities and wave speeds for the media are shown in Table 2.1.

Table 2.1: Material properties.

	Water	Brass	Titanium	Steel
ρ (kg/m^3)	1000	8100	4440	7860
v_d (m/s)	1480	4840	6110	5890
v_s (m/s)	N/A	2270	3270	3210

The calculated spectrum for the zero-order reflection coefficient R_0 is shown at the top of Figure 2.4. A spectrum by definition is not limited to discrete values of frequency, but for the purposes of the computations of the Rayleigh-Fourier method, the calculations must be limited to discrete frequency samples. Just as in any physical experiment, the sampling rate at which measurements are taken (or in this case, at which simulations are performed) should have a sufficiently fine resolution so that important features in the spectrum are not missed. The spectrum shown in Figure 2.4 has been computed with a 500 Hz frequency resolution. The results are consistent with those found in Refs. [51] and [58]. Large drops in the spectrum are seen at frequencies of 1.21 MHz and 2.42 MHz which correspond to plate thickness resonances for longitudinal waves normal to the plane of the plate. The plate thickness resonances correspond to cut-off (or rather cut-on) frequencies for Lamb modes, and these two frequencies correspond to the S_2 and A_3 modes, respectively. These "limiting frequencies" for a plate of a given thickness d can be calculated from the expressions shown in Equation 2.16 [19]. In these expressions, λ_d and λ_s are equal to the bulk wave speeds v_d (longitudinal) and v_s (shear), respectively, divided by frequency f.

$$\begin{array}{c|c}
\text{Symmetric modes} & \text{Antisymmetric modes} \\
\hline
d = \dfrac{\lambda_d}{2}\ ,\ \dfrac{3\lambda_d}{2}\ ,\ \dfrac{5\lambda_d}{2}\ ,\ \ldots & d = \lambda_d\ ,\ 2\lambda_d\ ,\ 3\lambda_d\ ,\ \ldots \\
d = \lambda_s\ ,\ 2\lambda_s\ ,\ 3\lambda_s\ ,\ \ldots & d = \dfrac{\lambda_s}{2}\ ,\ \dfrac{3\lambda_s}{2}\ ,\ \dfrac{5\lambda_s}{2}\ ,\ \ldots
\end{array} \tag{2.16}$$

Other than these two large drops in the spectrum, additional anomalies are visible.

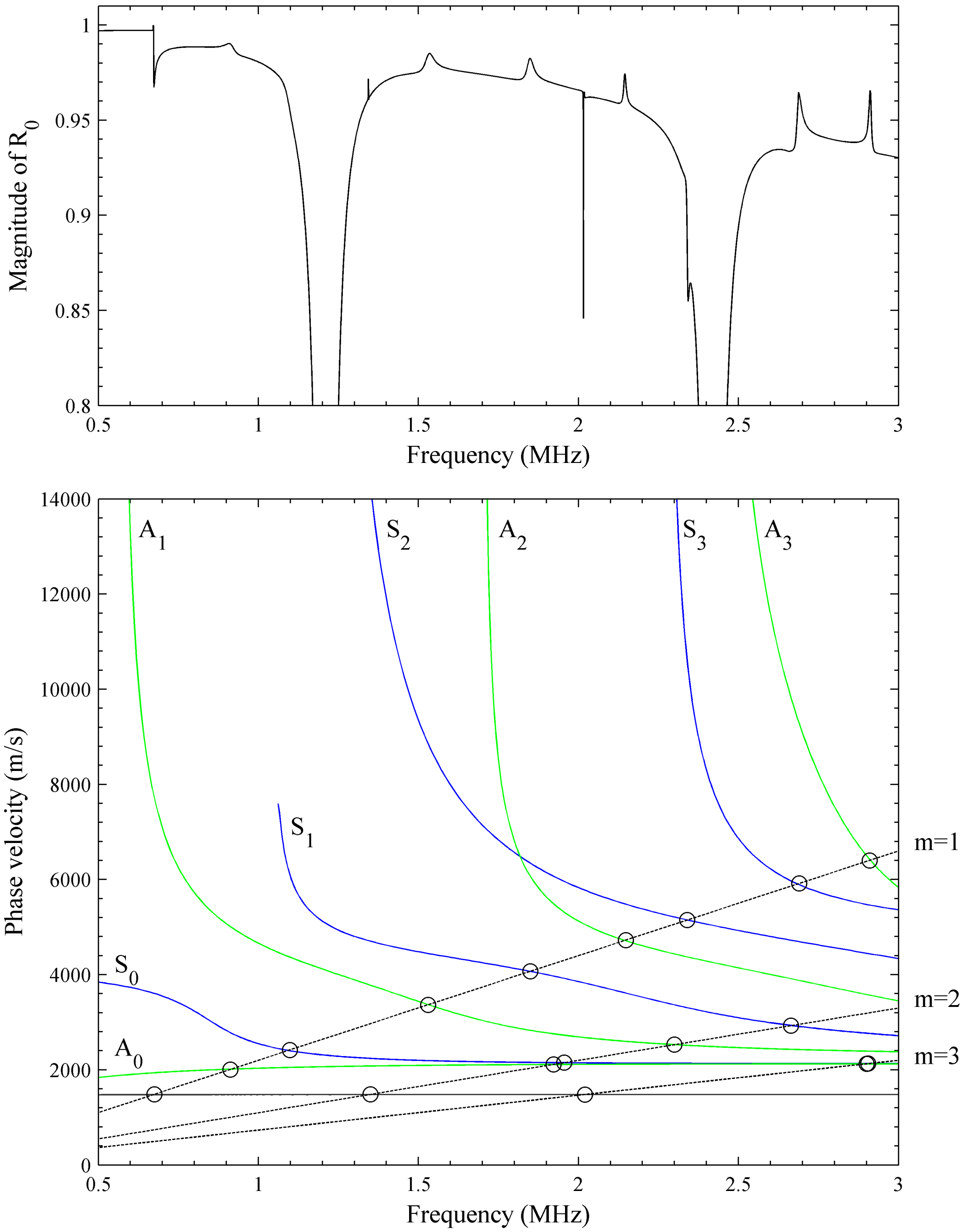

Figure 2.4: (Top) Magnitude of R_0 coefficient for brass plate with $d = 2\,\mathrm{mm}$ in water. One side periodic with $\Lambda = 2.2\,\mathrm{mm}$ and $h = 50\,\mu\mathrm{m}$. Consistent with results in [51, 58]. (Bottom) Dispersion curves for a (smooth) 2 mm thick brass plate in water. Velocity of diffracted modes plotted in dotted lines and intersection points circled.

These can be interpreted as Wood anomalies, which can occur when any one of the diffracted waves along the periodic surface phase matches to a Lamb mode. This can be investigated by comparing the locations of anomalies in the spectrum at the top of Figure 2.4 with frequency locations at which the family of curves $v_m = \frac{f\Lambda}{m}$ (plotted in dashed lines) intersect the dispersion curves plotted with phase velocity versus frequency. (This expression for the "diffracted mode velocity" v_m along the surface where f is frequency, Λ is the surface periodicity, and m is the order of diffraction, can be derived from the classical grating equation for this case by setting the incident angle θ_i to $0°$ and the angle of diffraction θ_m to $90°$.) This method of comparing the velocity of diffracted modes along the periodic surface with the Lamb dispersion curves was first employed in Refs. [51] and [58]. Three lines corresponding to the first, second, and third diffracted modes are plotted with the dispersion curves for a (smooth) brass plate at the bottom of Figure 2.4. The points of intersection with the Lamb mode dispersion curves are indicated by circled points on the bottom of Figure 2.4. Good agreement is seen between the frequency location of anomalies in the spectrum and the intersection points of the diffracted and Lamb modes. It should be noted that it may be difficult or impossible to identify anomalies that are located close to the limiting frequencies of 1.21 MHz and 2.42 MHz.

The dispersion curves shown in Figure 2.4 were calculated using the Disperse software developed by Imperial College, London. The computation of dispersion curves for a thin plate is in itself not a trivial matter, and although attempts have been made to create dispersion curves for plates (waveguides) with one or more periodic surfaces [84], the interpretation of the results is far from straightforward. Until the time that dispersion curves for plates with periodic surfaces can be created with more success and in a time-efficient manner, when a small periodic roughness is being considered, using dispersion curves calculated for smooth plates appears to result in satisfactory agreement with the simulated spectra.

2.3 New applications of the Rayleigh-Fourier method

Now that the R-F method with a direct displacement representation for shear waves has been shown to be consistent with results already present in the literature for a fluid-loaded plate with one side periodic, results from the four additional cases shown in Figure 2.3 will be presented.

2.3.1 Fluid-loaded plate with two sides periodic

The first case to be examined is that of a fluid-loaded plate where both sides are periodic. A diagram of the diffracted fields, the expressions for the total fields in the fluid and solid media, and the derivation of the boundary condition expressions can be found in Appendix B.

First, it will be assumed that the periodicities and peak-to-peak heights of both surface profiles are equal. (If the subscripts "1" and "2" are used to denote the upper and lower surfaces of the plate, respectively, then $\Lambda_1 = \Lambda_2$ and $h_1 = h_2$.) The only difference then that remains between the profiles of the two surfaces is their phase difference. Two possibilities for the phase difference will be examined. The first is that the two profiles are exactly in-phase, and in this case the plate will be referred to as "antisymmetric" since the two surface profiles appear antisymmetric with respect to the mid-line of the plate. The other possibility that will be examined is that where the two profiles are 180° out-of-phase. In this case, the plate will be considered "symmetric" since the reflection of the upper surface profile across the mid-line of the plate exactly matches the profile of the lower surface. These two possibilities are shown in Figure 2.5.

These two types of plates will now be compared with the brass plate with one periodic side that was examined in the previous section. All three plates are brass immersed in water (with all material properties as stated in Table 2.1), and the periodicities and peak-to-peak heights of the upper and lower surface profiles of the

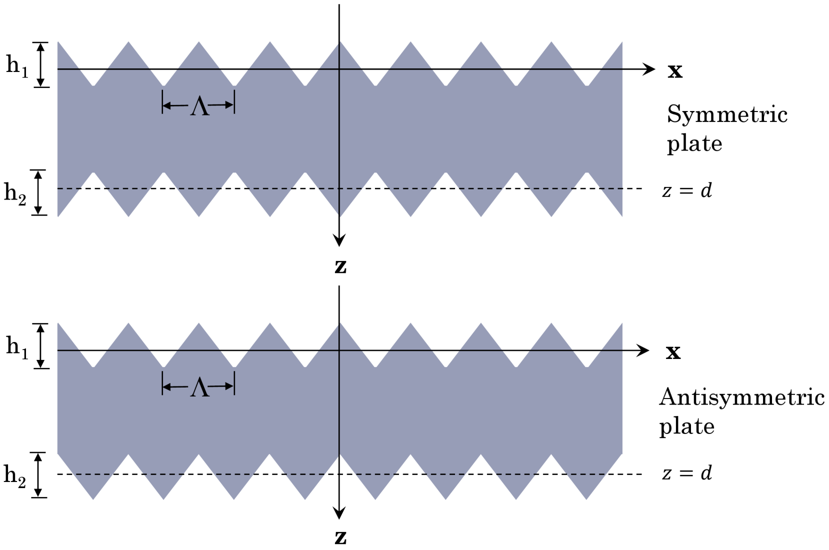

Figure 2.5: Illustration of symmetric and antisymmetric plates.

antisymmetric and symmetric plates are considered to be equal to 2.2 mm and 50 µm, respectively. These are identical to the periodicity and height parameters of the surface profile for the plate presented in the previous section that had one periodic side. The average thickness d of each plate is 2 mm.

Spectra for the R_0 coefficients for each type of plate have been calculated given a longitudinal wave normally incident from the water on the upper side of each plate, and these are shown in Figure 2.6. All the spectra have been computed with a 500 Hz frequency resolution. The spectrum for the plate with one periodic side that was originally presented in Figure 2.4 has been plotted at the top of the figure and the antisymmetric and symmetric cases of the plate with two sides periodic have been plotted below.

It can be seen that the spectra for the two-sided plates are nearly identical to that of the one-sided plate. There are some noticeable differences, however, at 1.1 MHz, 2.34 MHz, and 2.68 MHz, and these are frequencies at which the velocity of diffracted modes along the surface match phase velocities of Lamb modes for the smooth plate as shown in Figure 2.4. Therefore, it appears that the antisymmetric and symmetric

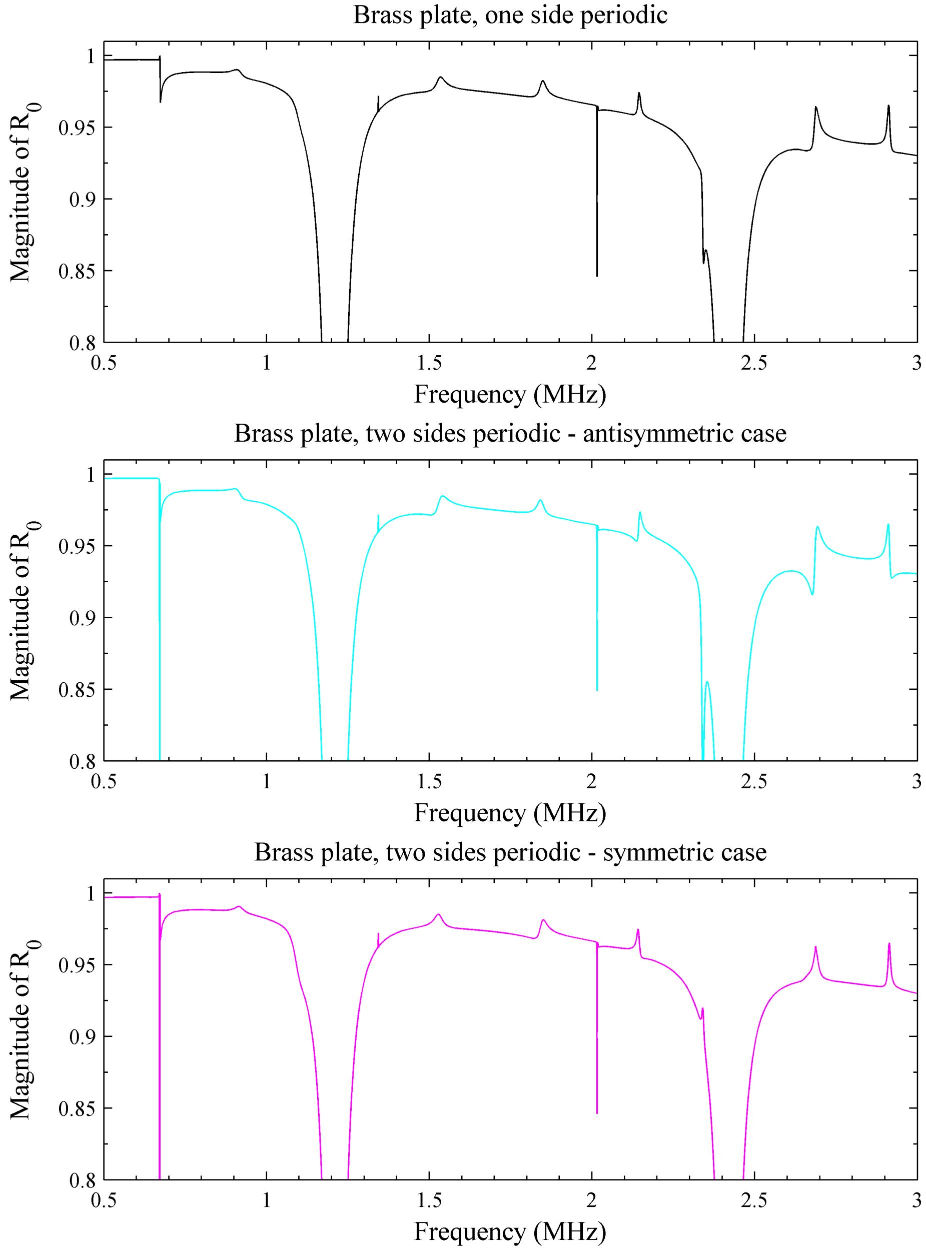

Figure 2.6: Magnitude of R_0 coefficient for brass plates with $d = 2\,\mathrm{mm}$ in water. (Top) Plate with one side periodic: $\Lambda = 2.2\,\mathrm{mm}$ with $h = 50\,\mu\mathrm{m}$. (Middle and Bottom) Plate with two sides periodic: $\Lambda_1 = \Lambda_2 = 2.2\,\mathrm{mm}$ and $h_1 = h_2 = 50\,\mu\mathrm{m}$. Antisymmetric (middle) and Symmetric (bottom) cases shown separately.

geometries result in slightly different Lamb wave stimulation.

The similarities between the spectra are not unexpected since once a wave of a given frequency enters the brass plate, its wavelength is significantly longer than its wavelength in water. The wavelength of a longitudinal wave in the brass plate will, for example, have a wavelength over three times that in water. It is well known that many wave behaviors, including diffraction, are sensitive to the relative size of the wavelength with respect to any obstacles the wave encounters. The change in wavelength that occurs upon transmission from the water to the brass results in different ratios between the incident wavelength and the surface periodicity and roughness height for the upper and lower surface profiles. The lower surface of the plate, although identical to the upper surface, appears much less rough to the wave once it is in the brass than the profile did when the wave was still in the water.

Therefore, the next question one may ask is how the spectra would change if the roughness of the lower surface of the plate approached a more appropriate value given the wavelengths within the brass plate. Since the longitudinal wavelengths in the plate have scaled up by roughly a factor of three between the water and brass, the profile height of the lower surface has been increased from 50 µm to 150 µm. The R_0 spectra for the three plates where the roughness of the lower surface of the antisymmetric and symmetric plates has changed (the plate with one side periodic remains unchanged) are shown in Figure 2.7. The spectra shown in the figure confirm that energy lost to diffraction increases with the increased roughness of the lower surface. One interesting observation is that the spectra of the antisymmetric and symmetric plates appear to be vertical mirror images of each other in the vicinity of certain anomalies. This appears, for example, in the frequency range 1.5 MHz-1.8 MHz.

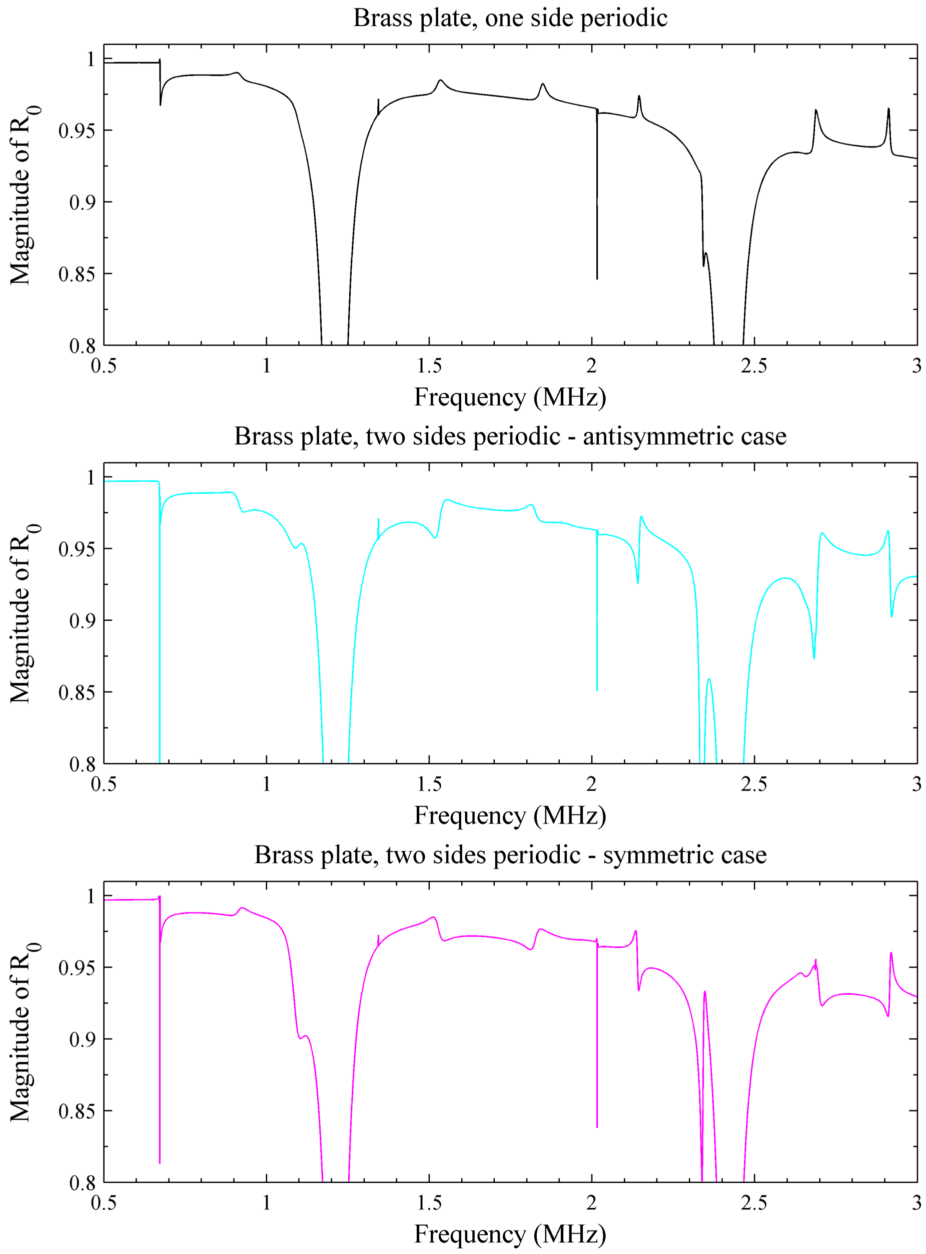

Figure 2.7: Magnitude of R_0 coefficient for brass plates with $d = 2\,\text{mm}$ in water. (Top) Plate with one side periodic: $\Lambda = 2.2\,\text{mm}$ with $h = 50\,\mu\text{m}$. (Middle and Bottom) Plate with two sides periodic: $\Lambda_1 = \Lambda_2 = 2.2\,\text{mm}$ with $h_1 = 50\,\mu\text{m}$ and $h_2 = 150\,\mu\text{m}$. Antisymmetric (middle) and Symmetric (bottom) cases shown separately.

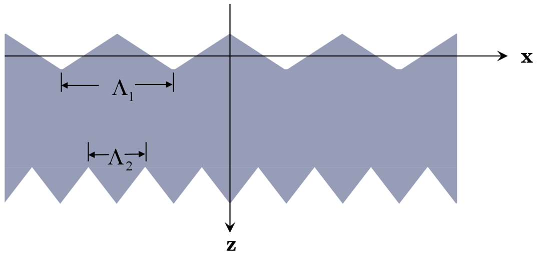

Figure 2.8: Illustration of plate with two sides periodic, $\Lambda_1 = 2\Lambda_2$.

2.3.1.1 On treating surfaces with different periodicities

The simulations developed here for plates with both sides periodic can accommodate roughnesses of different heights for the two surfaces of the plate as discussed in Appendix B. However, it is not so straightforward to accommodate a different periodicity for each of the two plate surfaces.

In order use the R-F method to treat the diffraction problem where surfaces with two different periodicities are present, several conditions must be satisfied. First, the ratio between the periodicities involved should be an integer ($\Lambda_1 = 2\Lambda_2$ as shown in Figure 2.8 for example). Second, the wave vector components k_m for all diffracted series present in the problem should be determined from the classical grating equation where the Λ substituted in the equation is equal to the largest periodicity present in the problem, whether or not that is the periodicity of the surface in closest proximity to the diffracted series concerned. The periodicity over which the Fourier coefficients are equated should also be equal to this Λ. Therefore, there will necessarily be a complicated integration over the profile with the smaller periodicity [85].

Even if these conditions are met, the possibility of the simulations satisfactorily predicting experimental reality remains uncertain. In general, in studies where only one periodicity has been present and results from the R-F method have been compared with experiments (in Ref. [41] for example), the numerically computed R_0 spectra have been compared with FFTs from pulse-echo experiments. The agreement of these results has been satisfactory even though the R-F method considers the problem in terms of time-harmonic waves of infinite extent and the experiments have employed pulsed bounded beams. However, for the case where surfaces with two different periodicities appear in the problem, the weakness in comparing the R-F results with experiments becomes apparent by considering a ray perspective.

If a pulse were to be employed in an experiment, and it was first incident on the side of the plate having periodicity Λ_1, a reflected diffracted field would be generated in the fluid from which the wave was incident, and a transmitted diffracted field would be generated in the solid plate. The wave vector components of the waves in these fields would be dependent on the periodicity Λ_1, whether or not it is larger than Λ_2.

The diffracted waves that are transmitted into the plate would then propagate towards the plate's second periodic surface with periodicity Λ_2, and upon reaching this surface, each one of the waves in the original transmitted series would experience diffraction and generate its own series of diffracted waves with wave vector components dependent on Λ_2. For the case where $\Lambda_1 = 2\Lambda_2$, these wave vector components "map" onto the wave vector components created using Λ_1 as shown in Table 2.2. Table 2.2 shows wave vector components denoted by k_{mn} where m and n are integers. With this notation, the integer m refers to the order of diffraction on the first surface encountered, which is the order from which the diffraction order n on the second surface is generated. When the largest Λ is used to determine the wave vector components for all the diffracted fields in the problem, all the diffracted waves generated by the diffraction occurring due to the multiple reflections within the plate will map onto this set. Having the wave vector components determined by the largest periodicity present in the problem results in the finest "resolution" of k_m because the largest Λ is located in the denominator of the term $\frac{2\pi}{\Lambda}$ in the grating equation. This mapping of wave vector components for diffracted waves originating from multiple reflections within the plate presents no difficulty when considering the time-harmonic problem, and it has in fact already been used for the case of a plate with one or both sides periodic with only one Λ present.

For the case where the incident wave originates in the fluid and is first incident on the surface with periodicity Λ_1, the wave vector components for the initial reflected diffracted series will be consistent between theory and experiment. The only complication in comparing the simulation results with experiments employing pulses is that the diffraction that will eventually occur on the lower surface of the plate (having periodicity Λ_2) will reflect back to the upper surface of the plate where some of the energy will be transmitted into the original reflected field, but with a time delay and shift along the x-axis from the original reflected diffracted waves. In addition, it is important to remember that the wavelength λ for a wave with frequency f becomes much longer (perhaps by as much as a factor of three) upon entering the plate from the fluid where the wave originated. The wave will "see" the second periodic surface as less rough even if the second surface profile is identical to the first surface profile. Therefore, for the case where $\Lambda_1 = 2\Lambda_2$, the diffraction on the Λ_1 surface may dominate and treatment of this case may be trivial.

This effect, however, might be counteracted if the second periodicity is an integer multiple of the first surface periodicity. For the case where the incident wave from the fluid first interacts with the Λ_2 surface (i.e. the wave is incident from underneath the plate as it is shown in Figure 2.8), the longer wavelengths within the plate would "see" the longer periodicity Λ_1. Therefore, the diffraction that occurs upon interaction with this surface may be more important than in the case where the incident wave is incident from the fluid first upon the surface with the longer periodicity. However, this case introduces an additional complication in terms of potentially comparing the simulation results with experiments. In this case, the R-F method would require that the wave vector components of the reflected diffracted series from the Λ_2 surface be expressed in terms of the longer periodicity Λ_1. In an experiment, waves with these

Table 2.2: Wave vector components k_m and k_{mn} for the case of two periodic surfaces where $\Lambda_1 = 2\Lambda_2$.

1st Surface		2nd Surface		
$m = 0$	$k_0 = k_i$	$n = 0$	$k_{00} = k_i$	$\rightarrow k_0$
		$n = 1$	$k_{01} = k_i + \dfrac{2\pi}{\Lambda_2} = k_i + \dfrac{2\pi}{\Lambda_1}(2)$	$\rightarrow k_2$
		$n = 2$	$k_{02} = k_i + \dfrac{2\pi}{\Lambda_2}(2) = k_i + \dfrac{2\pi}{\Lambda_1}(4)$	$\rightarrow k_4$
		$\vdots$	$\vdots$	$\vdots$
$m = 1$	$k_1 = k_i + \dfrac{2\pi}{\Lambda_1}$	$n = 0$	$k_{10} = k_i + \dfrac{2\pi}{\Lambda_1}$	$\rightarrow k_1$
		$n = 1$	$k_{11} = k_i + \dfrac{2\pi}{\Lambda_1} + \dfrac{2\pi}{\Lambda_2} = k_i + \dfrac{2\pi}{\Lambda_1}(3)$	$\rightarrow k_3$
		$n = 2$	$k_{12} = k_i + \dfrac{2\pi}{\Lambda_1} + \dfrac{2\pi}{\Lambda_2}(2) = k_i + \dfrac{2\pi}{\Lambda_1}(5)$	$\rightarrow k_5$
		$\vdots$	$\vdots$	$\vdots$
$m = 2$	$k_2 = k_i + \dfrac{2\pi}{\Lambda_1}(2)$	$n = 0$	$k_{20} = k_i + \dfrac{2\pi}{\Lambda_1}(2)$	$\rightarrow k_2$
		$n = 1$	$k_{21} = k_i + \dfrac{2\pi}{\Lambda_1}(2) + \dfrac{2\pi}{\Lambda_2} = k_i + \dfrac{2\pi}{\Lambda_1}(4)$	$\rightarrow k_4$
		$n = 2$	$k_{22} = k_i + \dfrac{2\pi}{\Lambda_1}(2) + \dfrac{2\pi}{\Lambda_2}(2) = k_i + \dfrac{2\pi}{\Lambda_1}(6)$	$\rightarrow k_6$
		$\vdots$	$\vdots$	$\vdots$
$m = 3$	$k_3 = k_i + \dfrac{2\pi}{\Lambda_1}(3)$	$n = 0$	$k_{30} = k_i + \dfrac{2\pi}{\Lambda_1}(3)$	$\rightarrow k_3$
		$n = 1$	$k_{31} = k_i + \dfrac{2\pi}{\Lambda_1}(3) + \dfrac{2\pi}{\Lambda_2} = k_i + \dfrac{2\pi}{\Lambda_1}(5)$	$\rightarrow k_5$
		$n = 2$	$k_{32} = k_i + \dfrac{2\pi}{\Lambda_1}(3) + \dfrac{2\pi}{\Lambda_2}(2) = k_i + \dfrac{2\pi}{\Lambda_1}(7)$	$\rightarrow k_7$
		$\vdots$	$\vdots$	$\vdots$

wave vector components would not exist until the diffraction on the second surface of the plate (with Λ_1) had occurred. Unfortunately, the wave vector components from the second plate surface do not map onto the set from the first surface; they are the set to which the wave vector components from the first plate surface should be mapped.

In the R-F method, the reflected diffracted field is assumed to already have waves with wave vector components associated with the periodicity of the second surface since the problem is time-harmonic (and the waves have always existed and they will always exist). Therefore, the results of R-F simulations would less accurately resemble the measured reflected diffracted field because the simulations includes waves in the reflected diffracted field that do not exist until diffraction on the second plate surface occurs. Even if the time-delayed and x-shifted contributions from diffraction occurring on the second surface of the plate are taken into account somehow in experiment, the R-F simulation may overestimate the contributions of these individual waves. Therefore, should the R-F method be considered in the future to treat the problem where each surface of the plate has a different periodicity, the simulation results may not realistically predict the results of pulse-echo experiments. The use of a function generator in experiments to send a sufficiently long time-harmonic wave (and this may need to be repeated over many frequencies) may be preferable to a pulse-echo technique.

2.3.2 Two solids separated by a periodic interface

The next case that will be studied with the Rayleigh-Fourier method is that of two semi-infinite solid media that are separated by a periodic interface. A diagram of the diffracted fields generated and the derivation of the boundary condition expressions can be found in Figure 2.9 which has been duplicated from Appendix C for the reader's convenience. The two media of the problem have been chosen to be steel (4340) and

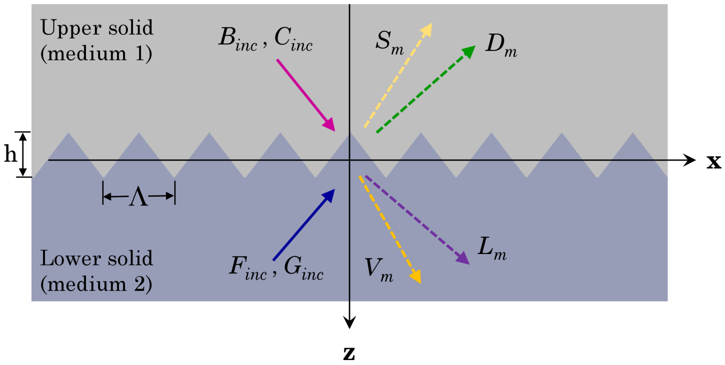

Figure 2.9: Diagram of diffracted fields for two solid media separated by a periodic interface. Diffracted wave series shown in dotted lines. Expressions for diffracted wave series derived in Appendix C.

titanium (6Al-4V), and their properties are shown in Table 2.1. This particular pair of materials has been chosen so that the possibility of exciting a Stoneley wave at their interface exists. Stoneley waves can exist for a very limited range of media pairs [45] because, broadly speaking, in order for a Stoneley wave to exist at the interface between two solid media, the shear wave speeds in the media must be very close. According to Ref. [25], the velocity of a Stoneley wave v_{St} at the (smooth) interface between these two media is 3209 m/s.

An incident longitudinal wave from the steel is considered normally incident upon the periodic interface with the titanium. Locations of anomalies in the reflected D_0 spectrum will be examined to determine if any anomalies are present that may indicate diffraction as a method of generating Stoneley waves at the interface. Here, D_0 denotes the longitudinal zero-order in the steel as shown in Figure 2.9. The interface has a sawtooth profile with a periodicity $\Lambda = 2.2\,\text{mm}$ and peak-to-peak height of $h = 150\,\mu\text{m}$. The frequency range that will be examined is identical to the frequency ranges examined in the cases of the prior sections. However, since the incident wave originates in one of the solid media, its wavelength will be longer and therefore a larger peak-to-peak roughness height has been chosen.

By setting $\theta_i = 0°$, $\theta_m = 90°$, and $v_m = v_{St} = 3209\,\text{m/s}$ in the classical grating equation, the frequency at which 1st order diffraction may result in the generation of a Stoneley wave is 1.458 MHz. Upon examining the D_0 spectrum shown in Figure 2.10, an anomaly in the spectrum is clearly visible at 1.46 MHz. There is also an additional anomaly visible in the spectrum at 2.92 MHz which is consistent with 2nd order diffraction. There is a small feature in the spectrum visible at 2.68 MHz and this may result from the generation of a 1st order longitudinal bulk wave along the interface.

The top of Figure 2.10 shows the complete spectrum computed between 0.5 MHz and 3.0 MHz computed with a 500 Hz resolution, and the bottom of the figure shows the same spectrum at a scale which is more convenient in order to see the two anomalies. Figure 2.11 shows the locations of the two anomalies in detail. The left and right sides of Figure 2.11 show the first and second anomalies, respectively.

2.3.3 Fluid-loaded bilayered plate containing an inner periodic interface

The next case that will be treated with the R-F method is that of a fluid-loaded bilayered plate where the interface between the two solid materials of the plate is periodic but the interfaces between each solid and the fluid are smooth. An illustration of the diffracted fields generated is shown in Figure 2.12, and the derivation of the associated boundary condition expressions can be found in Appendix D. The two solid materials will be considered to be steel and titanium with material properties shown in Table 2.1. Each solid layer making up the plate has an average thickness of 0.8 mm. The interface between the steel and titanium is of a sawtooth form with a periodicity $\Lambda = 2.2\,\mathrm{mm}$ and peak-to-peak roughness height $h = 150\,\mu\mathrm{m}$. The steel is considered to be the "upper" material of the plate, and it is immersed in water with the incident wave normal upon the steel side of the plate.

The R_0 spectrum has been generated between 0.5 MHz and 3.0 MHz with a 500 Hz resolution and is shown at the top of Figure 2.13. A large decrease in the spectrum

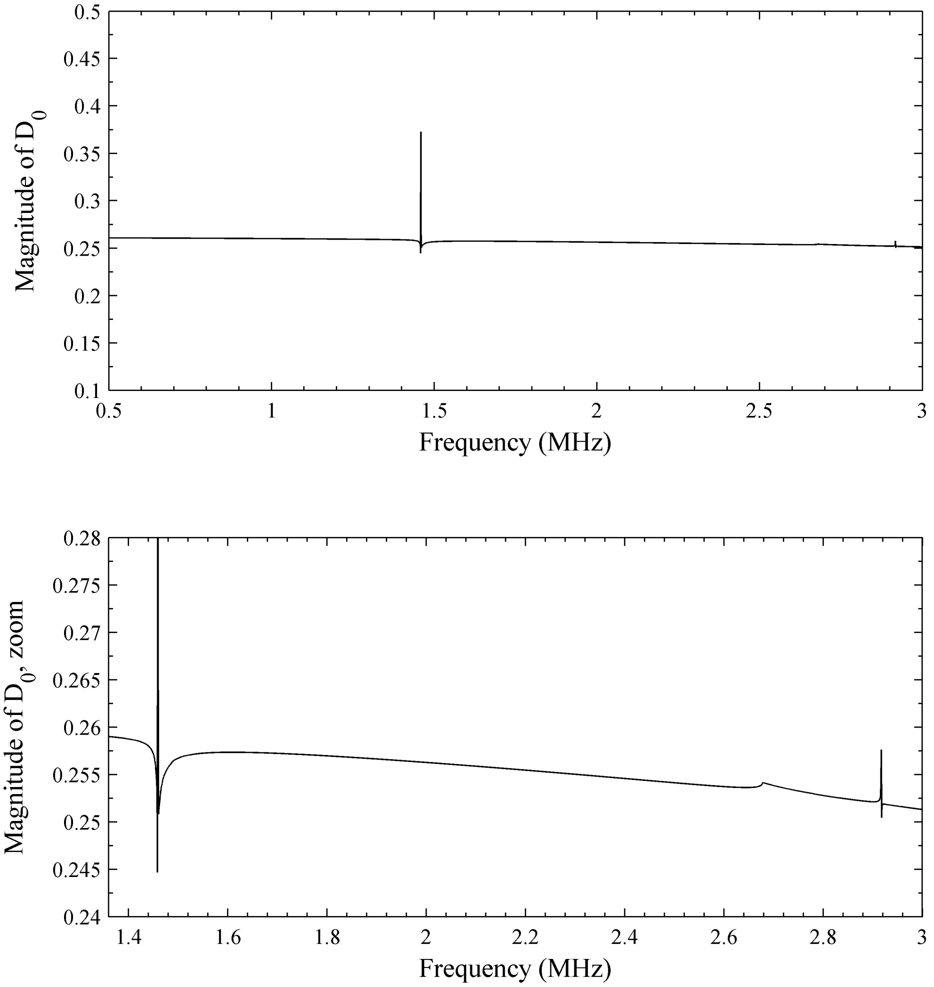

Figure 2.10: Magnitude of D_0 coefficient for a steel-titanium interface with $\Lambda = 2.2\,\mathrm{mm}$ and $h = 150\,\mu\mathrm{m}$. (Top) Entire spectrum between 0.5 MHz and 3.0 MHz (Bottom) Detail of spectrum between 1.36 MHz and 3.0 MHz

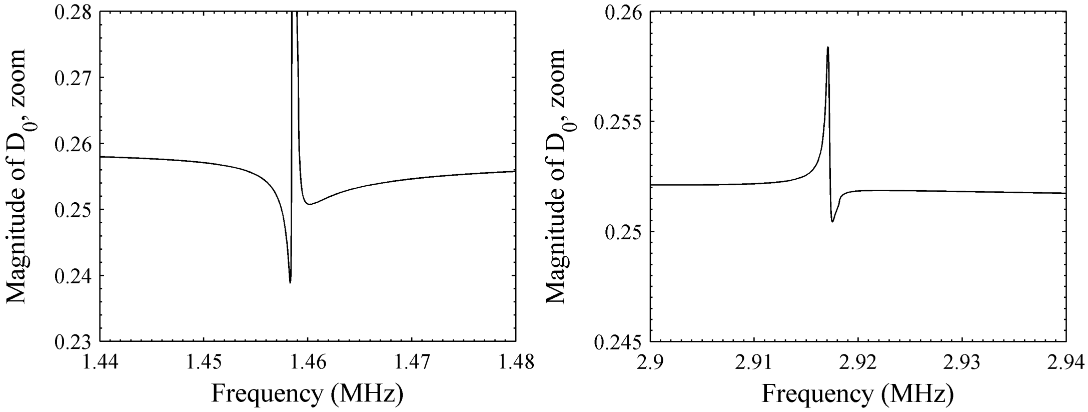

Figure 2.11: Magnitude of D_0 coefficient for a steel-titanium interface with $\Lambda = 2.2\,\text{mm}$ and $h = 150\,\mu\text{m}$. (Left) Detail of anomaly at 1.46 MHz. (Right) Detail of anomaly at 2.92 MHz.

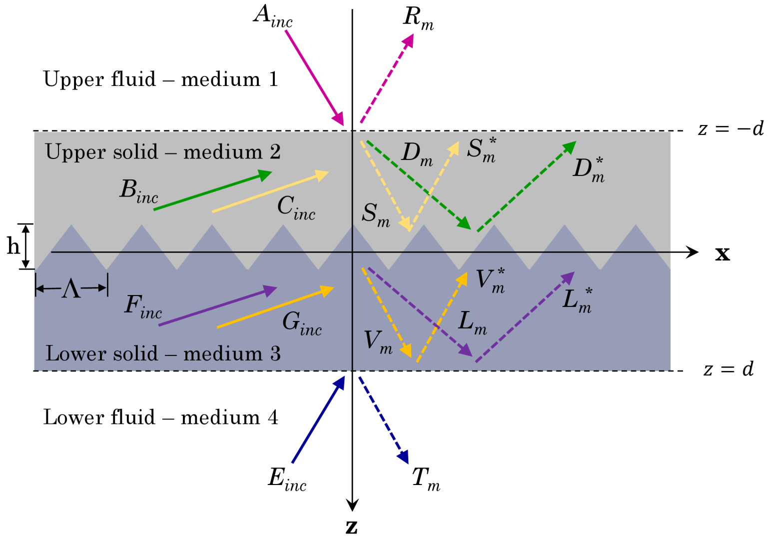

Figure 2.12: Diagram of diffracted fields for a fluid-loaded plate made of two solid media separated by a periodic interface. Diffracted wave series shown in dotted lines. Expressions for diffracted wave series derived in Appendix D.

is seen at approximately 1.88 MHz which is likely due to a plate thickness resonance as was the case for the brass plate treated in Section 2.2. The only other visible feature in the spectrum is at 2.68 MHz which is the frequency that would correspond to the generation of 1^{st} order longitudinal bulk waves propagating along the periodic interface between the two solids. In order to investigate this further, the $D_{\pm 1}$ and $L_{\pm 1}$ (coefficients for the longitudinal series in each of the solid media) spectra were examined and these are shown at the bottom of Figure 2.13. (Because the incident wave is normal to the plate surface, the coefficients for the diffraction orders m and $-m$ match. This is not the case when oblique incidence is considered.) In these spectra, peaks are visible at 2.68 MHz and this may indicate the transfer of energy to these diffraction orders. Interestingly, there is no evidence related to the possible generation of a Stoneley wave through diffraction at a frequency of 1.46 MHz at the periodic interface between the media. This is the case even when the roughness height h is increased to 300 µm, and this is shown in Figure 2.14.

2.3.4 Fluid-loaded bilayered plate with all interfaces periodic

The final case that will be considered with the R-F method is that of a fluid-loaded bilayered plate where all the interfaces between the media are periodic. The diffracted fields generated are shown in Figure 2.15, and the derivation of the boundary condition expressions are shown in Appendix E. This case is identical to that of Subsection 2.3.3 except that the external surfaces of the solid media making up the plate are now periodic as well. Again the case of a steel-titanium bilayer will be considered immersed in water. Media properties are shown in Table 2.1 and the average thickness of each solid layer is 0.8 mm. The periodicity of all surfaces is set to 2.2 mm and although the option exists to consider each solid layer as symmetric or antisymmetric as in Subsection 2.3.1, both layers will be considered antisymmetric since it was shown in Figure 2.7 that the cases of symmetric and antisymmetric layers were very similar.

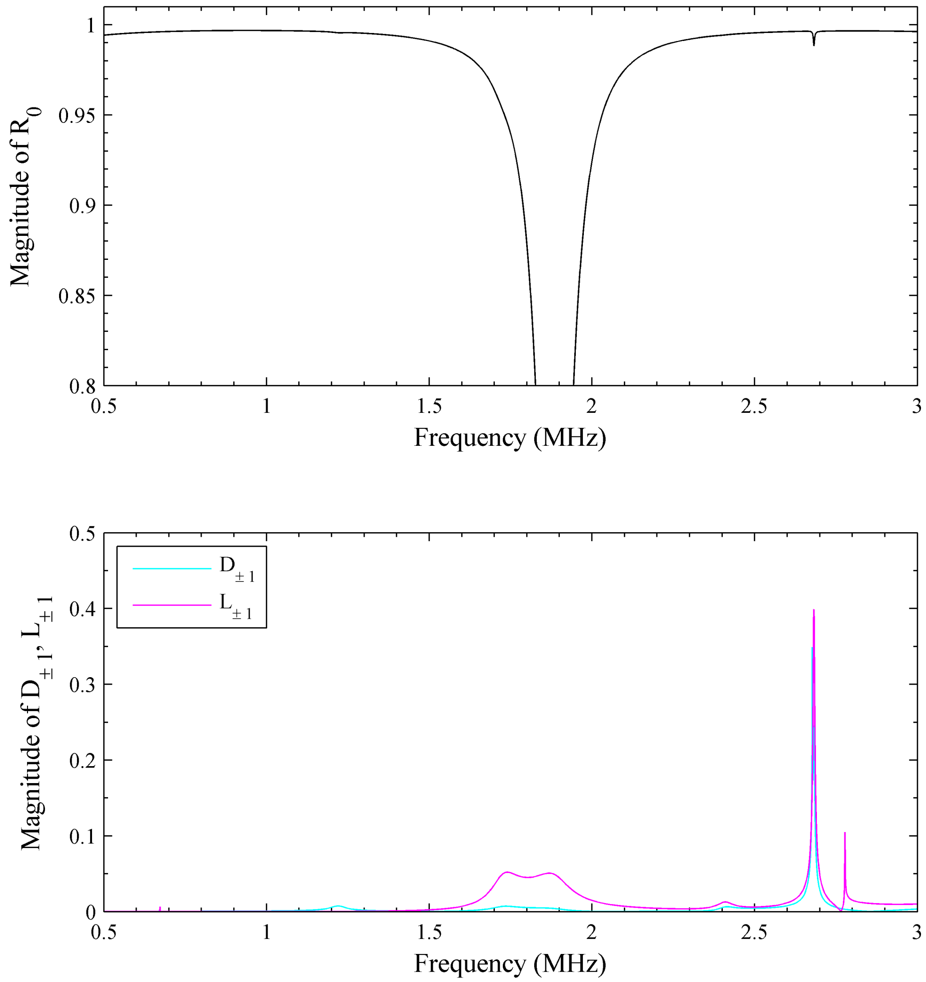

Figure 2.13: Spectra for a water-loaded steel-titanium plate with $\Lambda = 2.2\,\mathrm{mm}$ and $h = 150\,\mu\mathrm{m}$. (Top) Magnitude of R_0 coefficient. Anomaly related to lateral bulk wave generation visible at 2.68 MHz. (Bottom) Magnitudes of $D_{\pm 1}$ and $L_{\pm 1}$ coefficients. Anomaly related to lateral bulk wave generation visible at 2.68 MHz.

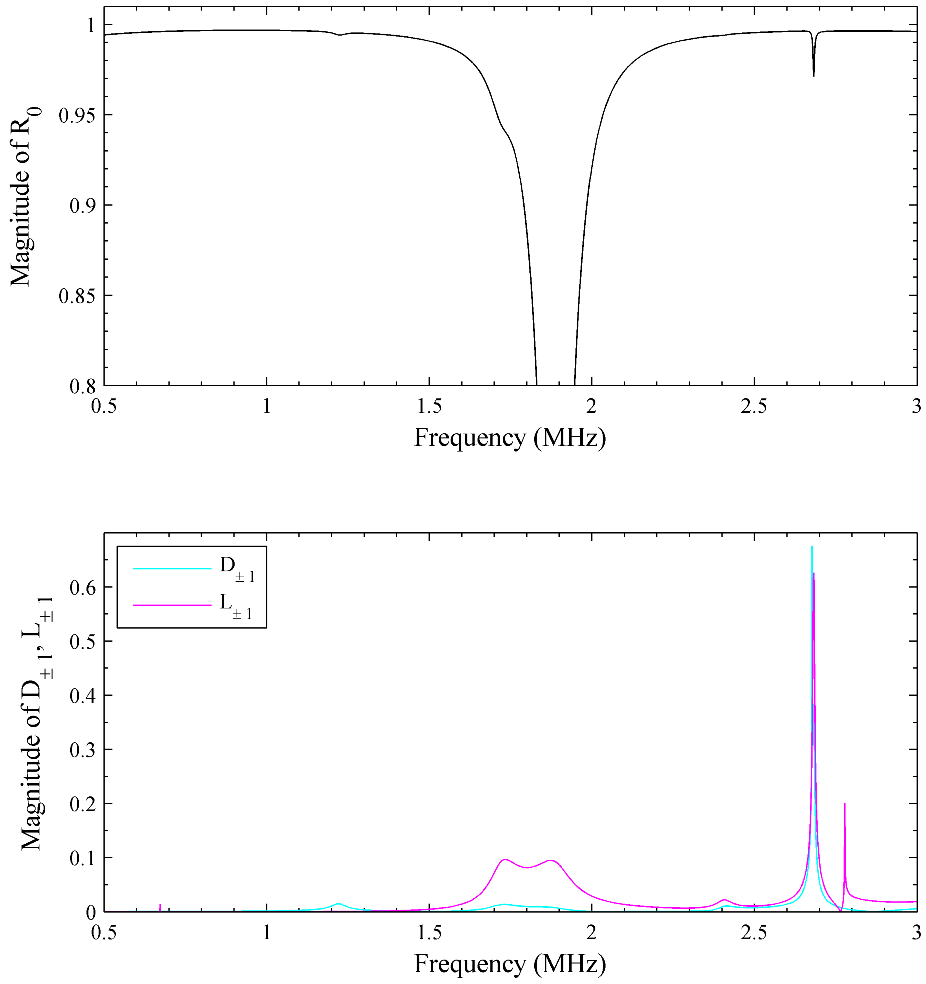

Figure 2.14: Spectra for a water-loaded steel-titanium plate with $\Lambda = 2.2\,\mathrm{mm}$ and $h = 300\,\mu\mathrm{m}$. (Top) Magnitude of R_0 coefficient. Anomaly related to lateral bulk wave generation visible at 2.68 MHz. (Bottom) Magnitudes of $D_{\pm 1}$ and $L_{\pm 1}$ coefficients. Anomaly related to lateral bulk wave generation visible at 2.68 MHz.

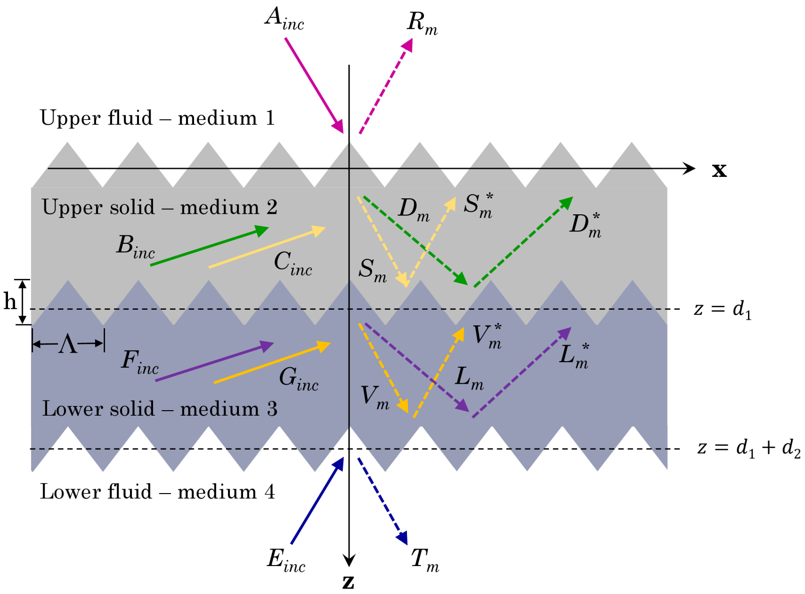

Figure 2.15: Diffracted fields for a fluid-loaded plate made of two solid media where all three interfaces between the various media are periodic. Diffracted wave series shown in dotted lines. Expressions for diffracted wave series derived in Appendix E.

The incident wave originates in the water on the steel side of the plate, and is directed normally incident on the plate surface. The magnitude of the R_0 coefficient was computed for three different values of the surface roughness height for the interface between the two solids. The remaining two interfaces are considered to have roughness heights equal to 50 µm. Although it is very simple to accommodate different roughness heights, it can be seen in Figure 2.16 that there is very little difference in the spectra for roughness heights equal to 50 µm, 150 µm, and 300 µm. The top of Figure 2.17 shows the R_0 spectrum for the case where the inner roughness height is 50 µm, and the bottom of the figure shows dispersion curves that have been calculated using the Disperse software for a (smooth) water-loaded steel-titanium bilayered plate. The dispersion curves for a bilayered plate can no longer be considered classified as "symmetric" or "antisymmetric" (with the exception of the two curves labeled "A" and "S") as was the case for a single material plate. The curves that represent the velocity of the diffracted modes along the surface of the plate, labeled as $m = 1$,

$m = 2$, and $m = 3$, have been plotted on top of the dispersion curves. This curve family has been plotted according to the expression $v_m = \frac{f\Lambda}{m}$ in a manner consistent with that of Figure 2.4.

The circled frequencies along the 1st order diffraction line that exhibit anomalous increases in the R_0 spectrum include 1.23 MHz, 2.41 MHz, and 2.69 MHz. However, any anomaly at 1.73 MHz that might have been observed is likely obscured due to the plate resonance feature. The anomalies at 0.67 MHz, 1.35 MHz, and 2.02 MHz in the spectrum are consistent with 1st, 2nd, and 3rd order diffraction matching to a Scholte-Stoneley wave velocity slightly less than the velocity of sound in water (1480 m/s). Since the only difference between the spectra shown at the middle and bottom of Figure 2.16 from the spectra shown at the top of Figures 2.14 and 2.13 is the presence of a periodicity on the external surfaces of the bilayered plate, it is clear that many features in the spectra of Figure 2.16 are due to the presence of these external periodicities. In fact, since the reflected spectra from single material plates with both sides periodic do not differ significantly from those with only the upper side periodic (see Figures 2.7 and 2.4), it is likely that the anomalous features in the spectra of Figure 2.16 that do not occur in those of Figures 2.14 and 2.13 are due to the periodicity of the uppermost surface of the bilayered plate.

2.4 Concluding remarks

This chapter has presented the extension of the Rayleigh-Fourier method for simulating diffraction on periodic surfaces to four cases that had not yet been treated with the method. All the cases that were examined considered a longitudinal wave normally incident on the periodic surface(s) present in the problem. The spectra of the zero-order reflection coefficients were examined for anomalies that might indicate the generation of surface or plate waves through diffraction.

First, a fluid-loaded plate with both sides periodic (where the periodicities of both

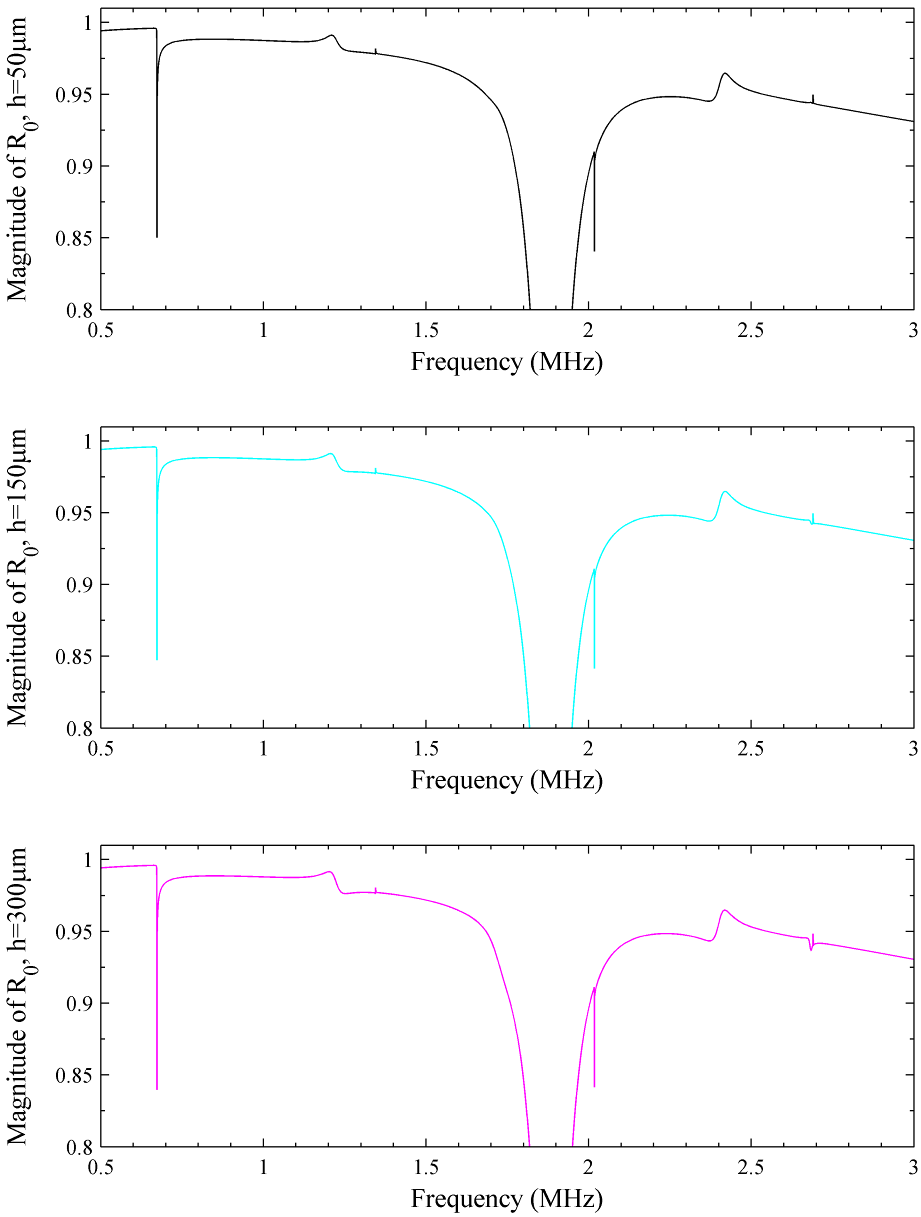

Figure 2.16: Magnitude of R_0 coefficient for a water-loaded steel-titanium plate where all interfaces are periodic with $\Lambda = 2.2\,\mathrm{mm}$. Antisymmetric case. (Top) Peak-to-peak roughness height (between solid media) $h = 50\,\mu\mathrm{m}$. (Middle) Peak-to-peak roughness height (between solid media) $h = 150\,\mu\mathrm{m}$. (Bottom) Peak-to-peak roughness height (between solid media) $h = 300\,\mu\mathrm{m}$.

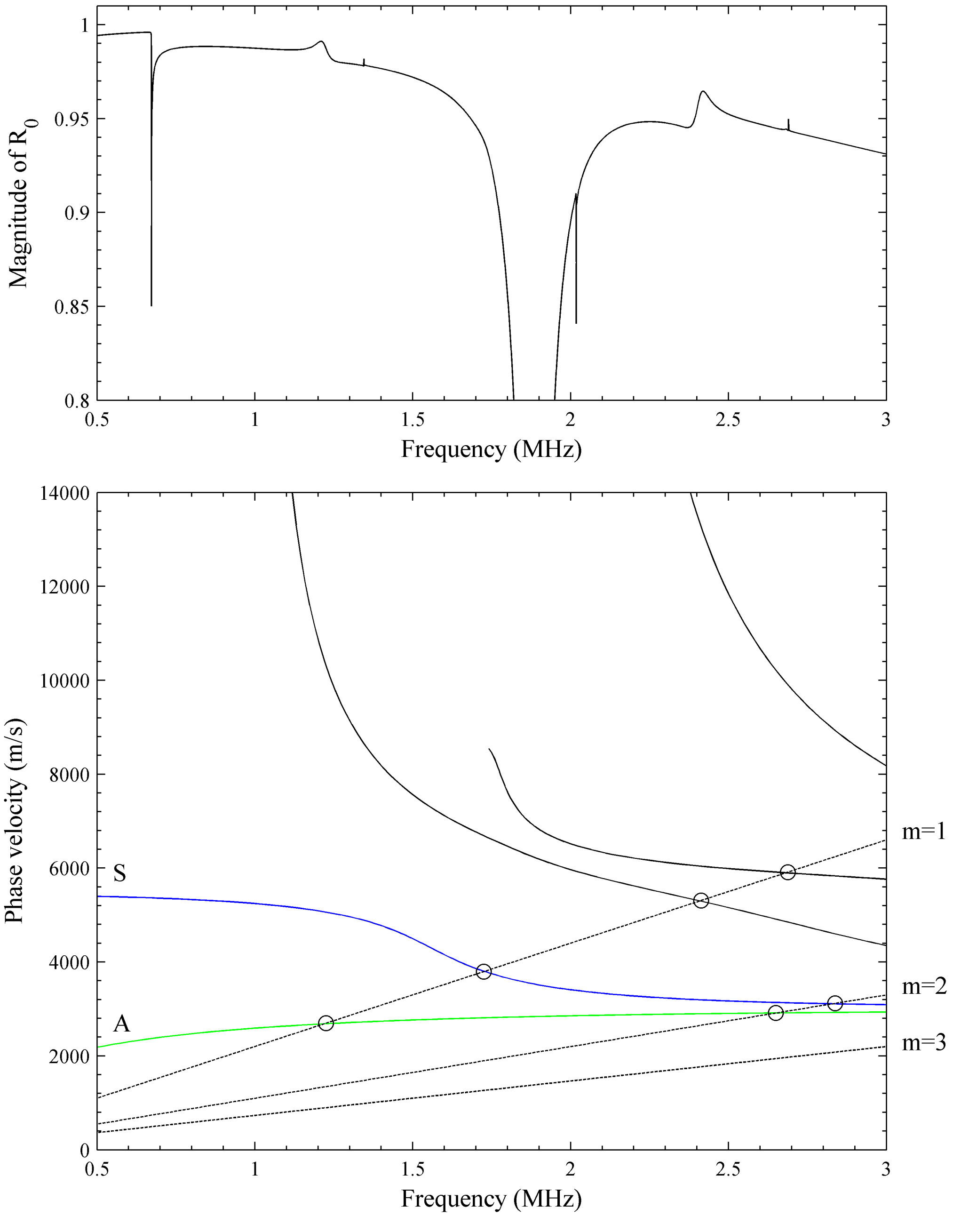

Figure 2.17: (Top) Magnitude of R_0 coefficient for a water-loaded steel-titanium plate where all interfaces are periodic with $\Lambda = 2.2\,\text{mm}$ and $h = 50\,\mu\text{m}$. Antisymmetric case. (Bottom) Dispersion curves for a (smooth) water-loaded steel-titanium bilayered plate. Possible frequencies where diffracted modes may phase match to Lamb modes shown with circles.

surfaces are equal) was examined. The spectra of antisymmetric and symmetric plates (classified as such based on the phase difference between their upper and lower surface profiles) were both examined. Some differences were observed in the spectra from the symmetric and antisymmetric plates, possibly due to differences in Lamb wave generation. Since at this time, dispersion curves (in the form of phase velocity versus frequency) are only available for smooth plates, it is difficult to make statements regarding differences in the Lamb modes that are possible for the two types of plates. The differences in the spectra become more pronounced as the roughness of the second side of the plate is increased.

The second case that was examined was that of two semi-infinite solid media in perfect contact at a periodic interface. Anomalies related to Stoneley wave generation through diffraction were observed. Interestingly enough, however, when the third case of a fluid-loaded bilayered plate with an interior periodic interface was considered, no anomalies related to Stoneley wave generation were visible. An anomaly related to lateral bulk wave generation along the interface was observed. The final case that was examined was a fluid-loaded bilayered plate where all the interfaces between the fluid and solid media were periodic. Here, features in the spectra that were related to diffraction on the external surfaces of the plate were observed.

Since these simulations using the R-F method are only possible for surfaces having perfect periodicities which is only an approximation of what one would encounter in practice, the next chapter will present the result of experimental work on surfaces that exhibit imperfect periodicities.

CHAPTER III

DIFFRACTION EFFECTS ON IMPERFECTLY PERIODIC SURFACES

As discussed in the introductory chapter of this thesis, the numerical simulation of diffraction that occurs on periodic surfaces naturally leads to the inverse problem: the characterization of periodically rough surfaces using experimentally determined diffraction spectra. Unfortunately, the use of theoretical techniques such as the Rayleigh-Fourier method is limited to "ideal" surfaces having perfect periodicities. Therefore, the purpose of this chapter is to present the experimental investigation of ultrasonic diffraction effects that occur on surfaces having imperfect periodicities. In particular, the application of ultrasound for the examination of rolled stainless steel plates having two-dimensional periodic surface textures is investigated. Experiments have been conducted in order to compare the use of two different ultrasonic techniques, namely normal incidence pulse-echo spectra and backscattered spectra, for the characterization of the surface profiles.

This chapter is organized in the following manner. First, the motivation driving ultrasonic techniques for the characterization of surface roughness in general is discussed. This is followed by a historical survey of ultrasonic methods that have been used in the past to investigate periodically rough surfaces. The sample that is investigated is then described along with the experimental setups that have been employed. Experimental results and conclusions are then presented.

3.1 Motivation behind ultrasonic methods for the characterization of surface roughness

The characterization of surface roughness or topography is important in many fields of science and engineering [86]. Surface roughness plays a role in the function of manufactured components on the macroscopic scale [87], and on the nanoscale it can influence not only bulk material properties but also chemical and biological reactions with a material [88]. The study of methods for surface metrology is well-developed and reviews of these methods can be found in the literature [89, 90].

Ultrasonic methods to evaluate surfaces have several advantages over other methods, especially in manufacturing environments [91]. For example, parts or surfaces being inspected need not be stationary so inspection time and cost can be reduced. On-line inspection is possible and therefore the collection of samples that must be removed from the process at regular intervals may not be necessary [92]. Ultrasonic inspection is possible to implement as a non-contact technique, which is in contrast with the use of a mechanical contact stylus [93]. Although optical techniques are popular, their application in a manufacturing environment can be limited. Ultrasonic methods can be applied on wet as well as dry surfaces and they can function in optically opaque environments [92]. Examples of applications for ultrasonic methods of surface characterization include quality control of machined parts and process control, such as in the monitoring of tool condition [94, 95, 96]. The ultrasonic characterization of rough surfaces has also recently gained attention in the study of bonded structures [97].

The ultrasonic characterization of rough surfaces, both periodic and random, has been an active area of experimental research for over 30 years. Initial investigations focused on randomly rough surfaces with the goal of determining signatures from the ultrasonic backscattering that could be used to characterize the surface roughness, and the backscattered intensity was found to increase with increasing roughness height [98]. Normal incidence was also investigated, and experiments showed that random surface roughness results in the attenuation of the specularly reflected signal [99]. With this knowledge, techniques were developed to determine the heights of randomly rough surfaces with good precision. However, the presence of even a quasi-periodicity on the surface was found to render these techniques inaccurate [57]. Therefore, different ultrasonic techniques than those used for the characterization of random rough surfaces must be applied when any periodicity is present in a surface's roughness.

3.2 Historical survey of techniques for the ultrasonic investigation of periodic surfaces

After the realization that the presence of a periodicity in a surface's roughness would require the development of different ultrasonic characterization techniques, the diffraction that occurs due to the periodicity was immediately identified as potentially useful. It was shown by Quentin et al. [57] that when surfaces with a one-dimensional periodicity (i.e. those with periodic grooves) are insonified with narrow-band pulses, maxima in the backscattered intensity can be observed at very specific angles of incidence [57, 100]. This was naturally due to the fact that such a periodic surface functions as an acoustic diffraction grating, generating diffracted modes at specific angles that can be predicted by the classical grating equation [13]. As the frequency of the narrowband pulse used to insonify the grating increases, more backscattered modes can be observed within a given angular range, and it was shown by Quentin et al. that if the angular locations of these backscattered modes are examined for several discrete frequencies, accurate predictions of the surface periodicity can be obtained [57]. This technique can also be applied using broadband pulses and has been shown to be feasible as a kind of ultrasonic spectroscopy [101]. These techniques can only be used to characterize the spatial periodicity of the profile: no information can be obtained regarding the profile height or form.

Prior studies have also addressed imperfect grooved surfaces, and secondary maxima in the backscattered intensity were observed at angles corresponding to an integer multiple of the surface periodicity [57]. These secondary backscattered peaks have been referred to as subharmonics since they satisfy the classical grating equation where the diffraction order has a fractional value (1/2, for example) rather than an integer value. It has been hypothesized that the amplitudes of these secondary maxima may be related to the imperfectness of the grating. Efforts have also been made to characterize surfaces having two-dimensional periodicity (meaning the surface's periodicity exists in two directions) such as wire grids, or surfaces deformed with a grid pattern [57, 101]. In these cases, depending on the orientation of the axis of rotation of the transducer, diffraction peaks can be observed at angles corresponding to the periodicities for both of the principal grid directions, but also for the periodicity seen along the diagonal of the sample surface [101, 102]. The success with which these backscattering methods were able to predict values for the periodicity of surfaces naturally led to the study of techniques to determine periodic profile heights (roughness) and/or the form of the profile for samples known to have identical spatial periodicities, and a rudimentary theoretical approach was developed whereby the influence of the form of the profile on the backscattered frequency spectra was studied [103].

Further studies on periodically rough surfaces were soon revealing the existence of Wood anomalies in normal incidence reflection spectra obtained from pulse-echo experiments [4]. These appeared as sharp discontinuities or valleys in the frequency spectra, and they were interpreted as being analogous to those found in optical spectra and as being due to mode conversion from bulk to surface waves on the periodic surface [41, 104]. At the time, no theoretical analysis was available to predict the location or depth of these anomalies for a given material and surface profile. Soon thereafter, however, the Rayleigh-Fourier method was extended from prior cases involving perfectly rigid or pressure-release profiles to the liquid-solid case, and the results from the method were shown to agree well with experiment [54]. With the introduction of this extension of the Rayleigh-Fourier method, theoretical reflection and transmission spectra could be calculated for the periodic interface separating liquid and solid media (with sound incident from the liquid), and the presence of anomalies could now be predicted for a given periodic surface profile. Just as the maxima in the backscattered intensity that corresponded to propagating modes generated by a periodic surface had previously been used to determine the periodicity of the profile, it was then shown that the frequency locations of anomalies present in the normal incidence spectrum could be used in order to predict the periodicity of the profile as well [55]. With the aid of this theoretical model, Mampaert et al. [55] hypothesized that the shape of the reflection spectrum especially in the vicinity of the anomalies was dependent on the height of the corrugation. Because analytical formulas for the reflection and transmission coefficients in general cannot be computed, numerical calculations were used to analyze the dependence of the coefficients on the corrugation height. Using the model, it was found that the magnitude of the depths of the anomalies in the reflection spectra increased linearly with an increase in the corrugation height, at least in the case of surfaces with periodic sawtooth profiles. A slight displacement of the minima with height was also found: as the profile height increased, the frequencies of the minima were found to decrease [55].

Soon thereafter, experiments were performed by Blessing et al. [68, 105] on precision machined samples that had identical periodicities but different profile heights. Their work showed an increase in anomaly depth with an increase in corrugation height in normal incidence reflection spectra. However, for the smallest roughness height they examined, no anomaly in the normal incidence reflection spectrum was visible. Therefore, as an alternate method, they examined the intensity of the (backscattered) 1st order diffraction peak generated for incidence at a single Bragg angle and found that it was possible to resolve very small surface roughness heights using this

Bragg angle reflection amplitude when it was not possible using anomalies in the normal incidence reflection spectra. It was also shown that the amplitude of the diffraction peak at this Bragg angle incidence increased with increasing corrugation height for a given periodicity. The work of Oh et al. [93] and Shin et al. [91] has also shown that non-normal angles of incidence may be more useful in the ultrasonic characterization of surface roughness.

The experiments described in this chapter differ from previous studies on ultrasonic characterization of periodic surface profiles in several ways. First, all the studies described thus far have been towards the examination of rough surface textures on thick solids, not thin plates. For thin plates, the wave propagation is more complicated due to the generation of Lamb waves. For thin plates with periodic textures, diffracted modes may phase-match to a Lamb mode and result in additional anomalies observed in the reflection spectra [51, 58]. Therefore, more anomalies may be observed in normal incidence reflection spectra from thin plates with periodic surfaces than for thick solids with such surfaces. This presents an opportunity for the examination of these anomalies for information on the periodic surface texture. Secondly, much of the work on ultrasonic inspection of periodic surface roughness has involved precision machined surfaces, not surfaces with imperfect periodic profiles such as those that result through a rolling manufacturing process. Finally, the comparison of normal incidence spectra with spectra obtained via backscattering has not yet been examined for two-dimensional periodic surfaces, where diffraction effects can also occur due to periodicities existing along the diagonal of the profile's unit cell.

As described earlier, incidence at a single Bragg angle has been shown to be promising for the examination of periodic surface profile heights for the case of precision machined samples [68]. However, the diffraction efficiencies (i.e. amplitudes of diffracted orders) may not be equal for all Bragg angles, especially in the case of imperfect periodic profiles. Therefore, the use of Bragg angle inspection may be sensitive to which angle is chosen for examination. The experiments described in this chapter have been performed with the polar/C-scan apparatus at Georgia Tech Lorraine that can perform rotational ultrasonic scans. In this manner, a broadband pulse is employed and multiple Bragg angles (as well as multiple frequencies at a single Bragg angle) can be investigated. This presents an opportunity to experimentally determine if certain Bragg angles are more promising for the investigation of periodic surface profiles.

Therefore, the objective of the investigation presented in this chapter is to compare the use of normal incidence pulse-echo reflection spectra and backscattered spectra for the characterization of surfaces of a thin plate with imperfect two-dimensional periodic surface textures. The backscattered spectra are obtained for incidence at multiple Bragg angles using a broadband pulse and a rotational scanning technique. From these spectra the goal is to obtain information on the characteristics on the periodic surface textures.

3.3 Description of the sample

The type of plate under investigation is rolled stainless steel with a thickness of 1.2 mm. Both sides of the plate contain regions with different surface textures arranged in a Penrose configuration. The regions are rhombi with a side length equal to 2.5 cm. A photograph of the plate studied is shown in Figure 3.1. Each side of each region is either smooth or has one of two two-dimensional periodic profiles, and the regions labeled in the photo of Figure 3.1 are all of adequate size for inspection and have different pairings of top and bottom surface profile types.

A surface with a two-dimensional periodicity has an "egg-crate" form rather than a series of periodic grooves as in the case of a one-dimensional periodic surface. The smooth surface profile will be referred to as "Profile 0" and the corrugated profiles as "Profile 1" and "Profile 2". Both corrugation profiles have square unit cells

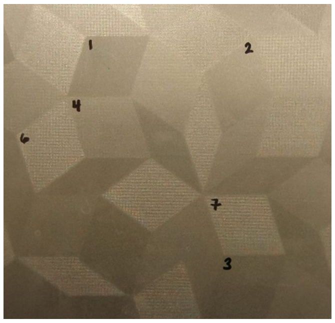

Figure 3.1: Photograph of plate with two-dimensional periodic surface regions.

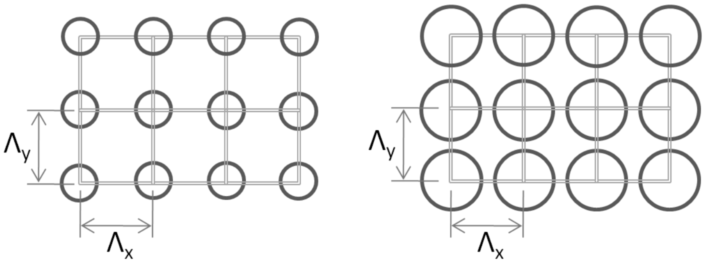

Figure 3.2: Representation of Profile 1 (left) and Profile 2 (right). Not drawn to scale.

and therefore identical periodicities in mutually perpendicular directions as shown in Figure 3.2.

The corrugated profiles (Profiles 1 and 2) are each formed by a pattern of circular indentations with a different circle size for each profile. This can be seen in photographs captured by a stylus profilometer (Veeco Dektak 6M) as shown in Figure 3.3. As the circular indentations are pressed into the surface during the manufacturing process, the surface of the plate is deformed, resulting in periodic but imperfect profiles.

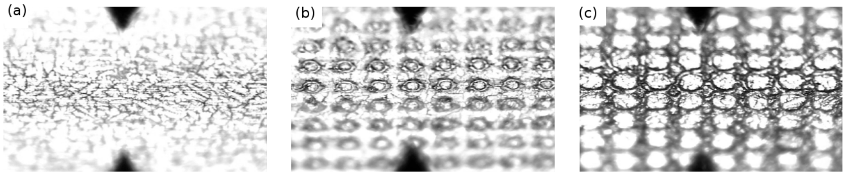

Figure 3.3: Images of the profiles captured by a stylus profilometer. (a) Profile 0, (b) Profile 1, (c) Profile 2.

Diffraction on periodic surfaces is sensitive to the magnitude of the incident wavelength with respect to the value of the spatial periodicity on the surface. Therefore, for the experiments described in this chapter, it is preferred to estimate the spatial periodicities of the profiles in advance in order to wisely choose the ultrasonic frequencies to be used. Measurements of the surface textures were performed with the stylus profilometer and because the surfaces did not exhibit perfect periodicities, spatial Fourier analysis was performed on the measured profiles to detect the periodicities present. Figure 3.4 shows the measured profiles (with approximately three periods shown) as well as the corresponding spatial FFTs.

The profilometer was used to measure the profile height along one of the principal axes of the unit cell, and its sampling resolution was $0.33\,\mu\mathrm{m}$. For the computation of the spatial FFTs, 3840 measurement points were available and this resulted in a spatial frequency resolution of $781.25\,\mathrm{m}^{-1}$. Although the "frequency bins" are located at multiples of this resolution, the spatial periodicity is actually the reciprocal of the frequency. Therefore, although the period-distinguishing resolution is very poor for low spatial frequencies, it improves for higher spatial frequency values. For example, the first two spatial frequency bins, $781.25\,\mathrm{m}^{-1}$ and $1562.5\,\mathrm{m}^{-1}$ correspond to periodicities of $1.28\,\mathrm{mm}$ and $640\,\mu\mathrm{m}$, respectively, resulting in a period resolution of $640\,\mu\mathrm{m}$. However, the period-distinguishing resolution decreases dramatically with increasing spatial frequency bins. For example, the spatial frequency bins of $8593\,\mathrm{m}^{-1}$ and $9375\,\mathrm{m}^{-1}$ have a spatial period difference of $9.70\,\mu\mathrm{m}$ between them, which is much lower than the $640\,\mu\mathrm{m}$ resolution for the first two bins of the series.

The spatial FFT for Profile 1 exhibits peaks at spatial frequencies of $3125\,\mathrm{m}^{-1}$ and $6250\,\mathrm{m}^{-1}$, which correspond to periodicities of $320\,\mu\mathrm{m}$ and $160\,\mu\mathrm{m}$, respectively. The spatial FFT for Profile 2 exhibits both of these same peaks as well as a peak at $9375\,\mathrm{m}^{-1}$ which corresponds to a periodicity of $106.7\,\mu\mathrm{m}$.

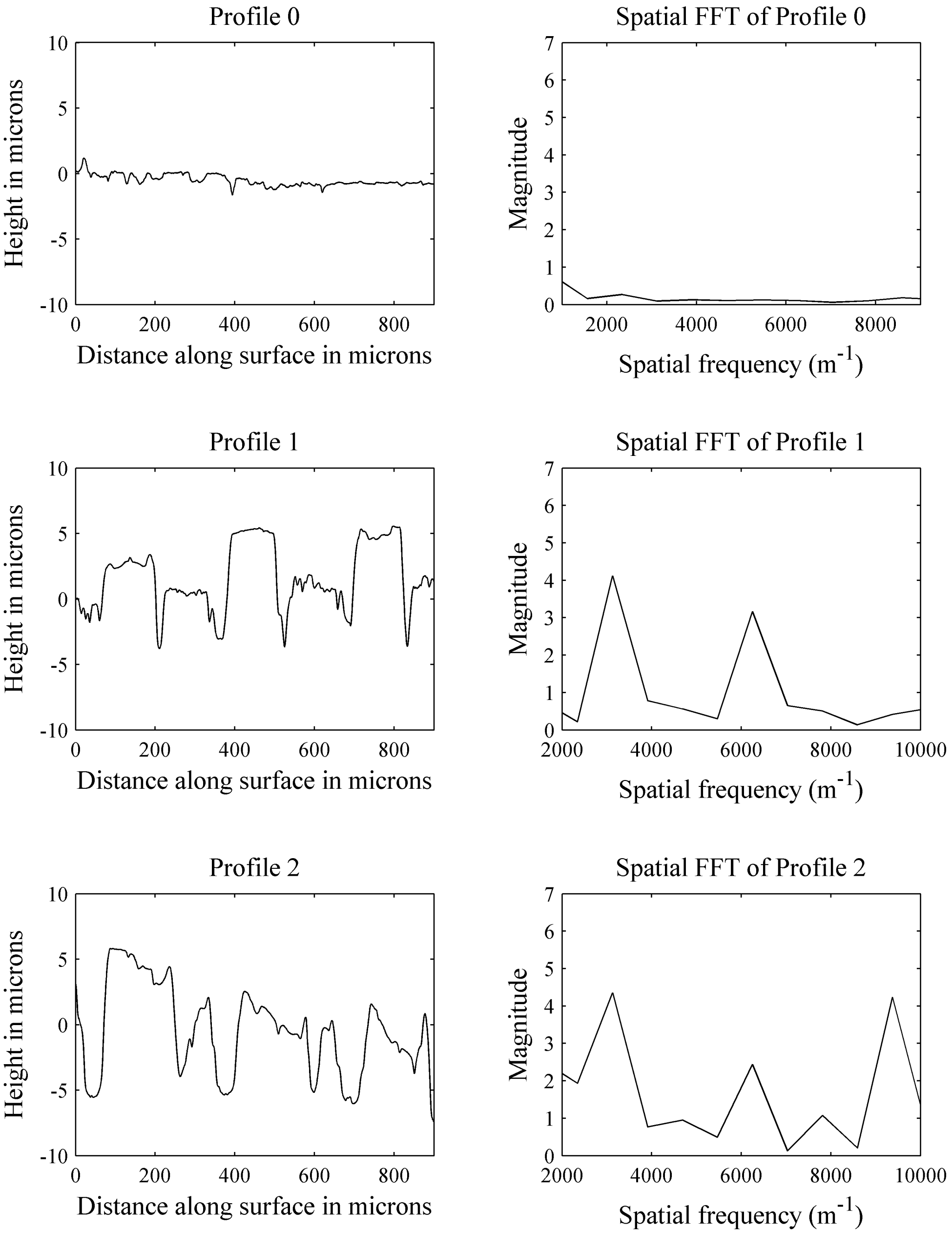

Figure 3.4: Profiles captured by the stylus profilometer (left) and the corresponding spatial FFTs (right).

In general, caution must be exercised when employing an FFT with a large frequency resolution, as it may be possible to miss detecting a frequency if it is located between bin frequencies. However, considering that the peaks identified in the spatial FFTs of the profiles are associated with higher bin frequencies (and thus better period resolution in this case since the period is the reciprocal of the frequency), it can be said with confidence that the periodicities identified in the FFTs are accurate. In addition, upon examination of the measured profiles (the left of Figure 3.4), it is clear that the dominant periodicity of the profiles is between 310 µm and 330 µm, which corresponds well with the 320 µm determined from the spatial FFTs.

It might be thought that 160 µm should be considered as the fundamental periodicity (since 320 µm is simply an integer multiple), but this is complicated by the mechanism of the formation of the profiles. In fact, 320 µm is the distance between consecutive circular impressions on the surface and it has a higher amplitude on the spatial FFTs for both periodic profiles, so this value may affect the spectra equally or more than the 160 µm periodicity. The 106.7 µm periodicity for Profile 2 is very likely due to the material that is pushed up between circular impressions in the profile.

In addition to the profile periodicity Λ, another surface parameter of interest is the h_{rms} (root-mean-square surface roughness height). The h_{rms} can be calculated using Eq. 3.1 where N is the number of measurement points along the profile, h_i is an individual height measurement, and $\bar{h}$ is the mean height calculated from all measurements.

$$h_{rms} = \sqrt{\frac{1}{N}\sum_{i=1}^{N}\left(h_i - \bar{h}\right)^2} \tag{3.1}$$

The h_{rms} values calculated and the main spatial periodicities Λ identified for each profile that were discussed above are summarized in Table 3.1.

As stated earlier, in order for diffraction to occur on a periodic surface, the wavelength of the incident sound should be on the order of the periodicity of the surface.

Table 3.1: Summary of h_{rms} and Λ values obtained from stylus profilometer measurements.

Profile type	h_{rms}	Λ
Profile 0 (smooth)	0.372 µm	None observed
Profile 1	2.294 µm	160 µm and 320 µm
Profile 2	3.688 µm	160 µm, 320 µm, and 106.7 µm

Based on the periodicities identified for the profiles and water with a sound speed equal to 1480 m/s, the frequencies having wavelengths of 320 µm and 160 µm are 4.625 MHz and 9.25 MHz, respectively. Therefore, commercial immersion transducers with nominal center frequencies of 5 MHz and 10 MHz were used to capture the experimental results presented in the next section.

3.4 Experimental setups

Two experimental setups have been employed, one for the normal incidence pulse-echo measurements and the other for the Bragg scattering measurements. All measurements have been performed underwater in the ultrasonic immersion tank of the polar/C-scan apparatus at Georgia Tech Lorraine. In order to better resemble a realistic inspection environment, tap water has been used with no further treatment or purification. The velocity of sound in the water used for the experiments has been found to be 1479.5 m/s.

For the normal incidence pulse-echo setup, one 10 MHz spherically focused transducer (Valpey-Fisher IS1003GP-SF3.0) transducer was used as both emitter and receiver and it was aimed normally at the plate surface. The incident pulse and its frequency spectrum are shown in Figure 3.5. The frequency spectrum was obtained with an FFT performed on 4000 time-waveform points (for a frequency resolution of 0.05 MHz) that were zero-padded to 32000 points. The transducer specifications indicated a nominal focal length of 3.0 inches, but the focal length was found to be

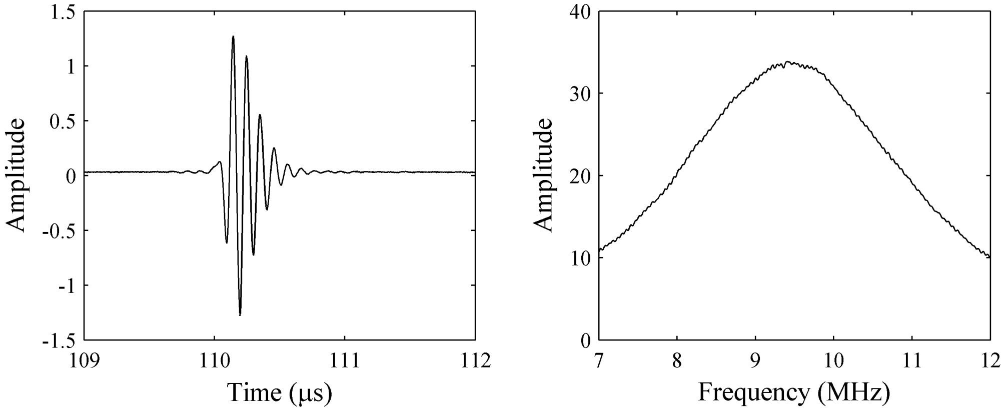

Figure 3.5: 10 MHz incident pulse (left) and corresponding frequency spectrum (right).

closer to 7.24 cm (2.85 inches) so this was set as the distance between the transducer and the sample surface.

The Bragg scattering setup used a single 5 MHz unfocused transducer as both emitter and receiver, but it was mounted in the rotating fork of the polar/C-scan apparatus so that the transducer could rotate with respect to the sample surface. More information on the polar/C-scan apparatus and the rotating fork can be found in Chapter 5.

The incident pulse and its frequency spectrum are shown in Figure 3.6. The frequency spectrum was obtained with an FFT performed on 8000 time-waveform points (for a frequency resolution of 0.025 MHz) that were zero-padded to 32000 points. In order to modify the angle of incidence to capture the backscattered signal at many angles, the sample was maintained stationary and the transducer was rotated around the sample by the polar/C-scan robot. The propagation distance between this transducer and the sample was chosen to be 45 mm in order to be compatible with the rotation of the polar-C-scan equipment.

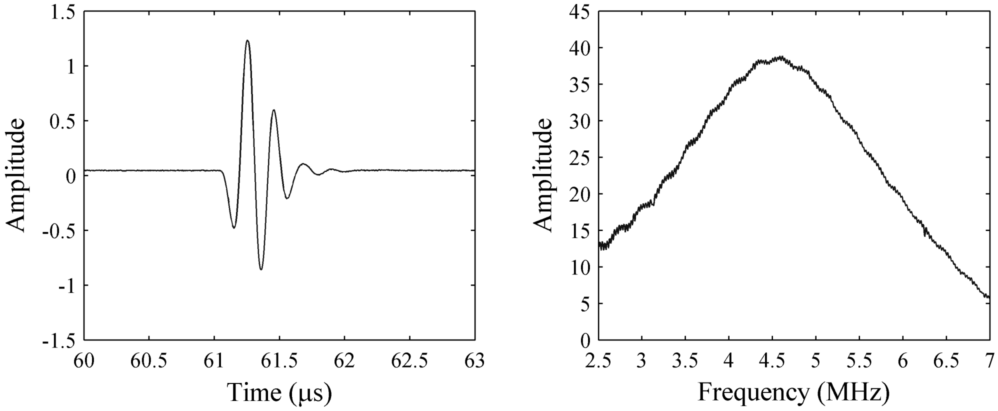

Figure 3.6: 5 MHz incident pulse (left) and corresponding frequency spectrum (right).

3.5 Experimental results

3.5.1 Ultrasonic inspection at normal incidence

The motivation behind the examination of reflection spectra obtained at normal incidence as explained in section 3.2 is the well-established fact that the locations of anomalies in the spectra exist as a function of the periodicity value and that the depths of anomalies depend mainly on the shape or height of the profile [55]. These anomalies can be correlated to generation of surface waves such as leaky Rayleigh or Scholte-Stoneley waves for liquid-solid surfaces and for thin plates, additional anomalies appear that are related to the generation of Lamb waves [51]. In particular, anomalies may appear at frequencies where the phase velocity of diffracted waves along the surface of the plate matches the phase velocity of a Lamb mode.

The reflection spectra obtained from the 10 MHz normal incidence pulse-echo measurements (normalized with respect to the incident pulse) are shown in Figures 3.7 and 3.8. The regions that have been investigated are labeled by the type of profiles they have on their surfaces. The first profile listed is the type of profile on the top (incident) side of the plate and the second profile listed is the type of profile on the bottom side. In Figure 3.7, the reflection spectra from three different regions are shown. The first region has smooth surfaces on both sides and is labeled as "Profile

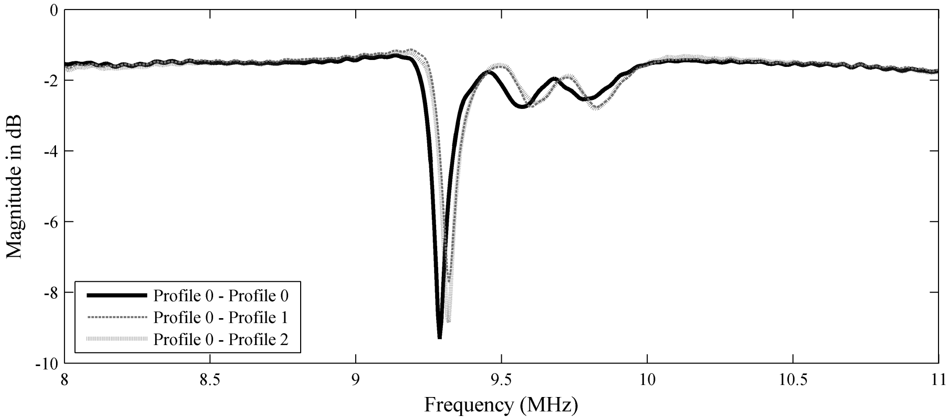

Figure 3.7: Reflection spectra obtained from normal incidence pulse-echo experiments for regions with two-dimensional corrugated profiles on the back side of each region.

0 - Profile 0" and the other two regions ("Profile 0 - Profile 1" and "Profile 0 - Profile 2") both have smooth surfaces on the top side and corrugated surfaces on the bottom side. Three anomalies in the spectra can be seen and their locations for each region are summarized in Table 3.2.

The fact that these anomalies appear for the 0-0 region leads us to conclude that they are not due to diffraction effects on the surfaces. For the anomaly in the vicinity of 9.3 MHz, the 0-0 region actually displays the deepest valley. The frequency of this anomaly is shifted slightly higher for both the 0-1 and the 0-2 regions. The depth of this valley is deeper for the 0-2 surface than for the 0-1 surface. Two additional anomalies can also be seen, namely at frequencies of 9.6 MHz and 9.8 MHz. The depths of these anomalies are not significantly different for the different regions but the frequencies have also been shifted slightly higher for the 0-1 and 0-2 regions in comparison with the 0-0 region.

In Figure 3.8, reflection spectra obtained for 0-0, 1-1 and 2-2 regions are shown. The anomalies in the spectra are similar to those observed in Figure 3.7. However, the depth of the first anomaly for the 2-2 region is noticeably larger and in general the amplitude of this spectrum at higher frequencies is lower. A slight flattening or

Table 3.2: Summary of anomaly frequencies for normal incidence reflection spectra seen in Figure 3.7.

Region Type	Anomaly frequencies		
Profile 0 - Profile 0	9.29 MHz	9.57 MHz	9.79 MHz
Profile 0 - Profile 1	9.32 MHz	9.60 MHz	9.83 MHz
Profile 0 - Profile 2	9.32 MHz	9.63 MHz	9.82 MHz

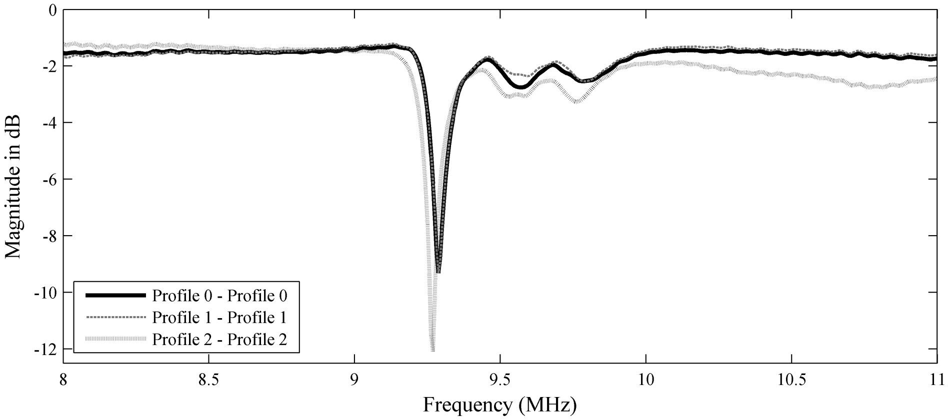

Figure 3.8: Reflection spectra obtained from normal incidence pulse-echo experiments for regions with identical corrugation profiles on front and back sides of each region.

peak within the valley of the second anomaly for the 2-2 region can be seen, possibly due to diffraction effects on the surfaces.

In summary, reflection spectra have been obtained from normal incidence pulse-echo experiments. Anomalies are observed in the spectra that are most likely due to Lamb wave generation. However, the differences in the spectra are not appreciable enough to gain information on the profile characteristics. Some variation in the location of the anomalies is seen which implies an evolution in the Lamb wave dispersion curves with the profile forms and height.

3.5.2 Ultrasonic inspection at Bragg angle incidence

According to the classical diffraction grating equation, backscattering or Bragg scattering should occur for frequency and angle pairs that satisfy Equation 3.2, where

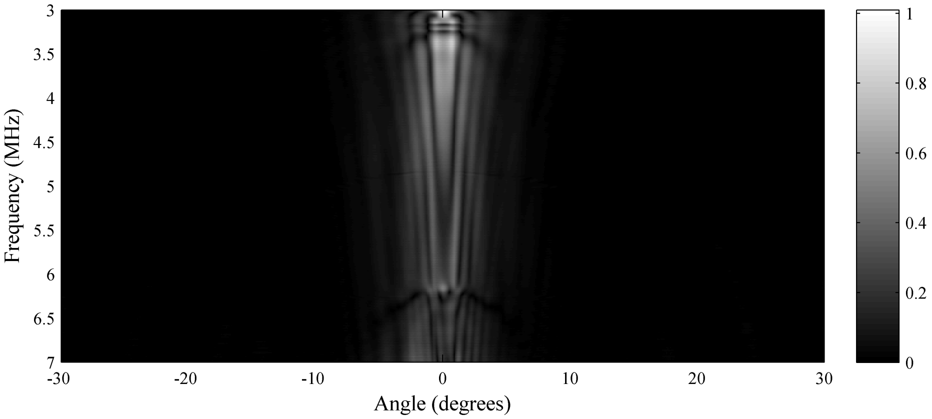

Figure 3.9: Backscattered spectra obtained from the 0-0 region.

f is the sound frequency, m is the diffraction order, v_{liq} is the sound velocity in the liquid (incident medium), Λ is the periodicity along the surface, and θ_i is the angle of incidence.

$$f = \frac{m v_{liq}}{2\Lambda}\frac{1}{\sin\theta_i} \tag{3.2}$$

Ultrasonic scans are performed for three different regions, namely 0-0, 1-1, and 2-2 type regions, and the axis of rotation of the transducer is aligned with one of the principal axes of the unit cell. With this technique, continuous Bragg scattering (1^{st} and/or 2^{nd} order backscattered diffraction) curves should be observed, and the relative amplitudes of these Bragg scattering curves may yield information on the surface profile characteristics. Angular spectrograms where the normalized amplitudes of frequencies detected as a function of angle are shown in Figures 3.9 through 3.13. The angular resolution of all scans performed is 0.1°.

Figure 3.9 shows the angular spectrogram obtained from the backscattered signals for the 0-0 region. The reflection at normal incidence is visible at 0 degrees, along with several discontinuities due to thickness resonances of the plate, but there is no backscatter visible. The angular range of this scan is ± 30° around normal incidence.

In Figure 3.10 an angular spectrogram obtained from the 1-1 region is shown and

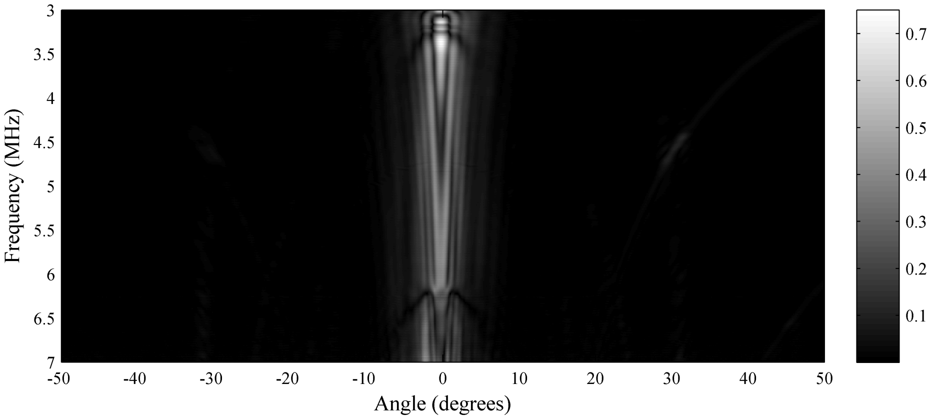

Figure 3.10: Backscattered spectra obtained from the 1-1 region.

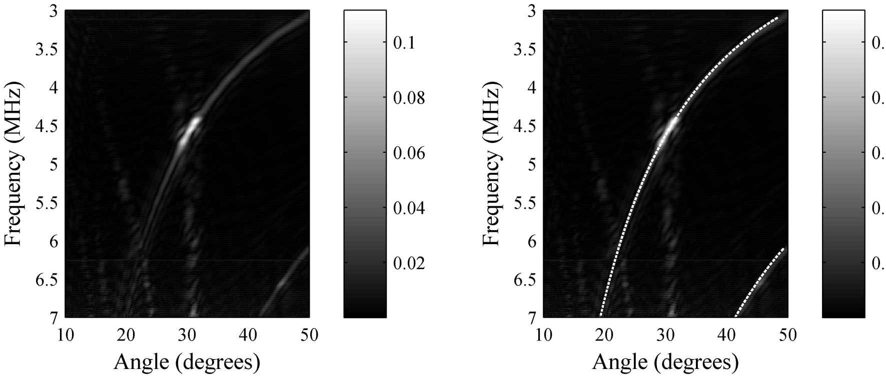

Figure 3.11: Close-up of backscattered spectra obtained for the 1-1 region. Bragg scattering visible (left). Bragg scattering and theoretical frequency-angle relationship shown by dotted line (right).

Bragg scattering is present but barely visible in a B&W color scheme. Figure 3.11 shows close-ups of the Bragg scattering curves from the right side of the scan which makes them more easily visible. The angular range of this scan was extended to ±50° around normal incidence in order to capture the 2^{nd}order Bragg scattering curve that appears for higher frequencies.

The left of Figure 3.11 is a close-up of the Bragg scattering shown in Figure 3.10, and the right of Figure 3.11 is the same as the left except that theoretical frequency and angle pairs that undergo Bragg scattering as predicted by the classical grating equation are superimposed as shown by the dotted lines. The top theoretical curve is calculated using a periodicity of 320 µm and a diffraction order of 1, and the bottom curve corresponds to a periodicity of 160 µm and a diffraction order of 1 or equivalently, a periodicity of 320 µm and a diffraction order of 2.

Along the top Bragg scattering curve it can be seen that the diffraction efficiency (amplitude) is not the same along the curve. In particular, the detected amplitude is noticeably higher around a position of 30° and frequency of 4.5 MHz than for other frequency/angle pairs on the Bragg scattering curve. However, upon further examination of the figure it can be seen that there is a vertical strip of additional frequencies that are detected at 30°. For a smooth steel plate with a thickness of 1.2 mm, the A0 and S0 Lamb wave modes have relatively constant phase velocities in the vicinity of 3000 m/s for the frequency range of 3-7 MHz. Therefore, at a single angle of incidence, it would be possible to phase-match to these Lamb modes for many frequencies, and an angle of approximately 30° would satisfy this requirement. Although in general one can expect the dispersion curves for the plate under investigation to be slightly different than those for a smooth steel plate, for purposes of this discussion one may refer to the dispersion curves for a smooth plate in the manner of Ref. [58]. Therefore, it can be assumed that these additional frequencies are backscattered leaky Lamb modes that have been detected. The detection of backscattered leaky Lamb waves at angles predicted theoretically for the generation of forward leaky Lamb waves has been previously experimentally observed for thin plates in water [106]. Additional strips of frequencies other than those corresponding to the Bragg curves also appear for smaller angles of incidence/backreflection. These are most likely due to phase velocity matching for higher-order Lamb modes with higher phase velocities, such as A1 or S1. These modes are more dispersive in this frequency range so they will not be generated for as many frequencies at the same angle of incidence, which accounts for the fact that these frequencies do not appear as vertical strips.

Figure 3.12 shows the angular spectrogram obtained from a scan of the 2-2 region.

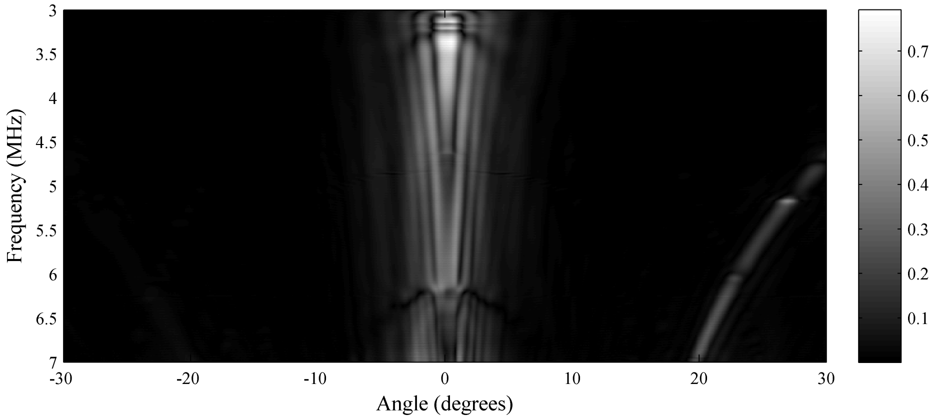

Figure 3.12: Backscattered spectra obtained from the 2-2 region.

The Bragg scattering curve is clearly visible on the right side of the scan and is also present but of lower amplitude on the left side. It is unknown at this time why this backscattering appears more strongly on the right side but it may be related to imperfections in the periodicity of the surface. Due to geometric constraints of the polar/C-scan apparatus, this scan was performed within an angular range of ±30° degrees around normal incidence.

Close-ups are shown in Figure 3.13 in a similar manner to those in Figure 3.11. The theoretical Bragg scattering curve has been superimposed with a dotted line on the right of Figure 3.13. Compared to the backscattering observed for the 1-1 region, the backscattering is definitely of higher amplitude over the entire range of the Bragg scattering curve for the 2-2 region.

One high amplitude area is observed along the Bragg curve at a frequency and angle combination of 5.18 MHz and 27°. The second order Bragg scattering curve is not observed in this case due to the limited angular range of scanning. The backscattered leaky Lamb waves shown in Figure 3.11 are not visible in Figure 3.13. This is most likely due to the low amplitude of the leaky Lamb backscatter compared to the amplitude of the Bragg curve as well as the limited angular range of the scan. Ref. [106] shows that backscattered leaky Lamb wave amplitude can decrease for smaller angles

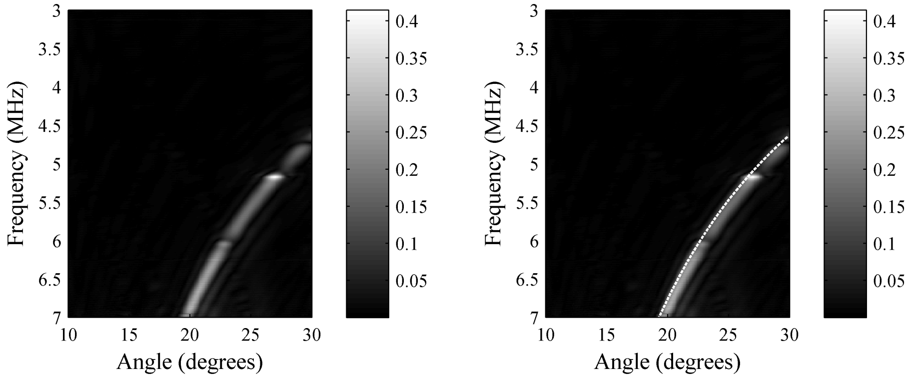

Figure 3.13: Close-up of backscattered spectra obtained for the 2-2 region. Bragg scattering visible (left). Bragg scattering and theoretical frequency-angle relationship shown by dotted line (right).

of incidence (backscatter).

From these angular spectrograms several general observations can be made. Bragg scattering is experimentally observed at many angle and frequency combinations such that it forms a continuous Bragg scattering curve. The amplitude along the normalized curves shows some variation (certain frequencies and angles exhibit noticeably higher amplitudes) which implies that, for the purposes of ultrasonic inspection, all Bragg angles are not equal. However, this increase in amplitude along the Bragg curve is complicated by the fact that backscattered leaky Lamb waves are also generated for thin plates in water. The high amplitude detected at 30° in Figure 3.11 may be a combination of the Bragg diffraction peak and the leaky backscattered Lamb waves. The amplitude along the entire Bragg scattering curve was higher for the 2-2 region than for the 1-1 region, which implies that more Bragg scattering may be observed for rougher (larger h_{rms}) periodic surfaces, even in cases of two-dimensional periodicity and imperfect surfaces. The classical grating equation follows the experimentally determined Bragg scattering curves for periodicities calculated from the profilometer measurements. Therefore we can say that continuous Bragg scattering curves obtained experimentally can be used to determine surface periodicities in a manner similar to the discrete data techniques described in section 3.2.

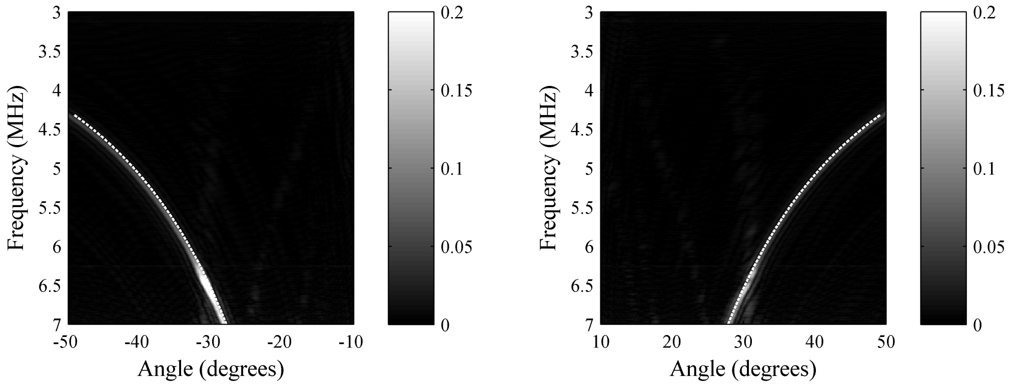

Figure 3.14: Backscattered spectra obtained from a scan performed at 45° with respect to the principal axes of the unit cell of the surface.

One important point regarding surfaces with two-dimensional periodicity is the fact that the periodicity corresponding to the detected Bragg scattering curve is dependent on the angle between the transducer rotation axis and the principal directions of the unit cell on the surface. In order for the Bragg scattering corresponding to the periodicity along one of the principal directions to be observed, the transducer rotation axis must be aligned perpendicular to that direction. Therefore, an additional application has been identified through these experiments: Bragg scattering curves can be used as part of an ultrasonic alignment technique.

Figure 3.14 shows the angular spectrogram obtained from a scan of the 2-2 region where the transducer rotation axis is at a 45° angle to each of the principal unit cell axes. The normal incidence reflection has been omitted in order to make the Bragg scattering curves more easily visible.

On the left side of the scan, the amplitude is not constant along the Bragg curve: a high amplitude area is seen at 6.5 MHz and 30°. The theoretical Bragg curves are plotted in dotted lines. The periodicity used to calculate the dotted curves is 229 µm which is equal to 0.707×324 µm or 1.414×162 µm with a diffraction order of 1. This value corresponds to a periodicity that exists along the 45° diagonal. Therefore, the periodicity that corresponds to a detected Bragg scattering curve can lead to the calculation of the angle of the tranducer rotation axis with respect to the principal axes of the unit cell and thus the alignment of the sample with respect to the transducer.

In summary, the experimental results presented show normal incidence reflection spectra obtained from pulse-echo measurements as well as angular spectrograms obtained from angular scans. The normal incidence reflection spectra seem to be of limited utility especially in the case studied here where the roughness is small, the plate is thin, and the periodicity is two-dimensional and imperfect. As an alternate method, backscattered spectra are examined in order to compare the Bragg scattering that occurs for non-normal incidence. These spectra seem more promising for the characterization of the surfaces studied here.

3.6 Conclusions

This chapter has presented a feasibility study on the use of ultrasound for the inspection of thin plates containing regions of doubly-periodic imperfect surface textures. Two experimental methods have been employed, namely reflection spectra obtained from normal incidence pulse-echo experiments and backscattered spectra obtained through rotational scans. The use of normal incidence reflection spectra has been shown to be limited. In order to use normal incidence reflection spectra to gain insight about periodic profile heights, detailed information on the dispersion curves is needed in order to examine any shifting of anomalies in the spectra. In general, the differences in anomaly heights are not sufficient to gain information to characterize the profile.

An alternate method of ultrasonic inspection, namely the use of Bragg scattering curves appears to be more sensitive to periodic profile heights. The amplitude of the backscattering is shown to increase with the profile height. Detailed theoretical simulations on the diffraction efficiency as a function of profile form can provide more information on the conditions under which this is true. The Bragg scattering curves, however, can be used to calculate surface profile periodicities, analogous to the discrete methods previously developed. The amplitude of the backscatter along the Bragg curve is shown to be unequal, which implies that all Bragg angles may not be equal for the purposes of ultrasonic inspection of imperfect periodic surfaces, although areas of higher amplitude along the Bragg scattering curves may be due to leaky Lamb wave backscattering. Finally, Bragg scattering curves can be used in an alignment technique since they can be used to detect the angle between a sample with a two-dimensional periodicity and a transducer's axis of rotation.

A few questions remain, such as why the Bragg scattering is unequal between the left and right sides of the regions, since theoretically it should be symmetric. This may be due to the imperfectness of the profiles. In order to investigate this, experiments should be performed on "perfect" profiles. Another question that remains is the origin of the higher amplitude for certain frequencies/angles on the Bragg scattering curves and what are the relative contributions of the diffraction and the backscattered leaky Lamb waves to this phenomenon. Detailed theoretical simulations on the diffraction efficiency as well as experiments on perfect profiles could shed light on this matter.

CHAPTER IV

BACKWARD DISPLACEMENT OF PULSED ULTRASONIC BEAMS DUE TO DIFFRACTION EFFECTS ON PERIODIC SURFACES

Thus far, this thesis has presented results of numerical simulations of ultrasonic diffraction as well as the results of experiments that were performed with the aim of studying diffraction effects on imperfectly periodic surfaces. This chapter will now focus on an unusual phenomenon that has been observed on periodically corrugated surfaces that can be attributed to diffraction effects, namely the lateral backward displacement of a bounded ultrasonic beam.

This chapter aims to investigate this phenomenon in three new ways. First, since the phenomenon has only ever been observed for the case of time-harmonic ultrasonic beams, the experiments presented in this chapter will address the occurrence of the phenomenon for pulsed ultrasonic beams (that are more commonly employed in ultrasonic NDE [19]). Second, all prior observations of the backward displacement that can be found in the literature have been performed using Schlieren imaging, which, although extremely useful for beam visualization, is not a quantitative tool. Therefore, the experiments presented in this chapter have employed commercial ultrasonic immersion transducers to quantitatively measure the diffracted ultrasonic fields generated. Finally, the backward displacement has only ever been observed in reflection. Therefore, this chapter will investigate the backward displacement not only in reflection but also in transmission.

This chapter is structured in the following manner. First, an introduction to the ultrasonic backward beam displacement will be given along with a history of its study. The second section is dedicated to the quantitative experiments that study the phenomenon for pulsed beams in reflection, and the third section presents the experiments performed for the transmission case. More specifically, the experiments that address the phenomenon in reflection aim to determine whether backward displaced frequency components can be observed for pulsed ultrasonic beams and whether these frequency components correspond to the frequencies of backward Scholte-Stoneley waves that can be generated through diffraction and mode conversion on the surface. The transmission measurements aim to determine whether the phenomenon can at all be observed in transmission.

4.1 Introduction to the ultrasonic backward beam displacement

The lateral displacement of ultrasonic beams is a well-documented effect. The Schoch effect occurs, for example, when a bounded beam experiences a forward displacement due to the generation of forward propagating Rayleigh waves along the surface [61, 33].

However, a backward ultrasonic beam displacement has only ever been observed on periodic surfaces. This can be attributed to the fact that the diffraction that occurs on the surface due to its periodicity is essential to the generation of the leaky backward surface wave that ultimately results in the lateral backward shift in the specularly reflected beam as shown in Figure 4.1. This phenomenon was first predicted theoretically in optics by Tamir and Bertoni [107], but the actual existence of the phenomenon was first confirmed in acoustics by Breazeale and Torbett [60] in 1976 when they observed the phenomenon using Schlieren imaging and a time-harmonic ultrasonic beam.

This introductory section is divided into two subsections. First, the original experiments of Breazeale and Torbett that confirmed the existence of the phenomenon will be discussed. Second, additional studies by Declercq et al. [63, 43, 74] that resulted in the displacement being attributed to leaky backward Scholte-Stoneley waves will

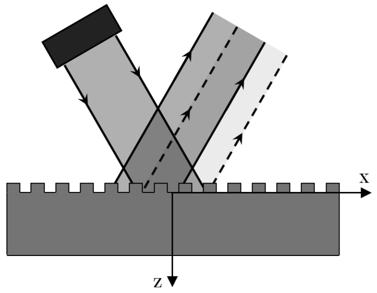

Figure 4.1: Diagram of the ultrasonic backward beam displacement on a periodically corrugated surface. The location of the specular beam predicted geometrically is shown by dashed lines. The backward shifted beam is shown in solid lines. The backward propagating leaky surface wave causing the beam shift propagates in the negative x-direction. Corrugation profile enlarged for illustration.

.

be summarized.

4.1.1 The experiments of Breazeale and Torbett

The first experimental observation of a backward beam displacement on a periodic surface was obtained by Breazeale and Torbett [60], and the motivation behind their work was to discover the acoustic phenomenon that would correspond to the optical phenomenon predicted by Tamir and Bertoni [107]. Tamir and Bertoni had predicted that for light reflection at a dielectric interface where a periodic structure had been superimposed, a leaky wave would be generated under certain conditions and it would then propagate in the backward direction, ultimately resulting in a backward displacement of the specularly reflected beam.

Breazeale and Torbett considered an ultrasonic bounded beam incident on a water-brass interface where the brass had been grooved with a periodicity Λ equal to 178 µm. The beam was incident at an angle of incidence θ_i (considered measured from the normal to the interface) and was time-harmonic with a frequency f. From the classical diffraction grating equation [13], Breazeale and Torbett formulated the expression shown in Equation 4.1 that gives the optimum angle of incidence in order to generate a backward propagating lateral wave along the surface with a diffraction order equal

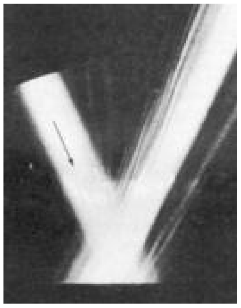

Figure 4.2: Schlieren image of the ultrasonic backward beam displacement as observed by Breazeale and Torbett for an ultrasonic beam having a frequency of 6 MHz at an angle of incidence equal to 22.5°. From Ref. [63].

to -1. In this expression, v_{liq} is the velocity of sound in water and v_{surf} is equal to the velocity of the backward surface wave.

$$\sin\theta_i = v_{liq}\left(\frac{1}{f\Lambda} - \frac{1}{v_{surf}}\right) \tag{4.1}$$

Breazeale and Torbett first assumed a value of 2015 m/s (the leaky Rayleigh wave velocity on a water-brass interface) for v_{surf} since they assumed the surface wave that would be responsible for the displacement would be a leaky Rayleigh wave. For their beam frequency f of 6 MHz and a v_{liq} of 1490 m/s, this resulted in a prediction of 41° for the angle of incidence at which the backward displacement would be observed. However, no backward displacement was observed for their 6 MHz beam at this angle of incidence. Instead, they observed the phenomenon for a θ_i equal to 22.5° as shown in the Schlieren image presented in Figure 4.2. This indicated that the velocity of the backward propagating surface wave responsible for the displacement was equal to approximately 1470 m/s, which differed considerably from the velocity of a leaky Rayleigh wave on a water-brass interface. This suggested that either the theory of Tamir and Bertoni did not accurately describe the backward beam displacement or that the surface wave responsible for the phenomenon was not, in fact, a leaky Rayleigh wave.

Although Breazeale and Torbett made this first observation of the ultrasonic backward beam displacement in 1976, the surface wave responsible for the phenomenon would remain unknown until further study that would only occur over 20 years later.

4.1.2 Further study of the backward beam displacement and its relation to leaky Scholte-Stoneley waves

Further study of the ultrasonic backward beam displacement would need to wait over 20 years after the original discovery until interest in the study of ultrasonic diffraction on periodic structures would receive more attention, in part due to the success of the development of the Rayleigh-Fourier (R-F) method (discussed in Chapter 2 of this thesis) for simulating diffraction on liquid-solid interfaces [54]. Once the R-F method was able to be successfully implemented to simulate the results of experiments on liquid-solid surfaces, it underwent a number of extensions. One of these included the use of incident inhomogeneous waves that could be used to simulate a bounded beam [59], in contrast to prior implementations of the R-F method that used incident plane waves of infinite extent.

This numerical technique employing imhomogeneous wave theory along with the R-F method was first proposed by Declercq et al. [63], and it enabled the simulation of the beam displacement. The ultimate conclusions of the simulations employing this theoretical technique [43] were that the displacement was caused by a leaky form of Scholte-Stoneley waves, and that the appearance of the backward displacement is highly dependent on the beam width.

Shortly after these discoveries, experiments were conducted by Teklu et al. [74] to investigate the agreement of experimental observations with the prior theoretical predictions concerning the influence of the beam width. These experiments that were also conducted using Schlieren imaging showed that the backward beam shift appeared when the negative 1^{st} order diffracted sound beam was barely visible along the surface of the sample. This observation was considered a signal of the transition of the negative 1st order from a bulk wave to a Scholte-Stoneley wave with decreasing angle of incidence. Although on homogeneous, planar solid surfaces, phase matching considerations prevent the coupling between bulk waves and Scholte-Stoneley waves, for the case of a homogeneous non-planar solid surface such as a periodically corrugated surface, a coupling between bulk waves and Scholte-Stoneley waves can exist [42].

Prior to this experimental work by Teklu et al., a numerical study on the behavior of Scholte-Stoneley waves when they encounter the corner of a solid plate [35] revealed that Scholte-Stoneley waves are scattered in the forward direction upon reaching the corner and do not propagate around the corner in the manner of leaky Rayleigh waves [108, 109]. This phenomenon has also been shown experimentally [36]. Although these studies do not concern Scholte-Stoneley waves on periodic surfaces, the observation that these waves propagate off the edge of a solid sample has relevance in the experimental measurements of the backward displacement in reflection that will now be presented.

4.2 Spectral analysis of the ultrasonic backward beam displacement in reflection

The experiments presented in this section have been conducted with two main objectives in mind. The first was to quantitatively show that the backward beam displacement exists at additional frequencies and angles of incidence other than the single frequency and angle of incidence pair (6 MHz, 22.5°) that has been studied in the past [60, 74] and to show that these frequency and angle pairs can be theoretically predicted by the classical grating equation. The second objective was to show that the backward displacement of frequency components within the pulsed beam is accompanied by a backward propagating Scholte-Stoneley wave, which results in the known transmission effect upon reaching the edge of the solid sample.

Both of these objectives are realized through the analysis of frequency spectra obtained from angular scans of the diffracted fields in water surrounding the solid sample. Angular spectrograms (frequency vs. angle) and classical spectrograms (frequency vs. time) are used to interpret the results. The angular scans have been accomplished with the polar/C-scan equipment at Georgia Tech Lorraine, and the same solid brass sample that was used in the original backward beam displacement observations of Breazeale and Torbett in 1976 has been used in these experiments.

This section is divided into four subsections. First, the theoretical considerations related to the experiments of Breazeale and Torbett that were discussed in the introduction to this chapter will be reviewed. The following subsection will describe the sample and the experimental setup. This will be followed by a presentation and discussion of the experimental results, including how the quantitative measurements confirm the original qualitative observations of Breazeale and Torbett. Finally, conclusions from the reflection measurements will be presented.

4.2.1 Theoretical considerations

As discussed in the subsection 4.1.1 of this chapter, Breazeale and Torbett used the classical grating equation to derive an expression, shown in Equation 4.1, to give the optimum angle of incidence for an ultrasonic beam to generate a backward propagating lateral wave on a periodic surface and thus experience a backward displacement in reflection. The expression can also be inverted in order to calculate the frequency of the backward propagating wave for a known angle of incidence.

They used the value of 2015 m/s for v_{surf} in Equation 4.1 since they hypothesized that the leaky surface wave responsible for the backward displacement would be of the Rayleigh type. However, the angle predicted by this velocity value, 41°, did not result in the observation of the phenomenon. Another angle, 22.5°, was the angle of incidence at which the backward displacement was observed for their 6 MHz beam.

It was not until the later theoretical studies revealed the cause of the backward displacement to be a leaky Scholte-Stoneley wave that an accurate prediction of the optimum angle of incidence could be made. Based on Breazeale and Torbett's original 22.5°±0.25° measurement, the surface wave responsible for the backward displacement would have a velocity between 1465.8 m/s and 1477.6 m/s with an average of 1471.7 m/s. Even though, in general, dispersion of Scholte-Stoneley waves on periodic surfaces may be expected, this value (1471.7 m/s) may be used as a basis in order to predict the frequency and angle of incidence pairs at which the backward displacement may appear on the surface being studied. Thus, frequency and angle pairs predicted by Equation 4.1, with a v_{surf} equal to 1471.7 m/s, will be compared to frequency and angle pairs observed experimentally. The velocity of water used in the experiments has been measured to be 1479.5 m/s, and this velocity will be used as v_{liq} in Equation 4.1.

In addition to predicting the frequency and angle of incidence combinations that should result in the backward displacement and the generation of a backward propagating Scholte-Stoneley wave, the classical grating equation also provides information on the propagation of diffracted bulk modes that are not confined to the surface of the sample. In the prior studies of the backward displacement, only single frequency beams were used, so the presence of the backward propagating Scholte-Stoneley wave was examined without the possibility of the other propagating bulk modes being present. Since the purpose of these experiments is to study the backward displacement for the case of pulsed ultrasonic beams, many frequency components will be present simultaneously in the pulse. This can result in the presence of additional propagating bulk modes in the fluid that are not confined to the surface of the sample. This would occur only for frequencies that are higher than the frequency of the backward Scholte-Stoneley wave that is generated for a given angle of incidence, and these frequencies will be present in the region of the liquid between the incident beam and the backward surface wave as shown in Figure 4.3 for a periodic surface with an arbitrary profile.

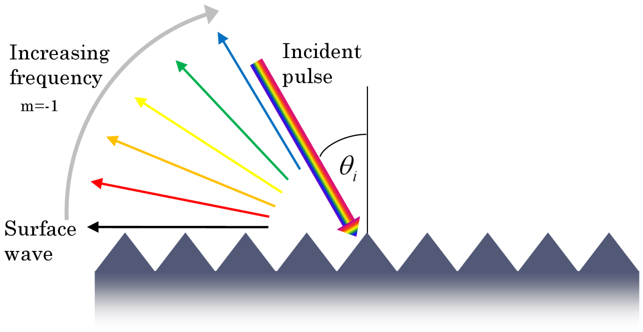

Figure 4.3: Schematic of propagating modes behind incident beam for a periodic surface with an arbitrary profile. Reflected field not shown.

The propagating bulk modes that should be observed will also be of the negative 1^{st} order, and their angles of propagation θ_{pm} can be predicted by Equation 4.2, which is also derived from the classical grating equation.

$$\sin\theta_{pm} = \frac{v_{liq}}{f\Lambda} - \sin\theta_i \tag{4.2}$$

Using Equation 4.2 for an incident pulsed beam at a given angle of incidence, the directions of the propagating bulk modes for many frequencies can be calculated.

4.2.2 Description of the sample and the experimental setup

The sample used to perform all of the backward displacement experiments in this chapter is the original grooved brass sample that was used by Breazeale and Torbett in their original observation of the phenomenon in 1976. The sample consists of a rectangular piece of brass (60 mm long, 25 mm wide, 12 mm high) with a section 25.4 mm long along its length that had been machined with periodic rectangular grooves having a periodicity equal to 178 µm and profile height equal to 25 µm.

A single experimental setup was used to accomplish both of the objectives of the reflection experiments. All measurements have been performed underwater in the water tank of the polar/C-scan equipment at Georgia Tech Lorraine. The experimental setup consisted of a pitch-catch transducer arrangement and two commercial immersion transducers (Valpey-Fisher ISO504GP) with nominal center frequencies of

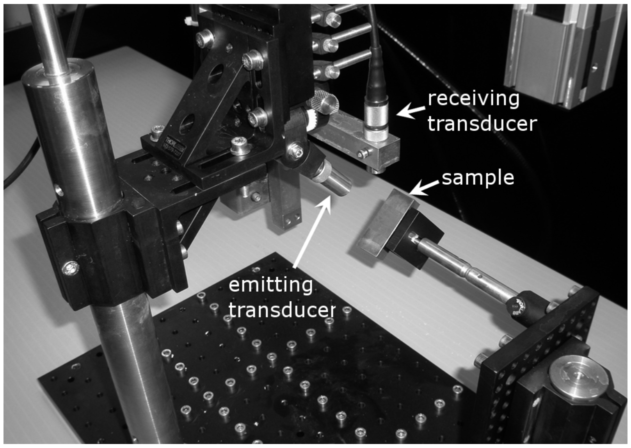

Figure 4.4: Photo of the experimental setup with the sample rotated so that the emitting transducer is directly normal to the sample's grooved surface. Photo was taken before submersion in the water tank.

5 MHz were used.

One transducer (the emitter) was mounted so that it was incident upon the grooved portion of the sample, and the other transducer (the receiver) was set in the rotating fork of the polar/C-scan equipment so that it could rotate through and measure the diffracted fields generated from the emitted pulse's interaction with the periodic surface of the sample. Because the emitter was stationary, the sample was mounted in such a way that it could be rotated in order to change the angle of incidence. A photograph of the experimental setup before it was submerged in the water tank is shown in Figure 4.4. The setup is shown with the sample rotated so that the beam from the emitter would be normally incident on the sample surface.

The propagation distance between the incident transducer and the sample surface was 66 mm and the beam width was approximately 12 mm. The beam used in the original experiments of Breazeale and Torbett was 10 mm in width, and it was shown by Teklu et al. [74] that the backward displacement is not necessarily visible for smaller beam widths. The distance between the sample and the receiving transducer was chosen to be 45 mm in order to be compatible with the rotation of the polar/C-scan equipment.

4.2.2.1 Angular scan types

Two types of scans were performed. First, in order to quantitatively observe any backward shifted frequency components present in the reflected field, scans were performed in the vicinity of the specularly reflected beam (in front of the emitting transducer). A scan was performed each time the angle of incidence was changed (with a clockwise rotation of the sample as it is shown in Figure 4.4). The measurements for the angles of incidence (i.e., the angles of rotation of the sample) were obtained with an inclinometer and should be considered as accurate to ±1°.

Although the scans performed by the polar/C-scan equipment appear continuous to the naked eye, waveforms are acquired and recorded at specific locations in the scan, determined by the scan's angular resolution. Each scan in these experiments covered a angular range of 70° with a resolution of 0.25° between each waveform acquisition. The start and end points for the scans were determined by the geometrical constraints of the setup and scanning equipment so they were identical for all angles of incidence measured. Although a higher angular resolution may have been desirable, it was set lower in order to better accommodate the limited memory of the PC integrated with the polar/C-scan equipment.

The second type of scan was designed to measure the diffracted field behind the emitting transducer, in order to quantitatively measure the field associated with the backward propagating surface wave that should accompany the backward displaced frequencies. It would also capture the bulk propagating modes behind the emitter (those shown in the schematic of Figure 4.3). In order to scan this area of the diffracted field, the sample was rotated in the counter-clockwise direction so that the receiving transducer was now in the field behind the emitting transducer. A scan was performed each time the sample was rotated. The angular range and resolution of these scans were also 70° and 0.25°, respectively. A diagram of the scan paths associated with these two types of scans is shown in Figure 4.5.

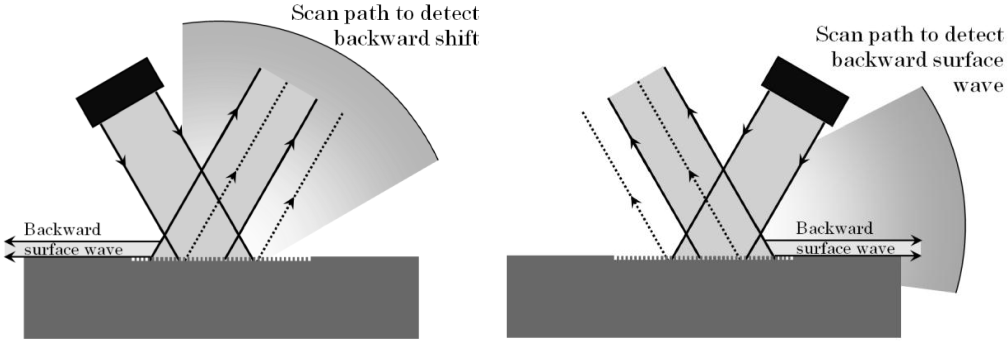

Figure 4.5: (Left) Scan path to detect the backward beam shift in reflection. (Right) Scan path to detect the accompanying backward propagating Scholte-Stoneley wave.

4.2.2.2 Comments on the angular scanning technique

Before the experimental results are presented, it is appropriate to discuss the rotational nature of the scans, namely their sensitivity to the magnitude of the backward displacement along the surface and to the angle of incidence (and specular reflection).

The backward beam displacement is considered to be a lateral shift of a time-harmonic beam along a periodic surface. However, since the experiments presented here have employed a pulsed beam, only a very narrow range of frequencies within the beam spectrum may be shifted backwards, while the other frequencies within the pulse spectrum should remain within the specularly reflected beam.

For a given angle of incidence, as the magnitude of the lateral shift of the backward displaced frequencies increases and they move away from the specularly reflected beam, their detection becomes more difficult with the use of an angular scanning technique. This is due to the fact that the backward shifted frequencies become less normal to the receiving transducer's surface as they increase in distance from the specular beam. If they are too close to the specular beam (indicating a very small backward shift), they may also be difficult to detect. Therefore, for a given angle of incidence, backward shifts that are very large or very small could be difficult to detect using the angular scanning technique employed here.

Likewise, for a given magnitude of the lateral backward shift, the backward displaced frequencies may be more difficult to detect for small angles of incidence since they would be less normal to the receiving transducer's surface than in the case of larger angles of incidence. In general, with the use of the commercial immersion transducers employed in these experiments, any time that the backward shifted frequency components are less than normal to the receiving transducer, their measured amplitudes will be lower than those actually present in the field and they may be more difficult to detect. The receiving transducer in the angular scanning technique used here only measures the *projection* of the backward shift on the transducer face. This is also particularly important to consider for the measurement of large angles of incidence, since in this case the projection of any backward shifted frequencies will be very close to the specularly reflected beam, although it might still be possible to identify them due to phase interference.

The conclusion of this discussion is that the use of an angular or rotational scanning technique like that employed in these experiments is best restricted to a middle range of angles of incidence. A restriction on the magnitudes of beam shifts it can accommodate cannot yet be made, since the study of the magnitudes of backward beam shifts as a function of frequency, surface periodicity, and beam width is a virtually untouched area of research.

In spite of the restrictions mentioned above, the angular scanning technique presented here is actually an ideal tool with which to measure both the presence of backward shifted frequencies *and* the accompanying backward surface wave generation and bulk propagating modes behind the emitting transducer. Because diffraction on a periodically grooved surface results in a hemispherical field with all the diffracted waves originating at the illuminated region of the surface, an angular technique is an ideal tool to capture this diffraction.

4.2.3 Experimental results

The experimental results are divided into two parts. First, the original observations of Breazeale and Torbett (6 MHz at 22.5°) will be confirmed using the quantitative scanning technique, and then results will be presented for three additional frequency and angle pairs. Since the experiments have used ultrasonic pulses in order to study many frequencies simultaneously, Fourier analysis by means of the Fast Fourier Transform (FFT) has been performed on the received waveforms after their acquisition. Results are reported in the form of angular spectrograms which show the amplitude of frequencies present in the waveforms detected by the receiving transducer as a function of the angle of the transducer within the field. In addition, classical spectrograms, which show frequencies present in the time waveform detected by the receiving transducer as a function of time, are presented. Classical spectrograms (sometimes called sonograms) are encountered in other areas of acoustics and ultrasonics. However, angular spectrograms are less commonly seen. They are amplitude plots as a function of frequency and position, and they show the measurements taken at a fixed radius from the illuminated area of the sample. All results have been normalized with respect to the incident signal, and its time-waveform and FFT spectrum are shown in Figure 4.6. The spectrum was created using 8000 time-waveform points and throughout this subsection, all time-waveforms have been sampled at 200 MHz and are zero-padded to 32000 points. The use of 8000 time-waveform points in the FFT results in a frequency resolution of 0.025 MHz and zero-padding to 32000 points results in a bin resolution of 0.006 25 MHz.

4.2.3.1 Confirmation of the observations of Breazeale and Torbett

For an angle of incidence equal to 22.5°, a scan of the region of the specularly reflected beam results in the angular spectrogram shown in the left side of Figure 4.7. The spectrogram was created from FFTs that were performed at each angular position

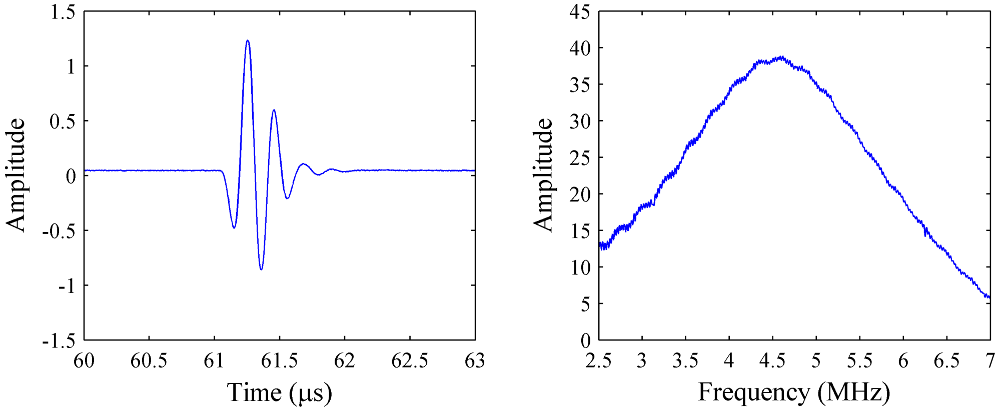

Figure 4.6: Time-waveform and frequency spectrum of incident signal for the 5 MHz transducer pair.

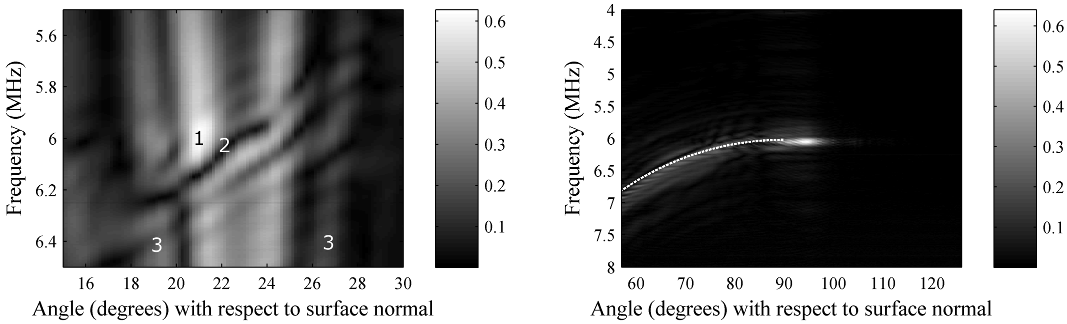

Figure 4.7: Angular spectrograms confirming the results obtained by Breazeale and Torbett (θ_i equal to 22.5°). (Left) Spectrogram from the region of the specularly reflected beam. (Right) Complementary spectrogram to detect the backward surface wave. Propagating bulk modes also detected and theoretical positions are shown by the dotted line.

using 8000 time-waveform points that were zero-padded to 32000 points.

The beam is centered at the angle of specular reflection as expected. There are also three note-worthy features within the spectrogram, and they are numbered on Figure 4.7. First, there is a bright zone of frequencies having higher amplitudes, labeled as "1" and centered approximately at an angular position of 21° and at a frequency of 6 MHz. If the angular spectrogram is examined closely, the maximum amplitude within this zone is found to be at an angular position of 21° and at a frequency of 5.98 MHz. Frequencies having high amplitudes (greater than 0.55 on the spectrogram) within the bright zone exist between 5.92 MHz and 6.08 MHz, and frequencies within this range do not have such high amplitudes on the opposite side of the beam. The existence of this high-amplitude bright zone indicates that the energy from the frequency components in this range is not distributed equally from left to right across the beam profile; these frequencies are disproportionately found on the left side. This result can be interpreted as evidence of these frequencies having shifted backward.

Before discussing the other noticeable features in the spectrogram, it is appropriate to discuss additional evidence that indicates that these frequencies experience a backward shift. This evidence can be found by examining classical spectrograms that were created for the waveform acquired with the receiver positioned within the bright zone. If the backward displacement occurs as it is currently understood, frequency components that are shifted backward should arrive after the other non-shifted frequencies in the beam. This is due to finite nature of wave propagation speeds; any frequency that is shifted backward with respect to the specular direction must first travel backward along the surface at the speed of the backward propagating surface wave before re-radiating from the sample surface to the receiving transducer.

Therefore, the classical spectrograms shown in Figures 4.8 and 4.9 were created by applying the Short-Time Fourier Transform (STFT) to the time-waveform that was captured at the 21° receiver position. The left side of Figure 4.8 shows a spectrogram created using time-windows 512 points in length with an overlap of 440 points. The windows were each zero-padded to 32000 points. The arrival of the specularly reflected pulsed beam can be seen as a solid vertical band of frequencies, and this specular beam arrival is followed by a faint trail of frequencies that can be seen more clearly in the close-up on the right side of the figure.

Upon visual inspection, the band of trailing frequencies has a bandwidth of 0.5 MHz, and the frequency of maximum amplitude of the band is 6.17 MHz along many of the

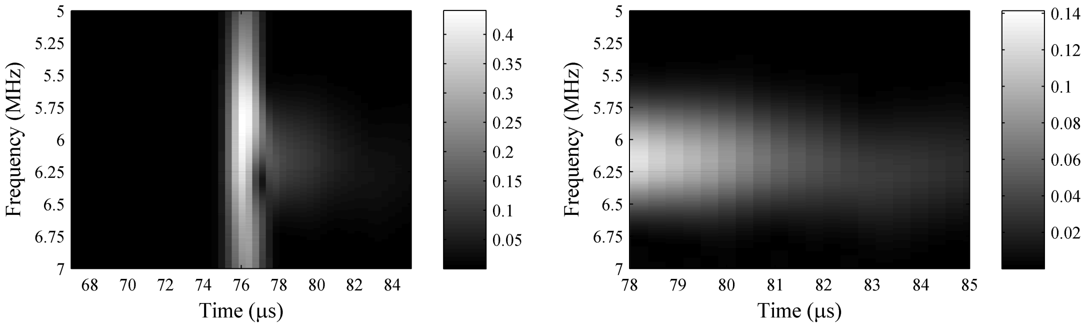

Figure 4.8: (Left) Classical spectrogram for a θ_i of 22.5° obtained from the time-waveform captured at a receiver angle of 21°. (Right) Close-up showing the trailing frequencies arriving after the initial pulse. Time-windows are 512 points long.

initial time windows of the spectrogram. This wide bandwidth of the trailing frequencies can be attributed to the size of the time-windows used to perform the STFT. Although the time-waveform windows used to create this spectrogram result in good time resolution (0.12 μs), the resulting frequency resolution is poor (0.39 MHz).

Therefore, larger time-windows were used to obtain the spectrograms shown in Figure 4.9. Figure 4.9 was created from exactly the same data as Figure 4.8; the only difference is the time-window length used for the STFT. For Figure 4.9, time-windows 1024 points in length with an overlap of 1000 points were used. These wider time-windows result in a lower time resolution of 0.36 μs. The longer "duration" of the specular beam can be attributed to this lower time resolution as well as to the large overlap value. However, a finer frequency resolution of 0.2 MHz is obtained. Based on the close-up on the right of Figure 4.9, the frequency having the highest amplitude within the trailing band is 6.1 MHz.

Returning to the labeled features on the left side of Figure 4.7, a null zone (with amplitudes lower than 0.1) is labeled as "2" within the region of the specular beam. The null zone extends between 20.75° and 23.75° with frequency decreasing from 6.15 MHz to 5.95 MHz as the receiver angle increases. The existence of this null zone can most likely be attributed to phase cancellation between specularly reflected sound and re-radiated (backward shifted) sound. The existence of null zones that

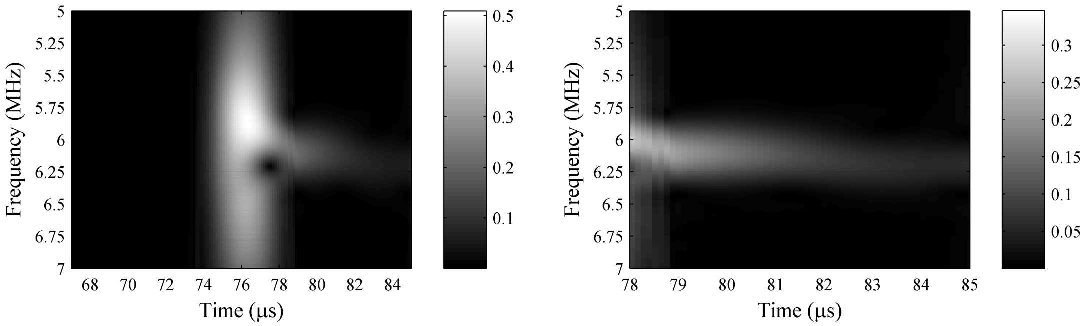

Figure 4.9: (Left) Classical spectrogram for a θ_i of 22.5° obtained from the time-waveform captured at a receiver angle of 21°. (Right) Close-up showing the trailing frequencies arriving after the initial pulse. Due to the increased time-waveform length, frequency resolution is improved. Time-windows are 1024 points long.

occur due to phase cancellation in reflected fields where beam shifts have occurred are well-documented, such as in the case of the Schoch effect [110, 62].

Finally in Figure 4.7, the presence of vertical bands that show frequencies present to the left and right of the specular beam labeled as "3" is noted. These bands occur at receiver angles of 19° and 26.5°, and they can be attributed to deformation of the beam that occurs upon reflection, which is not an uncommon occurrence especially for the case of periodically corrugated surfaces. Such beam deformation and beam widening can be seen in several references. For example, Figures 5 and 6 in the work of Teklu et al. [74] show the deformation of an ultrasonic beam in reflection from a periodically corrugated surface. Specular beam deformation is also seen in the original Schlieren image of the ultrasonic backward beam displacement made by Breazeale and Torbett in 1976 [60] that was shown in Figure 4.2.

The angular spectrogram created from the complementary scan in the region of the backward propagating surface wave is shown at the right side of Figure 4.7. This spectrogram was created with 8000 time-waveform points zero-padded to 32000 points for each angular position. Here a backward propagating surface wave can be observed, and the frequency at which the amplitude is a maximum is 6.05 MHz. Since the receiver was positioned a distance away from the sample, the waveform detected was that which had propagated off the surface of the sample, a behavior one would expect from a Scholte-Stoneley wave. Higher frequency propagating bulk orders are also visible. The dotted line plotted on the spectrogram corresponds to the theoretical angles of the bulk modes as a function of their frequency, and they were calculated from Equation 4.2. The presence of faint additional frequencies at the same angular position as the backward propagating Scholte-Stoneley wave can be explained as being evanescent waves, negative first order for frequencies below the Scholte-Stoneley frequency or higher order for higher frequencies.

A summary of these results is the following. From the scan in the region of the specular beam (angular spectrogram on the left of Figure 4.7), it is clear that there is an imbalance of frequencies across the beam profile from left to right for frequencies in the vicinity of 6 MHz (±0.08 MHz). There is also a null zone consisting of a band of frequencies between 5.95 MHz and 6.15 MHz that varies with the angle of the receiver. From the classical spectrograms (Figure 4.9), it can be seen that at a receiver angle of 21°, left of the center of the specular beam, a band of frequencies with an amplitude maximum at 6.1 MHz continues to arrive at the receiver well after the specular beam has passed. From the scan in the region behind the incident beam (angular spectrogram on the right of Figure 4.7), a backward propagating surface wave with an amplitude maximum at a frequency of 6.05 MHz was detected.

Now the experimental results will be compared with the diffraction grating theory. The theoretical Scholte-Stoneley wave frequency, f_{SSt}, calculated for an angle of incidence of 22.5° is equal to 5.99 MHz. It can be seen on the left side of Figure 4.7 that this frequency is within the bright high-amplitude zone at an angle of 21° and is in the null zone in the center of the specular beam. It is also a frequency contained within the trailing frequencies in the spectrogram of Figure 4.9, and it is close to the maximum amplitude of the detected backward propagating surface wave.

Based on the agreement among the pieces of experimental evidence as well as between the experiments and diffraction grating theory, it may be concluded that that for an angle of incidence of θ_i equal to 22.5°, frequencies very close to 6 MHz are displaced backward with respect to the specular beam and that the displacement is due to a backward propagating Scholte-Stoneley wave. For a pulse, it cannot be said that only a single frequency experiences the backward shift, since the identification of backward shifted frequencies is limited by the frequency resolution of the Fourier processing techniques used. In addition, any variation in the beam directivity or surface periodicity in the region of illumination could result in a small range of frequencies experiencing a backward shift.

Two final interesting observations bear addressing. First, in the classical spectrograms of Figures 4.8 and 4.9, the frequencies that correspond to the null zone at the 21° receiver position (i.e. frequencies close to 6.2 MHz) initially arrive along with all the other frequencies of the specularly reflected pulse, but they do not continue to arrive for its duration. Since the magnitude of the backward displacement is a currently unknown function of frequency, if a range of frequencies were to be shifted backwards, there is no guarantee that they would all experience a shift of the same magnitude and radiate to the receiver at the same position, so perhaps this null zone could be attributed to frequencies that shift backward but arrive at an angular position where they are more difficult to detect. However, the angular scans of the region of the backward surface wave don't support this explanation; the angular spectrogram on the right of Figure 4.7 shows a backward surface wave in a very narrow frequency range. A more likely explanation is that these frequencies experience some phase cancellation between the specular beam and the bulk propagating modes, which are not generated instantaneously.

This non-instantaneous generation of bulk propagating modes also applies to the backward propagating surface wave, and this is the second comment that should be made. From the classical spectrograms, it can be seen that the band of trailing frequencies (that were backward shifted and then re-radiated) continue to radiate into the field to the receiving transducer over time. This reveals that the backward displacement is an inherently time-dependent phenomenon.

4.2.3.2 Additional angles of incidence and associated frequencies

Results will now be presented for three additional angles of incidence, and these results are shown in Figures 4.10 through 4.15. All the angular spectrograms have been processed with identical parameters to those presented previously. The classical spectrograms have been processed with identical parameters as those used for Figure 4.9.

The results are also summarized in Table 4.1 along with the previous results concerning the frequency and angle pair studied by Breazeale and Torbett. For each angle of incidence, Table 4.1 shows

- the appropriate figure numbers,
- the angle of incidence θ_i,
- the frequency of maximum amplitude found within the bright zone in the angular spectrogram in the region of the specular beam,
- the range of frequencies found in the null zone on the same spectrogram (amplitudes < 0.1),
- the frequency of maximum amplitude in the trailing frequency band in the classical spectrogram created from a time-waveform obtained at a "bright zone" receiver position,
- the frequency of maximum amplitude of the backward propagating surface wave found in the complementary angular spectrogram of the region behind the emitting transducer, and

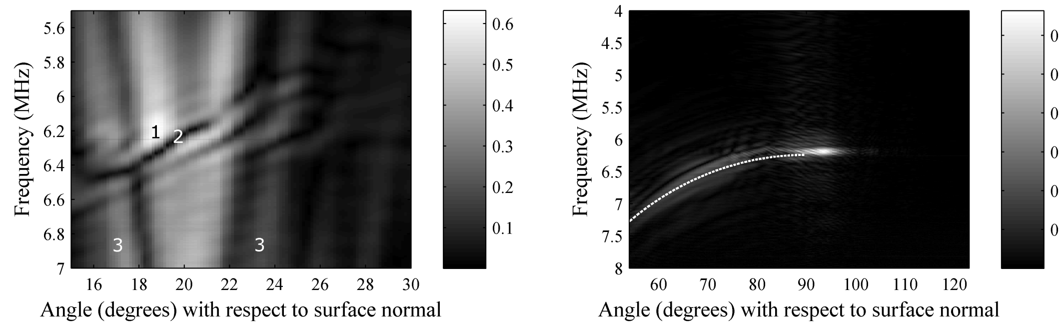

Figure 4.10: Angular spectrograms for a θ_i of 20°. (Left) Spectrogram showing backward shifted frequencies in the region of specular reflection. (Right) Complementary angular spectrogram showing the backward propagating Scholte-Stoneley wave and higher frequency propagating bulk modes (with theoretical locations plotted with the dotted line.)

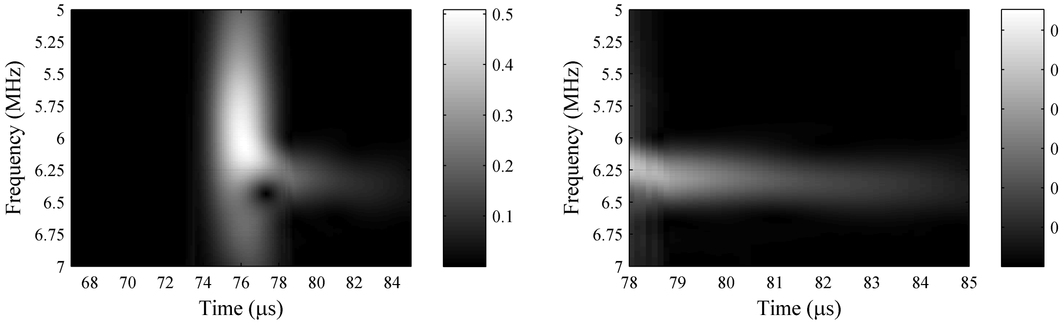

Figure 4.11: (Left) Classical spectrogram for a θ_i of 20° obtained from the time-waveform captured at a receiver angle of 18.5°.(Right) Close-up showing the trailing frequencies arriving after the initial pulse. Time windows 1024 points long.

- the theoretical Scholte-Stoneley wave frequency f_{SSt}.

Concerning the scans in the regions of specular reflection, the angular spectrograms on the left sides of Figures 4.10 and 4.12 exhibit features similar to those of Figure 4.7, and the figures have been labeled in a similar manner.

First, a bright zone of higher amplitude frequencies exists on the left side of each specular beam. The bright zone in the spectrogram on the left of Figure 4.14 does not occur to the left of the specular beam, but rather inside it. This is attributed to the fact that as the angles of incidence and specular reflection increase, the projection of a backward displacement appears closer to the center of the receiving transducer.

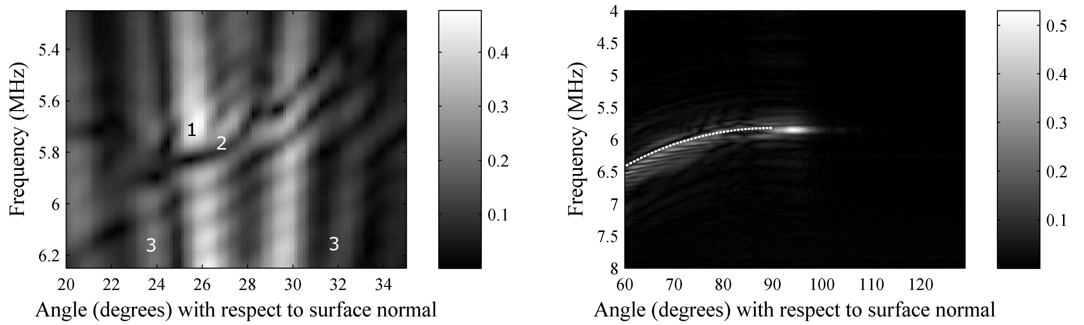

Figure 4.12: Angular spectrograms for a θ_i of 26.5°. (Left) Spectrogram showing backward shifted frequencies in the region of specular reflection. (Right) Complementary angular spectrogram showing the backward propagating Scholte-Stoneley wave and higher frequency propagating bulk modes (with theoretical locations plotted with the dotted line.)

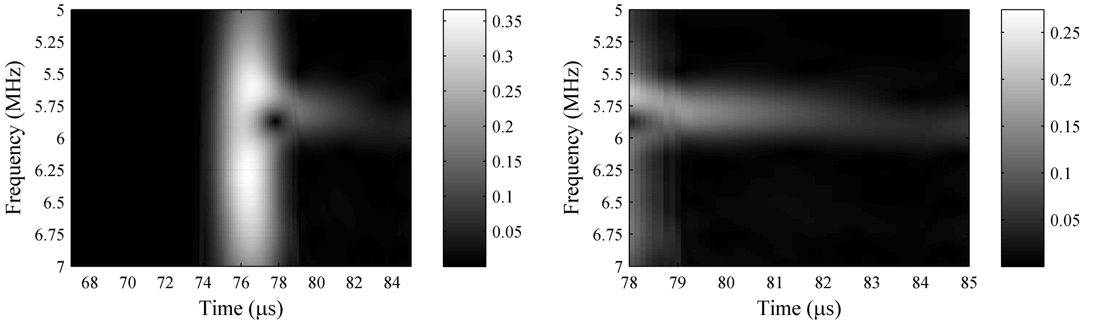

Figure 4.13: (Left) Classical spectrogram for a θ_i of 26.5° obtained from the time-waveform captured at a receiver angle of 25.75°.(Right) Close-up showing the trailing frequencies arriving after the initial pulse. Time windows 1024 points long.

The left of Figures 4.10 and 4.12 also show null zones of frequencies that can be found in the higher amplitude bright zone in the left side of the specular beam. For Figure 4.14, the null zone has a different form because higher frequencies drop off sharply in the center of the specular beam. This may be attributed to the efficiency with which higher frequency propagating modes are generated for these frequencies at this angle of incidence, as well as possible destructive interference occurring between these propagating modes and the specular beam. Therefore, the null zone for the left side of Figure 4.14 has been considered to occur where the frequencies drop off with amplitudes less than 0.1.

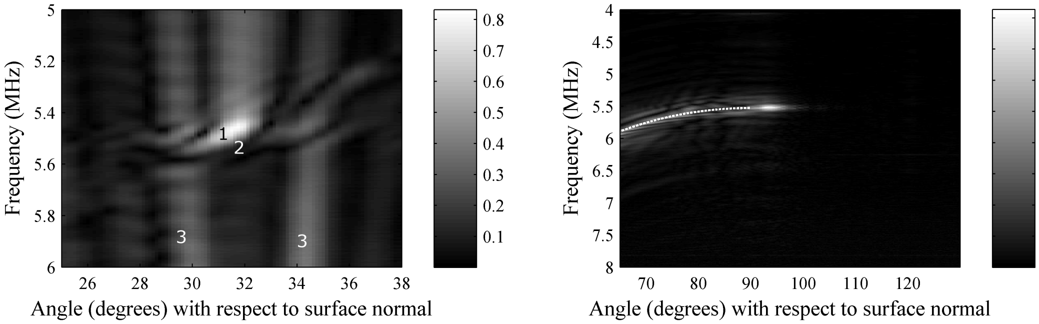

Figure 4.14: Angular spectrograms for a θ_i of 30.5°. (Left) Spectrogram showing backward shifted frequencies in the region of specular reflection. (Right) Complementary angular spectrogram showing the backward propagating Scholte-Stoneley wave and higher frequency propagating bulk modes (with theoretical locations plotted with the dotted line.)

Classical spectrograms obtained from time waveforms captured during the scans in the regions of the specular beams are shown in Figures 4.11, 4.13, and 4.15. Each spectrogram was obtained from a time waveform captured at an angular position to the left of the specular beam with the exception of Figure 4.15. In this case, it appears that the measurement of the angle of incidence was at the upper limit of its uncertainty and the classical spectrogram was obtained from a time waveform received at an angle of 31.5°. In all the classical spectrograms, the specular beam arrival is seen as a vertical band of frequencies followed by trailing frequencies that may be backward shifted frequencies since they arrive after the initial pulse. Close-ups of the spectrograms on the right side of each figure more clearly reveal the frequencies that trail the initial pulse and there is a definite trend: the trailing frequencies of maximum amplitude decrease with increasing angle of incidence, and this is consistent with the theoretical Scholte-Stoneley wave frequencies. Similar to Figure 4.9, all three of these classical spectrograms exhibit the null zone at the end of the specular beam arrival which could be due to destructive interference with the bulk propagating modes generated.

Concerning the complementary scans performed in the regions of the backward

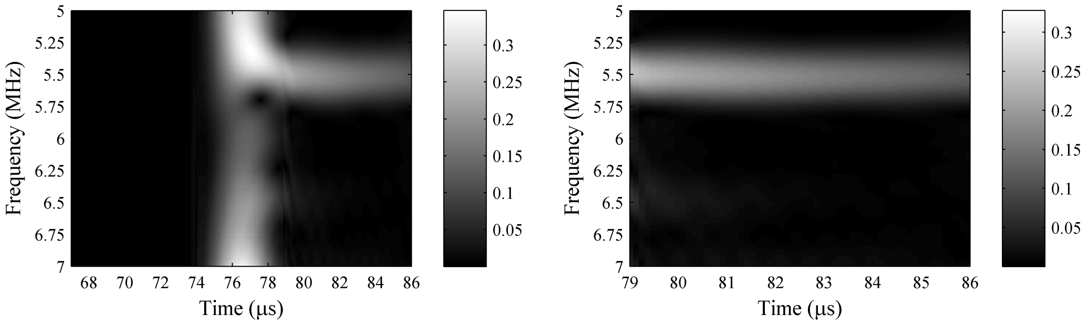

Figure 4.15: (Left) Classical spectrogram for a θ_i of 30.5° obtained from the time-waveform captured at a receiver angle of 31.5°.(Right) Close-up showing the trailing frequencies arriving after the initial pulse. Time windows 1024 points long.

propagating surface wave, shown on the right sides of Figures 4.10, 4.12, and 4.14, lateral waves are indeed observed at the surface of the sample in all cases, and the waves have propagated off the edge of the sample into the field of the receiving transducer. This evidence, along with the fact that the experimentally observed frequencies of this surface wave are consistent with the other experimental evidence of backward shifted frequencies and the theoretical Scholte-Stoneley frequencies f_{SSt} for each angle of incidence, supports the claim that a backward propagating Scholte-Stoneley wave accompanies and is responsible for backward displaced frequencies. In addition to the backward propagating Scholte-Stoneley wave, higher order propagating bulk modes are observed for each angle of incidence, and their locations are well-described by theory, as shown by each dotted line.

Table 4.1: Summary of reflection results. Comparison of experimental observations and theoretical f_{SSt}.

Figures	Angle θ_i	Frequency of max amplitude in angular spectrogram (MHz)	Frequency range of null zone in angular spectrogram (MHz)	Trailing frequency of max amplitude in classical spectrogram (MHz)	Frequency of max amplitude of backward surface wave (MHz)	Theoretical f_{SSt} (MHz)
4.7 and 4.9	22.5°	5.98	5.95–6.16	6.10	6.05	5.99
4.10 and 4.11	20.0°	6.20	6.18–6.38	6.29	6.19	6.17
4.12 and 4.13	26.5°	5.70	5.62–5.85	5.80	5.84	5.73
4.14 and 4.15	30.5°	5.46	5.46–5.55	5.51	5.52	5.49

In summary, it can be seen from the Figures 4.10 through 4.15 and from Table 4.1 that, in general, for all the angles of incidence studied here, experimental evidence has been observed that supports the existence of the backward beam displacement for multiple angles of incidence and frequencies and provides more insight as to the cause of that displacement. The frequencies of maximum amplitude found in the bright zones of the angular spectrograms, which, for three of the four angles studied, were observed to the left of the specular beam, are in reasonable agreement with the theoretically predicted backward Scholte-Stoneley frequencies, f_{SSt}. Also, the frequency ranges of all the null zones observed in the angular spectrograms contain the frequency of maximum amplitude observed in the bright zone and usually the appropriate f_{SSt} for each angle of incidence. The frequencies of maximum amplitude observed in the trailing frequencies in the classical spectrograms were well within the frequency ranges of the null zones and slightly higher than the theoretically predicted f_{SSt}. Finally, all the frequencies of maximum amplitude of the observed backward propagating surface waves were consistent with the other experimental results and were close to the theoretically predicted f_{SSt}. The agreement within the experimentally observed frequencies as well as between the experiments and the theory is more than satisfactory due to the frequency resolution of the Fourier analysis. Some improvement could be attained with additional research into the nature of the evolution of the Scholte-Stoneley wave velocity with frequency (dispersion) and the corrugation periodicity and form.

These results lead to the conclusions that the backward beam displacement can be observed for frequency components within pulsed beams, for multiple pairs of angle of incidence and frequency, and that the cause of the displacement is a backward propagating Scholte-Stoneley wave. Also, the classical grating equation is a useful tool for predicting frequency and angle pairs that would result in the backward displacement.

4.2.4 Conclusion of reflection results

This chapter section has presented new experiments concerning the ultrasonic backward beam displacement for pulsed beams in reflection. Through the use of a pulse instead of a time-harmonic beam, it has been possible to examine many frequencies at once. These experiments were conducted with two objectives: first, to quantitatively show that the backward beam displacement exists at additional frequencies and angles of incidence other than the single frequency and angle of incidence pair (6 MHz, 22.5°) studied in the past and second, to show that the backward displacement is accompanied by a backward propagating Scholte-Stoneley wave. The experimental method employed in these experiments was first used to verify the original observations of Breazeale and Torbett [60] and then experimental results were reported on additional angles of incidence where backward displaced frequencies and accompanying backward Scholte-Stoneley waves were detected. The theory of Tamir and Bertoni [107] and the ability of the classical grating equation to predict the backward beam displacement as well as the propagation directions of bulk modes at multiple frequency and angle pairs have been verified. It is possible, and highly likely, that the backward beam displacement is a continuous phenomenon that will occur for any frequency or angle of incidence on a periodically grooved solid as long as the classical grating equation applies and is satisfied.

4.3 Evidence of the ultrasonic backward beam displacement in transmission through a solid

As discussed in the introductory section to this chapter, the backward displacement of an ultrasonic beam has only ever been observed in reflection in liquid from a solid periodic surface. Since this backward displacement in reflection has been attributed to the generation of a leaky Scholte-Stoneley wave along the surface, the energy of which is mostly confined to the liquid side of the interface, the question has remained whether the backward displacement can also be observed in transmission through the solid. This chapter section presents experiments that were conducted with the aim of observing the backward displacement phenomenon in transmission.

The theoretical considerations that govern the appearance of the phenomenon are identical to those for the reflection case that were discussed in subsection 4.2.1. The relationship between the frequency f, angle of incidence θ_i, surface periodicity Λ, sound velocity in the liquid v_{liq}, and velocity of the Scholte-Stoneley wave v_{SSt}, that must be fulfilled in order for a backward beam displacement to occur is repeated here as Equation 4.3.

$$f = \frac{1}{\Lambda\left(\dfrac{\sin\theta_i}{v_{liq}} + \dfrac{1}{v_{SSt}}\right)} \tag{4.3}$$

The remainder of this chapter section is divided into three subsections. First, because the experimental setup and scanning technique differs between the reflection measurements of section 4.2 and these transmission measurements, the new experimental setup will be described. Then the experimental results will be presented, followed by conclusions.

4.3.1 Experimental setup

The same brass sample that was used by Breazeale and Torbett [60] in the original observation of the backward beam displacement and in the reflection measurements of section 4.2 has also been employed for the transmission measurements presented here. The sample characteristics are repeated here for the reader's convenience. It consists of a rectangular piece of brass (60 mm long, 25 mm wide, 12 mm high) with a section 25.4 mm long along its length that had been machined with periodic rectangular grooves having a periodicity equal to 178 µm and profile height equal to 25 µm. The polar/C-scan equipment at Georgia Tech Lorraine was employed to conduct the experiments, and the velocity of sound in the water v_{liq} was determined to be 1479.5 m/s.

A pulsed ultrasonic beam was generated by a stationary emitter, and the reflected and transmitted fields were measured and analyzed in order to observe any backward shifted frequencies present. The reflection and transmission results have been compared, and backward shifted frequencies evaluated with respect to those theoretically predicted by Equation 4.3.

The commercial ultrasonic transducers with nominal center frequencies of 5 MHz that have been employed are identical to those of section 4.2. Since transmitted results are compared with reflection results, two experimental setups were necessary. The transducers were arranged in a pitch-catch configuration, and the receiving transducer was placed in the reflected field in the first setup and in the transmitted field in the liquid on the far side of the sample in the second setup. An illustration of the two experimental setups is shown in Figure 4.16.

One angle of incidence is studied here, namely 30°, since it is beyond the longitudinal critical angle of approximately 17.8° for brass. Thus, the waves transmitted through the solid are of the shear type, and they return to longitudinal upon exiting the solid and entering the fluid. Eliminating the presence of longitudinal waves in the solid greatly improves the ability to isolate the specular beam in the reflected and transmitted fields.

The emitter was stationary and aimed at the sample surface with an angle of incidence equal to 30°. Instead of using an angular scanning technique in the manner of section 4.2, the receiver was kept at a constant angle with respect to the surface, also 30°. A scan was then performed by translating the receiver linearly along the length of the sample. This linear scanning method is in contrast with the angular method used in section 4.2. Since at the outset it was unknown whether the backward displacement would exist in transmission and be observable, it was desirable to set the receiving transducer at the angle where it would be most sensitive to the lateral displacement and then translate it linearly within the field.

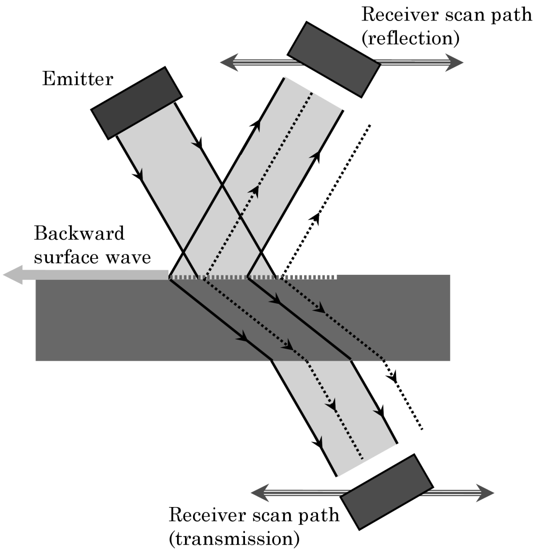

Figure 4.16: Scan paths for measurement of backward beam displacement in transmission. Specular beams shown in dotted lines and backward shifts shown in solid lines.

Waveforms were collected at 0.1 mm intervals and Fourier analysis (Fast Fourier Transform) was performed on the appropriately time-windowed waveforms. The frequencies present in the recorded waveforms have been plotted as a function of scan position in a spatial spectrogram in order to study the characteristics of the reflected and transmitted fields, including the specular beam and any backward shifted frequencies. All results have been normalized with respect to the frequency spectrum of the incident pulse (Figure 4.6).

4.3.2 Experimental results

The linear spectrogram of the reflected field obtained for the 30° angle of incidence is shown on the left side of Figure 4.17. The FFTs were performed using 8000 time waveform points zero-padded to 32000 points. A narrow range of frequencies (indicated by the circled area) is observed to have shifted backward several millimeters with respect to the specular beam which is indicated by the dotted lines. The frequency having maximum amplitude in this range is 5.51 MHz. This is observed to be in good agreement with the theoretical f_{SSt} of 5.52 MHz that can be calculated using

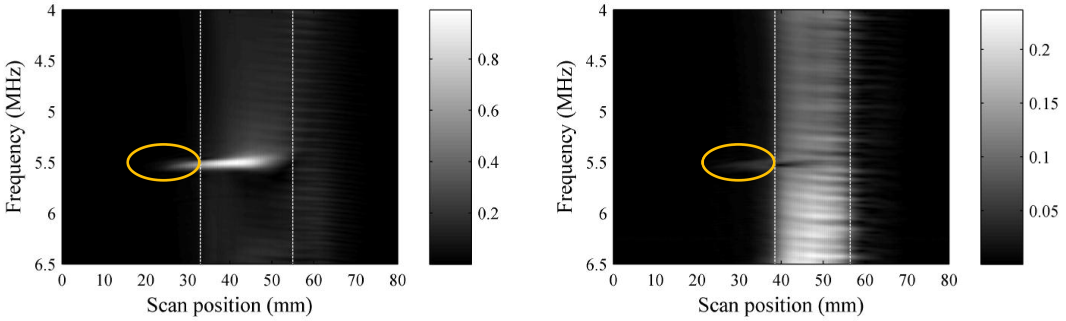

Figure 4.17: Spatial spectrograms for an angle of incidence of 30°. Backward displaced frequencies are circled and specular beams are shown with dashed lines. (Left) Reflected field. Backward frequencies at 5.51 MHz. (Right) Transmitted field. Backward frequencies at 5.52 MHz

.

Equation 4.3.

Using procedures and analysis identical to those employed for the reflected field, the spatial spectrogram showing frequencies detected as a function of position for the transmitted field is shown on the right side of Figure 4.17. The backward displaced frequencies are circled in the figure and the specular beam is contained within the dotted lines. Backward displaced frequencies are observed in the vicinity of 5.52 MHz (frequency of maximum amplitude) and this is in good agreement with the results obtained in reflection and the theoretical f_{SSt}.

Upon close inspection of both the reflection and transmission spectrograms, additional energy in the form of faint horizontal bands is seen to the right of the specular beam. This is due to the inclusion of an additional specular beam reflection from the bottom of the sample in the time windows under analysis. It is necessary to include this additional beam reflection in the time windows used to calculate the spectrograms because, as discussed in section 4.2, the backward displacement is time-dependent. A large time window is required to capture the energy associated with backward shifted frequency components since they radiate into the reflected (and transmitted) fields over time. The energy appears as horizontal bands due to some overlap with the detection of the specular beam, which is not unexpected since beam spreading has been observed to occur in Schlieren images of ultrasonic beams on periodic surfaces [74]. The effect of additional beam reflections from the bottom of the sample has been minimized through the use of an angle of incidence well beyond the critical angle for longitudinal waves in brass. This maximized the distance between any reflection and the specular beam, and the waves within the solid are only shear so the number of potential beam reflections is reduced by half.

In order to verify that the backward shift in transmission is in fact caused by the backward propagating Scholte-Stoneley wave on the upper surface of the sample, particle displacements parallel and perpendicular to the interface have been calculated for a 5.5 MHz Scholte-Stoneley wave along a water-brass interface. These are shown in Figure 4.18 where the interface is represented by a solid line with the fluid medium above (positive distance from interface) and the solid medium below (negative distance from interface). Expressions for the displacements [111] can be derived according to the methods outlined by Viktorov [22], and material parameters used in the calculation are identical to those in Ref. [43]. Since the displacement amplitudes are dependent on an arbitrary constant, they have been normalized. It can be seen, however, that the amplitude of the displacement drops off dramatically with increasing depth in the solid so that for a depth of 0.5 mm, there is virtually no energy from the wave present. Therefore, the backward propagating Scholte-Stoneley wave is confined to the upper surface of the sample.

4.3.3 Conclusion of transmission results

In summary, backward shifted frequencies that are observed in reflection from a periodically corrugated liquid-solid interface have also observed in transmission through the solid for an angle of incidence equal to 30°. These frequencies correspond very

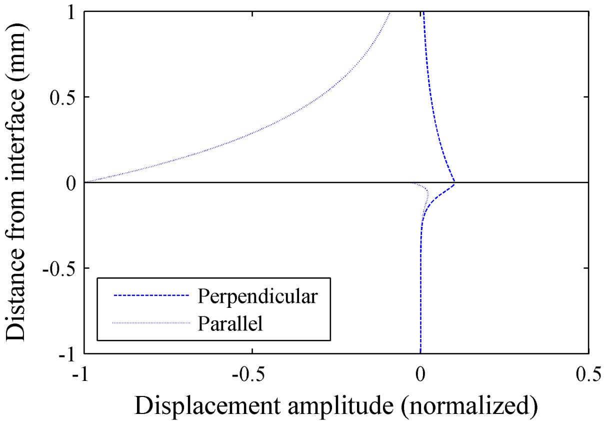

Figure 4.18: Particle displacement amplitudes calculated for a 5.5 MHz Scholte-Stoneley wave propagating on a water-brass interface. Displacement perpendicular to the interface shown with dashed lines and displacement parallel to the interface shown with dotted lines. Displacement amplitudes are observed to decrease dramatically with penetration depth in the solid (negative distance from interface).

closely to each other as well as to the theoretically predicted Scholte-Stoneley frequency for the given experimental parameters. The shift observed in transmission may also be attributed to the backward Scholte-Stoneley wave generation on the upper (periodic) surface of the sample.

The agreement between theory and experiment is despite the assumption of a constant Scholte-Stoneley wave velocity equal to that measured by Breazeale and Torbett for the case of a 6 MHz emitting transducer and a 22.5° angle of incidence [60]. This assumption is based on a non-dispersive nature of such surface waves, which may not be fully accurate and requires further study. In addition, although this study examined transmission of shear waves through the solid sample, the insight gained implies that a backward propagating Scholte-Stoneley wave generated for a certain frequency on a periodically corrugated surface may result in a backward shift for that frequency in all fields generated. Thus, ultrasonic backward beam displacements are not only a reflection phenomenon, but may also be observed in transmission.

CHAPTER V

AN EXPERIMENTAL STUDY OF DIFFRACTION OF BULK ULTRASONIC WAVES ON FINITE-SIZE PHONONIC CRYSTALS

5.1 Introduction and motivation

As mentioned in the introductory chapter of this thesis, research interest in sonic and phononic crystals [3, 112] has increased substantially within the last two decades. These artificial crystals are inhomogeneous materials that consist of periodic arrangements of inclusions embedded within a host material, and they are the acoustical analogs of photonic crystals in optics [113].

The interest in phononic crystals is mainly due to unique properties that stem from their periodicity, including the existence of bands of frequencies that are unable to propagate through the structure, usually referred to as band-gaps [114, 115]. This phenomenon is caused by the destructive interference of waves that occurs when they are multiply scattered from the periodic inclusions of the crystal [116]. Band-gaps may occur only for certain propagation directions through the crystal or they can be directionally independent. If the latter is true for a certain band-gap, it may be referred to as a *complete* or *absolute* band-gap [117]. The term *absolute* has also been used to refer to a band-gap that occurs for both longitudinal and shear wave polarizations, especially for crystals that consist of solid inclusions within a solid matrix [118, 119].

Several factors influence the presentation of band-gap phenomena. In general, it is necessary that the wavelength of the incident sound be on the order of the crystal periodicity or lattice constant [120]. Another influence is the filling fraction [121], or the relative size of the inclusions with respect to the lattice constant. Perhaps the most important factor, however, is the impedance mismatch between the constituent materials of the crystal. Many studies have already been performed in order to determine the width and location of band-gaps in various types of phononic crystals, and the results have revealed that the contrasts in the acoustic velocities (elastic constants) and mass densities of the crystal materials are of critical importance [117, 122].

Phononic crystals that consist of cylindrical inclusions in a host material like the crystal that will be examined in this chapter are considered two-dimensional (2D) since their periodicity exists in two directions. One-dimensional (1D) crystals can also exist as a series of material layers (superlattices) [123, 124], and three-dimensional (3D) crystals can exist as an array of spherical scatterers within a host medium [3]. For the 2D and 3D crystals, it is not required that the scatterers consist of cylinders or spheres, but these geometries are beneficial since they result in more isotropic scattering within the crystal than other geometries. Phononic crystals can be classified not only according to the number of dimensions in which they are periodic, but also according to the materials used in their construction. The crystal that will be examined in this chapter consists of solid cylinders in a fluid, but other possibilities include fluid-filled holes within a solid [125, 126], solid inclusions within another solid [127, 128, 129], etc. Since the geometry of phononic crystals can be scaled up or down (with a resulting change in the applicable frequency regime), physical concepts can be demonstrated with structures that exist on a relatively large scale, and then much smaller phononic crystals can be obtained through microfabrication techniques.

Potential applications for phononic crystals can be found in acoustic filtering and novel transducer designs [130, 131] as well as in the creation of vibrationless environments [132]. The introduction of line defects in phononic crystals can result in bent waveguides for frequencies within a complete band-gap [130]. For very high frequencies, goals include the development of devices that incorporate microelectronics and phononic crystals as well as structures that exhibit simultaneous phononic and photonic band gaps [133].

However, in order to bridge the gap between fundamental research of phononic crystals and the actual design of devices that may contain such crystals, a thorough understanding of effects that occur due to the crystal's finite size is required. It is with this aim that this chapter will present an experimental study of the diffraction that occurs on the surfaces of a 2D phononic crystal consisting of a triangular lattice arrangement of steel cylinders in water.

Prior studies have observed diffraction of surface acoustic waves (SAW) on finite-size phononic crystals [134] using heterodyne laser interferometry. Since this diffraction of incident *surface* waves has been observed, it is expected that diffraction will also be observed for *bulk* acoustic waves and that the surface of the crystal may behave as a diffraction grating for the bulk waves. Diffraction due to Bragg scattering from the cylinders should be expected, in both the incident half-space (reflected waves) and the exit half-space (transmitted waves). However, in the band-gap frequency ranges, transmitted waves are effectively suppressed and therefore enhanced diffraction efficiency for reflected waves in these frequency ranges might be observable.

The aim of the experiments that will be presented in this chapter is to quantitatively measure the diffraction of bulk ultrasonic waves that occurs in reflection from the surfaces of a 2D phononic crystal consisting of steel cylinders in water. The crystal itself was fabricated in V. Laude's laboratory at FEMTO-ST in Besançon, France, which is an associate member of the GT-CNRS UMI 2958. Through-transmission and diffraction measurements were then carried out using the polar/C-scan equipment (that was also used for the experiments in Chapters 3 and 4 in this thesis) at GT-Lorraine in Metz, France.

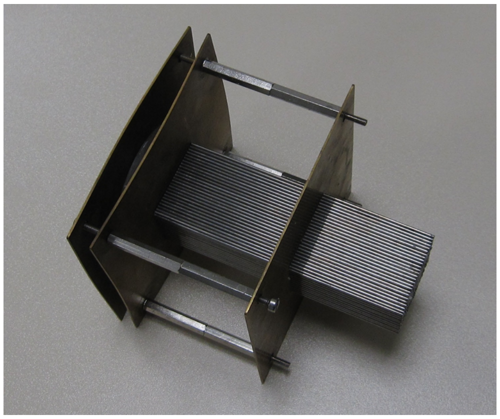

Figure 5.1: Photograph of the 2D phononic crystal.

This chapter is organized into the following sections. First, a description of the phononic crystal will be presented and then the experiments that were conducted will be explained. The experimental results will then be discussed, and the final section will contain conclusions and recommendations for future experiments.

5.2 Description of the phononic crystal

The phononic crystal under study consists of a triangular lattice arrangement of 575 steel cylinders, each having a diameter of 1.2 mm and a length of 150 mm. A photo of the crystal is shown in Figure 5.1, and additional studies on this crystal can be found in Ref. [135].

The cylinders were aligned using two supporting plates that had been machined to have periodic arrays of holes and Figure 5.2 shows the triangular lattice pattern of the cylinders as well as the directions of highest symmetry, which will be referred to in later sections as ΓM and ΓK. The lattice constant, which for this lattice arrangement is the distance between the centers of any two adjacent cylinders, was measured to be 1.4 mm. The matrix of the crystal is the water that surrounds the cylinders when the crystal is submerged in water.

Assuming a sound speed in water of 1500 m/s (the exact speed measured will

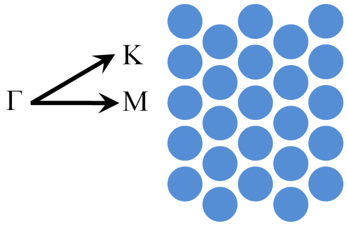

Figure 5.2: Diagram of the triangular lattice pattern of the crystal along with directions of highest symmetry.

be presented in the following section), incident ultrasound with a wavelength corresponding to the lattice constant would have a frequency on the order of 1 MHz. Some researchers may prefer to use the term *sonic crystal* or the general term *acoustic band-gap material* rather than *phononic crystal* when the lattice constant is on the order of the wavelengths of audible or ultrasonic frequencies, or when the host medium for the scatterers is a fluid. However, since the term *phononic crystal* finds widespread general use in the literature even for larger-scale crystals, this naming convention will be maintained in this chapter.

Steel and water were chosen as the constituent materials of the crystal due to the large contrast in their densities and elastic constants, as this has been shown to be an effective approach for the formation of band-gaps in other studies on phononic crystals [130, 136]. In order to determine whether enhanced diffraction can be observed for frequencies that lie within a band-gap, it was first necessary to determine the band-gap frequency ranges using through-transmission experiments.

5.3 Description of experiments

Two types of experiments have been performed on the crystal: through-transmission measurements and then diffraction measurements. Both types of experiments required a pair of transducers: one transducer to function as the emitter and the other as the receiver. The transducers employed were commercially available ultrasonic immersion transducers. In order to increase the frequency range under study, two pairs were used.

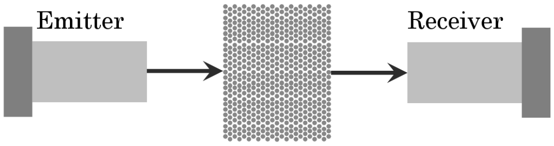

Figure 5.3: Schematic for through-transmission experiments.

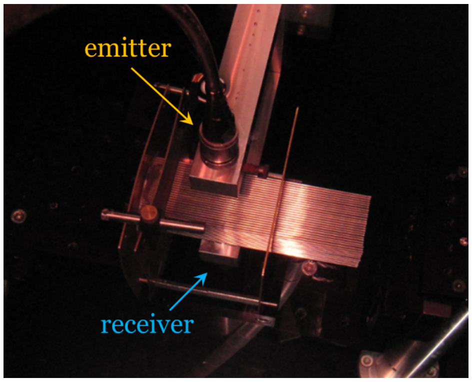

Figure 5.4: Photo of through-transmission experimental setup underwater.

The first pair had a nominal center frequency of 1 MHz (Valpey-Fisher IS0104GP), and the second had a nominal center frequency of 2.25 MHz (Technisonics ISL-0203-SP). The beam width of all the transducers was approximately 10 mm.

5.3.1 Through-transmission

For the through-transmission measurements, the transducers were mounted at normal incidence on opposite sides of the crystal in the manner shown in Figure 5.3. (In Figure 5.3, the transducers are shown to be aligned with the ΓM direction of the crystal, but the transducers were also directed along the ΓK direction by rotating the crystal 90°.) The transducers were fixed normal to the crystal surfaces with the aid of the transducer mounting fork that was part of the polar/C-scan equipment. A photo of the experimental setup underwater that shows the crystal along with the transducers in the fork is shown in Figure 5.4.

The distances between each transducer face and the crystal surfaces (rounded to

Table 5.1: Distances between transducers and crystal surfaces.

	1 MHz pair	2.25 MHz pair
ΓM direction	30 mm	26 mm
ΓK direction	28 mm	23 mm

the nearest millimeter) are shown in Table 5.1 for both transducer pairs and both crystal orientation directions. The distances are not identical due to different transducer case geometry for each pair and due to the fact that the crystal was not perfectly square. The through-transmission measurements were taken for the region of the crystal between the two support plates, in order to better guarantee the periodicity of the cylinders of the crystal.

Multiple examples of this type of through-transmission measurement have been reported in the phononic crystal literature, and most of these have been performed using pulsed ultrasound [126, 136, 137, 138]. In order to determine attenuation (or transmission) as a function of frequency, and thus the location and size of band-gaps, the general procedure is to perform Fourier analysis on the pulses that are received after they have propagated through the crystal. Most of the examples of through-transmission experiments found in the literature employ the Fast Fourier Transform (FFT) for this analysis. However, the use of the Short Time Fourier Transform (STFT), which presents the received signal in the form of a spectrogram, can reveal information on group velocity irregularities as a function of frequency in a straightforward manner.

Because the behavior of phononic crystals is inherently frequency-dependent, it is desirable to have transducers with as wide a bandwidth as possible. Therefore, the through-transmission measurements presented here have been performed not only with pulses (sent from the pulser-receiver that was integrated with the polar/C-scan equipment) but also with a swept frequency technique where a “long” signal consisting of a linear sweep in frequency over time was sent to the emitting transducer from a function generator. Results from the through-transmission of both the pulsed and swept ultrasound will be presented in the following section.

5.3.2 Diffraction

For the diffraction experiments, the emitting transducer was mounted so that it was stationary and normally incident on the crystal surface. The distance between the emitter and the crystal surface was approximately 74 mm but varied by a few millimeters depending on the transducer pair and the crystal orientation. The receiving transducer was then mounted in upper portion of the rotating fork of the polar/C-scan robot (the bottom section of the fork was removed) so that the diffracted field could be scanned as shown in Figure 5.5. The distances between the receiving transducer and the crystal surface were 45 mm and 40.6 mm for the 1 MHz and 2.25 MHz transducer pairs, respectively. The receiver was aimed at the point on the crystal surface where the emitter was incident, and the center of rotation of the receiver was always set to be even with the crystal surface.

In Figure 5.5, the emitting transducer is shown directed along the ΓM direction of the crystal but in a manner identical to that of the through-transmission measurements, the crystal could be rotated 90° so that the emitter would be directed along the ΓK direction. Figure 5.6 shows the setup for the diffraction measurements along with the emitter before it was placed underwater.

Experiments such as these to measure the diffracted fields generated external to the surfaces of phononic crystals are unique in the phononic crystal literature due to the special type of scanning robot that is required. Angular scans were performed so that waveforms could be captured at many positions within the diffracted field. Frequency analysis was then performed in order to determine the frequencies present in the field as a function of angle. The angular range for all the scans was 40°, from

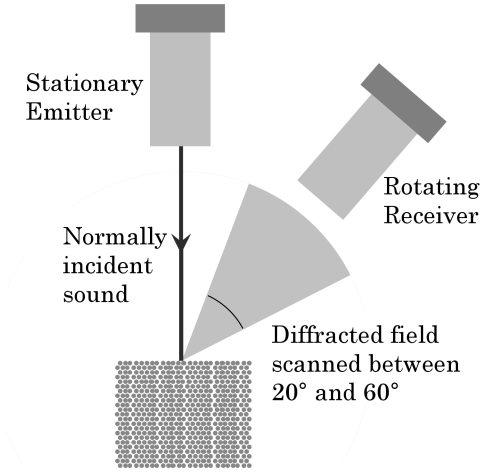

Figure 5.5: Schematic for diffraction measurements.

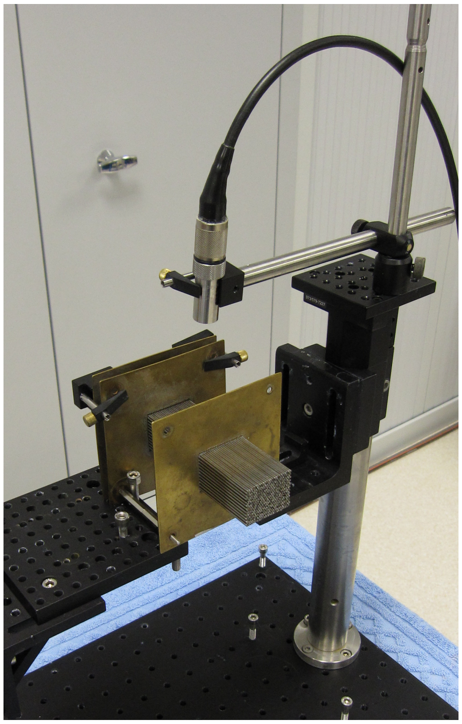

Figure 5.6: Photo of the setup for the diffraction measurements (including emitter) before being placed underwater.

20° to 60° with respect to the normal to the crystal surface. The angular resolution for the waveform acquisition was 0.1°.

The Fourier analysis required to analyze these diffraction measurements was similar in nature to that necessary to interpret the through-transmission experimental results. The only difference was that the analysis had to be performed on all the waveforms captured, and the resulting frequencies were then plotted as a function of angle in the form of angular spectrograms.

A large quantity of data must be acquired in order to capture a diffracted ultrasonic field. Since the use of swept ultrasound was prohibitively costly in terms of computer memory, pulsed ultrasound was deemed much more practical for these diffraction measurements. Therefore, the results in the following section will consist of those generated by pulsed ultrasound only.

5.4 Experimental results

Before conducting the through-transmission and diffraction measurements, it was necessary to characterize the spectra of the transducer pairs using both pulsed and swept ultrasound.

5.4.1 Transducer characterization

5.4.1.1 Characterization using pulsed ultrasound

To generate the pulsed ultrasound, the transducers were connected to the polar/C-scan equipment with the integrated JSR pulser/receiver. The pulser/receiver was triggered by the Winspect software that was installed on the PC that was also integrated with the system. This configuration of the polar/C-scan equipment has been employed in the work of Chapters 3 and 4 but a diagram is also included here in Figure 5.7 in order to provide a contrast with the configuration for swept ultrasound that is shown in Figure 5.9.

The frequency spectra obtained from pulsed transmission between the transducer

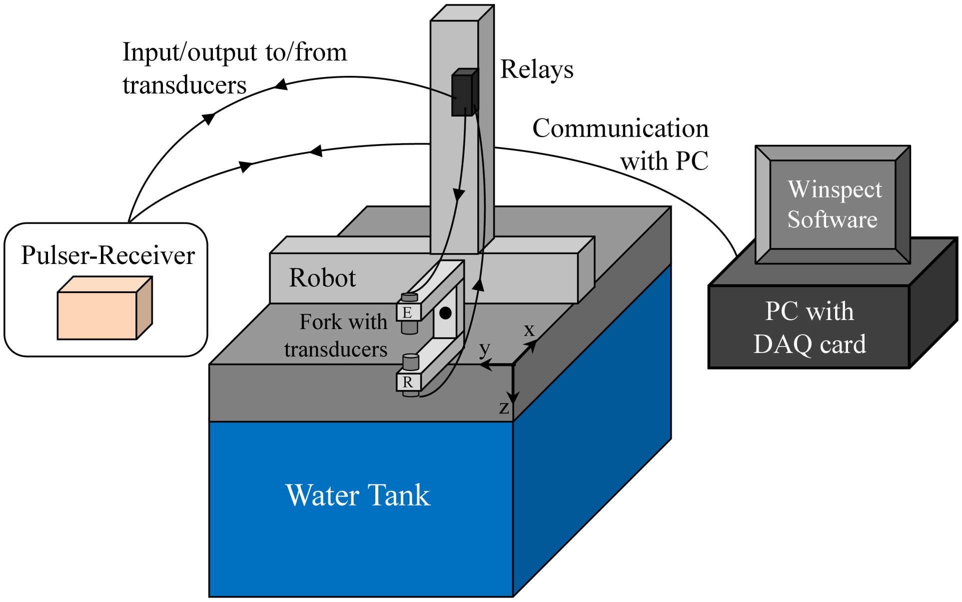

Figure 5.7: Polar/C-scan equipment configured for pulsed ultrasound. The letters E and R denote the emitter and receiver, respectively.

pairs are shown in Figure 5.8. These spectra were obtained from time-waveforms that were averaged over 16 received waveforms, and for each transducer pair, 20000 points were used in an FFT that was zero-padded to 32000 points. These time-windows, along with the sampling frequency of 200 MHz resulted in a frequency-distinguishing resolution of 0.01 MHz (equal to the sampling frequency divided by the number of samples) and an FFT bin resolution of 0.006 25 MHz.

Since the through-transmission measurements were to be performed with both transducers mounted in the fork that was part of the polar/C-scan equipment, the transducer characterization was performed with the transducers in the same positions, only without the presence of the crystal. The transducers had slightly different lengths, so when they were placed in the fork, the distance between the two was 90.2 mm for the 1 MHz transducer pair and 81 mm for the 2.25 MHz transducer pair. Based on this geometry, the time-of-flight between the transducers resulted in a calculated sound velocity in water, v_{liq}, of 1456.0 m/s based on the measurement from the 1 MHz transducer pair and 1459.5 m/s from the 2.25 MHz transducer pair.The

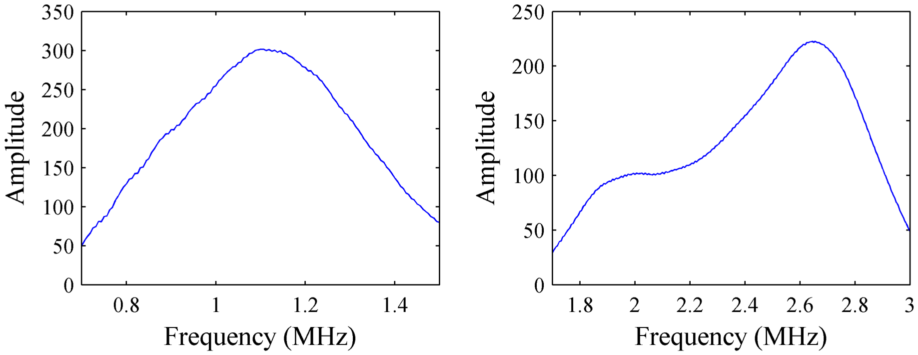

Figure 5.8: Frequency spectra of pulsed transmission between tranducer pairs. (Left) 1 MHz transducers. (Right) 2.25 MHz transducers.

difference between the two measurements can easily be attributed to uncertainties in the measurements of the transducer distances and times-of-flight, or possibly temperature fluctuations in the water tank between measurements. Due to the different characteristics of the transducer pairs, it was necessary to acquire the time-waveform for the 1 MHz transducer pair with 20 dB gain and the 2.25 MHz transducer pair with 0 dB gain.

5.4.1.2 Characterization using swept ultrasound

Using a function generator (Stanford Research Systems 30 MHz Synthesized Function Generator DS345), linear frequency sweeps were sent directly to the emitting transducers. The receiving transducers were still connected to the JSR pulser/receiver through the relays, and the trigger for the sweep was sent to the function generator from the Acquisition Logic (AL) data acquisition (DAQ) card from the Winspect software. This configuration of the polar/C-scan equipment is shown in Figure 5.9.

The sweeps were programmed so that they would begin upon the trigger sent through the AL card from the Winspect software, and when the sweep was completed the output from the function generator was programmed to return to the start frequency. The sweep performed for the 1 MHz transducers ranged from 0.5 MHz to 1.7 MHz with a sweep rate of 1 ms. For the 2.25 MHz transducers, the sweep was

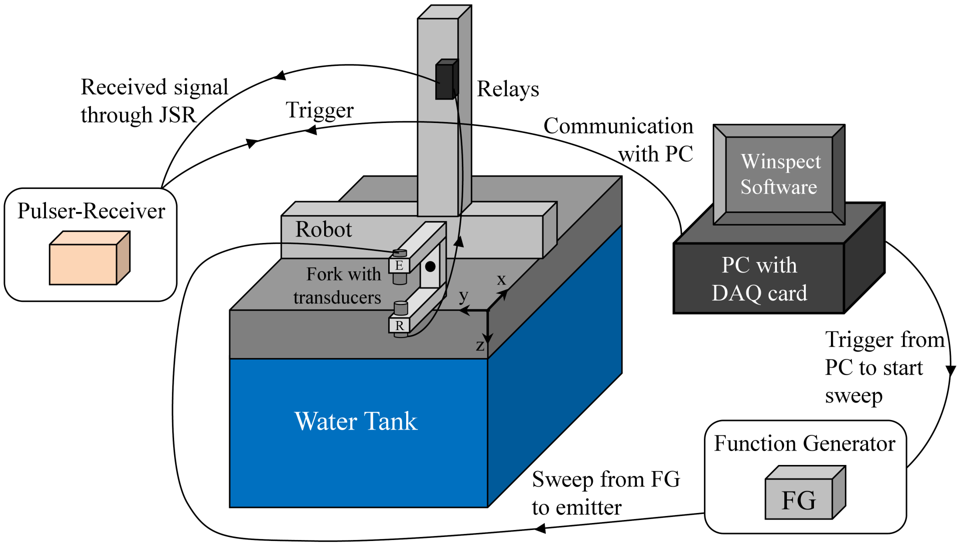

Figure 5.9: Polar/C-scan equipment configured for swept ultrasound. The letters *E* and *R* denote the emitter and receiver, respectively.

performed between 1.4 MHz and 4.0 MHz, also with a sweep rate of 1 kHz. The start and stop frequencies for the sweeping technique were set beyond the range of frequencies detected in the pulsed transmission spectra in an effort to increase the range of transducer response. The sweep rate is the reciprocal of the sweep duration, so the duration was equal to 1 ms. This was the fastest sweep possible with the function generator, and it was advantageous to use a fast sweep in order to reduce the number of reflections that would occur between the transducers during the sweep as well as to reduce the amount of data to be acquired. Some reflections could not be avoided and they can be seen as faint lines parallel to the sweep spectra, only shifted in time.

At the sampling rate used throughout the experimental work in this thesis (200 MHz), a 1 ms sweep results in the acquisition of 200000 data points. Therefore, given the limits of the PC RAM, the DAQ card, and the Winspect software, no averaging of the swept waveforms was possible. Figure 5.10 shows the classical spectrograms obtained using Short-Time Fourier Transforms (STFT) for the frequency sweeps between the 1 MHz and 2.25 MHz transducer pairs. Just as in the case of pulsed ultrasound, the signal from the 1 MHz signal was obtained with 20 dB gain and 0 dB gain from the

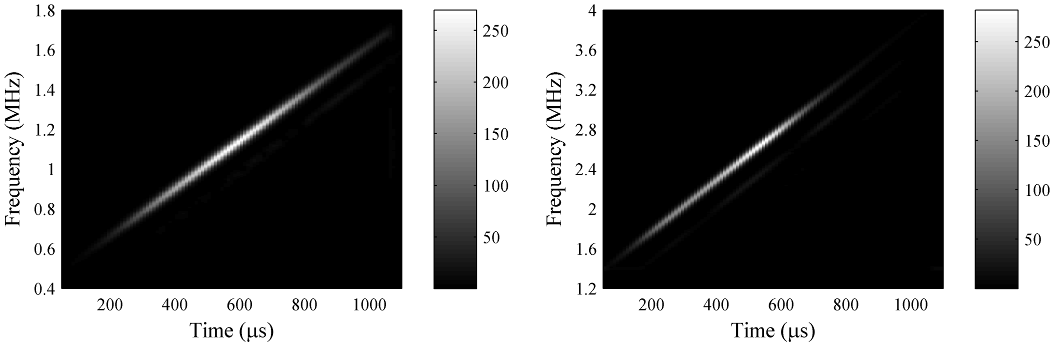

Figure 5.10: Spectrograms (STFT) of swept ultrasound between tranducer pairs. (Left) 1 MHz transducers. (Right) 2.25 MHz transducers.

2.25 MHz transducer pair. The STFTs were performed with Hamming windows consisting of 10000 points (resulting in a frequency-distinguishing resolution of 0.02 MHz) with overlaps of 8000 points. Each time-window was zero-padded to 32000 points so the FFT bin resolution for each time-window was 0.006 25 MHz. Unfortunately, inherent to the STFT is a trade-off between time resolution and frequency-distinguishing resolution, and the STFT parameters were chosen with consideration of this trade-off. In Figure 5.10 it can be seen that the swept frequency technique slightly increased the ranges of the transducers' responses, but not to a significant degree. Although there was no apparent advantage to using the swept ultrasound technique at the conclusion of the transducer characterization, a distinct advantage became apparent when was it was used to measure the transmission through the crystal.

5.4.2 Through-transmission results

First, through-transmission measurements were taken using pulsed ultrasound. All spectra have been normalized with respect to the spectra obtained in the absence of the crystal (that were shown in Figure 5.8).

Figure 5.11 shows the spectra and spectrograms that were obtained from pulsed ultrasound in through-transmission in the ΓM direction. The signals from both transducer pairs were obtained using 40 dB gain and 16 time-waveform averages. The spectra on the left of the figure were obtained using an FFT with 27700 points (for a frequency-distinguishing resolution equal to 0.007 MHz). The spectrograms on the right of the figure were obtained with a STFT having time-windows of 4000 point length (for a frequency-distinguishing resolution equal to 0.05 MHz) with an overlap of 3600 points to obtain better time resolution. Each FFT that was performed, including those performed for each time-window in the STFT, were zero-padded to 32000 points for a bin resolution equal to 0.006 25 MHz.

Good agreement exists between the FFT and STFT results, which is as expected since they come from the same time-waveform data. A lack of transmission can be observed between 0.9 MHz and 1.1 MHz as well as above 1.4 MHz. Drops in transmission also occur for frequencies between 1.8 MHz and 2.0 MHz and for those just above 2.2 MHz. These ranges of reduced transmission are all defined by dotted lines and shaded regions in Figure 5.11.

The through-transmission experiments in the ΓM direction were then repeated with the swept ultrasound technique, and the resulting spectrograms are shown in Figure 5.12. The signals from both the transducer pairs were obtained with 40 dB gain, and the STFT was performed with Hamming windows of 10000 points (for a frequency-distinguishing resolution of 0.02 MHz) that were zero-padded to 32000 points. For the 1 MHz frequency range, the results are in good agreement with the pulsed measurement: a drop in transmission is seen between 0.9 MHz and 1.1 MHz as well as above 1.4 MHz. Some agreement is also seen with the pulsed measurement for the 2.25 MHz transducer results: there is a drop in transmission for frequencies between 1.8 MHz and 2.0 MHz and another drop beginning around 2.2 MHz. However, frequencies in the vicinity of 2.6 MHz to 2.8 MHz, which do *not* arrive in the pulsed measurement are in fact observed with the use of swept ultrasound. These frequencies, however, experience a delay in their arrival time, and this is indicated by the horizontal shift from the line of the frequency sweep. The time delay that can be measured from

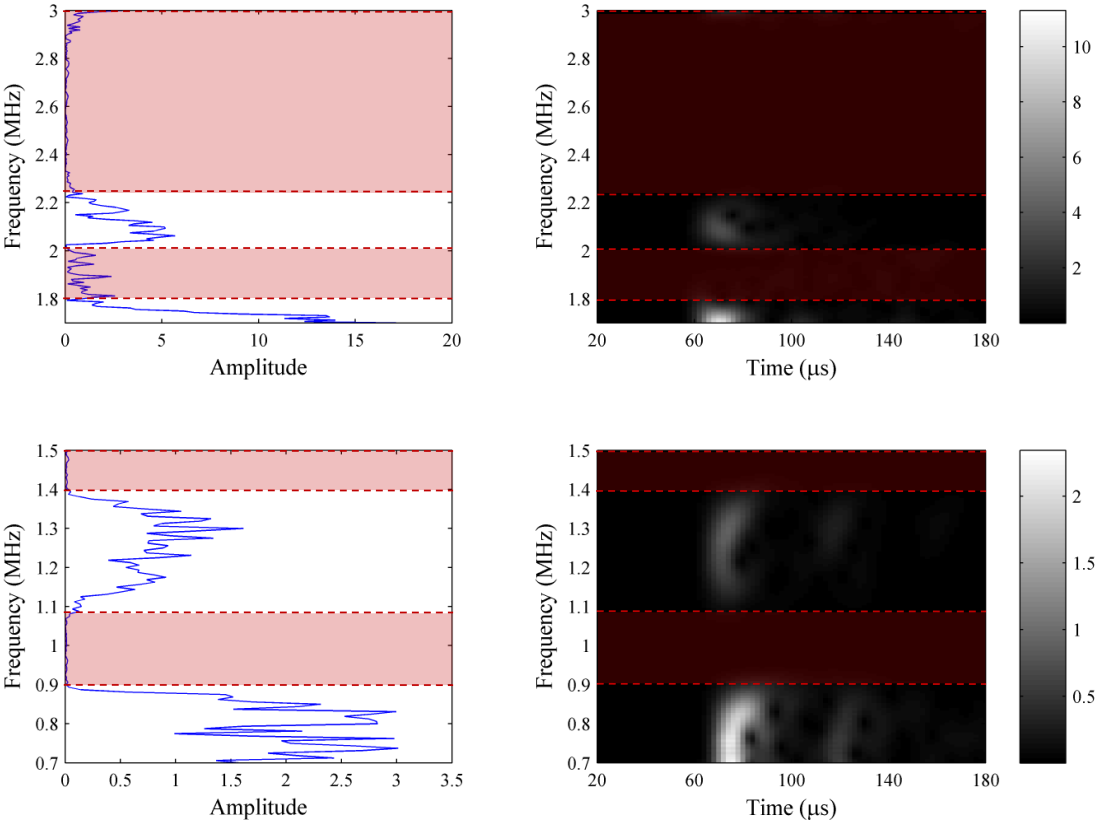

Figure 5.11: Through-transmission results from pulsed ultrasound in the ΓM direction. (Left) Spectra obtained using the FFT. (Right) Spectrograms obtained using the STFT.

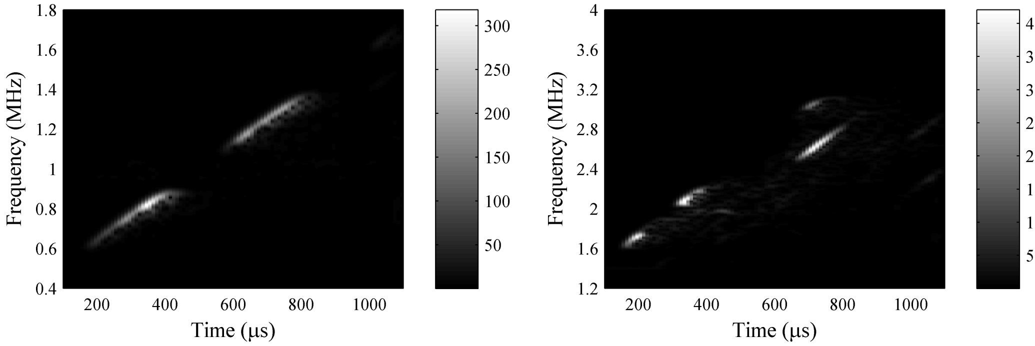

Figure 5.12: Through-transmission results from swept ultrasound in the ΓM direction. (Left) 1 MHz range. (Right) 2.25 MHz range.

the figure is approximately 170 μs.

The discrepancies between the pulsed and swept results can be seen more clearly in Figure 5.13 where the pulsed results are plotted on the left side of the figure, and the swept results (with frequency axes matching those of the pulsed ultrasound) are plotted on the right side. The frequencies that appear in the 2.25 MHz swept results that do not appear in the pulsed results are circled in the figure. Because only 200 μs of data was collected with the pulsed ultrasound, it was not possible to detect these late arriving frequencies.

Based on the observation of the late arriving frequencies in the swept results, a longer time window for the pulsed 2.25 MHz transducer pair was then used to measure the through-transmission (again with 40 dB gain and averaged over 16 time-waveforms). *If only a pulsed technique had been used, the deduction might have been made that these frequencies are within a band-gap.* The resulting spectrogram is shown in Figure 5.14. On the left of the figure is the STFT that has not been normalized, and on the right is the same spectrogram but normalized with respect to the pulsed signal between the transducers without the crystal present. The frequencies that were detected with the swept ultrasound can in fact be detected with the pulse but only if the time-window of data acquisition is long enough. The time-window used to acquire the data for Figure 5.14 was 500 μs long in contrast with the 200 μs

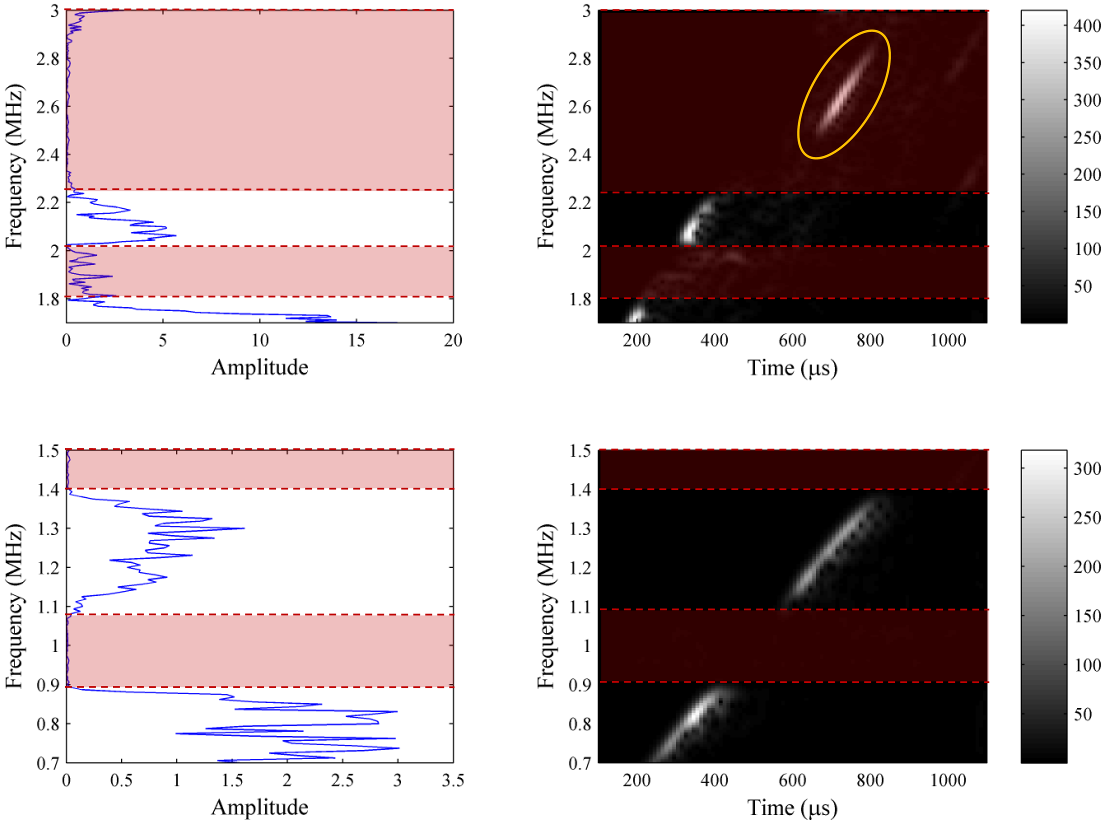

Figure 5.13: Comparison of pulsed and swept through-transmission results in the ΓM direction. (Left) Spectra obtained from FFT on pulsed ultrasound. (Right) Spectra obtained from STFT on swept ultrasound.

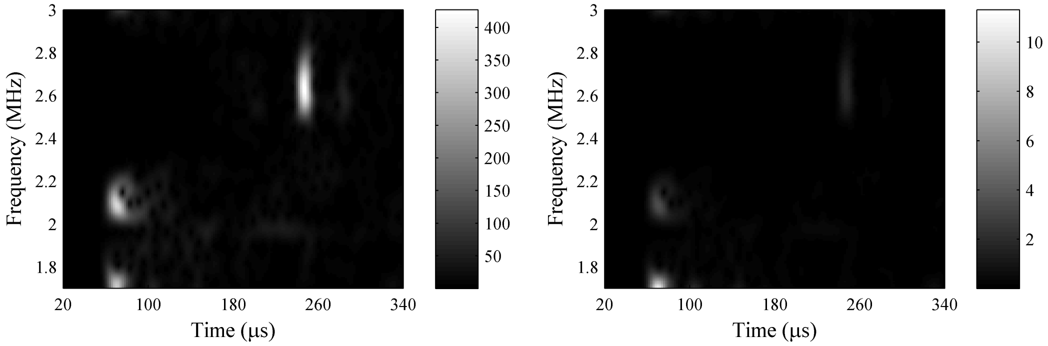

Figure 5.14: Extended spectrogram from 2.25 MHz pulsed ultrasound in through-transmission in the ΓM direction. (Left) As measured. (Right) Normalized with respect to spectrum without crystal present.

used in the earlier measurements. The time-delay that can be measured off of these spectrograms is approximately 180 μs which is in good agreement with the delay of 170 μs that was observed in the swept ultrasound results. It should be noted that there is an uncertainty associated with these measurements of the time-delays taken from spectrograms due to the time-resolutions of the STFTs (which must be reduced in order to increase the frequency resolution). For the swept ultrasound, the time-resolution of the spectrogram in Figure 5.12 was 10 μs whereas it was 2 μs for the spectrogram of the extended pulse through-transmission measurement shown in Figure 5.14.

After the through-transmission measurements were performed using both pulsed and swept ultrasound for the ΓM direction, the crystal was rotated and identical measurements were performed in the ΓK direction of the crystal. Figure 5.15 shows the FFT and STFT results from pulsed ultrasound in the ΓK direction. Band-gaps are observed for frequencies below 1.1 MHz, between 1.3 MHz and 1.4 MHz, between 1.8 MHz and 2.0 MHz, and above 2.4 MHz. The band-gap between 1.3 MHz and 1.4 MHz is not easily visible on the STFT results, but this is most likely due to the very low amplitude of the waveform that successfully propagated through the crystal. All signals were averaged over 16 received time-waveforms, and the 1 MHz results

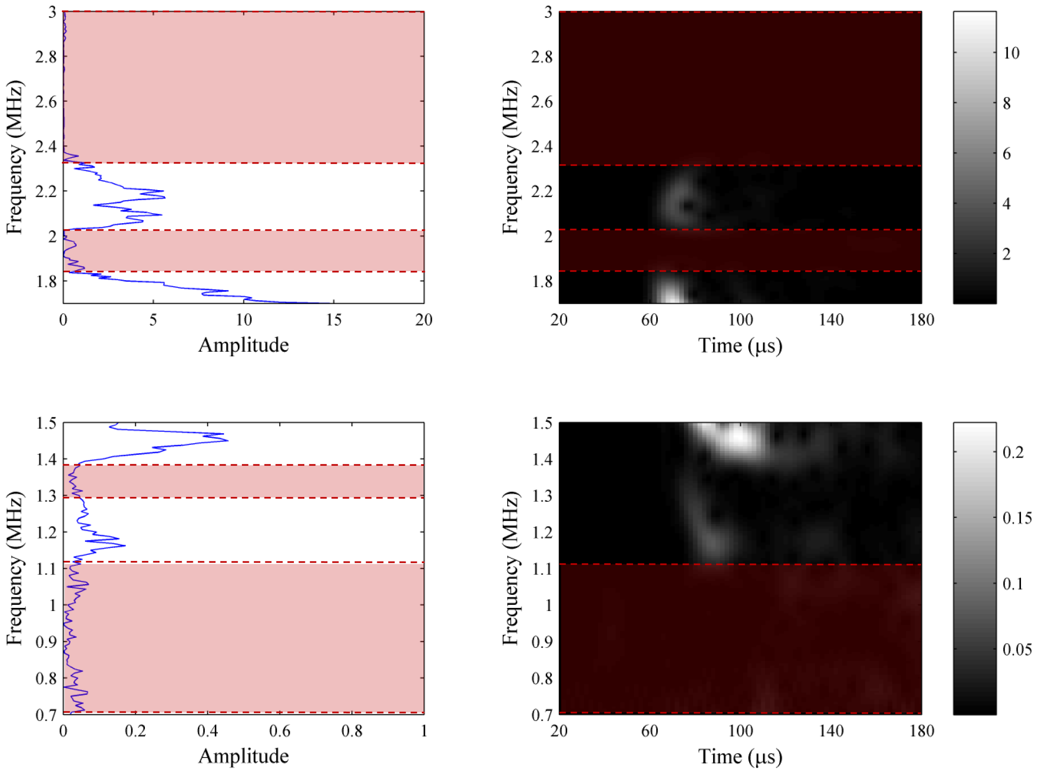

Figure 5.15: Through-transmission results from pulsed ultrasound in the ΓK direction. (Left) Spectra obtained using the FFT. (Right) Spectrograms obtained using the STFT.

were obtained using 40 dB gain and the 2.25 MHz were obtained using 26 dB gain. All time-window lengths for the FFT and STFT were identical to those for the ΓM direction. The through-transmission measurements for the ΓK direction were then performed using swept ultrasound, and the results, which are consistent with the pulsed results in Figure 5.15 are shown in Figure 5.16. Both signals were obtained with 40 dB gain as in the ΓM swept case and all the same parameters were used for the STFTs.

There are no time-delays observed in the spectrograms of Figure 5.16 that would indicate the presence of late arriving frequencies that could be missed by only acquiring 200 µs of pulsed-transmission data. The spectrogram of an additional measurement of the 2.25 MHz through-transmission over a longer time duration revealed no additional frequency arrivals, in contrast with the case of the ΓM direction.

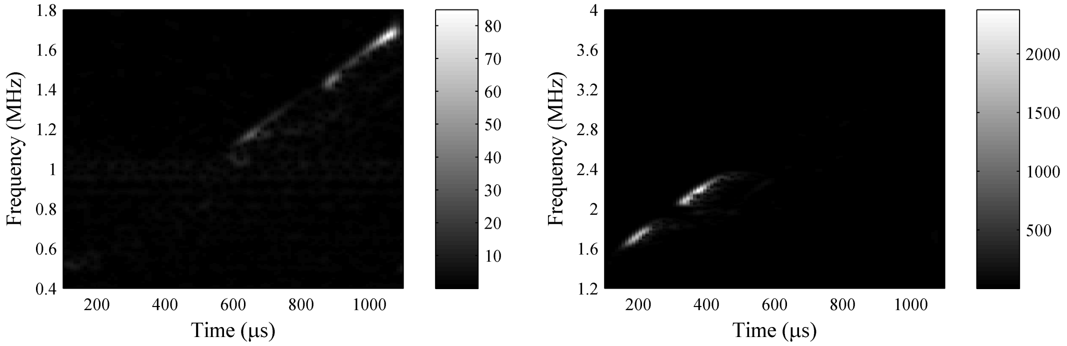

Figure 5.16: Through-transmission results from swept ultrasound in the ΓK direction. (Left) 1 MHz range. (Right) 2.25 MHz range.

In summary, the through-transmission measurements (both pulsed and swept) showed several band-gap regions in the frequency ranges under study. In addition, the swept ultrasound technique was shown to reveal a band of frequencies that would have been assumed to be in a band-gap if only a pulsed technique had been used. In fact, the swept ultrasound technique can reveal bands of frequencies that may have slow group velocity, and this should be investigated in the future with theoretical techniques as well.

After the through-transmission measurements were completed, the measurements of the diffracted fields generated in reflection from the crystal surfaces were conducted.

5.4.3 Diffraction results

The results obtained from the angular scans of the diffracted fields will now be presented. After the through-transmission experiments were performed, the lower portion of the fork on the polar/C-scan equipment was removed and the upper transducer was connected to the input of the transducer relays (that connect to the pulser/receiver) so that it could function as the receiver. The emitting transducer that was mounted stationary to the crystal was connected to the output of the transducer relays so it would receive the outward traveling pulse from the pulser/receiver.

Because the aligning plates of the crystal were large relative to the size of the rotating fork, it was necessary to take the diffraction measurements for a portion of the crystal that was not between the two plates. Although this allowed the measurement of a larger angular range than otherwise would have been possible, the ideal region of the crystal in which to take measurements is between the two alignment plates.

All results presented here were obtained with pulsed ultrasound (averaged over 16 time-waveforms) and have been normalized with respect to the pulsed transmission spectra obtained from the transducer pairs without the presence of the crystal. The 1 MHz and 2.25 MHz signals were obtained with 10 dB gain and 26 dB gain, respectively. All the FFTs performed used at least 20000 points for a frequency-distinguishing resolution of 0.01 MHz. Figure 5.18 shows the angular spectrograms (frequency detected as a function of angle within the field) created from the scans of the diffracted fields for incidence in both the ΓM and ΓK directions. The left side of the figure shows the results of the frequency analysis for the diffraction that occurs when the emitter was directed along the ΓM direction and the right side is reserved for the ΓK direction. The frequencies that were detected appear to follow Bragg scattering curves associated with the periodicity of the first layer of cylinders on the crystal surface.

In order to confirm this observation, dotted lines corresponding to the theoretical Bragg scattering curves were superimposed on Figure 5.18. The relation to theoretically predict the angle of the diffracted orders as a function of frequency can be derived from the classical diffraction grating equation, a form of which is shown in Equation 5.1, when the angle of incidence θ_i is equal to 0. In this equation, θ_m is equal to the angle of diffraction for diffraction order m (and for the frequency range and periodicity being considered, m would be equal to 1 or 2) of a particular frequency having wavelength λ. The periodicity of the first layer of cylinders that the incident sound encounters is Λ.

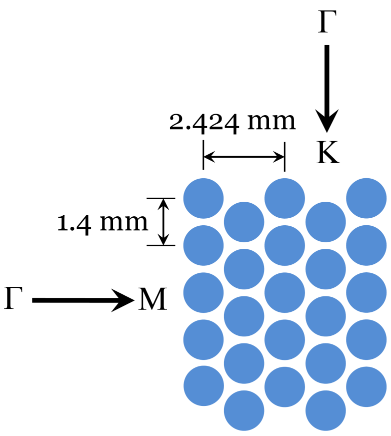

Figure 5.17: Periodicities of the phononic crystal surfaces.

$$\sin \theta_m = \sin \theta_i + \frac{m\lambda}{\Lambda} \tag{5.1}$$

Therefore, the frequency and angle pairs of the theoretical curves can be found from Equation 5.2, where the wavelength λ is expressed in terms of the sound speed in the surrounding water v_{liq} and frequency f. The value of v_{liq} that was used in the theoretical computations was 1459.5 m/s.

$$\sin \theta_m = \frac{v_{liq} m}{f\Lambda} \tag{5.2}$$

The values of Λ change according to the direction of incidence, as shown in Figure 5.17. For incidence in the ΓM direction, Λ corresponds to a value of 1.4 mm, but for incidence in the ΓK direction, the periodicity of the first layer of cylinders is no longer equal to the distance between the centers of two adjacent cylinders. It is instead equal to $1.4\sqrt{3}$ or 2.42 mm.

For the ΓM direction, the 1st order Bragg scattering curve nicely follows the observed diffraction detected with the 1 MHz transducer pair, and both the 1st and 2nd order Bragg scattering curves are visible in the field detected with the 2.25 MHz transducer pair. In particular, there is continuity of the 1st order curve between the

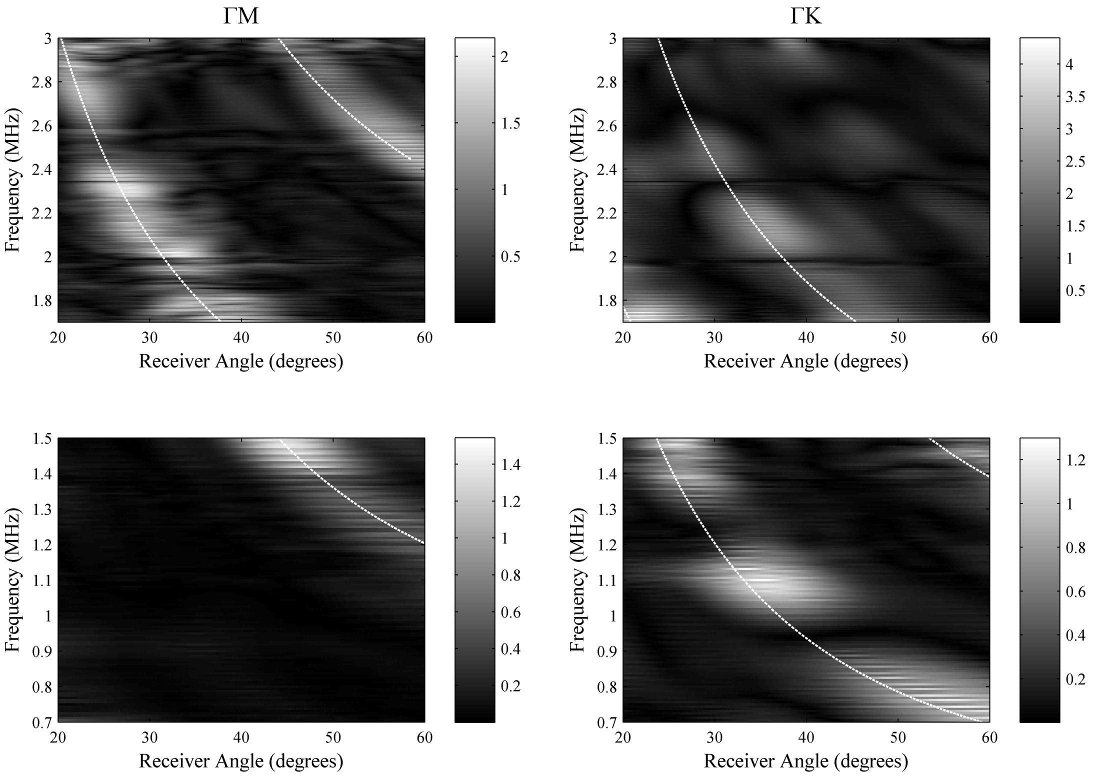

Figure 5.18: Diffraction results for both the ΓM and ΓK directions. All results obtained with pulsed ultrasound. Bragg scattering curves shown in dotted lines. (Left) ΓM direction. (Right) ΓK direction.

two frequency ranges. The diffraction does contain some disturbances but it is essentially continuous, so it cannot be said that enhanced diffraction for frequencies in the experimentally-determined band-gap regions has been observed.

For the ΓK direction, the 1st and 2nd order Bragg scattering curves are visible in the 1 MHz range and both the curves continue into the 2.25 MHz range, but only the 2nd order diffraction is easily visible due to the frequency and angle ranges measured. Much like the ΓM direction, enhanced diffraction for the frequency ranges of the band-gaps determined experimentally through the through-transmission measurements can't be clearly observed. However, the Bragg curves do exhibit some disturbance around 0.9 MHz and again between 1.2 MHz and 1.3 MHz which might be related to these frequencies being near the edges of band-gaps. Some disturbance is also seen at 2 MHz and 2.4 MHz, although it is too early to consider these related to band-gap phenomena.

Because the theoretical Bragg scattering curves closely follow the experimentally detected diffracted frequencies in the incident half-space of the crystal, it can be said that the surface of the crystal is functioning as an acoustic diffraction grating.

5.5 Conclusions

5.5.1 Summary of results

This chapter has presented through-transmission and diffraction experiments of bulk ultrasonic waves on a 2D phononic crystal consisting of a triangular lattice of steel cylinders in water. The through-transmission experiments were performed with both pulsed and swept ultrasound. The pulsed measurements were processed using both the FFT and STFT whereas the swept results were analyzed using the STFT. Although the use of the FFT is entirely possible for the swept ultrasound, an extremely large number of data points is required, and this can result in a great deal of "noise" appearing in the spectrum.

The results of the pulsed and swept techniques were consistent, with the exception of late-arriving frequencies that were more easily detected with the swept ultrasound technique. Frequencies experiencing time-delays of this nature may be subject to slow group velocities in the crystal, and this is certainly a matter for future theoretical investigation. The swept ultrasound may detect these frequencies when they might otherwise be missed in a pulsed measurement, and this has implications for the study of band-gap phenomena in phononic crystals using pulsed ultrasound.

Diffraction measurements were then performed using pulsed ultrasound. The diffraction that was observed to occur on the surface in the incident half-space was followed closely by theoretical Bragg scattering curves. Some discontinuities and regions of higher amplitude of the diffraction were observed, and these might be due to the location of these frequencies with respect to the band-gaps for the crystal but this requires additional research.

It is clear, however, that the surfaces of the phononic crystal can be said to function as an acoustic diffraction gratings. This has implications for the application of phononic crystals in actual devices, since any bulk wave incident upon the crystal will diffract on the surface and thus lose energy and create a diffracted field that could span the entire half-space.

5.5.2 Suggestions for future work

One issue that may have contributed to the lack of clarity in the diffraction results is the fact that the crystal aligning plates had not originally been designed to accommodate diffraction measurements with the polar/C-scan equipment. Therefore, it was impossible to access the diffracted field generated by the portion of the crystal between the support plates, and the periodicity of the cylinders may have been less than perfect. One area for future research is the sensitivity of band-gap phenomena to imperfections in the periodicity of phononic crystals. This may be less of a concern for crystals that can be manufactured using microfabrication techniques or for crystals on the acoustic wavelength scale (since hopefully the periodicities involved would be much larger than potential imperfections in the lattice spacing), it may be an issue for crystals that operate in the ultrasonic regime.

Another possible change that could be made for future diffraction experiments involves the size of the transducers used as the emitter and the receiver. The housing or case diameter of the transducers used in these experiments was equal to 1/2 inch (12.7 mm), and they had an element size just slightly smaller than the housing. Therefore, the incident beam covered a relatively small number of periods on the crystal, especially for incidence in the ΓK direction. Since diffraction depends on multiple "facets" of the surface being illuminated with incident sound, the beam width clearly plays an important role in the observation of diffraction phenomena. Therefore, future diffraction experiments should employ larger diameter transducers, especially for the emitter.

In terms of the receiver, the transducers that were employed in these experiments actually have the advantage of being very sensitive to sound that is normally incident upon their surfaces but much less sensitive to sound that is not normally incident upon them. Therefore, they are well-suited to measure diffracted fields as a function of angle since they detect sound that is propagating in the direction along which the transducer is directed. It might be interesting to use a needle hydrophone as a receiver since its small size would reduce the effect of its presence in the diffracted field.

Finally, some of the disturbances in the diffraction that were observed in these experiments may have been due to beam edge effects. For example, some beam spreading has been observed in Schlieren images of reflection on periodically grooved surfaces [74]. For the experiments presented in this chapter, the angular scans for the diffraction measurements were performed at a fixed distance from the crystal surfaces due to the geometric constraints of the transducer mounting fork on the polar/C-scan equipment. One option for future experiments is to change the geometry of the polar/C-scan equipment (essentially construct another mounting fork) to increase the distance between the crystal surface and the receiver so that some of this beam spreading would sufficiently attenuate before reaching the receiving transducer.

CHAPTER VI

CONCLUDING SUMMARY

The objective of the research presented in this thesis has been to provide new numerical and experimental tools that are capable of capturing important features that occur due to the diffraction of ultrasound on periodic solid surfaces. Although this interaction between ultrasound and periodic surfaces has many different potential areas of exploration, this thesis has focused on four main areas including

- the use of the Rayleigh-Fourier method for the simulation of reflection spectra from periodic surfaces,
- the ultrasonic characterization of imperfectly periodic surfaces,
- the analysis of the backward beam displacement which occurs due to ultrasonic diffraction, and
- the study of diffracted bulk waves on a 2D phononic crystal.

This brief chapter will summarize the scientific contributions made in these four areas and present opportunities that exist for future work.

First, in Chapter 2, simulations employing the Rayleigh-Fourier(R-F) method have been derived and used to study Wood anomalies in diffracted reflection spectra in order to identify frequencies at which surface and/or plate waves may be generated due to diffraction. Four new cases of structures containing one or more periodic surfaces were treated with the method. The first case studied was that of a fluid-loaded-plate with both sides periodic, and it was discovered that the reflection spectra this structure differs only somewhat from that obtained from a plate with only side periodic (when the incident wave originates in the fluid on the periodic side of the plate). It is likely that differences in the spectra are due to different Lamb wave generation on the two types of plates. When both sides of a plate are periodic, a phase difference between the two surface profiles may exist. In this thesis, the cases of symmetric and antisymmetric plates were studied, and the differences that exist between these spectra are also likely due to frequencies at which or efficiency with which Lamb waves are generated in these plates. In addition, the assumption was made that the periodicities of the two surfaces were identical. A discussion was presented on the feasibility of incorporating two surfaces with different periodicities into the Rayleigh-Fourier method, and this is an area in which future work with the Rayleigh-Fourier method might be conducted.

The second case studied in Chapter 2 was that of two solid surfaces in perfect contact with a periodic interface between them. The R-F simulations showed the existence of a Wood anomaly at the frequency for which a 1^{st} order Stoneley wave may be generated along a steel-titanium interface. Based on these results, the examination of Wood anomalies determined using the Rayleigh-Fourier method may be a technique for the prediction of Stoneley wave generation.

The third and fourth cases treated with the R-F method were those of fluid-loaded bilayered plates (i.e. plates consisting of two layers of solid materials). The first bilayered plate considered was smooth over its exterior surfaces but with an interior periodic interface. The reflection spectra revealed that plate resonances dominated over diffraction effects. The second bilayered plate had all of its interfaces periodic, and it was shown that the diffraction occurring due to periodicities present on the external plate surfaces dominated over the diffraction occurring at the interface between the two solids of the plate.

Recommendations for future work include the comparison of simulation with experiment. Because current manufacturing techniques at the length scale which would be appropriate for ultrasonic frequencies involves microfabrication techniques, it may be worthwhile to extend the use of the Rayleigh-Fourier method to anisotropic materials (single crystal silicon for example) so that any samples manufactured could be compared with experiment.

However, since the Rayleigh-Fourier method can really only be applied to surfaces which possess a perfect periodicity, the next area studied was the use of ultrasonic diffraction in the examination of surfaces that have imperfect periodicities, and this was presented in Chapter 3. Two techniques for the ultrasonic characterization of a thin plate with regions of imperfectly periodic surface textures were compared. A normal incidence pulse-echo technique, where anomalies in the reflection spectra may be a function of surface periodicity and height, was compared with a backscattering (or Bragg scattering) technique, where the backscattered -1$^{\mathrm{st}}$ order diffraction may be measured. The anomalies detected by the pulse-echo technique were most likely due to Lamb wave generation on the plate, and the backscattering method was found to be more promising, especially for the determination of surface periodicity. The Bragg curves that were obtained from the backscattering results show at least a qualitative difference for profiles with different roughness heights. Therefore, in situations where an optical inspection of a periodic surface may not be possible, ultrasound can be used to give some indication of periodic surface parameters.

One possibility for future work in this area includes the study of the same techniques on a thick solid with the same type of surface textures. It is important to study this case so that the diffraction occurring on the surface can be isolated from the Lamb wave generation. Of course, the long-standing search to quantitatively characterize a periodic surface's profile height with an experimentally measurable quantity remains. This problem remains to this day due to the very complex nature of quantifying diffraction efficiency on periodic surfaces.

Because the examination of surfaces like those examined in Chapter 3 often employs bounded beams, it is very important to understand diffraction effects on periodic surfaces which are sensitive to beam width, such as the backward beam displacement. This phenomenon was studied in Chapter 4. Until now, the backward beam displacement had only ever been observed (1) qualitatively using schlieren imaging, (2) at one frequency and angle of incidence (6 MHz at 22.5°), and (3) in reflection. However, it has now been quantitatively shown (through the use of immersion transducers) that the ultrasonic backward beam displacement exists at multiple frequency and incident angle combinations and in transmission as well as reflection. This has implications whenever a bounded beam is used as part of an inspection technique for a periodic surface. A definitive link between the backward displacement and backward Scholte-Stoneley wave generation has now also been shown. Possibilities for future work include simulation and measurement of the magnitude of the beam shift as a function of frequency, angle, and beam width.

Finally, since much of the current interest in periodic surfaces is being driven by the study of phononic crystals, a study on the diffraction that occurs on the surfaces of a two-dimensional crystal was presented in Chapter 5. Many studies have addressed phononic crystals under the assumption that they are of infinite size. However, if phononic crystals are ever to be successfully implemented in actual devices, the diffraction that will occur on their exterior surfaces must be taken into account. It has now been shown that bulk ultrasonic waves diffract on the exterior surfaces of a 2D phononic crystal much as they would on a solid periodic surface (diffraction grating). It is hypothesized that enhanced diffraction may be observable for frequencies within the crystal's band-gap. Although diffraction following Bragg curves was clearly observed, it is recommended that additional diffraction experiments be performed because it was found that the use of a immersion transducer (which has the advantage of being very directionally dependent) with a relatively large face size to measure the diffracted field does not yield the best resolution (in terms of frequency as a function of position within the diffracted field) that might be obtained, for example, with a needle hydrophone. In addition, it is recommended that additional experiments on diffraction on phononic crystals employ larger transducers as emitters. However, it is unknown at this time how diffraction on the surface of phononic crystals may be affected by beam width, and this is another area for future investigation.

One particularly interesting but accidental discovery occurred with the comparison of pulsed and swept ultrasound for the measurement of the crystal band-gaps in transmission. Most experimental studies on phononic crystals employ pulsed ultrasound and then use Fourier analysis to determine which frequencies are not transmitted through the crystal. However, it has now been shown that if a sufficiently long time window of transmission data is not collected, it may be possible to declare certain frequencies as belonging to a band-gap, when in fact, they may just be experiencing slow group velocity. This is a very important opportunity for future work, as it has implications regarding how experimental studies on phononic crystals should be conducted so that they can be accurately compared to the band-structures computed by theoreticians.

It is expected that research interest in acoustic and elastic wave interaction with periodic surfaces and structures such as phononic crystals will continue in the years to come. The research presented in this thesis has made distinct contributions within this broad field, in the study of diffraction in the ultrasonic frequency regime in particular. The results and suggestions for future work presented here should help scientists and engineers as they continue to develop advanced NDE techniques and devices that incorporate periodic structures.

APPENDIX A

DERIVATION OF BOUNDARY CONDITIONS FOR A FLUID-LOADED PLATE WITH ONE SIDE PERIODIC

This appendix contains the derivation of the boundary condition expressions for the case of a fluid-loaded plate that has one periodically corrugated side. A diagram of the possible incident waves along with the diffracted wave series is shown in Figure A.1. The three media can be characterized by their densities as well as their Lamé constants. The bulk wave speeds are a function of these parameters, and the notation used for these quantities is shown in Table A.1. The second Lamé constant μ is equal to 0 for the two fluid media since they cannot support shear stress, and the only bulk waves possible are longitudinal. For the solid medium, the subscripts d and s are used to indicate the longitudinal and shear wave speeds, respectively.

The boundary conditions derived here will eventually form the matrix $[A]$ in the linear system $[A]\,\vec{x} = \vec{b}$. The vector $\vec{b}$ will contain information regarding the incident wave and the vector $\vec{x}$ will contain the unknown coefficients for the diffracted wave series. Although several possibilities for incident waves are shown in Figure A, the MATLAB code that will be written to perform the $\vec{x} = [A]^{-1}\,\vec{b}$ calculation will accomodate only one incident wave.

Table A.1: Notation for media properties.

	Density	Lamé constants	Bulk wave speed(s)
Upper fluid (medium 1)	$\rho^{\mathbf{1}}$	$\lambda^{\mathbf{1}}$	v
Solid plate (medium 2)	$\rho^{\mathbf{2}}$	$\lambda^{\mathbf{2}}$, $\mu^{\mathbf{2}}$	v_d, v_s
Lower fluid (medium 3)	$\rho^{\mathbf{3}}$	$\lambda^{\mathbf{3}}$	v_t

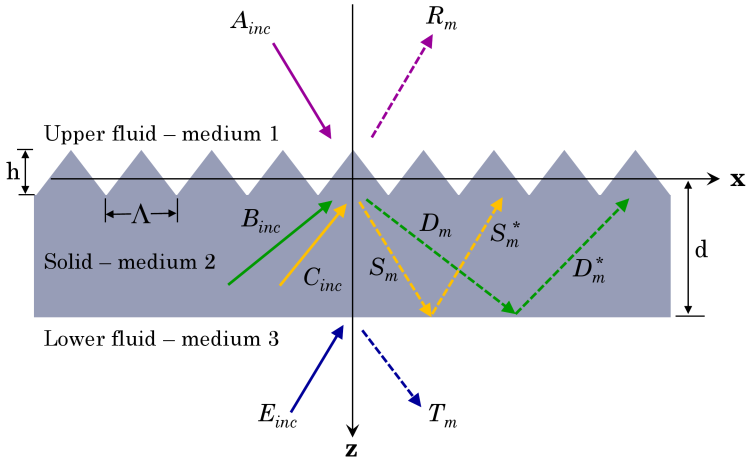

Figure A.1: Diagram of diffracted fields for a fluid-loaded plate having one side periodically corrugated. Diffracted wave series shown in dotted lines. Sound rays not drawn to scale with respect to wave number $\frac{\omega}{v}$.

This appendix consists of three sections. First, the field equations will be presented for the three media in the problem. Because the boundary conditions that must be satisfied at the plate surfaces are in terms of both displacement and stress, the second section will present preliminary derivations for stress components in the media. Finally, the third section will present the substitution of the displacement and stress components into the boundary conditions, the equating of Fourier coefficients, and the collection of terms per diffracted series.

A.1 Field equations

A.1.1 Field in the upper fluid (medium 1)

The total displacement field in the upper fluid (medium 1) can be expressed as the sum of the field due to the incident wave and the field due to a series of diffracted waves.

$$\vec{u}^{\mathbf{1}} = \vec{u}_{iA} + \vec{u}_R$$

The subscript iA is used for the incident longitudinal wave, and the subscript R represents the diffracted wave series. The letter R is used in convention with prior studies [51, 81] that examined diffraction occuring due to waves incident on the periodic side of the plate. Since this series of waves represented the reflected field, the letter R was used. Because all the waves in the fluid are longitudinal, they can be expressed via scalar potentials.

$$\varphi_{iA} = A_{inc} e^{i(k_{iA}x + K_{iA}z)}$$
$$\varphi_R = \sum \varphi_{Rm} = \sum R_m e^{i(k_m x + K_{Rm} z)}$$

Therefore, the total displacement field in the upper fluid (medium 1) is given by the following expression.

$$\vec{u}^{\mathbf{1}} = \nabla\varphi_{iA} + \nabla\varphi_R = \begin{bmatrix} ik_{iA}\varphi_{iA} \\ 0 \\ iK_{iA}\varphi_{iA} \end{bmatrix} + \sum \begin{bmatrix} ik_m\varphi_{Rm} \\ 0 \\ iK_{Rm}\varphi_{Rm} \end{bmatrix} \tag{A.1}$$

A.1.2 Field in the solid plate (medium 2)

The displacement field in the solid plate (medium 2) can be expressed as the sum of the fields created by an incident longitudinal or shear wave (if one of these is present) and four series of diffracted waves. The subscripts iB and iC are used for the incident longitudinal and shear waves, respectively. The subscripts D and S represent the diffracted longitudinal and shear wave series, respectively. Because the plate is of finite thickness, the diffracted wave series that are generated by the periodic surface will reflect off the smooth side of the plate, and the contribution of these reflections to the field within the plate must be included, so these are denoted by the asterisk superscripts.

$$\vec{u}^{\mathbf{2}} = \vec{u}_{iB} + \vec{u}_{iC} + \vec{u}_D + \vec{u}^*_D + \vec{u}_S + \vec{u}^*_S$$

The fields due to longitudinal waves can be expressed via scalar potentials just as they were in the upper fluid (medium 1). However, fields due to shear waves will be expressed directly in vector form. The polarization factors P_x, P_y, and P_z are used in the vectors to specify whether the polarization is vertical ($P_y = 0$) or horizontal ($P_x = P_z = 0$). The scalar potentials for the longitudinal wave fields $\vec{u}_{iB}$, $\vec{u}_D$, and $\vec{u}_D^*$ are given by the following expressions.

$$\begin{aligned}\varphi_{iB} &= B_{inc}e^{i(k_{iB}x+K_{iB}z)}\\ \varphi_D &= \sum \varphi_{Dm} = \sum D_m e^{i(k_m x+K_{Dm}z)}\\ \varphi_D^* &= \sum \varphi_{Dm}^* = \sum D_m^* e^{i(k_m x+K_{Dm}^* z)}\end{aligned}$$

The vectors for the shear wave fields $\vec{u}_{iC}$, $\vec{u}_S$, and $\vec{u}_S^*$ are expressed as

$$\vec{u}_{iC} = \begin{bmatrix} P_{xC}\psi_{iC} \\ P_{yC}\psi_{iC} \\ P_{zC}\psi_{iC} \end{bmatrix}, \vec{u}_S = \sum \begin{bmatrix} P_{xm}\psi_{Sm} \\ P_{ym}\psi_{Sm} \\ P_{zm}\psi_{Sm} \end{bmatrix}, \text{ and } \vec{u}_S^* = \sum \begin{bmatrix} P_{xm}^*\psi_{Sm}^* \\ P_{ym}^*\psi_{Sm}^* \\ P_{zm}^*\psi_{Sm}^* \end{bmatrix}$$

$$\begin{aligned}\text{where}\quad \psi_{iC} &= C_{inc}e^{i(k_{iC}x+K_{iC}z)}\\ \psi_{Sm} &= S_m e^{i(k_m x+K_{Sm}z)}\\ \psi_{Sm}^* &= S_m^* e^{i(k_m x+K_{Sm}^* z)}.\end{aligned}$$

Combining the longitudinal and shear waves results in

$$\vec{u}^{\mathbf{2}} = \nabla\varphi_{iB} + \begin{bmatrix} P_{xC}\psi_{iC} \\ P_{yC}\psi_{iC} \\ P_{zC}\psi_{iC} \end{bmatrix} + \nabla\varphi_D + \nabla\varphi_D^* + \sum \begin{bmatrix} P_{xm}\psi_{Sm} \\ P_{ym}\psi_{Sm} \\ P_{zm}\psi_{Sm} \end{bmatrix} + \sum \begin{bmatrix} P_{xm}^*\psi_{Sm}^* \\ P_{ym}^*\psi_{Sm}^* \\ P_{zm}^*\psi_{Sm}^* \end{bmatrix}$$

which gives the final expression for the field in the solid plate.

$$\begin{aligned}\vec{u}^{\mathbf{2}} = &\begin{bmatrix} ik_{iB}\varphi_{iB} \\ 0 \\ iK_{iB}\varphi_{iB} \end{bmatrix} + \begin{bmatrix} P_{xC}\psi_{iC} \\ P_{yC}\psi_{iC} \\ P_{zC}\psi_{iC} \end{bmatrix} + \sum \begin{bmatrix} ik_m\varphi_{Dm} \\ 0 \\ iK_{Dm}\varphi_{Dm} \end{bmatrix} \\ &+ \sum \begin{bmatrix} ik_m\varphi_{Dm}^* \\ 0 \\ iK_{Dm}^*\varphi_{Dm}^* \end{bmatrix} + \sum \begin{bmatrix} P_{xm}\psi_{Sm} \\ P_{ym}\psi_{Sm} \\ P_{zm}\psi_{Sm} \end{bmatrix} + \sum \begin{bmatrix} P_{xm}^*\psi_{Sm}^* \\ P_{ym}^*\psi_{Sm}^* \\ P_{zm}^*\psi_{Sm}^* \end{bmatrix}\end{aligned} \qquad \text{(A.2)}$$

A.1.3 Field in the lower fluid (medium 3)

The total field in the lower fluid (medium 3) can be expressed in a manner identical to that of the upper fluid. The subscript iE is used to indicate an incident longitudinal wave and the subscript T is used for the diffracted wave series. All the waves in the fluid are longitudinal and can therefore be represented via scalar potential functions. The field equation and the potential functions are shown below.

$$\vec{u}^{\mathbf{3}} = \vec{u}_{iE} + \vec{u}_T = \nabla\varphi_{iE} + \nabla\varphi_T = \begin{bmatrix} ik_{iE}\varphi_{iE} \\ 0 \\ iK_{iE}\varphi_{iE} \end{bmatrix} + \sum \begin{bmatrix} ik_m\varphi_{Tm} \\ 0 \\ iK_{Tm}\varphi_{Tm} \end{bmatrix} \tag{A.3}$$

$$\begin{aligned} \varphi_{iE} &= E_{inc}e^{i(k_{iE}x+K_{iE}z)} \\ \varphi_T &= \sum \varphi_{Tm} = \sum T_m e^{i(k_m x+K_{Tm}z)} \end{aligned}$$

A.2 Stress Components

The stress tensor components can now be calculated from the fields in the three media.

A.2.1 Upper Fluid (medium 1)

The fluid cannot support shear stress ($\mu^{\mathbf{1}} = 0$) so all that remains is the calculation of the normal stress components which are given in the following expression.

$$\begin{aligned} T^{\mathbf{1}}_{xx} &= T^{\mathbf{1}}_{zz} = \lambda^{\mathbf{1}}\left(\frac{\partial u^{\mathbf{1}}_x}{\partial x} + \frac{\partial u^{\mathbf{1}}_z}{\partial z}\right) \\ &= \lambda^{\mathbf{1}}\left[-(k_{iA})^2\varphi_{iA} - \sum(k_m)^2\varphi_{Rm} - (K_{iA})^2\varphi_{iA} - \sum(K_{Rm})^2\varphi_{Rm}\right] \\ &= \lambda^{\mathbf{1}}\left[-\left(\frac{\omega}{v}\right)^2\varphi_{iA} + \sum -\left(\frac{\omega}{v}\right)^2\varphi_{Rm}\right] \end{aligned} \tag{A.4}$$

A.2.2 Solid Plate (medium 2)

Because the field within the plate is more complicated than those of the fluid media, some preliminary expressions are derived before the stress components.

$$
\begin{aligned}
\frac{\partial u_x^{\mathbf{2}}}{\partial x} &= -\left(k_{iB}\right)^2 \varphi_{iB} + i k_{iC} P_{xC} \psi_{iC} \\
&\quad - \sum k_m^2 \varphi_{Dm} - \sum k_m^2 \varphi_{Dm}^* \\
&\quad + \sum i k_m P_{xm} \psi_{Sm} + \sum i k_m P_{xm}^* \psi_{Sm}^* \\
\frac{\partial u_y^{\mathbf{2}}}{\partial y} &= 0 \\
\frac{\partial u_z^{\mathbf{2}}}{\partial z} &= -\left(K_{iB}\right)^2 \varphi_{iB} + i K_{iC} P_{zC} \psi_{iC} \\
&\quad - \sum (K_{Dm})^2 \varphi_{Dm} - \sum (K_{Dm}^*)^2 \varphi_{Dm}^* \\
&\quad + \sum i K_{Sm} P_{zm} \psi_{Sm} + \sum i K_{Sm}^* P_{zm}^* \psi_{Sm}^*
\end{aligned} \tag{A.5}
$$

Combining these yields the following expression.

$$
\begin{aligned}
\left(\frac{\partial u_x^{\mathbf{2}}}{\partial x} + \frac{\partial u_y^{\mathbf{2}}}{\partial y} + \frac{\partial u_z^{\mathbf{2}}}{\partial z}\right) &= \left[-\left(\frac{\omega}{v_d}\right)^2\right] \varphi_{iB} + i k_{iC} P_{xC} \psi_{iC} + i K_{iC} P_{zC} \psi_{iC} \\
&\quad + \sum \left[-\left(\frac{\omega}{v_d}\right)^2\right] \varphi_{Dm} + \sum \left[-\left(\frac{\omega}{v_d}\right)^2\right] \varphi_{Dm}^* \\
&\quad + \sum i k_m P_{xm} \psi_{Sm} + \sum i K_{Sm} P_{zm} \psi_{Sm} \\
&\quad + \sum i k_m P_{xm}^* \psi_{Sm}^* + \sum i K_{Sm}^* P_{zm}^* \psi_{Sm}^*
\end{aligned} \tag{A.6}
$$

Also needed to calculate the stress components are the following derivatives.

$$
\begin{aligned}
\frac{\partial u_x^{\mathbf{2}}}{\partial z} &= -k_{iB} K_{iB} \varphi_{iB} + i K_{iC} P_{xC} \psi_{iC} \\
&\quad + \sum -k_m K_{Dm} \varphi_{Dm} + \sum -k_m K_{Dm}^* \varphi_{Dm}^* \\
&\quad + \sum i K_{Sm} P_{xm} \psi_{Sm} + \sum i K_{Sm}^* P_{xm}^* \psi_{Sm}^* \\
\frac{\partial u_z^{\mathbf{2}}}{\partial x} &= -k_{iB} K_{iB} \varphi_{iB} + i k_{iC} P_{zC} \psi_{iC} \\
&\quad + \sum -k_m K_{Dm} \varphi_{Dm} + \sum -k_m K_{Dm}^* \varphi_{Dm}^* \\
&\quad + \sum i k_m P_{zm} \psi_{Sm} + \sum i k_m P_{zm}^* \psi_{Sm}^*
\end{aligned} \tag{A.7}
$$

Then, the stress tensor components are equal to the following three expressions.

$$
\begin{aligned}
T^{\mathbf{2}}_{xx} &= \lambda^{\mathbf{2}}\left(\frac{\partial u^{\mathbf{2}}_x}{\partial x}+\frac{\partial u^{\mathbf{2}}_y}{\partial y}+\frac{\partial u^{\mathbf{2}}_z}{\partial z}\right)+2\mu^{\mathbf{2}}\left(\frac{\partial u^{\mathbf{2}}_x}{\partial x}\right)\\
&= \lambda^{\mathbf{2}}\left[-\left(\frac{\omega}{v_d}\right)^2\varphi_{iB}+ik_{iC}P_{xC}\psi_{iC}+iK_{iC}P_{zC}\psi_{iC}\right]\\
&\quad+\lambda^{\mathbf{2}}\left[\sum-\left(\frac{\omega}{v_d}\right)^2\varphi_{Dm}+\sum-\left(\frac{\omega}{v_d}\right)^2\varphi^*_{Dm}\right]\\
&\quad+\lambda^{\mathbf{2}}\left[\sum ik_mP_{xm}\psi_{Sm}+\sum iK_{Sm}P_{zm}\psi_{Sm}\right]\\
&\quad+\lambda^{\mathbf{2}}\left[\sum ik_mP^*_{xm}\psi^*_{Sm}+\sum iK^*_{Sm}P^*_{zm}\psi^*_{Sm}\right]\\
&\quad+2\mu^{\mathbf{2}}\left[-(k_{iB})^2\varphi_{iB}+ik_{iC}P_{xC}\psi_{iC}\right]\\
&\quad+2\mu^{\mathbf{2}}\left[-\sum k_m^2\varphi_{Dm}-\sum k_m^2\varphi^*_{Dm}\right]\\
&\quad+2\mu^{\mathbf{2}}\left[\sum ik_mP_{xm}\psi_{Sm}+\sum ik_mP^*_{xm}\psi^*_{Sm}\right]
\end{aligned}
\tag{A.8}
$$

$$
\begin{aligned}
T^{\mathbf{2}}_{xz}=T^{\mathbf{2}}_{zx} &= 2\mu^{\mathbf{2}}\frac{1}{2}\left(\frac{\partial u^{\mathbf{2}}_x}{\partial z}+\frac{\partial u^{\mathbf{2}}_z}{\partial x}\right)=\mu^{\mathbf{2}}\left(\frac{\partial u^{\mathbf{2}}_x}{\partial z}+\frac{\partial u^{\mathbf{2}}_z}{\partial x}\right)\\
&= \mu^{\mathbf{2}}\left[-2k_{iB}K_{iB}\varphi_{iB}+iK_{iC}P_{xC}\psi_{iC}+ik_{iC}P_{zC}\psi_{iC}\right]\\
&\quad+\mu^{\mathbf{2}}\left[\sum -2k_mK_{Dm}\varphi_{Dm}+\sum -2k_mK^*_{Dm}\varphi^*_{Dm}\right]\\
&\quad+\mu^{\mathbf{2}}\left[\sum iK_{Sm}P_{xm}\psi_{Sm}+\sum ik_mP_{zm}\psi_{Sm}\right]\\
&\quad+\mu^{\mathbf{2}}\left[+\sum iK^*_{Sm}P^*_{xm}\psi^*_{Sm}+\sum ik_mP^*_{zm}\psi^*_{Sm}\right]
\end{aligned}
\tag{A.9}
$$

$$
\begin{aligned}
T^{\mathbf{2}}_{zz} &= \lambda^{\mathbf{2}}\left(\frac{\partial u^{\mathbf{2}}_x}{\partial x}+\frac{\partial u^{\mathbf{2}}_y}{\partial y}+\frac{\partial u^{\mathbf{2}}_z}{\partial z}\right)+2\mu^{\mathbf{2}}\left(\frac{\partial u^{\mathbf{2}}_z}{\partial z}\right)\\
&= \lambda^{\mathbf{2}}\left[-\left(\frac{\omega}{v_d}\right)^2\varphi_{iB}+ik_{iC}P_{xC}\psi_{iC}+iK_{iC}P_{zC}\psi_{iC}\right]\\
&\quad+\lambda^{\mathbf{2}}\left[\sum-\left(\frac{\omega}{v_d}\right)^2\varphi_{Dm}+\sum-\left(\frac{\omega}{v_d}\right)^2\varphi^*_{Dm}\right]\\
&\quad+\lambda^{\mathbf{2}}\left[\sum ik_mP_{xm}\psi_{Sm}+\sum iK_{Sm}P_{zm}\psi_{Sm}\right]\\
&\quad+\lambda^{\mathbf{2}}\left[\sum ik_mP^*_{xm}\psi^*_{Sm}+\sum iK^*_{Sm}P^*_{zm}\psi^*_{Sm}\right]\\
&\quad+2\mu^{\mathbf{2}}\left[-(K_{iB})^2\varphi_{iB}+iK_{iC}P_{zC}\psi_{iC}\right]\\
&\quad+2\mu^{\mathbf{2}}\left[-\sum(K_{Dm})^2\varphi_{Dm}-\sum(K^*_{Dm})^2\varphi^*_{Dm}\right]\\
&\quad+2\mu^{\mathbf{2}}\left[\sum iK_{Sm}P_{zm}\psi_{Sm}+\sum iK^*_{Sm}P^*_{zm}\psi^*_{Sm}\right]
\end{aligned}
\tag{A.10}
$$

A.2.3 Lower Fluid (medium 3)

The (normal) stress components in the lower fluid can be derived in a manner identical to that of the upper fluid.

$$\begin{aligned}
T^{\mathbf{3}}_{xx} &= T^{\mathbf{3}}_{zz} = \lambda^{\mathbf{3}}\left(\frac{\partial u^{\mathbf{3}}_x}{\partial x} + \frac{\partial u^{\mathbf{3}}_z}{\partial z}\right) \\
&= \lambda^{\mathbf{3}}\left[-(k_{iE})^2\varphi_{iE} + \sum -(k_m)^2\varphi_{Tm} - (K_{iE})^2\varphi_{iE} + \sum -(K_{Tm})^2\varphi_{Tm}\right] \qquad (A.11) \\
&= \lambda^{\mathbf{3}}\left[-\left(\frac{\omega}{v_t}\right)^2\varphi_{iE} + \sum -\left(\frac{\omega}{v_t}\right)^2\varphi_{Tm}\right]
\end{aligned}$$

A.3 Boundary Conditions

The expressions for the stress components that were obtained in the previous section will now be substituted into the boundary conditions for the plate surfaces. A total of six boundary conditions (three for the upper surface and three for the lower surface) will be presented in this section.

The first boundary conditions to be derived will be those associated with the upper (periodic) surface of the plate. One will be associated with the continuity of particle displacement normal to the periodic surface and the remaining two will be associated with the continuity of stress.

A.3.1 Periodic (upper) surface boundary conditions

The periodically grooved surface of the plate can be defined by Equation A.12 which is shown graphically in Figure A.2. In this equation, h represents the peak-to-peak height of the profile and Λ is the periodicity.

$$f(x) = \begin{cases} \dfrac{2h}{\Lambda}x - \dfrac{h}{2} & \text{for } 0 \le x \le \dfrac{\Lambda}{2} \\ \dfrac{3h}{2} - \dfrac{2h}{\Lambda}x & \text{for } \dfrac{\Lambda}{2} \le x \le \Lambda \end{cases} \qquad (A.12)$$

Since the surface is described by $h_1(x,z) = f(x) - z = 0$, the vector ∇h_1 represents a vector normal to the surface. Therefore, the continuity of normal particle displacement between the upper fluid (medium 1) and the solid plate (medium 2) can be

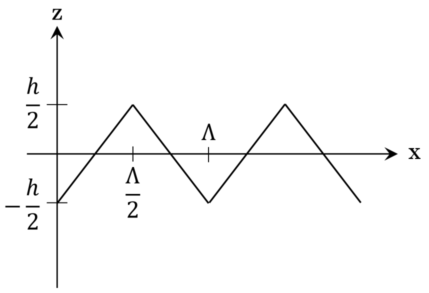

Figure A.2: Sawtooth profile function.

expressed as

$$\vec{u}^{\mathbf{1}} \cdot \nabla h_1 = \vec{u}^{\mathbf{2}} \cdot \nabla h_1 \qquad \text{where } \nabla h_1 = \begin{bmatrix} f'(x) \\ 0 \\ -1 \end{bmatrix} . \tag{A.13}$$

From Equation 2.15, the two boundary conditions representing continuity of stress at the surface are

$$T^{\mathbf{1}}_{xx} f'(x) = T^{\mathbf{2}}_{xx} f'(x) - T^{\mathbf{2}}_{xz} \tag{A.14}$$

$$-T^{\mathbf{1}}_{zz} = T^{\mathbf{2}}_{zx} f'(x) - T^{\mathbf{2}}_{zz} \tag{A.15}$$

A.3.1.1 Derivation of Boundary Condition 1

Substituting the fields for media 1 and 2 into the first boundary condition given in Equation A.13 results in the following equation.

$$\begin{aligned} &\left(ik_{iA}\varphi_{iA} + \sum ik_m\varphi_{Rm}\right) f'(x) - \left(iK_{iA}\varphi_{iA} + \sum iK_{Rm}\varphi_{Rm}\right) \\ &\quad = \left[ik_{iB}\varphi_{iB} + P_{xC}\psi_{iC} + \sum \left(ik_m\varphi_{Dm} + ik_m\varphi^*_{Dm} + P_{xm}\psi_{Sm} + P^*_{xm}\psi^*_{Sm}\right)\right] f'(x) \\ &\quad - \left[iK_{iB}\varphi_{iB} + P_{zC}\psi_{iC} + \sum \left(iK_{Dm}\varphi_{Dm} + iK^*_{Dm}\varphi^*_{Dm} + P_{zm}\psi_{Sm} + P^*_{zm}\psi^*_{Sm}\right)\right] \end{aligned} \tag{A.16}$$

In order to equate Fourier coefficients, the equation is multiplied by $\int\limits_0^\Lambda e^{-ik_n x}$ and integrated over dx. This results in certain terms in the above expression being of the form

$$\int_0^\Lambda e^{i[(k_m-k_n)x+K_{\sigma m}f(x)]} f'(x)\, dx$$

where σ may represent any one of the diffracted wave series (R_m, D_m, D^*_m, S_m, or S^*_m) . Integration by parts ($\int u\,dv = uv - \int v\,du$) must be performed where u, v, and their derivatives are equal to the following.

$$\begin{aligned}
u &= e^{i(k_m-k_n)x} \\
du &= i(k_m-k_n)e^{i(k_m-k_n)x} \\
dv &= f'(x)e^{iK_{\sigma m}f(x)} \\
v &= \frac{1}{iK_{\sigma m}}e^{iK_{\sigma m}f(x)}
\end{aligned}$$

The result of this procedure is that

$$\begin{aligned}
\int_0^{\Lambda} e^{i[(k_m-k_n)x+K_{\sigma m}f(x)]}f'(x)dx &= -\frac{(k_m-k_n)}{K_{\sigma m}}\int_0^{\Lambda} e^{i[(k_m-k_n)x+K_{\sigma m}f(x)]}\,dx \\
&= -(k_m-k_n)I^{\sigma}_{mn} \ .
\end{aligned}$$

This expression has introduced the variable I^{σ}_{mn} which is defined as

$$I^{\sigma}_{mn} = \frac{1}{K_{\sigma m}}\int_0^{\Lambda} e^{i[(k_m-k_n)x+K_{\sigma m}f(x)]}dx \ . \tag{A.17}$$

Therefore,

$$\int_0^{\Lambda} e^{i[(k_m-k_n)x+K_{\sigma m}f(x)]}\,dx = K_{\sigma m}I^{\sigma}_{mn}$$

This integration process ultimately transforms Equation A.16 into Equation A.18.

$$\begin{aligned}
&-ik_{iA}(k_{iA}-k_n)I^{A}_{inc}A_{inc} + \sum -ik_m(k_m-k_n)I^{R}_{mn}R_m \qquad \text{(A.18)}\\
&-i(K_{iA})^2I^{A}_{inc}A_{inc} + \sum -i(K_{Rm})^2I^{R}_{mn}R_m \\
&\quad = -ik_{iB}(k_{iB}-k_n)I^{B}_{inc}B_{inc} - (k_{iC}-k_n)I^{C}_{inc}P_{xC}C_{inc} \\
&\qquad + \sum -ik_m(k_m-k_n)I^{D}_{mn}D_m + \sum -ik_m(k_m-k_n)I^{D*}_{mn}D^*_m \\
&\qquad + \sum -(k_m-k_n)I^{S}_{mn}P_{xm}S_m + \sum -(k_m-k_n)I^{S*}_{mn}P^*_{xm}S^*_m \\
&\qquad - i(K_{iB})^2I^{B}_{inc}B_{inc} - K_{iC}I^{C}_{inc}P_{zC}C_{inc} \\
&\qquad + \sum -i(K_{Dm})^2I^{D}_{mn}D_m + \sum -i(K^*_{Dm})^2I^{D*}_{mn}D^*_m \\
&\qquad + \sum -K_{Sm}I^{S}_{mn}P_{zm}S_m + \sum -K^*_{Sm}I^{S*}_{mn}P^*_{zm}S^*_m
\end{aligned}$$

Substituting Equation A.12 for $f(x)$ in Equation A.17 ultimately results in

$$I^{\sigma}_{mn} = ih\Lambda e^{-iK_{\sigma m}\frac{h}{2}} \frac{\left[1 - (-1)^{m-n} \, e^{ihK_{\sigma m}}\right]}{(hK_{\sigma m})^2 - (\pi(m-n))^2} \ . \tag{A.19}$$

Likewise, the variable I^{τ}_{inc} in Equation A.18 where τ may refer to any one of the incident waves (A_{inc}, B_{inc}, or C_{inc}) is given by

$$I^{\tau}_{inc} = ih\Lambda e^{-iK_{i\tau}\frac{h}{2}} \frac{\left[1 - (-1)^{-n} \, e^{ihK_{i\tau}}\right]}{(hK_{i\tau})^2 - (\pi n)^2} \ . \tag{A.20}$$

Collecting terms by diffracted series results in Equation A.21, the final form of the first boundary condition.

$$\begin{aligned}
&\sum i \left[k_m k_n - \left(\frac{\omega}{v}\right)^2\right] I^R_{mn} R_m \\
&+ \sum i \left[\left(\frac{\omega}{v_d}\right)^2 - k_m k_n\right] I^D_{mn} D_m + \sum i \left[\left(\frac{\omega}{v_d}\right)^2 - k_m k_n\right] I^{D*}_{mn} D^*_m \\
&+ \sum (k_m - k_n) I^S_{mn} P_{xm} S_m + \sum K_{Sm} I^S_{mn} P_{zm} S_m \\
&+ \sum (k_m - k_n) I^{S*}_{mn} P^*_{xm} S^*_m + \sum K^*_{Sm} I^{S*}_{mn} P^*_{zm} S^*_m \\
&\qquad = i \left[\left(\frac{\omega}{v}\right)^2 - k_{iA} k_n\right] I^A_{inc} A_{inc} - i \left[\left(\frac{\omega}{v_d}\right)^2 - k_{iB} k_n\right] I^B_{inc} B_{inc} \\
&\qquad\quad - (k_{iC} - k_n) I^C_{inc} P_{xC} C_{inc} - K_{iC} I^C_{inc} P_{zC} C_{inc}
\end{aligned} \tag{A.21}$$

A.3.1.2 Derivation of Boundary Condition 2

Substituting the stress tensor components for media 1 and 2 into the second boundary condition given in Equation A.14 results in the following equation.

$$
\begin{aligned}
&\lambda^{\mathbf{1}}\left[-\left(\frac{\omega}{v}\right)^2\varphi_{iA}+\sum-\left(\frac{\omega}{v}\right)^2\varphi_{Rm}\right]f'(x)\\
&\quad=\lambda^{\mathbf{2}}\left[-\left(\frac{\omega}{v_d}\right)^2\varphi_{iB}+ik_{iC}P_{xC}\psi_{iC}+iK_{iC}P_{zC}\psi_{iC}\right]f'(x)\\
&\quad+\lambda^{\mathbf{2}}\left[\sum-\left(\frac{\omega}{v_d}\right)^2\varphi_{Dm}+\sum-\left(\frac{\omega}{v_d}\right)^2\varphi^*_{Dm}\right]f'(x)\\
&\quad+\lambda^{\mathbf{2}}\left[\sum ik_mP_{xm}\psi_{Sm}+\sum iK_{Sm}P_{zm}\psi_{Sm}\right]f'(x)\\
&\quad+\lambda^{\mathbf{2}}\left[\sum ik_mP^*_{xm}\psi^*_{Sm}+\sum iK^*_{Sm}P^*_{zm}\psi^*_{Sm}\right]f'(x)\\
&\quad+2\mu^{\mathbf{2}}\left[-(k_{iB})^2\varphi_{iB}+ik_{iC}P_{xC}\psi_{iC}-\sum k_m^2\varphi_{Dm}-\sum k_m^2\varphi^*_{Dm}\right]f'(x)\\
&\quad+2\mu^{\mathbf{2}}\left[\sum ik_mP_{xm}\psi_{Sm}+\sum ik_mP^*_{xm}\psi^*_{Sm}\right]f'(x)\\
&\quad-\mu^{\mathbf{2}}\left[-2k_{iB}K_{iB}\varphi_{iB}+iK_{iC}P_{xC}\psi_{iC}+ik_{iC}P_{zC}\psi_{iC}\right]\\
&\quad-\mu^{\mathbf{2}}\left[\sum-2k_mK_{Dm}\varphi_{Dm}+\sum-2k_mK^*_{Dm}\varphi^*_{Dm}\right]\\
&\quad-\mu^{\mathbf{2}}\left[\sum iK_{Sm}P_{xm}\psi_{Sm}+\sum ik_mP_{zm}\psi_{Sm}\right]\\
&\quad-\mu^{\mathbf{2}}\left[+\sum iK^*_{Sm}P^*_{xm}\psi^*_{Sm}+\sum ik_mP^*_{zm}\psi^*_{Sm}\right]
\end{aligned}
\tag{A.22}
$$

Multiplying by $\int\limits_0^\Lambda e^{-ik_nx}$ and integrating over dx in a manner identical to that of the first boundary condition results in the following equation. The variables I^{σ}_{mn} and I^{τ}_{inc} are those that have been defined in Equations A.19 and A.20.

$$\begin{aligned}
&\sum \rho^{\mathbf{1}}(k_m - k_n)I^R_{mn}R_m \\
&+\sum -\rho^{\mathbf{2}}\left[k_m - k_n + 2\left(\frac{v_s}{\omega}\right)^2 (K_{Dm})^2 k_n\right] I^D_{mn}D_m \\
&+\sum -\rho^{\mathbf{2}}\left[k_m - k_n + 2\left(\frac{v_s}{\omega}\right)^2 (K^*_{Dm})^2 k_n\right] I^{D*}_{mn}D^*_m \\
&+\sum i\rho^{\mathbf{2}}\left[\left(\frac{v_d}{\omega}\right)^2 k_m(k_m - k_n) + \left(\frac{v_s}{\omega}\right)^2 (K_{Sm})^2\right] I^S_{mn}P_{xm}S_m \\
&+\sum i\rho^{\mathbf{2}}\left[\left(\frac{v_d}{\omega}\right)^2 k_m(k_m - k_n) + \left(\frac{v_s}{\omega}\right)^2 (K^*_{Sm})^2\right] I^{S*}_{mn}P^*_{xm}S^*_m \\
&+\sum i\rho^{\mathbf{2}}K_{Sm}\left[\left(\frac{v_d}{\omega}\right)^2 (k_m - k_n) - \left(\frac{v_s}{\omega}\right)^2 (k_m - 2k_n)\right] I^S_{mn}P_{zm}S_m \\
&+\sum i\rho^{\mathbf{2}}K^*_{Sm}\left[\left(\frac{v_d}{\omega}\right)^2 (k_m - k_n) - \left(\frac{v_s}{\omega}\right)^2 (k_m - 2k_n)\right] I^{S*}_{mn}P^*_{zm}S^*_m \\
&\quad = -\rho^{\mathbf{1}}(k_{iA} - k_n)I^A_{inc}A_{inc} + \rho^{\mathbf{2}}\left[k_{iB} - k_n + 2\left(\frac{v_s}{\omega}\right)^2 (K_{iB})^2 k_n\right] I^B_{inc}B_{inc} \\
&\qquad - i\rho^{\mathbf{2}}\left[\left(\frac{v_d}{\omega}\right)^2 k_{iC}(k_{iC} - k_n) + \left(\frac{v_s}{\omega}\right)^2 (K_{iC})^2\right] I^C_{inc}P_{xC}C_{inc} \\
&\qquad - i\rho^{\mathbf{2}}K_{iC}\left[\left(\frac{v_d}{\omega}\right)^2 (k_{iC} - k_n) - \left(\frac{v_s}{\omega}\right)^2 (k_{iC} - 2k_n)\right] I^C_{inc}P_{zC}C_{inc}
\end{aligned} \tag{A.23}$$

A.3.1.3 Derivation of Boundary Condition 3

Substituting the stress tensor components for media 1 and 2 into the third boundary condition given in Equation A.15 results in the following equation.

$$
\begin{aligned}
&\lambda^{\mathbf{1}} \left[-\left(\frac{\omega}{v}\right)^2 \varphi_{iA} + \sum -\left(\frac{\omega}{v}\right)^2 \varphi_{Rm} \right] f'(x) \qquad \text{(A.24)} \\
&= \lambda^{\mathbf{2}} \left[-\left(\frac{\omega}{v_d}\right)^2 \varphi_{iB} + ik_{iC} P_{xC} \psi_{iC} + iK_{iC} P_{zC} \psi_{iC} \right] f'(x) \\
&\quad + \lambda^{\mathbf{2}} \left[\sum -\left(\frac{\omega}{v_d}\right)^2 \varphi_{Dm} + \sum -\left(\frac{\omega}{v_d}\right)^2 \varphi^*_{Dm} \right] f'(x) \\
&\quad + \lambda^{\mathbf{2}} \left[\sum -\left(\frac{\omega}{v_d}\right)^2 \varphi_{Dm} + \sum -\left(\frac{\omega}{v_d}\right)^2 \varphi^*_{Dm} \right] f'(x) \\
&\quad + \lambda^{\mathbf{2}} \left[\sum ik_m P_{xm} \psi_{Sm} + \sum iK_{Sm} P_{zm} \psi_{Sm} \right] f'(x) \\
&\quad + \lambda^{\mathbf{2}} \left[\sum ik_m P^*_{xm} \psi^*_{Sm} + \sum iK^*_{Sm} P^*_{zm} \psi^*_{Sm} \right] f'(x) \\
&\quad + 2\mu^{\mathbf{2}} \left[-(k_{iB})^2 \varphi_{iB} + ik_{iC} P_{xC} \psi_{iC} - \sum k_m^2 \varphi_{Dm} - \sum k_m^2 \varphi^*_{Dm} \right] f'(x) \\
&\quad + 2\mu^{\mathbf{2}} \left[\sum ik_m P_{xm} \psi_{Sm} + \sum ik_m P^*_{xm} \psi^*_{Sm} \right] f'(x) \\
&\quad - \mu^{\mathbf{2}} \left[-2k_{iB} K_{iB} \varphi_{iB} + iK_{iC} P_{xC} \psi_{iC} + ik_{iC} P_{zC} \psi_{iC} \right] \\
&\quad - \mu^{\mathbf{2}} \left[\sum -2k_m K_{Dm} \varphi_{Dm} + \sum -2k_m K^*_{Dm} \varphi^*_{Dm} \right] \\
&\quad - \mu^{\mathbf{2}} \left[\sum iK_{Sm} P_{xm} \psi_{Sm} + \sum ik_m P_{zm} \psi_{Sm} \right] \\
&\quad - \mu^{\mathbf{2}} \left[\sum iK^*_{Sm} P^*_{xm} \psi^*_{Sm} + \sum ik_m P^*_{zm} \psi^*_{Sm} \right]
\end{aligned}
$$

Upon performing the integration and collecting terms, the result is the following expression.

$$\begin{aligned}
&\sum \rho^{\mathbf{1}} K_{Rm} I^{R}_{mn} R_m \\
&+\sum -\rho^{\mathbf{2}} K_{Dm} \left[1-2\left(\frac{v_s}{\omega}\right)^2 k_m k_n\right] I^{D}_{mn} D_m \\
&+\sum -\rho^{\mathbf{2}} K^*_{Dm} \left[1-2\left(\frac{v_s}{\omega}\right)^2 k_m k_n\right] I^{D*}_{mn} D^*_m \\
&+\sum i\rho^{\mathbf{2}} K_{Sm} \left[\left(\frac{v_d}{\omega}\right)^2 k_m - \left(\frac{v_s}{\omega}\right)^2 (k_m+k_n)\right] I^{S}_{mn} P_{xm} S_m \\
&+\sum i\rho^{\mathbf{2}} K^*_{Sm} \left[\left(\frac{v_d}{\omega}\right)^2 k_m - \left(\frac{v_s}{\omega}\right)^2 (k_m+k_n)\right] I^{S*}_{mn} P^*_{xm} S^*_m \\
&+\sum i\rho^{\mathbf{2}} \left[\left(\frac{v_s}{\omega}\right)^2 (k_m)^2 - \left(\frac{v_s}{\omega}\right)^2 k_m k_n + \left(\frac{v_d}{\omega}\right)^2 (K_{Sm})^2\right] I^{S}_{mn} P_{zm} S_m \\
&+\sum i\rho^{\mathbf{2}} \left[\left(\frac{v_s}{\omega}\right)^2 (k_m)^2 - \left(\frac{v_s}{\omega}\right)^2 k_m k_n + \left(\frac{v_d}{\omega}\right)^2 (K^*_{Sm})^2\right] I^{S*}_{mn} P^*_{zm} S^*_m \\
&\quad = -\rho^{\mathbf{1}} K_{iA} I^{A}_{inc} A_{inc} \\
&\qquad + \rho^{\mathbf{2}} K_{iB} \left[1-2\left(\frac{v_s}{\omega}\right)^2 k_{iB} k_n\right] I^{B}_{inc} B_{inc} \\
&\qquad - i\rho^{\mathbf{2}} K_{iC} \left[\left(\frac{v_d}{\omega}\right)^2 k_{iC} - \left(\frac{v_s}{\omega}\right)^2 (k_{iC}+k_n)\right] I^{C}_{inc} P_{xC} C_{inc} \\
&\qquad - i\rho^{\mathbf{2}} \left[\left(\frac{v_s}{\omega}\right)^2 (k_{iC})^2 - \left(\frac{v_s}{\omega}\right)^2 k_{iC} k_n + \left(\frac{v_d}{\omega}\right)^2 (K_{iC})^2\right] I^{C}_{inc} P_{zC} C_{inc}
\end{aligned} \tag{A.25}$$

A.3.2 Smooth (lower) surface boundary conditions

The diffraction problem has been defined such that the x-axis crosses the periodic profile of the upper surface halfway between its highest and lowest points. Therefore, the smooth lower surface of the plate is located at $z = d$ where d is the average plate thickness as shown in Figure A.1. The surface can be defined by $h_2(z) = z - d = 0$.

Therefore, the continuity of normal particle displacement between the solid plate (medium 2) and the lower fluid (medium 3) can be expressed as

$$\vec{u}^{\mathbf{2}} \cdot \nabla h_2 = \vec{u}^{\mathbf{3}} \cdot \nabla h_2 \qquad \text{where } \nabla h_2 = \begin{bmatrix} 0 \\ 0 \\ 1 \end{bmatrix}. \tag{A.26}$$

From Equation 2.15, the two boundary conditions representing continuity of stress along the surface are the following.

$$T^{\mathbf{2}}_{xz} = 0 \tag{A.27}$$

$$T^{\mathbf{2}}_{zz} = T^{\mathbf{3}}_{zz} \tag{A.28}$$

A.3.2.1 Derivation of Boundary Condition 4

Substituting the fields for media 2 and 3 into the fourth boundary condition given in Equation A.26 results in the following equation.

$$\begin{aligned} &iK_{iB}\varphi_{iB} + P_{zC}\psi_{iC} \\ &+\sum iK_{Dm}\varphi_{Dm} + \sum iK^{*}_{Dm}\varphi^{*}_{Dm} + \sum P_{zm}\psi_{Sm} + \sum P^{*}_{zm}\psi^{*}_{Sm} \\ &\quad = iK_{iE}\varphi_{iE} + \sum iK_{Tm}\varphi_{Tm} \end{aligned}$$

Upon multiplying each term by $e^{-ik_n x}$, integrating from 0 to Λ, and then collecting terms, the following expression is the result.

$$\begin{aligned} &\sum iK_{Dm}J^{D}_{mn}D_m + \sum iK^{*}_{Dm}J^{D*}_{mn}D^{*}_m \\ &+\sum J^{S}_{mn}P_{zm}S_m + \sum J^{S*}_{mn}P^{*}_{zm}S^{*}_m + \sum -iK_{Tm}J^{T}_{mn}T_m \\ &\quad = -iK_{iB}J^{B}_{inc}B_{inc} + -J^{C}_{inc}P_{zC}C_{inc} + iK_{iE}J^{E}_{inc}E_{inc} \end{aligned} \tag{A.29}$$

In this expression J^{σ}_{mn} is equal to $\int_0^{\Lambda} e^{i[(k_m-k_n)+K_{\sigma m}z]}\,dx$. However, instead of the z-coordinate being equal to the sawtooth periodic profile $f(x)$, it is equal to the z-coordinate of the lower surface, d. The final result from that integration is the following expression, where δ_{mn} is the Kronecker delta.

$$J^{\sigma}_{mn} = e^{iK_{\sigma m}d}\,\Lambda\,\delta_{mn} \tag{A.30}$$

For the incident waves, the integral is equal to

$$J^{\tau}_{inc} = \begin{cases} e^{iK_{i\tau}d}\Lambda & \text{for } n = 0 \\ 0 & \text{for all other n} \end{cases} \tag{A.31}$$

where τ can represent any one of the incident waves.

A.3.2.2 Derivation of Boundary Condition 5

Substituting the fields for media 2 and 3 into the fifth boundary condition given in Equation A.27 results in the following equation.

$$\begin{aligned}
&\boldsymbol{\mu^2}\left[-2k_{iB}K_{iB}\varphi_{iB} + iK_{iC}P_{xC}\psi_{iC} + ik_{iC}P_{zC}\psi_{iC}\right]\\
&+\boldsymbol{\mu^2}\left[\sum -2k_mK_{Dm}\varphi_{Dm} + \sum -2k_mK^*_{Dm}\varphi^*_{Dm}\right]\\
&+\boldsymbol{\mu^2}\left[\sum iK_{Sm}P_{xm}\psi_{Sm} + \sum ik_mP_{zm}\psi_{Sm}\right]\\
&+\boldsymbol{\mu^2}\left[+\sum iK^*_{Sm}P^*_{xm}\psi^*_{Sm} + \sum ik_mP^*_{zm}\psi^*_{Sm}\right]\\
&\qquad = 0
\end{aligned}$$

Upon integration and collection of terms, the boundary condition expression becomes

$$\begin{aligned}
&\sum -2k_mK_{Dm}J^D_{mn}D_m + \sum -2k_mK^*_{Dm}J^{D*}_{mn}D^*_m\\
&+\sum iK_{Sm}J^S_{mn}P_{xm}S_m + \sum ik_mJ^S_{mn}P_{zm}S_m\\
&+\sum iK^*_{Sm}J^{S*}_{mn}P^*_{xm}S^*_m + \sum ik_mJ^{S*}_{mn}P^*_{zm}S^*_m\\
&\qquad = 2k_{iB}K_{iB}J^B_{inc}B_{inc} - iK_{iC}J^C_{inc}P_{xC}C_{inc} - ik_{iC}J^C_{inc}P_{zC}C_{inc}.
\end{aligned} \tag{A.32}$$

A.3.2.3 Derivation of Boundary Condition 6

Substituting the fields for media 2 and 3 into the sixth boundary condition given in Equation A.27 results in the following equation.

$$
\begin{aligned}
&\lambda^{\mathbf{2}}\left[-\left(\frac{\omega}{v_d}\right)^2\varphi_{iB}+ik_{iC}P_{xC}\psi_{iC}+iK_{iC}P_{zC}\psi_{iC}\right]\\
&+\lambda^{\mathbf{2}}\left[\sum-\left(\frac{\omega}{v_d}\right)^2\varphi_{Dm}+\sum-\left(\frac{\omega}{v_d}\right)^2\varphi^*_{Dm}\right]\\
&+\lambda^{\mathbf{2}}\left[\sum ik_mP_{xm}\psi_{Sm}+\sum iK_{Sm}P_{zm}\psi_{Sm}\right]\\
&+\lambda^{\mathbf{2}}\left[\sum ik_mP^*_{xm}\psi^*_{Sm}+\sum iK^*_{Sm}P^*_{zm}\psi^*_{Sm}\right]\\
&+2\mu^{\mathbf{2}}\left[-(K_{iB})^2\varphi_{iB}+iK_{iC}P_{zC}\psi_{iC}-\sum(K_{Dm})^2\varphi_{Dm}-\sum(K^*_{Dm})^2\varphi^*_{Dm}\right]\\
&+2\mu^{\mathbf{2}}\left[\sum iK_{Sm}P_{zm}\psi_{Sm}+\sum iK^*_{Sm}P^*_{zm}\psi^*_{Sm}\right]\\
&\qquad=\lambda^{\mathbf{3}}\left[-\left(\frac{\omega}{v_t}\right)^2\varphi_{iE}+\sum-\left(\frac{\omega}{v_t}\right)^2\varphi_{Tm}\right]
\end{aligned}
$$

Upon integration and collection of terms, the boundary condition expression becomes

$$
\begin{aligned}
&\sum-\rho^{\mathbf{2}}\left[1-2\left(\frac{v_s}{\omega}\right)^2(k_m)^2\right]J^D_{mn}D_m\\
&+\sum-\rho^{\mathbf{2}}\left[1-2\left(\frac{v_s}{\omega}\right)^2(k_m)^2\right]J^{D*}_{mn}D^*_m\\
&+\sum i\rho^{\mathbf{2}}\left[\left(\frac{v_d}{\omega}\right)^2k_m-2\left(\frac{v_s}{\omega}\right)^2k_m\right]J^S_{mn}P_{xm}S_m\\
&+\sum i\rho^{\mathbf{2}}\left[\left(\frac{v_d}{\omega}\right)^2k_m-2\left(\frac{v_s}{\omega}\right)^2k_m\right]J^{S*}_{mn}P^*_{xm}S^*_m\\
&+\sum i\rho^{\mathbf{2}}\left(\frac{v_d}{\omega}\right)^2K_{Sm}J^S_{mn}P_{zm}S_m+\sum i\rho^{\mathbf{2}}\left(\frac{v_d}{\omega}\right)^2K^*_{Sm}J^{S*}_{mn}P^*_{zm}S^*_m\\
&+\sum\rho^{\mathbf{3}}J^T_{mn}T_m\\
&\qquad=\rho^{\mathbf{2}}\left[1-2\left(\frac{v_s}{\omega}\right)^2(k_{iB})^2\right]J^B_{inc}B_{inc}-\rho^{\mathbf{3}}J^E_{inc}E_{inc}\\
&\qquad\quad-i\rho^{\mathbf{2}}\left[\left(\frac{v_d}{\omega}\right)^2k_{iC}-2\left(\frac{v_s}{\omega}\right)^2k_{iC}\right]J^C_{inc}P_{xC}C_{inc}\\
&\qquad\quad-i\rho^{\mathbf{2}}\left(\frac{v_d}{\omega}\right)^2K_{iC}J^C_{inc}P_{zC}C_{inc}.
\end{aligned}
\tag{A.33}
$$

A.3.3 Conditions of shear waves

The boundary condition derivations that have just been presented considered the case of shear waves of arbitrary polarization by accounting for the shear wave fields directly through displacement vectors. Instead, if only a vertical shear polarization is to be examined, the shear waves in the initial field expressions can be represented by $\nabla \times \vec{\psi}$ where $\vec{\psi}$ is a vector function equal to $\psi(x, z)\vec{e_y}$. This reduces the number of unknown shear wave series coefficients by half and a total of six boundary conditions (for six diffracted series R_m, D_m, D_m^*, S_m, S_m^*, and T_m) would be sufficient to solve the system.

However, the approach employed here has created a total of eight diffracted series that must be accomodated by the system. The particle motion that would have been accounted for through S_m and S_m^* as mentioned above is instead represented by $P_{xm}S_m$, $P_{xm}^*S_m^*$, $P_{zm}S_m$, and $P_{zm}^*S_m^*$. Therefore, two additional conditions are necessary to solve the system. These two additional conditions do not come from the continuity of normal particle displacement or continuity of stress conditions. They consist of requiring that the propagation directions of the shear waves be perpendicular to the particle displacement vectors. They can be expressed in the following manner.

$$\begin{aligned} k_m P_{xm} S_m + K_{Sm} P_{zm} S_m &= 0 \\ k_m P_{xm}^* S_m^* + K_{Sm}^* P_{zm}^* S_m^* &= 0 \end{aligned} \tag{A.34}$$

(More information on the approach that accomodates vertical shear waves only can be found in Refs. [51, 54, 55, 75, 81]. In general, it is not necessary to write the simulation to accomodate shear waves of arbitrary polarization, i.e. horizontal as well as vertical, unless it is specifically desired to examine horizontally polarized waves. This is due to the fact that the propagation of horizontally polarized waves is independent of the vertically polarized waves [30].)

APPENDIX B

BOUNDARY CONDITIONS FOR A FLUID-LOADED PLATE WITH TWO SIDES PERIODIC

This appendix contains the derviation of the boundary condition expressions for the case of a fluid-loaded plate where both sides are periodic. A diagram of the possible incident waves along with the resulting diffracted fields is shown in Figure B.1. This situation is identical to that of Appendix A except that the lower surface of the plate is now periodic. The material properties (densities, Lamé constants, and bulk sound speeds) use identical notation to that of Appendix A.

The first three boundary conditions are identical to those shown in Appendix A. However, the three boundary conditions associated with the (formerly) smooth side of the plate must now be satisfied along a periodic profile. There are two possibilities that will be considered here. The profile that separates the solid plate (medium 2) from the lower fluid (medium 3) will either be "symmetric" to that of the upper profile so that it is a mirror image of the upper profile across $z = \frac{d}{2}$, as shown in Figure B.1, or it will be "antisymmetric" so that it appears just like the upper profile, only shifted by a distance of $z = d$, where d is the average plate thickness. For the symmetric case, the lower boundary is defined by

$$g_s(x) = \begin{cases} \dfrac{h_g}{2} - \dfrac{2h_g}{\Lambda}x + d & \text{for } 0 \leq x \leq \dfrac{\Lambda}{2} \\ \dfrac{-3h_g}{2} + \dfrac{2h_g}{\Lambda}x + d & \text{for } \dfrac{\Lambda}{2} \leq x \leq \Lambda \end{cases} \tag{B.1}$$

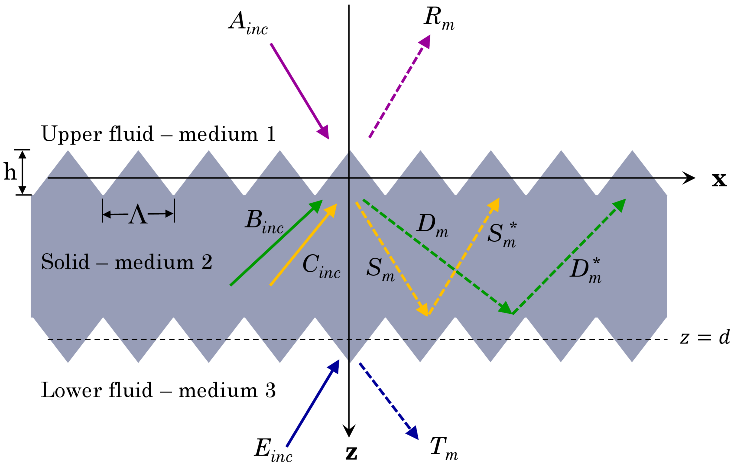

Figure B.1: Diagram of diffracted fields for a fluid-loaded plate having both sides periodically corrugated. Symmetric profile case shown. Diffracted wave series shown in dotted lines.

which is the mirror image of the upper profile across the line $z = \frac{d}{2}$. For the antisymmetric case, the lower boundary is defined by

$$g_a(x) = \begin{cases} \dfrac{2h_g}{\Lambda}x - \dfrac{h_g}{2} + d & \text{for } 0 \leq x \leq \dfrac{\Lambda}{2} \\ \dfrac{3h_g}{2} - \dfrac{2h_g}{\Lambda}x + d & \text{for } \dfrac{\Lambda}{2} \leq x \leq \Lambda. \end{cases} \tag{B.2}$$

The profiles of the upper and lower surfaces have been considered to have the same periodicity Λ, but it is not necessary to require the profile heights to be the same. Therefore, the peak-to-peak height h of the lower periodic profile $g(x)$ has been represented with h_g.

The boundary condition equations are in fact the same for the symmetric and antisymmetric cases. The difference will be seen in the value for the integral term analogous to I^{σ}_{mn} that was derived in Equation A.17 and appeared in the first three boundary conditions.

The boundary conditions for the lower surface can be derived in a manner identical to that employed for the upper surface. The displacement fields and stress components for this case are identical to those derived in Appendix A. The displacement fields and stress components for the solid plate (medium 2) and lower fluid (medium 3) can then be substituted into the boundary conditions for the lower periodic profile.

The fourth boundary condition (and first associated with the lower surface) comes from continuity of normal particle displacement between the solid plate (medium 2) and the lower fluid (medium 3) and can be expressed as

$$\vec{u}^{\mathbf{2}} \cdot \nabla h_2 = \vec{u}^{\mathbf{3}} \cdot \nabla h_2 \qquad \text{where } \nabla h_2 = \begin{bmatrix} g'(x) \\ 0 \\ -1 \end{bmatrix} \tag{B.3}$$

and where the function $g(x)$ may refer to either $g_s(x)$ or $g_a(x)$. From Equation 2.15, the two boundary conditions representing continuity of stress along the surface are

$$T^{\mathbf{2}}_{xx} g'(x) - T^{\mathbf{2}}_{xz} = T^{\mathbf{3}}_{xx} g'(x) \tag{B.4}$$

$$T^{\mathbf{2}}_{zx} g'(x) - T^{\mathbf{2}}_{zz} = -T^{\mathbf{3}}_{zz} \ . \tag{B.5}$$

After substituting the fields and stress components for media 2 and 3 into Equations B.3 - B.5, each expression was multiplied by $\int\limits_0^\Lambda e^{-ik_n x}$ and integrated over dx. The resulting equations have had their terms collected by diffracted wave series. The final form of the fourth boundary condition is shown below.

$$\begin{aligned}
&\sum -i\left[\left(\frac{\omega}{v_d}\right)^2 - k_m k_n\right] Q^D_{mn} D_m + \sum -i\left[\left(\frac{\omega}{v_d}\right)^2 - k_m k_n\right] Q^{D*}_{mn} D^*_m \\
&+ \sum -(k_m - k_n) Q^S_{mn} P_{xm} S_m + \sum -(k_m - k_n) Q^{S*}_{mn} P^*_{xm} S^*_m \\
&+ \sum -K_{Sm} Q^S_{mn} P_{zm} S_m + \sum -K^*_{Sm} Q^{S*}_{mn} P^*_{zm} S^*_m \\
&+ \sum i\left[\left(\frac{\omega}{v_t}\right)^2 - k_m k_n\right] Q^T_{mn} T_m \\
&\quad = i\left[\left(\frac{\omega}{v_d}\right)^2 - k_{iB} k_n\right] Q^B_{inc} B_{inc} \\
&\qquad + (k_{iC} - k_n) Q^C_{inc} P_{xC} C_{inc} + K_{iC} Q^C_{inc} P_{zC} C_{inc} \\
&\qquad - i\left[\left(\frac{\omega}{v_t}\right)^2 - k_{iE} k_n\right] Q^E_{inc} E_{inc}
\end{aligned} \tag{B.6}$$

In this equation, the variable Q^{σ}_{mn} is analogous to I^{σ}_{mn} in the first three boundary conditions. The only difference is that instead of the z-coordinate in the exponent being equal to $f(x)$, the profile of the upper periodic surface, it is equal to $g(x)$, the periodic profile of the lower surface. For the symmetric case, Q^{σ}_{mn} is as follows.

$$\begin{aligned} Q^{\sigma}_{mn} &= \frac{1}{K_{\sigma m}} \int_0^{\Lambda} e^{i[(k_m - k_n)x + K_{\sigma m} g_s(x)]}\, dx \\ &= e^{iK_{\sigma m} d} i h_g \Lambda \left(-e^{iK_{\sigma m}\frac{h_g}{2}} \right) \frac{\left[1 - (-1)^{m-n} e^{-ih_g K_{\sigma m}}\right]}{\left(h_g K_{\sigma m}\right)^2 - \left(\pi(m-n)\right)^2} \end{aligned} \tag{B.7}$$

For the antisymmetric case, because $g(x)$ is identical to $f(x)$ but shifted by $z = d$, Q^{σ}_{mn} is equal to I^{σ}_{mn} multiplied by a constant $e^{iK_{\sigma m} d}$.

$$\begin{aligned} Q^{\sigma}_{mn} &= \frac{1}{K_{\sigma m}} \int_0^{\Lambda} e^{i[(k_m - k_n)x + K_{\sigma m} g_a(x)]}\, dx \\ &= \frac{1}{K_{\sigma m}} \int_0^{\Lambda} e^{i[(k_m - k_n)x + K_{\sigma m}(f(x)+d)]}\, dx \\ &= \frac{e^{iK_{\sigma m} d}}{K_{\sigma m}} \int_0^{\Lambda} e^{i[(k_m - k_n)x + K_{\sigma m} f(x)]}\, dx = e^{iK_{\sigma m} d} I^{\sigma}_{mn} \end{aligned}$$

Then,

$$Q^{\sigma}_{mn} = e^{iK_{\sigma m} d} i h_g \Lambda e^{-iK_{\sigma m}\frac{h_g}{2}} \frac{\left[1 - (-1)^{m-n} e^{ih_g K_{\sigma m}}\right]}{\left(h_g K_{\sigma m}\right)^2 - \left(\pi(m-n)\right)^2}. \tag{B.8}$$

Likewise, the variable Q^{τ}_{inc} where τ represents one of the incident waves is

$$Q^{\tau}_{inc} = e^{iK_{i\tau} d} i h_g \Lambda \left(-e^{iK_{i\tau}\frac{h_g}{2}} \right) \frac{\left[1 - (-1)^{-n} e^{-ih_g K_{i\tau}}\right]}{\left(h_g K_{i\tau}\right)^2 - (\pi n)^2} \tag{B.9}$$

for the symmetric case, and for the antisymmetric case it is

$$Q^{\tau}_{inc} = e^{iK_{i\tau} d} i h_g \Lambda e^{-iK_{i\tau}\frac{h_g}{2}} \frac{\left[1 - (-1)^{-n} e^{ih_g K_{i\tau}}\right]}{\left(h_g K_{i\tau}\right)^2 - (\pi n)^2}. \tag{B.10}$$

After substituting the fields for the solid plate and lower fluid into the boundary conditions given in Equations B.4 and B.5 and equating the Fourier coefficients, the final forms of the fifth and sixth boundary conditions are the following two expressions.

$$\begin{aligned}
&\sum \rho^{\mathbf{2}} \left[k_m - k_n + 2\left(\frac{v_s}{\omega}\right)^2 (K_{Dm})^2 k_n\right] Q_{mn}^{D} D_m \\
&+ \sum \rho^{\mathbf{2}} \left[k_m - k_n + 2\left(\frac{v_s}{\omega}\right)^2 (K_{Dm}^{*})^2 k_n\right] Q_{mn}^{D*} D_m^{*} \\
&+ \sum -i\rho^{\mathbf{2}} \left[\left(\frac{v_d}{\omega}\right)^2 k_m(k_m - k_n) + \left(\frac{v_s}{\omega}\right)^2 (K_{Sm})^2\right] Q_{mn}^{S} P_{xm} S_m \\
&+ \sum -i\rho^{\mathbf{2}} \left[\left(\frac{v_d}{\omega}\right)^2 k_m(k_m - k_n) + \left(\frac{v_s}{\omega}\right)^2 (K_{Sm}^{*})^2\right] Q_{mn}^{S*} P_{xm}^{*} S_m^{*} \\
&+ \sum -i\rho^{\mathbf{2}} K_{Sm} \left[\left(\frac{v_d}{\omega}\right)^2 (k_m - k_n) - \left(\frac{v_s}{\omega}\right)^2 (k_m - 2k_n)\right] Q_{mn}^{S} P_{zm} S_m \\
&+ \sum -i\rho^{\mathbf{2}} K_{Sm}^{*} \left[\left(\frac{v_d}{\omega}\right)^2 (k_m - k_n) - \left(\frac{v_s}{\omega}\right)^2 (k_m - 2k_n)\right] Q_{mn}^{S*} P_{zm}^{*} S_m^{*} \\
&+ \sum -\rho^{\mathbf{3}} (k_m - k_n) Q_{mn}^{T} T_m \\
&\qquad = -\rho^{\mathbf{2}} \left[k_{iB} - k_n + 2\left(\frac{v_s}{\omega}\right)^2 (K_{iB})^2 k_n\right] Q_{inc}^{B} B_{inc} \\
&\qquad\quad + i\rho^{\mathbf{2}} \left[\left(\frac{v_d}{\omega}\right)^2 k_{iC}(k_{iC} - k_n) + \left(\frac{v_s}{\omega}\right)^2 (K_{iC})^2\right] Q_{inc}^{C} P_{xC} C_{inc} \\
&\qquad\quad + i\rho^{\mathbf{2}} K_{iC} \left[\left(\frac{v_d}{\omega}\right)^2 (k_{iC} - k_n) - \left(\frac{v_s}{\omega}\right)^2 (k_{iC} - 2k_n)\right] Q_{inc}^{C} P_{zC} C_{inc} \\
&\qquad\quad + \rho^{\mathbf{3}} (k_{iE} - k_n) Q_{inc}^{E} E_{inc}
\end{aligned} \tag{B.11}$$

$$
\begin{aligned}
&\sum \rho^{\mathbf{2}} K_{Dm}\left[1-2\left(\frac{v_s}{\omega}\right)^2 k_m k_n\right] Q^{D}_{mn} D_m \\
&+\sum \rho^{\mathbf{2}} K^{*}_{Dm}\left[1-2\left(\frac{v_s}{\omega}\right)^2 k_m k_n\right] Q^{D*}_{mn} D^{*}_m \\
&+\sum -i\rho^{\mathbf{2}} K_{Sm}\left[\left(\frac{v_d}{\omega}\right)^2 k_m-\left(\frac{v_s}{\omega}\right)^2 (k_m+k_n)\right] Q^{S}_{mn} P_{xm} S_m \\
&+\sum -i\rho^{\mathbf{2}} K^{*}_{Sm}\left[\left(\frac{v_d}{\omega}\right)^2 k_m-\left(\frac{v_s}{\omega}\right)^2 (k_m+k_n)\right] Q^{S*}_{mn} P^{*}_{xm} S^{*}_m \\
&+\sum -i\rho^{\mathbf{2}} \left[\left(\frac{v_s}{\omega}\right)^2 k_m(k_m-k_n)+\left(\frac{v_d}{\omega}\right)^2 (K_{Sm})^2\right] Q^{S}_{mn} P_{zm} S_m \\
&+\sum -i\rho^{\mathbf{2}} \left[\left(\frac{v_s}{\omega}\right)^2 k_m(k_m-k_n)+\left(\frac{v_d}{\omega}\right)^2 (K^{*}_{Sm})^2\right] Q^{S*}_{mn} P^{*}_{zm} S^{*}_m \\
&+\rho^{\mathbf{3}}\sum -K_{Tm} Q^{T}_{mn} T_m \\
&\qquad = -\rho^{\mathbf{2}} K_{iB}\left[1-2\left(\frac{v_s}{\omega}\right)^2 k_{iB} k_n\right] Q^{B}_{inc} B_{inc} \\
&\qquad\quad + i\rho^{\mathbf{2}} K_{iC}\left[\left(\frac{v_d}{\omega}\right)^2 k_{iC}-\left(\frac{v_s}{\omega}\right)^2 (k_{iC}+k_n)\right] Q^{C}_{inc} P_{xC} C_{inc} \\
&\qquad\quad + i\rho^{\mathbf{2}} \left[\left(\frac{v_s}{\omega}\right)^2 k_{iC}(k_{iC}-k_n)+\left(\frac{v_d}{\omega}\right)^2 (K_{iC})^2\right] Q^{C}_{inc} P_{zC} C_{inc} \\
&\qquad\quad + \rho^{\mathbf{3}} K_{iE} Q^{E}_{inc} E_{inc}
\end{aligned}
\tag{B.12}
$$

The final two boundary conditions that are required to solve the system are those that require the propagation direction of the shear waves to be perpendicular to the particle displacement. These were presented in Section A.3.3 of Appendix A.

APPENDIX C

BOUNDARY CONDITIONS FOR TWO SOLID MEDIA SEPARATED BY A PERIODIC INTERFACE

This appendix contains the derivation of the boundary condition expressions for the case of two solids that are separated by a periodic interface. A diagram of the possible incident waves along with the resulting diffracted fields is shown in Figure C.1. The two media can be characterized by their densities and Lamé constants. The bulk wave speeds are a function of these parameters. The variables used to designate these parameters are shown in Table C.1.

C.1 Field equations

The displacement fields in the two media can be constructed by summing the diffracted fields with any of the incident waves that may be present.

The field in the upper solid (medium 1) can be expressed as the sum of the fields created by an incident longitudinal or shear wave and two series of diffracted waves. The subscripts iB and iC are used for the incident longitudinal and shear waves,

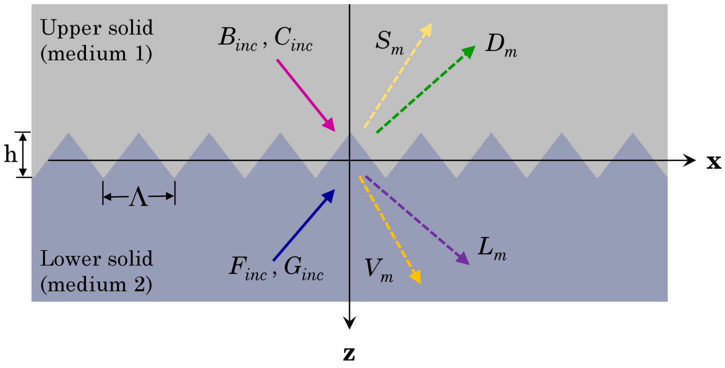

Figure C.1: Diagram of diffracted fields for two solid media separated by a periodic interface. Diffracted wave series shown in dotted lines.

Table C.1: Notation for media properties.

	Density	Lamé constants	Bulk wave speeds longitudinal	 shear
Upper solid (medium 1)	$\rho^{\mathbf{1}}$	$\lambda^{\mathbf{1}}$, $\mu^{\mathbf{1}}$	v_d	v_s
Lower solid (medium 2)	$\rho^{\mathbf{2}}$	$\lambda^{\mathbf{2}}$, $\mu^{\mathbf{2}}$	v_l	v_v

respectively. The subscripts D and S represent the diffracted longitudinal and shear wave series, respectively. The fields due to longitudinal waves can be expressed via scalar potentials. However, fields due to shear waves will be expressed directly in vector form. The polarization factors P_x, P_y, and P_z are used in the vectors to specify whether the polarization is vertical ($P_y = 0$) or horizontal ($P_x = P_z = 0$).

$$\vec{u}^{\mathbf{1}} = \nabla\varphi_{iB} + \vec{u}_{iC} + \nabla\varphi_D + \vec{u}_S$$

The potential functions for the longitudinal waves are given in the following expressions.

$$\begin{aligned}\varphi_{iB} &= B_{inc}e^{i(k_{iB}x+K_{iB}z)} \\ \varphi_D &= \sum\varphi_{Dm} = \sum D_m e^{i(k_m x+K_{Dm}z)}\end{aligned}$$

The vectors used to represent the shear waves directly are given by

$$\vec{u}_{iC} = \begin{bmatrix} P_{xC}\psi_{iC} \\ P_{yC}\psi_{iC} \\ P_{zC}\psi_{iC} \end{bmatrix} \qquad \text{and} \qquad \vec{u}_S = \sum \begin{bmatrix} P_{xm,S}\psi_{Sm} \\ P_{ym,S}\psi_{Sm} \\ P_{zm,S}\psi_{Sm} \end{bmatrix}$$

where

$$\begin{aligned}\psi_{iC} &= C_{inc}e^{i(k_{iC}x+K_{iC}z)} \\ \psi_{Sm} &= S_m e^{i(k_m x+K_{Sm}z)}.\end{aligned}$$

Then, the complete expression for the field in the upper solid is as follows.

$$\vec{u}^{\mathbf{1}} = \begin{bmatrix} ik_{iB}\varphi_{iB} \\ 0 \\ iK_{iB}\varphi_{iB} \end{bmatrix} + \begin{bmatrix} P_{xC}\psi_{iC} \\ P_{yC}\psi_{iC} \\ P_{zC}\psi_{iC} \end{bmatrix} + \sum \begin{bmatrix} ik_m\varphi_{Dm} \\ 0 \\ iK_{Dm}\varphi_{Dm} \end{bmatrix} + \sum \begin{bmatrix} P_{xm,S}\psi_{Sm} \\ P_{ym,S}\psi_{Sm} \\ P_{zm,S}\psi_{Sm} \end{bmatrix} \tag{C.1}$$

The field in the lower solid (medium 2) can be created in a manner identical to that of the upper solid. The field consists of incident longitudinal and shear waves (either one or none may be present) along with two diffracted series, one longitudinal and one shear.

$$\vec{u}^{\mathbf{2}} = \nabla\varphi_{iF} + \vec{u}_{iG} + \nabla\varphi_L + \vec{u}_V$$

The potential functions for the longitudinal waves are given in the following expressions.

$$\begin{aligned} \varphi_{iF} &= F_{inc}e^{i(k_{iF}x+K_{iF}z)} \\ \varphi_L &= \sum\varphi_{Lm} = \sum L_m e^{i(k_m x+K_{Lm}z)} \end{aligned}$$

The vectors used to represent the shear waves directly are given by

$$\vec{u}_{iG} = \begin{bmatrix} P_{xG}\psi_{iG} \\ P_{yG}\psi_{iG} \\ P_{zG}\psi_{iG} \end{bmatrix} \qquad \text{and} \qquad \vec{u}_V = \sum \begin{bmatrix} P_{xm,V}\psi_{Vm} \\ P_{ym,V}\psi_{Vm} \\ P_{zm,V}\psi_{Vm} \end{bmatrix}$$

where

$$\begin{aligned} \psi_{iF} &= F_{inc}e^{i(k_{iF}x+K_{iF}z)} \\ \psi_{Vm} &= V_m e^{i(k_m x+K_{Vm}z)}. \end{aligned}$$

Then, the complete expression for the field in the lower solid is as follows.

$$\vec{u}^{\mathbf{2}} = \begin{bmatrix} ik_{iF}\varphi_{iF} \\ 0 \\ iK_{iF}\varphi_{iF} \end{bmatrix} + \begin{bmatrix} P_{xG}\psi_{iG} \\ P_{yG}\psi_{iG} \\ P_{zG}\psi_{iG} \end{bmatrix} + \sum \begin{bmatrix} ik_m\varphi_{Lm} \\ 0 \\ iK_{Lm}\varphi_{Lm} \end{bmatrix} + \sum \begin{bmatrix} P_{xm,V}\psi_{Vm} \\ P_{ym,V}\psi_{Vm} \\ P_{zm,V}\psi_{Vm} \end{bmatrix} \tag{C.2}$$

C.2 Stress Components

The stress tensor components can now be calculated from the fields in the two solid media. These are shown in Equations C.3- C.8.

$$\begin{aligned}
T^{\mathbf{1}}_{xx} = {} & \lambda^{\mathbf{1}}\left(\frac{\partial u^{\mathbf{1}}_x}{\partial x}+\frac{\partial u^{\mathbf{1}}_y}{\partial y}+\frac{\partial u^{\mathbf{1}}_z}{\partial z}\right)+2\mu^{\mathbf{1}}\left(\frac{\partial u^{\mathbf{1}}_x}{\partial x}\right) \\
= {} & \lambda^{\mathbf{1}}\left[-\left(\frac{\omega}{v_d}\right)^2\varphi_{iB}+ik_{iC}P_{xC}\psi_{iC}+iK_{iC}P_{zC}\psi_{iC}\right] \\
& +\lambda^{\mathbf{1}}\left[\sum-\left(\frac{\omega}{v_d}\right)^2\varphi_{Dm}+\sum ik_mP_{xm,S}\psi_{Sm}+\sum iK_{Sm}P_{zm,S}\psi_{Sm}\right] \\
& +2\mu^{\mathbf{1}}\left[-(k_{iB})^2\varphi_{iB}+ik_{iC}P_{xC}\psi_{iC}-\sum k_m^2\varphi_{Dm}+\sum ik_mP_{xm,S}\psi_{Sm}\right]
\end{aligned} \tag{C.3}$$

$$\begin{aligned}
T^{\mathbf{1}}_{xz}=T^{\mathbf{1}}_{zx} = {} & \mu^{\mathbf{1}}\left(\frac{\partial u^{\mathbf{1}}_x}{\partial z}+\frac{\partial u^{\mathbf{1}}_z}{\partial x}\right) \\
= {} & \mu^{\mathbf{1}}\left[-2k_{iB}K_{iB}\varphi_{iB}+iK_{iC}P_{xC}\psi_{iC}+ik_{iC}P_{zC}\psi_{iC}\right] \\
& +\mu^{\mathbf{1}}\sum -2k_mK_{Dm}\varphi_{Dm} \\
& +\mu^{\mathbf{1}}\left[\sum iK_{Sm}P_{xm,S}\psi_{Sm}+\sum ik_mP_{zm,S}\psi_{Sm}\right]
\end{aligned} \tag{C.4}$$

$$\begin{aligned}
T^{\mathbf{1}}_{zz} = {} & \lambda^{\mathbf{1}}\left(\frac{\partial u^{\mathbf{1}}_x}{\partial x}+\frac{\partial u^{\mathbf{1}}_y}{\partial y}+\frac{\partial u^{\mathbf{1}}_z}{\partial z}\right)+2\mu^{\mathbf{1}}\left(\frac{\partial u^{\mathbf{1}}_z}{\partial z}\right) \\
= {} & \lambda^{\mathbf{1}}\left[-\left(\frac{\omega}{v_d}\right)^2\varphi_{iB}+ik_{iC}P_{xC}\psi_{iC}+iK_{iC}P_{zC}\psi_{iC}\right] \\
& +\lambda^{\mathbf{1}}\left[\sum-\left(\frac{\omega}{v_d}\right)^2\varphi_{Dm}+\sum ik_mP_{xm,S}\psi_{Sm}+\sum iK_{Sm}P_{zm,S}\psi_{Sm}\right] \\
& +2\mu^{\mathbf{1}}\left[-(K_{iB})^2\varphi_{iB}+iK_{iC}P_{zC}\psi_{iC}\right] \\
& +2\mu^{\mathbf{1}}\left[-\sum(K_{Dm})^2\varphi_{Dm}+\sum iK_{Sm}P_{zm,S}\psi_{Sm}\right]
\end{aligned} \tag{C.5}$$

$$\begin{aligned}
T^{\mathbf{2}}_{xx} = &\quad \lambda^{\mathbf{2}}\left(\frac{\partial u^{\mathbf{2}}_x}{\partial x}+\frac{\partial u^{\mathbf{2}}_y}{\partial y}+\frac{\partial u^{\mathbf{2}}_z}{\partial z}\right)+2\mu^{\mathbf{2}}\left(\frac{\partial u^{\mathbf{2}}_x}{\partial x}\right) \\
= &\quad \lambda^{\mathbf{2}}\left[-\left(\frac{\omega}{v_l}\right)^2\varphi_{iF}+ik_{iG}P_{xG}\psi_{iG}+iK_{iG}P_{zG}\psi_{iG}\right] \\
&+\lambda^{\mathbf{2}}\left[\sum-\left(\frac{\omega}{v_l}\right)^2\varphi_{Lm}+\sum ik_mP_{xm,V}\psi_{Vm}+\sum iK_{Vm}P_{zm,V}\psi_{Vm}\right] \\
&+2\mu^{\mathbf{2}}\left[-(k_{iF})^2\varphi_{iF}+ik_{iG}P_{xG}\psi_{iG}-\sum k_m^2\varphi_{Lm}+\sum ik_mP_{xm,V}\psi_{Vm}\right]
\end{aligned} \tag{C.6}$$

$$\begin{aligned}
T^{\mathbf{2}}_{xz} = T^{\mathbf{2}}_{zx} = &\quad \mu^{\mathbf{2}}\left(\frac{\partial u^{\mathbf{2}}_x}{\partial z}+\frac{\partial u^{\mathbf{2}}_z}{\partial x}\right) \\
= &\quad \mu^{\mathbf{2}}\left[-2k_{iF}K_{iF}\varphi_{iF}+iK_{iG}P_{xG}\psi_{iG}+ik_{iG}P_{zG}\psi_{iG}\right] \\
&+\mu^{\mathbf{2}}\left[\sum-2k_mK_{Lm}\varphi_{Lm}+\sum iK_{Vm}P_{xm,V}\psi_{Vm}+\sum ik_mP_{zm,V}\psi_{Vm}\right]
\end{aligned} \tag{C.7}$$

$$\begin{aligned}
T^{\mathbf{2}}_{zz} = &\quad \lambda^{\mathbf{2}}\left(\frac{\partial u^{\mathbf{2}}_x}{\partial x}+\frac{\partial u^{\mathbf{2}}_y}{\partial y}+\frac{\partial u^{\mathbf{2}}_z}{\partial z}\right)+2\mu^{\mathbf{2}}\left(\frac{\partial u^{\mathbf{2}}_z}{\partial z}\right) \\
= &\quad \lambda^{\mathbf{2}}\left[-\left(\frac{\omega}{v_l}\right)^2\varphi_{iF}+ik_{iG}P_{xG}\psi_{iG}+iK_{iG}P_{zG}\psi_{iG}\right] \\
&+\lambda^{\mathbf{2}}\left[\sum-\left(\frac{\omega}{v_l}\right)^2\varphi_{Lm}+\sum ik_mP_{xm,V}\psi_{Vm}+\sum iK_{Vm}P_{zm,V}\psi_{Vm}\right] \\
&+2\mu^{\mathbf{2}}\left[-(K_{iF})^2\varphi_{iF}+iK_{iG}P_{zG}\psi_{iG}-\sum(K_{Lm})^2\varphi_{Lm}+\sum iK_{Vm}P_{zm,V}\psi_{Vm}\right]
\end{aligned} \tag{C.8}$$

C.3 Boundary Conditions

The first two boundary conditions associated with the interface come from continuity of displacement across the interface. Since perfect contact between the two solids is assumed, the conditions can be written in the following manner.

$$u_x^{\mathbf{1}} = u_x^{\mathbf{2}} \tag{C.9}$$

$$u_z^{\mathbf{1}} = u_z^{\mathbf{2}} \tag{C.10}$$

It should be noted that it is also possible to equate the components of displacement normal to the periodic surface through the use of $\vec{u} \cdot \nabla h$ as has been the case for fluid-solid interfaces. The components of velocity parallel to the periodic surface could be stated by using $\vec{u} \cdot \nabla h_\perp$, where $\nabla h_\perp$ is a vector perpendicular to ∇h, that is to say, parallel to the surface. However, these two conditions are algebraically equivalent to the two expressions shown in Equations C.9 and C.10.

The third and fourth boundary conditions are obtained from continuity of stresses along the interface according to Equation 2.15.

$$T_{xx}^{\mathbf{1}} f'(x) - T_{xz}^{\mathbf{1}} = T_{xx}^{\mathbf{2}} f'(x) - T_{xz}^{\mathbf{2}} \tag{C.11}$$

$$T_{zx}^{\mathbf{1}} f'(x) - T_{zz}^{\mathbf{1}} = T_{zx}^{\mathbf{2}} f'(x) - T_{zz}^{\mathbf{2}} \tag{C.12}$$

The surface profile $f(x)$ has appeared, and it takes the form of the profile in Appendix A. Therefore, the variable I_{mn}^{σ} that will eventually appear in the boundary conditions that follow is equal to the expression given in Equation A.19.

C.3.1 Boundary Condition 1

Substituting the fields for the two media into Equation C.9 results in the following expression.

$$\begin{aligned} &ik_{iB}\varphi_{iB} + P_{xC}\psi_{iC} + \sum ik_m\varphi_{Dm} + \sum P_{xm,S}\psi_{Sm} \\ &= ik_{iF}\varphi_{iF} + P_{xG}\psi_{iG} + \sum ik_m\varphi_{Lm} + \sum P_{xm,V}\psi_{Vm} \end{aligned}$$

After multiplying the terms by $\int_0^\Lambda e^{-ik_n x}$, integrating over dx, and collecting terms, the final expression is the following.

$$\begin{aligned}
&\sum ik_m K_{Dm} I_{mn}^D D_m + \sum K_{Sm} I_{mn}^S P_{xm,S} S_m \\
&+ \sum -ik_m K_{Lm} I_{mn}^L L_m + \sum -K_{Vm} I_{mn}^V P_{xm,V} V_m \\
&= -ik_{iB} K_{iB} I_{inc}^B B_{inc} - K_{iC} I_{inc}^C P_{xC} C_{inc} \\
&\quad +ik_{iF} K_{iF} I_{inc}^F F_{inc} + K_{iG} I_{inc}^G P_{xG} G_{inc}
\end{aligned} \tag{C.13}$$

C.3.2 Boundary Condition 2

Substituing the fields for the two media into Equation C.10 results in the following expression.

$$\begin{aligned}
&iK_{iB}\varphi_{iB} + P_{zC}\psi_{iC} + \sum iK_{Dm}\varphi_{Dm} + \sum P_{zm,S}\psi_{Sm} \\
&= iK_{iF}\varphi_{iF} + P_{zG}\psi_{iG} + \sum iK_{Lm}\varphi_{Lm} + \sum P_{zm,V}\psi_{Vm}
\end{aligned} \tag{C.14}$$

The final expression after equating Fourier coefficients is shown below.

$$\begin{aligned}
&\sum i(K_{Dm})^2 I_{mn}^D D_m + \sum K_{Sm} I_{mn}^S P_{zm,S} S_m \\
&+ \sum -i(K_{Lm})^2 I_{mn}^L L_m + \sum -K_{Vm} I_{mn}^V P_{zm,V} V_m \\
&= -i(K_{iB})^2 I_{inc}^B B_{inc} - K_{iC} I_{inc}^C P_{zC} C_{inc} \\
&\quad +i(K_{iF})^2 I_{inc}^F F_{inc} + K_{iG} I_{inc}^G P_{zG} G_{inc}
\end{aligned} \tag{C.15}$$

C.3.3 Boundary Condition 3

Substituting the fields for the two media into Equation C.11 results in the following expression.

$$
\begin{aligned}
&\lambda^{\mathbf{1}}\left[-\left(\frac{\omega}{v_d}\right)^2\varphi_{iB}+ik_{iC}P_{xC}\psi_{iC}+iK_{iC}P_{zC}\psi_{iC}\right]f'(x) \\
&+\lambda^{\mathbf{1}}\left[\sum-\left(\frac{\omega}{v_d}\right)^2\varphi_{Dm}+\sum ik_mP_{xm,S}\psi_{Sm}+\sum iK_{Sm}P_{zm,S}\psi_{Sm}\right]f'(x) \\
&+2\mu^{\mathbf{1}}\left[-(k_{iB})^2\varphi_{iB}+ik_{iC}P_{xC}\psi_{iC}-\sum k_m^2\varphi_{Dm}+\sum ik_mP_{xm,S}\psi_{Sm}\right]f'(x) \\
&-\mu^{\mathbf{1}}\left[-2k_{iB}K_{iB}\varphi_{iB}+iK_{iC}P_{xC}\psi_{iC}+ik_{iC}P_{zC}\psi_{iC}\right] \\
&-\mu^{\mathbf{1}}\left[\sum-2k_mK_{Dm}\varphi_{Dm}+\sum iK_{Sm}P_{xm,S}\psi_{Sm}+\sum ik_mP_{zm,S}\psi_{Sm}\right] \\
&\quad=\lambda^{\mathbf{2}}\left[-\left(\frac{\omega}{v_l}\right)^2\varphi_{iF}+ik_{iG}P_{xG}\psi_{iG}+iK_{iG}P_{zG}\psi_{iG}\right]f'(x) \\
&\quad+\lambda^{\mathbf{2}}\left[\sum-\left(\frac{\omega}{v_l}\right)^2\varphi_{Lm}+\sum ik_mP_{xm,V}\psi_{Vm}+\sum iK_{Vm}P_{zm,V}\psi_{Vm}\right]f'(x) \\
&\quad+2\mu^{\mathbf{2}}\left[-(k_{iF})^2\varphi_{iF}+ik_{iG}P_{xG}\psi_{iG}-\sum k_m^2\varphi_{Lm}+\sum ik_mP_{xm,V}\psi_{Vm}\right]f'(x) \\
&\quad-\mu^{\mathbf{2}}\left[-2k_{iF}K_{iF}\varphi_{iF}+iK_{iG}P_{xG}\psi_{iG}+ik_{iG}P_{zG}\psi_{iG}\right] \\
&\quad-\mu^{\mathbf{2}}\left[\sum-2k_mK_{Lm}\varphi_{Lm}+\sum iK_{Vm}P_{xm,V}\psi_{Vm}+\sum ik_mP_{zm,V}\psi_{Vm}\right]
\end{aligned}
\tag{C.16}
$$

Upon equating Fourier coefficients and collecting terms, the final form of the third boundary condition becomes the equation shown below.

$$\begin{aligned}
&\sum \rho^{\mathbf{1}} \left[(k_m - k_n) + 2\left(\frac{v_s}{\omega}\right)^2 (K_{Dm})^2 k_n\right] I^D_{mn} D_m \\
&+ \sum -i\rho^{\mathbf{1}} \left[\left(\frac{v_d}{\omega}\right)^2 k_m(k_m - k_n) + \left(\frac{v_s}{\omega}\right)^2 (K_{Sm})^2\right] I^S_{mn} P_{xm,S} S_m \\
&+ \sum -i\rho^{\mathbf{1}} K_{Sm} \left[\left(\frac{v_d}{\omega}\right)^2 (k_m - k_n) - \left(\frac{v_s}{\omega}\right)^2 (k_m - 2k_n)\right] I^S_{mn} P_{zm,S} S_m \\
&+ \sum -\rho^{\mathbf{2}} \left[(k_m - k_n) + 2\left(\frac{v_v}{\omega}\right)^2 (K_{Lm})^2 k_n\right] I^L_{mn} L_m \\
&+ \sum i\rho^{\mathbf{2}} \left[\left(\frac{v_l}{\omega}\right)^2 k_m(k_m - k_n) + \left(\frac{v_v}{\omega}\right)^2 (K_{Vm})^2\right] I^V_{mn} P_{xm,V} V_m \\
&+ \sum i\rho^{\mathbf{2}} K_{vm} \left[\left(\frac{v_l}{\omega}\right)^2 (k_m - k_n) - \left(\frac{v_v}{\omega}\right)^2 (k_m - 2k_n)\right] I^V_{mn} P_{zm,V} V_m \\
&\quad = -\rho^{\mathbf{1}} \left[k_{iB} - k_n + 2\left(\frac{v_s}{\omega}\right)^2 (K_{iB})^2 k_n\right] I^B_{inc} B_{inc} \\
&\qquad + i\rho^{\mathbf{1}} \left[\left(\frac{v_d}{\omega}\right)^2 k_{iC}(k_{iC} - k_n) + \left(\frac{v_s}{\omega}\right)^2 (K_{iC})^2\right] I^C_{inc} P_{xC} C_{inc} \\
&\qquad + i\rho^{\mathbf{1}} K_{iC} \left[\left(\frac{v_d}{\omega}\right)^2 (k_{iC} - k_n) - \left(\frac{v_s}{\omega}\right)^2 (k_{iC} - 2k_n)\right] I^C_{inc} P_{zC} C_{inc} \\
&\qquad + \rho^{\mathbf{2}} \left[k_{iF} - k_n + 2\left(\frac{v_v}{\omega}\right)^2 (K_{iF})^2 k_n\right] I^F_{inc} F_{inc} \\
&\qquad - i\rho^{\mathbf{2}} \left[\left(\frac{v_l}{\omega}\right)^2 k_{iG}(k_{iG} - k_n) + \left(\frac{v_v}{\omega}\right)^2 (K_{iG})^2\right] I^G_{inc} P_{xG} G_{inc} \\
&\qquad - i\rho^{\mathbf{2}} K_{iG} \left[\left(\frac{v_l}{\omega}\right)^2 (k_{iG} - k_n) - \left(\frac{v_v}{\omega}\right)^2 (k_{iG} - 2k_n)\right] I^G_{inc} P_{zG} G_{inc}
\end{aligned} \tag{C.17}$$

C.3.4 Boundary Condition 4

Substituting the fields for the two media into Equation C.12 results in the following expression.

$$\begin{aligned}
&\mu^{\mathbf{1}}\left[-2k_{iB}K_{iB}\varphi_{iB}+iK_{iC}P_{xC}\psi_{iC}+ik_{iC}P_{zC}\psi_{iC}\right]f'(x)\\
&+\mu^{\mathbf{1}}\left[\sum -2k_{m}K_{Dm}\varphi_{Dm}+\sum iK_{Sm}P_{xm,S}\psi_{Sm}+\sum ik_{m}P_{zm,S}\psi_{Sm}\right]f'(x)\\
&-\lambda^{\mathbf{1}}\left[-\left(\frac{\omega}{v_{d}}\right)^{2}\varphi_{iB}+ik_{iC}P_{xC}\psi_{iC}+iK_{iC}P_{zC}\psi_{iC}\right]\\
&-\lambda^{\mathbf{1}}\left[\sum-\left(\frac{\omega}{v_{d}}\right)^{2}\varphi_{Dm}+\sum ik_{m}P_{xm,S}\psi_{Sm}+\sum iK_{Sm}P_{zm,S}\psi_{Sm}\right]\\
&-2\mu^{\mathbf{1}}\left[-(K_{iB})^{2}\varphi_{iB}+iK_{iC}P_{zC}\psi_{iC}-\sum(K_{Dm})^{2}\varphi_{Dm}+\sum iK_{Sm}P_{zm,S}\psi_{Sm}\right]\\
&\qquad=\mu^{\mathbf{2}}\left[-2k_{iF}K_{iF}\varphi_{iF}+iK_{iG}P_{xG}\psi_{iG}+ik_{iG}P_{zG}\psi_{iG}\right]f'(x)\\
&\qquad+\mu^{\mathbf{2}}\left[\sum -2k_{m}K_{Lm}\varphi_{Lm}+\sum iK_{Vm}P_{xm,V}\psi_{Vm}+\sum ik_{m}P_{zm,V}\psi_{Vm}\right]f'(x)\\
&\qquad-\lambda^{\mathbf{2}}\left[-\left(\frac{\omega}{v_{l}}\right)^{2}\varphi_{iF}+ik_{iG}P_{xG}\psi_{iG}+iK_{iG}P_{zG}\psi_{iG}\right]\\
&\qquad-\lambda^{\mathbf{2}}\left[\sum-\left(\frac{\omega}{v_{l}}\right)^{2}\varphi_{Lm}+\sum ik_{m}P_{xm,V}\psi_{Vm}+\sum iK_{Vm}P_{zm,V}\psi_{Vm}\right]\\
&\qquad-2\mu^{\mathbf{2}}\left[-(K_{iF})^{2}\varphi_{iF}+iK_{iG}P_{zG}\psi_{iG}-\sum(K_{Lm})^{2}\varphi_{Lm}+\sum iK_{Vm}P_{zm,V}\psi_{Vm}\right]
\end{aligned}\tag{C.18}$$

Upon equating Fourier coefficients and collecting terms, the final form of the fourth boundary condition equation is obtained.

$$\begin{aligned}
&\sum \rho^{\mathbf{1}} K_{Dm} \left[1 - 2\left(\frac{v_s}{\omega}\right)^2 k_m k_n\right] I^D_{mn} D_m \\
&+ \sum -i\rho^{\mathbf{1}} K_{Sm} \left[\left(\frac{v_d}{\omega}\right)^2 k_m - \left(\frac{v_s}{\omega}\right)^2 (k_m + k_n)\right] I^S_{mn} P_{xm,S} S_m \\
&+ \sum -i\rho^{\mathbf{1}} \left[\left(\frac{v_s}{\omega}\right)^2 k_m(k_m - k_n) + \left(\frac{v_d}{\omega}\right)^2 (K_{Sm})^2\right] I^S_{mn} P_{zm,S} S_m \\
&+ \sum -\rho^{\mathbf{2}} K_{Lm} \left[1 - 2\left(\frac{v_v}{\omega}\right)^2 k_m k_n\right] I^L_{mn} L_m \\
&+ \sum i\rho^{\mathbf{2}} K_{Vm} \left[\left(\frac{v_l}{\omega}\right)^2 k_m - \left(\frac{v_v}{\omega}\right)^2 (k_m + k_n)\right] I^V_{mn} P_{xm,V} V_m \\
&+ \sum i\rho^{\mathbf{2}} \left[\left(\frac{v_v}{\omega}\right)^2 k_m(k_m - k_n) + \left(\frac{v_l}{\omega}\right)^2 (K_{Vm})^2\right] I^V_{mn} P_{zm,V} V_m \\
&\quad = -\rho^{\mathbf{1}} K_{iB} \left[1 - 2\left(\frac{v_s}{\omega}\right)^2 k_{iB} k_n\right] I^B_{inc} B_{inc} \\
&\qquad + i\rho^{\mathbf{1}} K_{iC} \left[\left(\frac{v_d}{\omega}\right)^2 k_{iC} - \left(\frac{v_s}{\omega}\right)^2 (k_{iC} + k_n)\right] I^C_{inc} P_{xC} C_{inc} \\
&\qquad + i\rho^{\mathbf{1}} \left[\left(\frac{v_s}{\omega}\right)^2 k_{iC}(k_{iC} - k_n) + \left(\frac{v_d}{\omega}\right)^2 (K_{iC})^2\right] I^C_{inc} P_{zC} C_{inc} \\
&\qquad + \rho^{\mathbf{2}} K_{iF} \left[1 - 2\left(\frac{v_v}{\omega}\right)^2 k_{iF} k_n\right] I^F_{inc} F_{inc} \\
&\qquad - i\rho^{\mathbf{2}} K_{iG} \left[\left(\frac{v_l}{\omega}\right)^2 k_{iG} - \left(\frac{v_v}{\omega}\right)^2 (k_{iG} + k_n)\right] I^G_{inc} P_{xG} G_{inc} \\
&\qquad - i\rho^{\mathbf{2}} \left[\left(\frac{v_v}{\omega}\right)^2 k_{iG}(k_{iG} - k_n) + \left(\frac{v_l}{\omega}\right)^2 (K_{iG})^2\right] I^G_{inc} P_{zG} G_{inc}
\end{aligned} \tag{C.19}$$

C.3.5 Additional shear wave conditions

A total of four boundary conditions have just been derived for the case of two solids separated by a periodic interface. However, there are a total of six unknowns in the system: D_m, $P_{xm,S}S_m$, $P_{zm,S}S_m$, L_m, $P_{xm,V}V_m$, and $P_{zm,V}V_m$. Therefore, two additional conditions are necessary to solve the system, and these conditions are associated with the polarization of the shear waves. These conditions are shown below.

$$\begin{aligned}
k_m P_{xm,S} S_m + K_{Sm} P_{zm,S} S_m = 0 \\
k_m P_{xm,V} V_m + K_{Vm} P_{zm,V} V_m = 0
\end{aligned} \tag{C.20}$$

APPENDIX D

BOUNDARY CONDITIONS FOR A FLUID-LOADED PLATE CONSISTING OF TWO SOLID MEDIA SEPARATED BY A PERIODIC INTERFACE

This appendix contains the boundary conditions associated with a fluid-loaded plate consisting of two solid media that are separated by a periodic interface. This case is shown in Figure D.1. The variables used to indicate material properties are shown in Table D.1.

The possible incident waves and diffracted wave series are indicated by variables that are consistent with those of Appendices A, B, and C. Because the derivation of the boundary conditions is performed in a manner identical to that of the prior appendices, not all the details will be repeated here. Essentially, the displacement fields in each one of the media have been expressed as summations of the diffracted wave series present along with with the applicable incident wave(s). Then stress components are derived and substituted into the appropriate boundary conditions. Integration is performed in order to equate Fourier coefficients and terms are then

Table D.1: Notation for media properties.

	Density	Lamé constants	Bulk wave speeds	
			longitudinal	shear
Upper fluid (medium 1)	$\rho^{\mathbf{1}}$	$\lambda^{\mathbf{1}}$	v	
Upper solid (medium 2)	$\rho^{\mathbf{2}}$	$\lambda^{\mathbf{2}}$, $\mu^{\mathbf{2}}$	v_d	v_s
Lower solid (medium 3)	$\rho^{\mathbf{3}}$	$\lambda^{\mathbf{3}}$, $\mu^{\mathbf{3}}$	v_l	v_v
Lower fluid (medium 4)	$\rho^{\mathbf{4}}$	$\lambda^{\mathbf{4}}$	v_t	

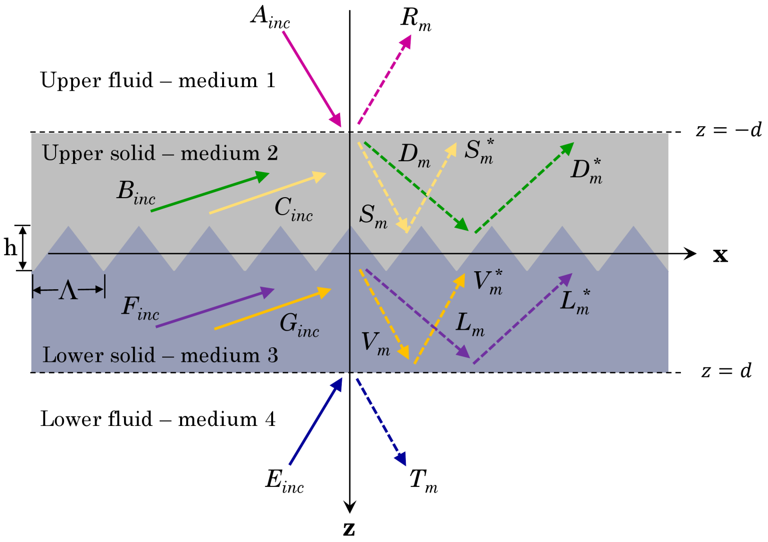

Figure D.1: Diagram of diffracted fields for a fluid-loaded plate made of two solid media separated by a periodic interface. Diffracted wave series shown in dotted lines.

collected with respect to the unknown coefficient series. The boundary conditions in their final forms are presented in the sections that follow.

D.1 Interface between upper fluid (medium 1) and upper solid (medium 2)

For the upper surface, there is one boundary condition associated with continuity of normal particle displacement. Two other boundary conditions come from continuity of normal stress and the vanishing of shear stress in the fluid. These three conditions are the following.

$$u_z^{\mathbf{1}} = u_z^{\mathbf{2}} \tag{D.1}$$

$$T_{zz}^{\mathbf{1}} = T_{zz}^{\mathbf{2}} \tag{D.2}$$

$$T_{xz}^{\mathbf{2}} = 0 \tag{D.3}$$

The final forms of these three boundary conditions are as follows.

$$\begin{aligned}
&\sum iK_{Rm}H^{R}_{mn}R_m \\
&+\sum -iK_{Dm}H^{D}_{mn}D_m+\sum -iK^{*}_{Dm}H^{D*}_{mn}D^{*}_m \\
&+\sum -H^{S}_{mn}P_{zm}S_m+\sum -H^{S*}_{mn}P^{*}_{zm}S^{*}_m \\
&\qquad = -iK_{iA}H^{A}_{inc}A_{inc}+iK_{iB}H^{B}_{inc}B_{inc}+H^{C}_{inc}P_{zC}C_{inc}
\end{aligned} \tag{D.4}$$

$$\begin{aligned}
&\sum -2k_mK_{Dm}H^{D}_{mn}D_m+\sum -2k_mK^{*}_{Dm}H^{D*}_{mn}D^{*}_m \\
&+\sum iK_{Sm}H^{S}_{mn}P_{xm}S_m+\sum ik_mH^{S}_{mn}P_{zm}S_m \\
&+\sum iK^{*}_{Sm}H^{S*}_{mn}P^{*}_{xm}S^{*}_m+\sum ik_mH^{S*}_{mn}P^{*}_{zm}S^{*}_m \\
&\qquad = 2k_{iB}K_{iB}H^{B}_{inc}B_{inc}-iK_{iC}H^{C}_{inc}P_{xC}C_{inc}-ik_{iC}H^{C}_{inc}P_{zC}C_{inc}
\end{aligned} \tag{D.5}$$

$$\begin{aligned}
&\sum -\rho^{\mathbf{1}}H^{R}_{mn}R_m \\
&+\sum \rho^{\mathbf{2}}\left[1-2\left(\frac{v_s}{\omega}\right)^2(k_m)^2\right]H^{D}_{mn}D_m \\
&+\sum \rho^{\mathbf{2}}\left[1-2\left(\frac{v_s}{\omega}\right)^2(k_m)^2\right]H^{D*}_{mn}D^{*}_m \\
&+\sum -i\rho^{\mathbf{2}}\left[\left(\frac{v_d}{\omega}\right)^2k_m-2\left(\frac{v_s}{\omega}\right)^2k_m\right]H^{S}_{mn}P_{xm}S_m \\
&+\sum -i\rho^{\mathbf{2}}\left[\left(\frac{v_d}{\omega}\right)^2k_m-2\left(\frac{v_s}{\omega}\right)^2k_m\right]H^{S*}_{mn}P^{*}_{xm}S^{*}_m \\
&+\sum -i\rho^{\mathbf{2}}\left(\frac{v_d}{\omega}\right)^2K_{sm}H^{s}_{mn}P_{zm}S_m \\
&+\sum -i\rho^{\mathbf{2}}\left(\frac{v_d}{\omega}\right)^2K^{*}_{sm}H^{s*}_{mn}P^{*}_{zm}S^{*}_m \\
&\qquad = \rho^{\mathbf{1}}H^{A}_{inc}A_{inc}-\rho^{\mathbf{2}}\left[1-2\left(\frac{v_s}{\omega}\right)^2(k_{iB})^2\right]H^{B}_{inc}B_{inc} \\
&\qquad\quad +i\rho^{\mathbf{2}}\left[\left(\frac{v_d}{\omega}\right)^2k_{iC}-2\left(\frac{v_s}{\omega}\right)^2k_{iC}\right]H^{C}_{inc}P_{xC}C_{inc} \\
&\qquad\quad +i\rho^{\mathbf{2}}\left(\frac{v_d}{\omega}\right)^2K_{iC}H^{C}_{inc}P_{zC}C_{inc}
\end{aligned} \tag{D.6}$$

In Equations D.4- D.6, the variables H^{σ}_{mn} and H^{τ}_{inc} appear. These are analogous to the J^{σ}_{mn} and J^{τ}_{inc} in Equations A.30 and A.31 of Appendix A. However, since the H variables are for the smooth surface of the plate located at $z=-d$, they are instead equal to

$$H^{\sigma}_{mn}=e^{-iK_{\sigma m}d}\,\Lambda\,\delta_{mn}\text{ and} \tag{D.7}$$

$$H^{\tau}_{inc} = \begin{cases} e^{-iK_{i\tau}d}\Lambda & \text{for } n = 0 \\ 0 & \text{for all other n.} \end{cases} \tag{D.8}$$

D.2 Interface between upper solid (medium 2) and lower solid (medium 3)

The interface between the two solid media requires four boundary conditions.

$$u_x^{\mathbf{2}} = u_x^{\mathbf{3}} \tag{D.9}$$

$$u_z^{\mathbf{2}} = u_z^{\mathbf{3}} \tag{D.10}$$

$$T_{xx}^{\mathbf{2}} f'(x) - T_{xz}^{\mathbf{2}} = T_{xx}^{\mathbf{3}} f'(x) - T_{xz}^{\mathbf{3}} \tag{D.11}$$

$$T_{zx}^{\mathbf{2}} f'(x) - T_{zz}^{\mathbf{2}} = T_{zx}^{\mathbf{3}} f'(x) - T_{zz}^{\mathbf{3}} \tag{D.12}$$

The final forms of these boundary conditions are shown in Equations D.13- D.16.

$$\begin{aligned} &\sum ik_m K_{Dm} I_{mn}^{D} D_m + \sum ik_m K_{Dm}^* I_{mn}^{D*} D_m^* \\ &+ \sum K_{Sm} I_{mn}^{S} P_{xm} S_m + \sum K_{Sm}^* I_{mn}^{S*} P_{xm}^* S_m^* \\ &+ \sum -ik_m K_{Lm} I_{mn}^{L} L_m + \sum -ik_m K_{Lm}^* I_{mn}^{L*} L_m^* \\ &+ \sum -K_{Vm} I_{mn}^{V} P_{xm,V} V_m + \sum -K_{Vm}^* I_{mn}^{V*} P_{xm,V}^* V_m^* \\ &\quad = -ik_{iB} K_{iB} I_{inc}^{B} B_{inc} - K_{iC} I_{inc}^{C} P_{xC} C_{inc} \\ &\qquad + ik_{iF} K_{iF} I_{inc}^{F} F_{inc} + K_{iG} I_{inc}^{G} P_{xG} G_{inc} \end{aligned} \tag{D.13}$$

$$\begin{aligned} &\sum i(K_{Dm})^2 I_{mn}^{D} D_m + \sum i(K_{Dm}^*)^2 I_{mn}^{D*} D_m^* \\ &+ \sum K_{Sm} I_{mn}^{S} P_{zm} S_m + \sum K_{Sm}^* I_{mn}^{S*} P_{zm}^* S_m^* \\ &+ \sum -i(K_{Lm})^2 I_{mn}^{L} L_m + \sum -i(K_{Lm}^*)^2 I_{mn}^{L*} L_m^* \\ &+ \sum -K_{Vm} I_{mn}^{V} P_{zm,V} V_m + \sum -K_{Vm}^* I_{mn}^{V*} P_{zm,V}^* V_m^* \\ &\quad = -i(K_{iB})^2 I_{inc}^{B} B_{inc} - K_{iC} I_{inc}^{C} P_{zC} C_{inc} \\ &\qquad + i(K_{iF})^2 I_{inc}^{F} F_{inc} + K_{iG} I_{inc}^{G} P_{zG} G_{inc} \end{aligned} \tag{D.14}$$

$$
\begin{aligned}
&\sum \rho^{\mathbf{2}} \left[(k_m - k_n) + 2\left(\frac{v_s}{\omega}\right)^2 (K_{Dm})^2 k_n\right] I^{D}_{mn} D_m \\
&+ \sum \rho^{\mathbf{2}} \left[(k_m - k_n) + 2\left(\frac{v_s}{\omega}\right)^2 (K^*_{Dm})^2 k_n\right] I^{D*}_{mn} D^*_m \\
&+ \sum -i\rho^{\mathbf{2}} \left[\left(\frac{v_d}{\omega}\right)^2 k_m(k_m - k_n) + \left(\frac{v_s}{\omega}\right)^2 (K_{Sm})^2\right] I^{S}_{mn} P_{xm} S_m \\
&+ \sum -i\rho^{\mathbf{2}} \left[\left(\frac{v_d}{\omega}\right)^2 k_m(k_m - k_n) + \left(\frac{v_s}{\omega}\right)^2 (K^*_{Sm})^2\right] I^{S*}_{mn} P^*_{xm} S^*_m \\
&+ \sum -i\rho^{\mathbf{2}} K_{sm} \left[\left(\frac{v_d}{\omega}\right)^2 (k_m - k_n) - \left(\frac{v_s}{\omega}\right)^2 (k_m - 2k_n)\right] I^{S}_{mn} P_{zm} S_m \\
&+ \sum -i\rho^{\mathbf{2}} K^*_{Sm} \left[\left(\frac{v_d}{\omega}\right)^2 (k_m - k_n) - \left(\frac{v_s}{\omega}\right)^2 (k_m - 2k_n)\right] I^{S*}_{mn} P^*_{zm} S^*_m \\
&+ \sum -\rho^{\mathbf{3}} \left[(k_m - k_n) + 2\left(\frac{v_v}{\omega}\right)^2 (K_{Lm})^2 k_n\right] I^{L}_{mn} L_m \\
&+ \sum -\rho^{\mathbf{3}} \left[(k_m - k_n) + 2\left(\frac{v_v}{\omega}\right)^2 (K^*_{Lm})^2 k_n\right] I^{L*}_{mn} L^*_m \\
&+ \sum i\rho^{\mathbf{3}} \left[\left(\frac{v_l}{\omega}\right)^2 k_m(k_m - k_n) + \left(\frac{v_v}{\omega}\right)^2 (K_{Vm})^2\right] I^{V}_{mn} P_{xm,V} V_m \\
&+ \sum i\rho^{\mathbf{3}} \left[\left(\frac{v_l}{\omega}\right)^2 k_m(k_m - k_n) + \left(\frac{v_v}{\omega}\right)^2 (K^*_{Vm})^2\right] I^{V*}_{mn} P^*_{xm,V} V^*_m \\
&+ \sum i\rho^{\mathbf{3}} K_{Vm} \left[\left(\frac{v_l}{\omega}\right)^2 (k_m - k_n) - \left(\frac{v_v}{\omega}\right)^2 (k_m - 2k_n)\right] I^{V}_{mn} P_{zm,V} V_m \\
&+ \sum i\rho^{\mathbf{3}} K^*_{Vm} \left[\left(\frac{v_l}{\omega}\right)^2 (k_m - k_n) - \left(\frac{v_v}{\omega}\right)^2 (k_m - 2k_n)\right] I^{V*}_{mn} P^*_{zm,V} V^*_m \\
&\qquad = -\rho^{\mathbf{2}} \left[k_{iB} - k_n + 2\left(\frac{v_s}{\omega}\right)^2 (K_{iB})^2 k_n\right] I^{B}_{inc} B_{inc} \\
&\qquad\quad + i\rho^{\mathbf{2}} \left[\left(\frac{v_d}{\omega}\right)^2 k_{iC}(k_{iC} - k_n) + \left(\frac{v_s}{\omega}\right)^2 (K_{iC})^2\right] I^{C}_{inc} P_{xC} C_{inc} \\
&\qquad\quad + i\rho^{\mathbf{2}} K_{iC} \left[\left(\frac{v_d}{\omega}\right)^2 (k_{iC} - k_n) - \left(\frac{v_s}{\omega}\right)^2 (k_{iC} - 2k_n)\right] I^{C}_{inc} P_{zC} C_{inc} \\
&\qquad\quad + \rho^{\mathbf{3}} \left[k_{iF} - k_n + 2\left(\frac{v_v}{\omega}\right)^2 (K_{iF})^2 k_n\right] I^{F}_{inc} F_{inc} \\
&\qquad\quad - i\rho^{\mathbf{3}} \left[\left(\frac{v_l}{\omega}\right)^2 k_{iG}(k_{iG} - k_n) + \left(\frac{v_v}{\omega}\right)^2 (K_{iG})^2\right] I^{G}_{inc} P_{xG} G_{inc} \\
&\qquad\quad - i\rho^{\mathbf{3}} K_{iG} \left[\left(\frac{v_l}{\omega}\right)^2 (k_{iG} - k_n) - \left(\frac{v_v}{\omega}\right)^2 (k_{iG} - 2k_n)\right] I^{G}_{inc} P_{zG} G_{inc}
\end{aligned}
\tag{D.15}
$$

$$
\begin{aligned}
&\sum \rho^{\mathbf{2}} K_{Dm} \left[1 - 2\left(\frac{v_s}{\omega}\right)^2 k_m k_n\right] I_{mn}^{D} D_m \\
&+ \sum \rho^{\mathbf{2}} K_{Dm}^{*} \left[1 - 2\left(\frac{v_s}{\omega}\right)^2 k_m k_n\right] I_{mn}^{D*} D_m^{*} \\
&+ \sum -i\rho^{\mathbf{2}} K_{Sm} \left[\left(\frac{v_d}{\omega}\right)^2 k_m - \left(\frac{v_s}{\omega}\right)^2 (k_m + k_n)\right] I_{mn}^{S} P_{xm} S_m \\
&+ \sum -i\rho^{\mathbf{2}} K_{Sm}^{*} \left[\left(\frac{v_d}{\omega}\right)^2 k_m - \left(\frac{v_s}{\omega}\right)^2 (k_m + k_n)\right] I_{mn}^{S*} P_{xm}^{*} S_m^{*} \\
&+ \sum -i\rho^{\mathbf{2}} \left[\left(\frac{v_s}{\omega}\right)^2 k_m(k_m - k_n) + \left(\frac{v_d}{\omega}\right)^2 (K_{Sm})^2\right] I_{mn}^{S} P_{zm} S_m \\
&+ \sum -i\rho^{\mathbf{2}} \left[\left(\frac{v_s}{\omega}\right)^2 k_m(k_m - k_n) + \left(\frac{v_d}{\omega}\right)^2 (K_{Sm}^{*})^2\right] I_{mn}^{S*} P_{zm}^{*} S_m^{*} \\
&+ \sum -\rho^{\mathbf{3}} K_{Lm} \left[1 - 2\left(\frac{v_v}{\omega}\right)^2 k_m k_n\right] I_{mn}^{L} L_m \\
&+ \sum -\rho^{\mathbf{3}} K_{Lm}^{*} \left[1 - 2\left(\frac{v_v}{\omega}\right)^2 k_m k_n\right] I_{mn}^{L*} L_m^{*} \\
&+ \sum i\rho^{\mathbf{3}} K_{Vm} \left[\left(\frac{v_l}{\omega}\right)^2 k_m - \left(\frac{v_v}{\omega}\right)^2 (k_m + k_n)\right] I_{mn}^{V} P_{xm,V} V_m \\
&+ \sum i\rho^{\mathbf{3}} K_{Vm}^{*} \left[\left(\frac{v_l}{\omega}\right)^2 k_m - \left(\frac{v_v}{\omega}\right)^2 (k_m + k_n)\right] I_{mn}^{V*} P_{xm,V}^{*} V_m^{*} \\
&+ \sum i\rho^{\mathbf{3}} \left[\left(\frac{v_v}{\omega}\right)^2 k_m(k_m - k_n) + \left(\frac{v_l}{\omega}\right)^2 (K_{Sm})^2\right] I_{mn}^{V} P_{zm,V} V_m \\
&+ \sum i\rho^{\mathbf{3}} \left[\left(\frac{v_v}{\omega}\right)^2 k_m(k_m - k_n) + \left(\frac{v_l}{\omega}\right)^2 (K_{Sm}^{*})^2\right] I_{mn}^{V*} P_{zm,V}^{*} V_m^{*} \\
&\quad = -\rho^{\mathbf{2}} K_{iB} \left[1 - 2\left(\frac{v_s}{\omega}\right)^2 k_{iB} k_n\right] I_{inc}^{B} B_{inc} \\
&\qquad + i\rho^{\mathbf{2}} K_{iC} \left[\left(\frac{v_d}{\omega}\right)^2 k_{iC} - \left(\frac{v_s}{\omega}\right)^2 (k_{iC} + k_n)\right] I_{inc}^{C} P_{xC} C_{inc} \\
&\qquad + i\rho^{\mathbf{2}} \left[\left(\frac{v_s}{\omega}\right)^2 k_{iC}(k_{iC} - k_n) + \left(\frac{v_d}{\omega}\right)^2 (K_{iC})^2\right] I_{inc}^{C} P_{zC} C_{inc} \\
&\qquad + \rho^{\mathbf{3}} K_{iF} \left[1 - 2\left(\frac{v_v}{\omega}\right)^2 k_{iF} k_n\right] I_{inc}^{F} F_{inc} \\
&\qquad - i\rho^{\mathbf{3}} K_{iG} \left[\left(\frac{v_l}{\omega}\right)^2 k_{iG} - \left(\frac{v_v}{\omega}\right)^2 (k_{iG} + k_n)\right] I_{inc}^{G} P_{xG} G_{inc} \\
&\qquad - i\rho^{\mathbf{3}} \left[\left(\frac{v_v}{\omega}\right)^2 k_{iG}(k_{iG} - k_n) + \left(\frac{v_l}{\omega}\right)^2 (K_{iG})^2\right] I_{inc}^{G} P_{zG} G_{inc}
\end{aligned}
\tag{D.16}
$$

In these equations the variables I^{σ}_{mn} and I^{τ}_{inc} appear. These are based on the periodic profile $f(x)$ that was shown in Appendix A, and the values of these variables are given by Equations A.19 and A.20, respectively.

D.3 Interface between lower solid (medium 3) and lower fluid (medium 4)

The interface between the lower solid and the lower fluid has three boundary conditions associated with it, just as there were three associated with the interface between the upper fluid and the upper solid.

$$u_z^{\mathbf{3}} = u_z^{\mathbf{4}} \tag{D.17}$$

$$T_{xz}^{\mathbf{3}} = 0 \tag{D.18}$$

$$T_{zz}^{\mathbf{3}} = T_{zz}^{\mathbf{4}} \tag{D.19}$$

After substituting in the field and stress tensor components, equating Fourier coefficients, and collecting terms, the final boundary condition expressions are Equations D.20- D.22. The variables J^{σ}_{mn} and J^{τ}_{inc} are identical to those in Equations A.30 and A.31 since the smooth surface that separates the lower solid from the lower fluid is located at $z = -d$.

$$\begin{aligned} &\sum iK_{Lm}J^{L}_{mn}L_m + \sum iK^{*}_{Lm}J^{L*}_{mn}L^{*}_m \\ &+ \sum J^{V}_{mn}P_{zm,V}V_m + \sum J^{V*}_{mn}P^{*}_{zm,V}V^{*}_m + \sum -iK_{Tm}J^{T}_{mn}T_m \\ &\qquad = -iK_{iF}J^{F}_{inc}F_{inc} - J^{G}_{inc}P_{zG}G_{inc} + iK_{iE}J^{E}_{inc}E_{inc} \end{aligned} \tag{D.20}$$

$$\begin{aligned} &\sum -2k_m K_{Lm}J^{L}_{mn}L_m + \sum -2k_m K^{*}_{Lm}J^{L*}_{mn}L^{*}_m \\ &+ \sum iK_{Vm}J^{V}_{mn}P_{xm,V}V_m + \sum ik_m J^{V}_{mn}P_{zm,V}V_m \\ &+ \sum iK^{*}_{Vm}J^{V*}_{mn}P^{*}_{xm,V}V^{*}_m + \sum ik_m J^{V*}_{mn}P^{*}_{zm,V}V^{*}_m \\ &\qquad = 2k_{iF}K_{iF}J^{F}_{inc}F_{inc} + -iK_{iG}J^{G}_{inc}P_{xG}G_{inc} - ik_{iG}J^{G}_{inc}P_{zG}G_{inc} \end{aligned} \tag{D.21}$$

$$\begin{aligned}
&\sum -\rho^{\mathbf{3}} \left[1 - 2\left(\frac{v_v}{\omega}\right)^2 (k_m)^2\right] J^L_{mn} L_m \\
&+ \sum -\rho^{\mathbf{3}} \left[1 - 2\left(\frac{v_v}{\omega}\right)^2 (k_m)^2\right] J^{l*}_{mn} L^*_m \\
&+ \sum i\rho^{\mathbf{3}} \left[\left(\frac{v_l}{\omega}\right)^2 k_m - 2\left(\frac{v_v}{\omega}\right)^2 k_m\right] J^V_{mn} P_{xm,V} V_m \\
&+ \sum i\rho^{\mathbf{3}} \left[\left(\frac{v_l}{\omega}\right)^2 k_m - 2\left(\frac{v_v}{\omega}\right)^2 k_m\right] J^{V*}_{mn} P^*_{xm,V} V^*_m \\
&+ \sum i\rho^{\mathbf{3}} \left(\frac{v_l}{\omega}\right)^2 K_{Vm} J^V_{mn} P_{zm,V} V_m \\
&+ \sum i\rho^{\mathbf{3}} \left(\frac{v_l}{\omega}\right)^2 K^*_{Vm} J^{V*}_{mn} P^*_{zm,V} V^*_m \\
&+ \sum \rho^{\mathbf{4}} J^T_{mn} T_m \\
&\quad = \rho^{\mathbf{3}} \left[1 - 2\left(\frac{v_v}{\omega}\right)^2 (k_{iF})^2\right] J^F_{inc} F_{inc} \\
&\qquad - i\rho^{\mathbf{3}} \left[\left(\frac{v_l}{\omega}\right)^2 k_{iG} - 2\left(\frac{v_v}{\omega}\right)^2 k_{iC}\right] J^G_{inc} P_{xG} G_{inc} \\
&\qquad - i\rho^{\mathbf{3}} \left(\frac{v_l}{\omega}\right)^2 K_{iG} U^G_{inc} P_{zG} G_{inc} - \rho^{\mathbf{4}} J^E_{inc} E_{inc}
\end{aligned} \tag{D.22}$$

A total of ten boundary conditions have been presented. However, there are a total of fourteen unknown coefficient series in the system. Therefore, four additional conditions are required. These are given by the shear wave conditions shown below.

$$\begin{aligned}
k_m P_{xm,S} S_m + K_{Sm} P_{zm,S} S_m &= 0 \\
k_m P^*_{xm,S} S^*_m + K^*_{Sm} P^*_{zm,S} S^*_m &= 0 \\
k_m P_{xm,V} V_m + K_{Vm} P_{zm,V} V_m &= 0 \\
k_m P^*_{xm,V} V^*_m + K^*_{Vm} P^*_{zm,V} V^*_m &= 0
\end{aligned} \tag{D.23}$$

APPENDIX E

BOUNDARY CONDITIONS FOR A FLUID-LOADED PLATE CONSISTING OF TWO SOLID MEDIA WHERE ALL INTERFACES ARE PERIODIC

This appendix contains the boundary conditions associated with a fluid-loaded plate that consists of two solid media where all the interfaces are periodic. This case is shown in Figure E.1. The variables used to indicate material properties are identical to those shown in Table D.1. Since the field equations and stress components for the media are identical to those of Appendix D, they will not be repeated here. Only the initial and final forms of the boundary conditions for the three interfaces will be presented here.

E.1 Interface between upper fluid (medium 1) and upper solid (medium 2)

These boundary conditions and the variables I^{σ}_{mn} and I^{τ}_{mn} are identical to those for the periodic interface in Appendix A. In terms of displacement and stress tensor components, the boundary conditions are the following three equations.

$$\vec{u}^{\mathbf{1}} \cdot \nabla h_1 = \vec{u}^{\mathbf{2}} \cdot \nabla h_1 \tag{E.1}$$

$$T^{\mathbf{1}}_{xx} f'(x) = T^{\mathbf{2}}_{xx} f'(x) - T^{\mathbf{2}}_{xz} \tag{E.2}$$

$$-T^{\mathbf{1}}_{zz} = T^{\mathbf{2}}_{zx} f'(x) - T^{\mathbf{2}}_{zz} \tag{E.3}$$

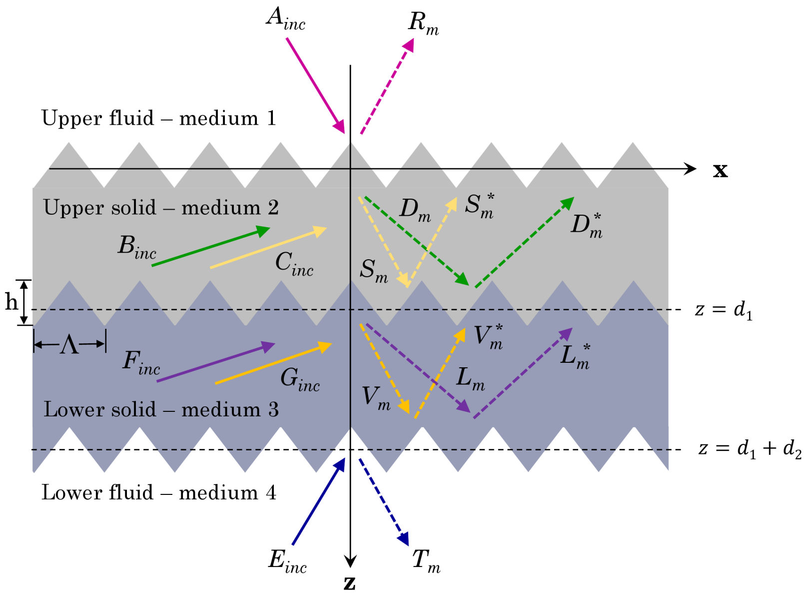

Figure E.1: Diffracted fields for a fluid-loaded plate made of two solid media where all three interfaces between the various media are periodic. Diffracted wave series shown in dotted lines.

The final forms in terms of unknown series coefficients are shown in Equations E.4-E.6.

$$\begin{aligned}
&\sum i\left[k_m k_n - \left(\frac{\omega}{v}\right)^2\right] I_{mn}^R R_m \\
&+ \sum i\left[\left(\frac{\omega}{v_d}\right)^2 - k_m k_n\right] I_{mn}^D D_m + \sum i\left[\left(\frac{\omega}{v_d}\right)^2 - k_m k_n\right] I_{mn}^{D*} D_m^* \\
&+ \sum (k_m - k_n)\, I_{mn}^S P_{xm,S} S_m + \sum K_{Sm} I_{mn}^S P_{zm,S} S_m \\
&+ \sum (k_m - k_n)\, I_{mn}^{S*} P_{xm,S}^* S_m^* + \sum K_{Sm}^* I_{mn}^{S*} P_{zm,S}^* S_m^* \\
&\qquad = i\left[\left(\frac{\omega}{v}\right)^2 - k_{iA} k_n\right] I_{inc}^A A_{inc} - i\left[\left(\frac{\omega}{v_d}\right)^2 - k_{iB} k_n\right] I_{inc}^B B_{inc} \\
&\qquad\quad - (k_{iC} - k_n) I_{inc}^C P_{xC} C_{inc} - K_{iC} I_{inc}^C P_{zC} C_{inc}
\end{aligned} \tag{E.4}$$

$$
\begin{aligned}
&\sum \rho^{\mathbf{1}}(k_m - k_n) I^R_{mn} R_m \\
&+ \sum -\rho^{\mathbf{2}} \left[k_m - k_n + 2\left(\frac{v_s}{\omega}\right)^2 (K_{Dm})^2 k_n \right] I^D_{mn} D_m \\
&+ \sum -\rho^{\mathbf{2}} \left[k_m - k_n + 2\left(\frac{v_s}{\omega}\right)^2 (K^*_{Dm})^2 k_n \right] I^{D*}_{mn} D^*_m \\
&+ \sum i\rho^{\mathbf{2}} \left[\left(\frac{v_d}{\omega}\right)^2 k_m(k_m - k_n) + \left(\frac{v_s}{\omega}\right)^2 (K_{Sm})^2 \right] I^S_{mn} P_{xm,S} S_m \\
&+ \sum i\rho^{\mathbf{2}} \left[\left(\frac{v_d}{\omega}\right)^2 k_m(k_m - k_n) + \left(\frac{v_s}{\omega}\right)^2 (K^*_{Sm})^2 \right] I^{S*}_{mn} P^*_{xm,S} S^*_m \\
&+ \sum i\rho^{\mathbf{2}} K_{Sm} \left[\left(\frac{v_d}{\omega}\right)^2 (k_m - k_n) - \left(\frac{v_s}{\omega}\right)^2 (k_m - 2k_n) \right] I^S_{mn} P_{zm,S} S_m \\
&+ \sum i\rho^{\mathbf{2}} K^*_{Sm} \left[\left(\frac{v_d}{\omega}\right)^2 (k_m - k_n) - \left(\frac{v_s}{\omega}\right)^2 (k_m - 2k_n) \right] I^{S*}_{mn} P^*_{zm} S^*_m \\
&\quad = \rho^{\mathbf{1}}(k_{iA} - k_n) I^A_{inc} A_{inc} \\
&\qquad + \rho^{\mathbf{2}} \left[k_{iB} - k_n + 2\left(\frac{v_s}{\omega}\right)^2 (K_{iB})^2 k_n \right] I^B_{inc} B_{inc} \\
&\qquad - i\rho^{\mathbf{2}} \left[\left(\frac{v_d}{\omega}\right)^2 k_{iC}(k_{iC} - k_n) + \left(\frac{v_s}{\omega}\right)^2 (K_{iC})^2 \right] I^C_{inc} P_{xC} C_{inc} \\
&\qquad - i\rho^{\mathbf{2}} K_{iC} \left[\left(\frac{v_d}{\omega}\right)^2 (k_{iC} - k_n) - \left(\frac{v_s}{\omega}\right)^2 (k_{iC} - 2k_n) \right] I^C_{inc} P_{zC} C_{inc}
\end{aligned}
\tag{E.5}
$$

$$
\begin{aligned}
&\sum \rho^{\mathbf{1}} K_{Rm} I_{mn}^{R} R_m \\
&+ \sum -\rho^{\mathbf{2}} K_{Dm} \left[1 - 2\left(\frac{v_s}{\omega}\right)^2 k_m k_n\right] I_{mn}^{D} D_m \\
&+ \sum -\rho^{\mathbf{2}} K_{Dm}^{*} \left[1 - 2\left(\frac{v_s}{\omega}\right)^2 k_m k_n\right] I_{mn}^{D*} D_m^{*} \\
&+ \sum i\rho^{\mathbf{2}} K_{Sm} \left[\left(\frac{v_d}{\omega}\right)^2 k_m - \left(\frac{v_s}{\omega}\right)^2 (k_m + k_n)\right] I_{mn}^{S} P_{xm,S} S_m \\
&+ \sum i\rho^{\mathbf{2}} K_{Sm}^{*} \left[\left(\frac{v_d}{\omega}\right)^2 k_m - \left(\frac{v_s}{\omega}\right)^2 (k_m + k_n)\right] I_{mn}^{S*} P_{xm,S}^{*} S_m^{*} \\
&+ \sum i\rho^{\mathbf{2}} \left[\left(\frac{v_s}{\omega}\right)^2 (k_m)^2 - \left(\frac{v_s}{\omega}\right)^2 k_m k_n + \left(\frac{v_d}{\omega}\right)^2 (K_{Sm})^2\right] I_{mn}^{S} P_{zm,S} S_m \\
&+ \sum i\rho^{\mathbf{2}} \left[\left(\frac{v_s}{\omega}\right)^2 (k_m)^2 - \left(\frac{v_s}{\omega}\right)^2 k_m k_n + \left(\frac{v_d}{\omega}\right)^2 (K_{Sm}^{*})^2\right] I_{mn}^{S*} P_{zm,S}^{*} S_m^{*} \\
&\qquad = -\rho^{\mathbf{1}} K_{iA} I_{inc}^{A} A_{inc} + \rho^{\mathbf{2}} K_{iB} \left[1 - 2\left(\frac{v_s}{\omega}\right)^2 k_{iB} k_n\right] I_{inc}^{B} B_{inc} \\
&\qquad\quad - i\rho^{\mathbf{2}} K_{iC} \left[\left(\frac{v_d}{\omega}\right)^2 k_{iC} - \left(\frac{v_s}{\omega}\right)^2 (k_{iC} + k_n)\right] I_{inc}^{C} P_{xC} C_{inc} \\
&\qquad\quad - i\rho^{\mathbf{2}} \left[\left(\frac{v_s}{\omega}\right)^2 (k_{iC})^2 - \left(\frac{v_s}{\omega}\right)^2 k_{iC} k_n + \left(\frac{v_d}{\omega}\right)^2 (K_{iC})^2\right] I_{inc}^{C} P_{zC} C_{inc}
\end{aligned}
\tag{E.6}
$$

E.2 Interface between upper solid (medium 2) and lower solid (medium 3)

These boundary conditions are essentially identical to those that exist between the two solid media in Appendix D. However, the periodic profile between the solids is defined by the $g(x)$ given in Appendix B, and it may be either symmetric or antisymmetric to that of the first interface. The variables Q_{mn}^{σ} and Q_{inc}^{τ} that appear in the final expressions (instead of the I_{mn}^{σ} and I_{inc}^{τ} in Appendix D) are given in Equations B.7 (symmetric Q_{mn}^{σ}), B.8 (antisymmetric Q_{mn}^{σ}), B.9 (symmetric Q_{inc}^{τ}), and B.10 (antisymmetric Q_{inc}^{τ}) . The four boundary conditions in terms of displacement and stress tensor components that must be satisfied at the interface are shown below.

$$u_x^{\mathbf{2}} = u_x^{\mathbf{3}} \tag{E.7}$$

$$u_z^{\mathbf{2}} = u_z^{\mathbf{3}} \tag{E.8}$$

$$T_{xx}^{\mathbf{2}} g'(x) - T_{xz}^{\mathbf{2}} = T_{xx}^{\mathbf{3}} g'(x) - T_{xz}^{\mathbf{3}} \tag{E.9}$$

$$T_{zx}^{\mathbf{2}} g'(x) - T_{zz}^{\mathbf{2}} = T_{zx}^{\mathbf{3}} g'(x) - T_{zz}^{\mathbf{3}} \tag{E.10}$$

The final forms of these expressions in terms of the unknown series coefficients are shown in Equations E.11- E.14.

$$\begin{aligned}
&\sum ik_m K_{Dm} Q_{mn}^{D} D_m + \sum ik_m K_{Dm}^{*} Q_{mn}^{D*} D_m^{*} \\
&+ \sum K_{Sm} Q_{mn}^{S} P_{xm,S} S_m + \sum K_{Sm}^{*} Q_{mn}^{S*} P_{xm,S}^{*} S_m^{*} \\
&+ \sum -ik_m K_{Lm} Q_{mn}^{L} L_m + \sum -ik_m K_{Lm}^{*} Q_{mn}^{L*} L_m^{*} \\
&+ \sum -K_{Vm} Q_{mn}^{V} P_{xm,V} V_m + \sum -K_{Vm}^{*} Q_{mn}^{V*} P_{xm,V}^{*} V_m^{*} \\
&\qquad = -ik_{iB} K_{iB} Q_{inc}^{B} B_{inc} - K_{iC} Q_{inc}^{C} P_{xC} C_{inc} \\
&\qquad\quad + ik_{iF} K_{iF} Q_{inc}^{F} F_{inc} + K_{iG} Q_{inc}^{G} P_{xG} G_{inc}
\end{aligned} \tag{E.11}$$

$$\begin{aligned}
&\sum i(K_{Dm})^2 Q_{mn}^{D} D_m + \sum i(K_{Dm}^{*})^2 Q_{mn}^{D*} D_m^{*} \\
&+ \sum K_{Sm} Q_{mn}^{S} P_{zm,S} S_m + \sum K_{Sm}^{*} Q_{mn}^{S*} P_{zm,S}^{*} S_m^{*} \\
&+ \sum -i(K_{Lm})^2 Q_{mn}^{L} L_m + \sum -i(K_{Lm}^{*})^2 Q_{mn}^{L*} L_m^{*} \\
&+ \sum -K_{Vm} Q_{mn}^{V} P_{zm,V} V_m + \sum -K_{Vm}^{*} Q_{mn}^{V*} P_{zm,V}^{*} V_m^{*} \\
&\qquad = -i(K_{iB})^2 Q_{inc}^{B} B_{inc} - K_{iC} Q_{inc}^{C} P_{zC} C_{inc} \\
&\qquad\quad + i(K_{iF})^2 Q_{inc}^{F} F_{inc} + K_{iG} Q_{inc}^{G} P_{zG} G_{inc}
\end{aligned} \tag{E.12}$$

$$
\begin{aligned}
&\sum \rho^{\mathbf{2}} \left[(k_m - k_n) + 2\left(\frac{v_s}{\omega}\right)^2 (K_{Dm})^2 k_n\right] Q_{mn}^{D} D_m \\
&+ \sum \rho^{\mathbf{2}} \left[(k_m - k_n) + 2\left(\frac{v_s}{\omega}\right)^2 (K_{Dm}^*)^2 k_n\right] Q_{mn}^{D*} D_m^* \\
&+ \sum -i\rho^{\mathbf{2}} \left[\left(\frac{v_d}{\omega}\right)^2 k_m(k_m - k_n) + \left(\frac{v_s}{\omega}\right)^2 (K_{Sm})^2\right] Q_{mn}^{S} P_{xm,S} S_m \\
&+ \sum -i\rho^{\mathbf{2}} \left[\left(\frac{v_d}{\omega}\right)^2 k_m(k_m - k_n) + \left(\frac{v_s}{\omega}\right)^2 (K_{Sm}^*)^2\right] Q_{mn}^{S*} P_{xm,S}^* S_m^* \\
&+ \sum -i\rho^{\mathbf{2}} K_{Sm} \left[\left(\frac{v_d}{\omega}\right)^2 (k_m - k_n) - \left(\frac{v_s}{\omega}\right)^2 (k_m - 2k_n)\right] Q_{mn}^{S} P_{zm,S} S_m \\
&+ \sum -i\rho^{\mathbf{2}} K_{Sm}^* \left[\left(\frac{v_d}{\omega}\right)^2 (k_m - k_n) - \left(\frac{v_s}{\omega}\right)^2 (k_m - 2k_n)\right] Q_{mn}^{S*} P_{zm,S}^* S_m^* \\
&+ \sum -\rho^{\mathbf{3}} \left[(k_m - k_n) + 2\left(\frac{v_v}{\omega}\right)^2 (K_{Lm})^2 k_n\right] Q_{mn}^{L} L_m \\
&+ \sum -\rho^{\mathbf{3}} \left[(k_m - k_n) + 2\left(\frac{v_v}{\omega}\right)^2 (K_{Lm}^*)^2 k_n\right] Q_{mn}^{L*} L_m^* \\
&+ \sum i\rho^{\mathbf{3}} \left[\left(\frac{v_l}{\omega}\right)^2 k_m(k_m - k_n) + \left(\frac{v_v}{\omega}\right)^2 (K_{Vm})^2\right] Q_{mn}^{V} P_{xm,V} V_m \\
&+ \sum i\rho^{\mathbf{3}} \left[\left(\frac{v_l}{\omega}\right)^2 k_m(k_m - k_n) + \left(\frac{v_v}{\omega}\right)^2 (K_{Vm}^*)^2\right] Q_{mn}^{V*} P_{xm,V}^* V_m^* \\
&+ \sum i\rho^{\mathbf{3}} K_{Vm} \left[\left(\frac{v_l}{\omega}\right)^2 (k_m - k_n) - \left(\frac{v_v}{\omega}\right)^2 (k_m - 2k_n)\right] Q_{mn}^{V} P_{zm,V} V_m \\
&+ \sum i\rho^{\mathbf{3}} K_{Vm}^* \left[\left(\frac{v_l}{\omega}\right)^2 (k_m - k_n) - \left(\frac{v_v}{\omega}\right)^2 (k_m - 2k_n)\right] Q_{mn}^{V*} P_{zm,V}^* V_m^* \\
&\quad = -\rho^{\mathbf{2}} \left[k_{iB} - k_n + 2\left(\frac{v_s}{\omega}\right)^2 (K_{iB})^2 k_n\right] Q_{inc}^{B} B_{inc} \\
&\qquad + i\rho^{\mathbf{2}} \left[\left(\frac{v_d}{\omega}\right)^2 k_{iC}(k_{iC} - k_n) + \left(\frac{v_s}{\omega}\right)^2 (K_{iC})^2\right] Q_{inc}^{C} P_{xC} C_{inc} \\
&\qquad + i\rho^{\mathbf{2}} K_{iC} \left[\left(\frac{v_d}{\omega}\right)^2 (k_{iC} - k_n) - \left(\frac{v_s}{\omega}\right)^2 (k_{iC} - 2k_n)\right] Q_{inc}^{C} P_{zC} C_{inc} \\
&\qquad + \rho^{\mathbf{3}} \left[k_{iF} - k_n + 2\left(\frac{v_v}{\omega}\right)^2 (K_{iF})^2 k_n\right] Q_{inc}^{F} F_{inc} \\
&\qquad - i\rho^{\mathbf{3}} \left[\left(\frac{v_l}{\omega}\right)^2 k_{iG}(k_{iG} - k_n) + \left(\frac{v_v}{\omega}\right)^2 (K_{iG})^2\right] Q_{inc}^{G} P_{xG} G_{inc} \\
&\qquad - i\rho^{\mathbf{3}} K_{iG} \left[\left(\frac{v_l}{\omega}\right)^2 (k_{iG} - k_n) - \left(\frac{v_v}{\omega}\right)^2 (k_{iG} - 2k_n)\right] Q_{inc}^{G} P_{zG} G_{inc}
\end{aligned}
\tag{E.13}
$$

$$
\begin{aligned}
&\sum \rho^{\mathbf{2}} K_{Dm} \left[1 - 2\left(\frac{v_s}{\omega}\right)^2 k_m k_n\right] Q^{D}_{mn} D_m \\
&+ \sum \rho^{\mathbf{2}} K^*_{Dm} \left[1 - 2\left(\frac{v_s}{\omega}\right)^2 k_m k_n\right] Q^{D*}_{mn} D^*_m \\
&+ \sum -i\rho^{\mathbf{2}} K_{Sm} \left[\left(\frac{v_d}{\omega}\right)^2 k_m - \left(\frac{v_s}{\omega}\right)^2 (k_m + k_n)\right] Q^{S}_{mn} P_{xm,S} S_m \\
&+ \sum -i\rho^{\mathbf{2}} K^*_{Sm} \left[\left(\frac{v_d}{\omega}\right)^2 k_m - \left(\frac{v_s}{\omega}\right)^2 (k_m + k_n)\right] Q^{S*}_{mn} P^*_{xm,S} S^*_m \\
&+ \sum -i\rho^{\mathbf{2}} \left[\left(\frac{v_s}{\omega}\right)^2 k_m(k_m - k_n) + \left(\frac{v_d}{\omega}\right)^2 (K_{Sm})^2\right] Q^{S}_{mn} P_{zm,S} S_m \\
&+ \sum -i\rho^{\mathbf{2}} \left[\left(\frac{v_s}{\omega}\right)^2 k_m(k_m - k_n) + \left(\frac{v_d}{\omega}\right)^2 (K^*_{Sm})^2\right] Q^{S*}_{mn} P^*_{zm,S} S^*_m \\
&+ \sum -\rho^{\mathbf{3}} K_{Lm} \left[1 - 2\left(\frac{v_v}{\omega}\right)^2 k_m k_n\right] Q^{L}_{mn} L_m \\
&+ \sum -\rho^{\mathbf{3}} K^*_{Lm} \left[1 - 2\left(\frac{v_v}{\omega}\right)^2 k_m k_n\right] Q^{L*}_{mn} L^*_m \\
&+ \sum i\rho^{\mathbf{3}} K_{Vm} \left[\left(\frac{v_l}{\omega}\right)^2 k_m - \left(\frac{v_v}{\omega}\right)^2 (k_m + k_n)\right] Q^{V}_{mn} P_{xm,V} V_m \\
&+ \sum i\rho^{\mathbf{3}} K^*_{Vm} \left[\left(\frac{v_l}{\omega}\right)^2 k_m - \left(\frac{v_v}{\omega}\right)^2 (k_m + k_n)\right] Q^{V*}_{mn} P^*_{xm,V} V^*_m \\
&+ \sum i\rho^{\mathbf{3}} \left[\left(\frac{v_v}{\omega}\right)^2 k_m(k_m - k_n) + \left(\frac{v_l}{\omega}\right)^2 (K_{Sm})^2\right] Q^{V}_{mn} P_{zm,V} V_m \\
&+ \sum i\rho^{\mathbf{3}} \left[\left(\frac{v_v}{\omega}\right)^2 k_m(k_m - k_n) + \left(\frac{v_l}{\omega}\right)^2 (K^*_{Sm})^2\right] Q^{V*}_{mn} P^*_{zm,V} V^*_m \\
&\qquad = -\rho^{\mathbf{2}} K_{iB} \left[1 - 2\left(\frac{v_s}{\omega}\right)^2 k_{iB} k_n\right] Q^{B}_{inc} B_{inc} \\
&\qquad\quad + i\rho^{\mathbf{2}} K_{iC} \left[\left(\frac{v_d}{\omega}\right)^2 k_{iC} - \left(\frac{v_s}{\omega}\right)^2 (k_{iC} + k_n)\right] Q^{C}_{inc} P_{xC} C_{inc} \\
&\qquad\quad + i\rho^{\mathbf{2}} \left[\left(\frac{v_s}{\omega}\right)^2 k_{iC}(k_{iC} - k_n) + \left(\frac{v_d}{\omega}\right)^2 (K_{iC})^2\right] Q^{C}_{inc} P_{zC} C_{inc} \\
&\qquad\quad + \rho^{\mathbf{3}} K_{iF} \left[1 - 2\left(\frac{v_v}{\omega}\right)^2 k_{iF} k_n\right] Q^{F}_{inc} F_{inc} \\
&\qquad\quad - i\rho^{\mathbf{3}} K_{iG} \left[\left(\frac{v_l}{\omega}\right)^2 k_{iG} - \left(\frac{v_v}{\omega}\right)^2 (k_{iG} + k_n)\right] Q^{G}_{inc} P_{xG} G_{inc} \\
&\qquad\quad - i\rho^{\mathbf{3}} \left[\left(\frac{v_v}{\omega}\right)^2 k_{iG}(k_{iG} - k_n) + \left(\frac{v_l}{\omega}\right)^2 (K_{iG})^2\right] Q^{G}_{inc} P_{zG} G_{inc}
\end{aligned}
\tag{E.14}
$$

E.3 Interface between lower solid (medium 3) and lower fluid (medium 4)

The boundary conditions between the lower solid and the lower fluid take a similar form to those for the second interface of the plate with two periodic sides (Appendix B), but with the diffracted series L_m and V_m instead of D_m and S_m and with notation for the incident waves consistent with Figure E.1. In addition, the integral terms for this interface are represented by the variables W^{σ}_{mn} and W^{τ}_{inc} (analogous to their respective Q terms with the same considerations regarding the symmetry of the profile).

The periodic profile associated with the interface between the lower solid and lower fluid will be referred to as $w(x)$, and it can be symmetric or antisymmetric with respect to uppermost profile, $f(x)$. The interface can be defined by the function $h_3(x,z) = w(x) - z = 0$. The W integral terms will be identical to the Q integral terms but multiplied by a constant $e^{iK_{\sigma m}(d_1+d_2)}$ to account for the profile's average z-coordinate being $d_1 + d_2$.

The boundary conditions that must be satisfied at the interface in terms of displacements and stress tensor components are shown in the following three equations.

$$\vec{u}^{\mathbf{3}} \cdot \nabla h_3 = \vec{u}^{\mathbf{4}} \cdot \nabla h_3 \tag{E.15}$$

$$T^{\mathbf{3}}_{xx} w'(x) - T^{\mathbf{3}}_{xz} = T^{\mathbf{4}}_{xx} w'(x) \tag{E.16}$$

$$T^{\mathbf{3}}_{zx} w'(x) - T^{\mathbf{3}}_{zz} = -T^{\mathbf{4}}_{zz} \tag{E.17}$$

Upon substituting field quantities and stress components, equating Fourier coefficients, and collecting terms, the final boundary condition expressions become Equations E.18-E.20.

$$\begin{aligned}
&\sum -i\left[\left(\frac{\omega}{v_l}\right)^2 - k_m k_n\right] W^{L}_{mn} L_m + \sum -i\left[\left(\frac{\omega}{v_l}\right)^2 - k_m k_n\right] W^{L*}_{mn} L^*_m \\
&+ \sum -(k_m - k_n) W^{V}_{mn} P_{xm,V} V_m + \sum -(k_m - k_n) W^{V*}_{mn} P^*_{xm,V} V^*_m \\
&+ \sum -K_{Vm} W^{V}_{mn} P_{zm,V} V_m + \sum -K^*_{Vm} W^{V*}_{mn} P^*_{zm,V} V^*_m \\
&+ \sum i\left[\left(\frac{\omega}{v_t}\right)^2 - k_m k_n\right] W^{T}_{mn} T_m \\
&\qquad = i\left[\left(\frac{\omega}{v_l}\right)^2 - k_{iF} k_n\right] W^{F}_{inc} F_{inc} - i\left[\left(\frac{\omega}{v_t}\right)^2 - k_{iE} k_n\right] W^{E}_{inc} E_{inc} \\
&\qquad\quad + (k_{iG} - k_n) W^{G}_{inc} P_{xG} G_{inc} + K_{iG} W^{G}_{inc} P_{zG} G_{inc}
\end{aligned} \tag{E.18}$$

$$\begin{aligned}
&\sum \rho^{\mathbf{3}}\left[k_m - k_n + 2\left(\frac{v_v}{\omega}\right)^2 (K_{Lm})^2 k_n\right] W^{L}_{mn} L_m \\
&+ \sum \rho^{\mathbf{3}}\left[k_m - k_n + 2\left(\frac{v_v}{\omega}\right)^2 (K^*_{Lm})^2 k_n\right] W^{L*}_{mn} L^*_m \\
&+ \sum -i\rho^{\mathbf{3}}\left[\left(\frac{v_l}{\omega}\right)^2 k_m(k_m - k_n) + \left(\frac{v_v}{\omega}\right)^2 (K_{Vm})^2\right] W^{V}_{mn} P_{xm,V} V_m \\
&+ \sum -i\rho^{\mathbf{3}}\left[\left(\frac{v_l}{\omega}\right)^2 k_m(k_m - k_n) + \left(\frac{v_v}{\omega}\right)^2 (K^*_{Vm})^2\right] W^{V*}_{mn} P^*_{xm,V} V^*_m \\
&+ \sum -i\rho^{\mathbf{3}} K_{Vm}\left[\left(\frac{v_l}{\omega}\right)^2 (k_m - k_n) - \left(\frac{v_v}{\omega}\right)^2 (k_m - 2k_n)\right] W^{V}_{mn} P_{zm,V} V_m \\
&+ \sum -i\rho^{\mathbf{3}} K^*_{Vm}\left[\left(\frac{v_l}{\omega}\right)^2 (k_m - k_n) - \left(\frac{v_v}{\omega}\right)^2 (k_m - 2k_n)\right] W^{V*}_{mn} P^*_{zm,V} V^*_m \\
&+ \sum -\rho^{\mathbf{4}}(k_m - k_n) W^{T}_{mn} T_m \\
&\qquad = -\rho^{\mathbf{3}}\left[k_{iF} - k_n + 2\left(\frac{v_v}{\omega}\right)^2 (K_{iF})^2 k_n\right] W^{F}_{inc} F_{inc} \\
&\qquad\quad + i\rho^{\mathbf{3}}\left[\left(\frac{v_l}{\omega}\right)^2 k_{iG}(k_{iG} - k_n) + \left(\frac{v_v}{\omega}\right)^2 (K_{iG})^2\right] W^{G}_{inc} P_{xG} G_{inc} \\
&\qquad\quad + i\rho^{\mathbf{3}} K_{iG}\left[\left(\frac{v_l}{\omega}\right)^2 (k_{iG} - k_n) - \left(\frac{v_v}{\omega}\right)^2 (k_{iG} - 2k_n)\right] W^{G}_{inc} P_{zG} G_{inc} \\
&\qquad\quad + \rho^{\mathbf{4}}(k_{iE} - k_n) W^{E}_{inc} E_{inc}
\end{aligned} \tag{E.19}$$

$$
\begin{aligned}
&\sum \rho^{\mathbf{3}} K_{Lm}\left[1-2\left(\frac{v_v}{\omega}\right)^2 k_m k_n\right] W^L_{mn} L_m \\
&+\sum \rho^{\mathbf{3}} K^*_{Lm}\left[1-2\left(\frac{v_v}{\omega}\right)^2 k_m k_n\right] W^{L*}_{mn} L^*_m \\
&+\sum -i\rho^{\mathbf{3}} K_{Vm}\left[\left(\frac{v_l}{\omega}\right)^2 k_m-\left(\frac{v_v}{\omega}\right)^2 (k_m+k_n)\right] W^V_{mn} P_{xm,V} V_m \\
&+\sum -i\rho^{\mathbf{3}} K^*_{Vm}\left[\left(\frac{v_l}{\omega}\right)^2 k_m-\left(\frac{v_v}{\omega}\right)^2 (k_m+k_n)\right] W^{V*}_{mn} P^*_{xm,V} V^*_m \\
&+\sum -i\rho^{\mathbf{3}}\left[\left(\frac{v_v}{\omega}\right)^2 k_m(k_m-k_n)+\left(\frac{v_l}{\omega}\right)^2 (K_{Vm})^2\right] W^V_{mn} P_{zm,V} V_m \\
&+\sum -i\rho^{\mathbf{3}}\left[\left(\frac{v_v}{\omega}\right)^2 k_m(k_m-k_n)+\left(\frac{v_l}{\omega}\right)^2 (K^*_{Vm})^2\right] W^{V*}_{mn} P^*_{zm,V} V^*_m \\
&+\rho^{\mathbf{4}}\sum -K_{Tm} W^T_{mn} T_m \\
&\quad = -\rho^{\mathbf{3}} K_{iF}\left[1-2\left(\frac{v_v}{\omega}\right)^2 k_{iF} k_n\right] W^F_{inc} F_{inc} \\
&\qquad + i\rho^{\mathbf{3}} K_{iG}\left[\left(\frac{v_l}{\omega}\right)^2 k_{iG}-\left(\frac{v_v}{\omega}\right)^2 (k_{iG}+k_n)\right] W^G_{inc} P_{xG} G_{inc} \\
&\qquad + i\rho^{\mathbf{3}}\left[\left(\frac{v_v}{\omega}\right)^2 k_{iG}(k_{iG}-k_n)+\left(\frac{v_l}{\omega}\right)^2 (K_{iG})^2\right] W^G_{inc} P_{zG} G_{inc} \\
&\qquad + \rho^{\mathbf{4}} K_{iE} W^E_{inc} E_{inc}
\end{aligned}
\tag{E.20}
$$

Finally, four additional expressions are required in order to solve the system for the coefficients of the fourteen diffracted series. These are the conditions that govern the propagation and polarization of the shear waves, and they have been presented at the conclusion of Appendix D.

REFERENCES

[1] Rayleigh, J., *The Theory of Sound.* New York: Dover, 1945.

[2] Lord Rayleigh, "On the dynamical theory of gratings," *Proceedings of the Royal Society of London, Series A*, vol. 79, no. 532, pp. 399–416, 1907.

[3] Page, J., Sukhovich, A., Yang, S., Cowan, M. L., Van Der Biest, F., Tourin, A., Fink, M., Liu, Z., Chan, C. T., and Sheng, P., "Phononic crystals," *Physica Status Solidi (b)*, vol. 241, no. 15, pp. 3454–3462, 2004.

[4] Jungman, A., Adler, L., and Quentin, G., "Ultrasonic anomalies in the spectrum of acoustic waves diffracted by periodic interfaces," *Journal of Applied Physics*, vol. 53, no. 7, pp. 4673–4680, 1982.

[5] Declercq, N. F. and Dekeyser, C. S., "Acoustic diffraction effects at the hellenistic amphitheater of epidaurus: Seat rows responsible for the marvelous acoustics," *Journal of the Acoustical Society of America*, vol. 121, no. 4, pp. 2011–2022, 2007.

[6] Declercq, N. F., Degrieck, J., Briers, R., and Leroy, O., "A theoretical study of special acoustic effects caused by the staircase of el castillo pyramid at the maya ruins of chichen-itza in mexico," *Journal of the Acoustical Society of America*, vol. 116, no. 6, pp. 3328–3335, 2004.

[7] Fortuin, L., "Survey of literature on reflection and scattering of sound waves at the sea surface," *Journal of the Acoustical Society of America*, vol. 47, no. 5, pp. 1209–1228, 1970.

[8] E. O. LaCasce, J. and Tamarkin, P., "Underwater sound reflection from a corrugated surface," *Journal of Applied Physics*, vol. 27, no. 2, pp. 138–148, 1956.

[9] Bishop, G. C. and Smith, J., "A scattering model for nondifferentiable periodic surface roughness," *Journal of the Acoustical Society of America*, vol. 91, no. 2, pp. 744–770, 1992.

[10] Greenwood, M. S., Brodsky, A., Burgess, L., Bond, L. J., and Hamad, M., "Ultrasonic diffraction grating spectroscopy and characterization of fluids and slurries," *Ultrasonics*, vol. 42, pp. 531–536, 2004.

[11] Humphryes, R. and Ash, E., "Acoustic bulk-surface-wave transducer," *Electronics Letters*, vol. 5, no. 9, pp. 175–176, 1969.

[12] Glass, N. and Maradudin, A., "Leaky surface-elastic waves on both flat and strongly corrugated surfaces for isotropic, non-dissipative media," *Journal of Applied Physics*, vol. 54, no. 2, pp. 796–805, 1983.

[13] Loewen, E. G. and Popov, E., *Diffraction Gratings and Applications.* New York: Marcel-Dekker, 1997.

[14] Maystre, D., *Selected Papers on Diffraction Gratings.* Bellingham, Washington: SPIE Optical Engineering Press, 1993.

[15] Shull, P. J. and Tittman, B. R., *Nondestructive Evaluation: Theory, Techniques, and Applications.* New York: Marcel Dekker, 2002.

[16] Hellier, C., *Handbook of Nondestructive Evaluation.* New York: McGraw-Hill, 2001.

[17] Krautkramer, J., *Ultrasonic Testing of Materials.* Berlin: Springer-Verlag, 1969.

[18] Bray, D. E. and Stanley, R. K., *Nondestructive Evaluation: A Tool in Design, Manufacturing, and Service.* CRC Press, 1997.

[19] Cheeke, J. D. N., *Fundamentals and Applications of Ultrasonic Waves.* CRC Press, 2002.

[20] Shull, P. J. and Tittman, B. R., "Ultrasound," in *Nondestructive Evaluation: Theory, Techniques, and Applications* (Shull, P. J., ed.), New York: Marcel Dekker, 2002.

[21] Uberall, H., "Surface waves in acoustics," in *Physical acoustics: principles and methods* (Mason, W. and Thurston, R., eds.), vol. 10, pp. 1–60, New York: Academic, 1973.

[22] Viktorov, I., *Rayleigh and Lamb Waves: Physical Theory and Applications.* New York: Plenum Press, 1967.

[23] Rose, J. L., "A baseline and vision of ultrasonic guided wave inspection potential," *Journal of Pressure Vessel Technology*, vol. 124, pp. 273–282, 2002.

[24] Stoneley, R., "Elastic waves at the surface of separation of two solids," *Proceedings of the Royal Socity of London, Series A*, vol. 106, no. 738, pp. 416–428, 1924.

[25] Lee, D. A. and Corbly, D. M., "Use of interface waves for nondestructive inspection," *IEEE Transactions on Sonics and Ultrasonics*, vol. SU-24, no. 3, pp. 206–212, 1977.

[26] Claus, R. O. and Palmer, C. H., "Direction measurement of ultrasonic stoneley waves," *Applied Physics Letters*, vol. 31, no. 8, pp. 547–548, 1977.

[27] de Billy, M. and Quentin, G., "Experimental study of the scholte wave propagation on a plane surface partially immersed in a liquid," *Journal of Applied Physics*, vol. 54, no. 6, pp. 4314–4322, 1983.

[28] Lord Rayleigh, "On waves propagated along the plane surface of an elastic solid," *Proceedings of the London Mathematical Society*, vol. 17, pp. 4–11, 1885.

[29] Rose, J. L., *Ultrasonic Waves in Solid Media.* Cambridge: Cambridge University Press, 1999.

[30] Brekhovskikh, L. and Godin, O., *Acoustics of Layered Media I: Plane and Quasi-Plane Waves.* Berlin: Springer-Verlag, 1990.

[31] Hess, P., "Surface acoustic waves in materials science," *Physics Today*, vol. 55, no. 3, pp. 42–47, 2002.

[32] Hallermeier, R. J. and Diachok, O. I., "Simple technique for exciting and probing elastic surface waves," *Journal of Applied Physics*, vol. 41, no. 12, pp. 4763–4764, 1970.

[33] Breazeale, M., Adler, L., and Scott, G. W., "Interaction of ultrasonic waves incident at the rayleigh angle on a liquid-solid interface," *Journal of Applied Physics*, vol. 48, no. 2, pp. 530–537, 1977.

[34] Plona, T., Behravesh, M., and Mayer, W., "Rayleigh and lamb waves at liquid-solid boundaries," *Ultrasonics*, vol. 13, no. 4, pp. 171–174, 1975.

[35] Briers, R., Leroy, O., and Shkerdin, G. N., "Conversion of a stoneley wave at the extremity of a fluid loaded plate," *Journal of the Acoustical Society of America*, vol. 101, no. 3, pp. 1347–1357, 1997.

[36] Tinel, A. and Duclos, J., "Diffraction and conversion of the scholte-stoneley wave at the extremity of a solid," *Journal of the Acoustical Society of America*, vol. 95, no. 1, pp. 13–20, 1994.

[37] Chamuel, J. R. and Brooke, G. H., "Transient scholte wave transmission along rough liquid-solid interfaces," *Journal of the Acoustical Society of America*, vol. 83, no. 4, pp. 1336–1344, 1988.

[38] Scholte, J., "On true and pseudo-rayleigh waves," *Proceedings of the Koninklijke Nederlandse Akademie van Wetenschappen*, vol. 52, pp. 652–653, 1949.

[39] Nasr, S., Duclos, J., and Leduc, M., "Scholte wave characterization and its decay for various materials," *Journal of the Acoustical Society of America*, vol. 87, no. 2, pp. 507–511, 1990.

[40] Luppé, F. and Doucet, J., "Experimental study of the stoneley wave at a plane liquid-solid interface," *Journal of the Acoustical Society of America*, vol. 83, no. 4, pp. 1276–1279, 1988.

[41] Jungman, A., Leroy, O., Quentin, G., and Mampaert, K., "Theoretical and experimental study of ultrasonic surface modes at a solid-fluid periodic interface," *Journal of Applied Physics*, vol. 63, no. 10, pp. 4860–4871, 1988.

[42] Every, A. G., Vines, R., and Wolfe, J., "Observation of scholte-like waves on the liquid-loaded surfaces of periodic structures," *Ultrasonics*, vol. 38, pp. 761–766, 2000.

[43] Declercq, N. F., Degrieck, J., Briers, R., and Leroy, O., "Theory of the backward beam displacement on periodically corrugated surfaces and its relation to leaky scholte-stoneley waves," *Journal of Applied Physics*, vol. 96, no. 11, pp. 6869–6877, 2004.

[44] Ginzbarg, A. and Strick, E., "Stoneley wave velocities for a solid-solid interface," *Bulletin or the Seismological Society of America*, vol. 48, pp. 51–63, 1958.

[45] Owen, T., "Surface wave phenomena in ultrasonics," *Progress in Applied Materials Research*, vol. 6, pp. 69–87, 1964.

[46] Hsieh, T., Lindgren, E., and Rosen, M., "Effect of interfacila properties on stoneley wave propagation," *Ultrasonics*, vol. 29, pp. 38–44, 1991.

[47] Claus, R. O. and Palmer, C. H., "Optical measurements of ultrasonic waves on interfaces between bonded solids," *IEEE Transactions on Sonics and Ultrasonics*, vol. SU-27, no. 3, pp. 97–103, 1980.

[48] Laude, V., Wilm, M., Benchabane, S., and Khelif, A., "On waves in an elastic plate," *Proceedings of the Royal Society of London: Series A*, vol. 93, no. 648, pp. 114–128, 1917.

[49] Pitts, L. E., Plona, T. J., and Mayer, W. G., "Theoretical similiarities of rayleigh and lamb modes of vibration," *Journal of the Acoustical Society of America*, vol. 60, no. 2, pp. 374–377, 1976.

[50] Su, Z., Ye, L., and Lu, Y., "Guided lamb waves for identification of damage in composite structures: A review," *Journal of Sound and Vibration*, vol. 295, pp. 753–780, 2006.

[51] Briers, R., *Contributions to the study of acoustic scattering and conversion phenomena in discontinuous structures by introducing a mode theory and by applying the inhomogeneous wave theory.* PhD thesis, Katholieke Universiteit Leuven, Kortrijk, Belgium, 1995.

[52] Wood, R., "On a remarkable case of uneven distribution of light in a diffraction grating spectrum," *Philosophical Magazine*, vol. 4, pp. 396–402, 1902.

[53] Claeys, J. and Leroy, O., "Diffraction of plane waves by periodic surfaces," *Revue du Cethedec*, vol. 72, pp. 183–193, 1982.

[54] Claeys, J. and Leroy, O., "Diffraction of ultrasonic waves from periodically rough liquid-solid surface," *Journal of Applied Physics*, vol. 54, no. 10, pp. 5657–5662, 1983.

[55] Mampaert, K. and Leroy, O., "Reflection and transmission of normally incident ultrasonic waves on periodic solid-liquid interfaces," *Journal of the Acoustical Society of America*, vol. 83, no. 4, pp. 1390–1398, 1988.

[56] Jungman, A., Adler, L., Achenbach, J., and Roberts, R., "Reflection from a boundary with periodic roughness: Theory and experiment," *Journal of the Acoustical Society of America*, vol. 74, no. 3, pp. 1025–1032, 1983.

[57] Quentin, G., de Billy, M., Cohen-Ténoudji, F., Doucet, J., and Jungman, A., "Experimental results on the scattering of ultrasound by randomly or periodically rough surfaces in the frequency range 2 to 25 mhz," in *Proceedings of the 1975 IEEE Ultrasonics Symposium*, pp. 102–106, 1975.

[58] Van Den Abeele, K., Briers, R., and Leroy, O., "Inhomogeneous plane-wave scattering and mode stimulation on periodic rough surfaces," *Journal of the Acoustical Society of America*, vol. 99, no. 5, pp. 2883–2897, 1996.

[59] Declercq, N. F., Degrieck, J., and Leroy, O., "The representation of 3d gaussian beams by means of inhomogeneous waves," *Ultrasonics*, vol. 42, pp. 273–276, 2004.

[60] Breazeale, M. and Torbett, M. A., "Backward displacement of waves reflected from an interface having superimposed periodicity," *Applied Physics Letters*, vol. 29, no. 8, pp. 456–458, 1976.

[61] Neubauer, W. G., "Ultrasonic reflection of a bounded beam at rayleigh and critical angles for a plane liquid-solid interface," *Journal of Applied Physics*, vol. 44, no. 1, pp. 48–55, 1973.

[62] Neubauer, W. G. and Dragonette, L. R., "Measurement of rayleigh phase velocity and estimates of shear speed by schlieren visualization," *Journal of Applied Physics*, vol. 45, no. 2, pp. 618–622, 1974.

[63] Declercq, N. F., Degrieck, J., Briers, R., and Leroy, O., "Theoretical verification of the backward displacement of waves reflected from an interface having superimposed periodicity," *Applied Physics Letters*, vol. 82, no. 15, pp. 2533–2534, 2003.

[64] Christensen, J., Fernandez-Dominguez, A., de Leon-Perez, F., Martin-Moreno, L., and Garcia-Vidal, F., "Collimation of sound assisted by acoustic surface waves," *Nature Physics*, vol. 3, pp. 851–852, 2007.

[65] Kundu, T., Banerjee, S., and Jata, K. V., "An experimental investigation of guided wave propagation in corrugated plates showing stop bands and pass

bands," *Journal of the Acoustical Society of America*, vol. 120, no. 3, pp. 1217–1226, 2006.

[66] Leduc, D., Morvan, B., Hladky, A.-C., Pareige, P., and Izbicki, J., "Lamb wave propagation in a plate with a grooved surface with several spatial periodicities," *Ultrasonics*, vol. 44, pp. e1359–e1363, 2006.

[67] Heckl, M. A. and Mulholland, L., "Some recent developments in the theory of acoustic transmission in tube bundles," *Journal of Sound and Vibration*, vol. 179, no. 1, pp. 37–62, 1995.

[68] Blessing, G. V., Slotwinski, J. A., Eitzen, D. G., and Ryan, H. M., "Ultrasonic measurements of surface roughness," *Applied Optics*, vol. 32, no. 19, pp. 3433–3437, 1993.

[69] Krasnova, T. and Jansson, P.-Å., "Wave scattering from a slightly wavy interface between two anisotropic media," *Journal of Nondestructive Evaluation*, vol. 25, no. 4, pp. 155–164, 2006.

[70] Beckmann, P. and Spizzichino, A., *The Scattering of Electromagnetic Waves from Rough Surfaces*. New York: Macmillan Pergamon Press, 1963.

[71] Ogilvy, J., *Theory of Wave Scattering from Random Rough Surfaces*. Bristol: IOP Publishing Ltd., 1991.

[72] Wauer, J. and Rother, T., "Considerations to rayleighs hypothesis," *Optics Communications*, vol. 282, pp. 339–350, 2009.

[73] Berman, D. H. and Perkins, J. S., "Rayleigh method for scattering from random and deterministic interfaces," *Journal of the Acoustical Society of America*, vol. 88, no. 2, pp. 1032–1044, 1990.

[74] Teklu, A., Breazeale, M. A., Declercq, N. F., Hasse, R. D., and McPherson, M. S., "Backward displacement of ultrasonic waves reflected from a periodically corrugated interface," *Journal of Applied Physics*, vol. 97, p. 084904, 2005.

[75] Declercq, N. F., Briers, R., Degrieck, J., and Leroy, O., "Diffraction of horizontally polarized ultrasonic plane waves on a periodically corrugated solid- liquid interface for normal incidence and brewster angle incidence," *IEEE Transactions on Ultrasonics, Ferroelectrics and Frequency Control*, vol. 49, no. 11, pp. 1516–1521, 2002.

[76] Millar, R., "The rayleigh hypothesis and a related least-squares solution to scattering problems for periodic surfaces and other scatterers," *Radio Science*, vol. 8, pp. 785–796, 1973.

[77] Lippmann, B., "Note of the theory of gratings," *Journal of the Optical Society of America*, vol. 43, p. 408, 1953.

[78] Meecham, W., "Variational method for the calculation of the distribution of energy reflected from a periodic surface. i.," *Journal of Applied Physics*, vol. 27, pp. 361–367, 1956.

[79] Achenbach, J., *Wave Propagation in Solids.* Amsterdam: North Holland Elsevier, 1973.

[80] Lowe, M. J., "Matrix techniques for modeling ultrasonic waces in multilayered media," *IEEE Transactions on Ultrasonics, Ferroelectrics, and Frequency Control*, vol. 42, no. 4, pp. 525–542, 1995.

[81] Mampaert, K., *Diffraction of ultrasonic plane waves at a periodic grating: fundamental theory and experimental verification.* PhD thesis, Katholieke Universiteit Leuven, Kortrijk, Belgium, 1989.

[82] Wirgin, A., "Reflection from a corrugated surface," *Journal of the Acoustical Society of America*, vol. 68, no. 2, pp. 692–699, 1980.

[83] Briers, R., Leroy, O., Poncelet, O., and Deschamps, M., "Experimental verification of the calculated diffraction field generated by inhomogeneous waves obliquely incident on a periodically rough liquid-solid boundary," *Journal of the Acoustical Society of America*, vol. 106, no. 2, pp. 682–687, 1999.

[84] Banerjee, S. and Kundu, T., "Symmetric and anti-symmetric rayleigh-lamb modes in sinusoidally corrugated waveguides: An analytical approach," *International Journal of Solids and Structures*, vol. 43, pp. 6551–6567, 2006.

[85] Declercq, N. F. and Sarens, B., "Increased efficiency of surface wave stimulation on the inaccessible side of a thick isotropic plate with superimposed periodicity," *IEEE Transactions on Ultrasonics, Ferroelectrics and Frequency Control*, vol. 54, no. 7, pp. 1409–1422, 2007.

[86] Thomas, T., *Rough Surfaces.* London: Imperial College Press, 1999.

[87] Vorburger, T., "Characterization of surface topography," in *Beam Effects, Surface Topography, and Depth Profiling in Surface Analysis* (Czanderna, A. W., Madley, T. E., and Powell, C. J., eds.), pp. 223–233, New York: Plenum Press, 1988.

[88] Assender, H., Bliznyuk, V., and Porfyrakis, K., "How surface topography relates to surfaces' material properties," *Science*, vol. 297, pp. 973–976, 2002.

[89] Vorburger, T., "Methods for characterizing surface topography," in *Tutorials in Optics* (Moore, D., ed.), Washington DC: Optical Society of America, 1992.

[90] Huynh, V. and Fan, Y., “Surface texture measurement and characterization with applications to machine-tool monitoring,” *International Journal of Advanced Manufacturing Technology*, vol. 7, pp. 2–10, 1992.

[91] Shin, Y., Oh, S., and Coker, S., “Surface roughness measurement by ultrasonic sensing for in-process monitoring,” *Transactions of the ASME, Journal of Engineering for Industry*, vol. 117, pp. 439–447, 1995.

[92] Blessing, G. and Eitzen, D., “Ultrasonic sensor for measuring surface roughness,” in *Proceedings of SPIE - Surface Measurement and Characterization*, vol. 1009, pp. 281–289, 1988.

[93] Oh, S., Shin, Y., and Fergason, E., “Surface roughness evaluation via ultrasonic scanning,” in *Proceedings of IEEE 1993 Ultrasonics Symposium*, pp. 741–744, 1993.

[94] Coker, S. A. and Shin, Y. C., “In-process control of surface roughness due to tool wear using a new ultrasonic system,” *International Journal of Machine Tools and Manufacture*, vol. 36, no. 3, pp. 411–422, 1996.

[95] Blessing, G., Bagley, P., and James, J., “The effect of surface roughness on echo amplitude in steel,” in *Proceedings of the 1983 IEEE Ultrasonics Symposium*, pp. 923–927, 1983.

[96] Blessing, G., Bagley, P., and James, J., “The effect of surface roughness on echo amplitude in steel,” *Materials Evaluation*, vol. 42, pp. 1389–1392, 1984.

[97] Leduc, D., Morvan, B., Pareige, P., and Izbicki, J.-L., “Measurement of the effects of rough surfaces on lamb waves propagation,” *NDT&E International*, vol. 37, pp. 207–211, 2004.

[98] de Billy, M., Doucet, J., and Quentin, G., “Angular dependence of the backscattered intensity of acoustic waves from rough surfaces,” in *Ultrasonics International 1975 Conference Proceedings*, (Guilford), pp. 218–223, IPC Sci. Tech., 1975.

[99] Nagy, P. B. and Adler, L., “Surface roughness induced attenuation of reflected and transmitted ultrasonic waves,” *Journal of the Acoustical Society of America*, vol. 82, no. 1, pp. 193–197, 1987.

[100] de Billy, M. and Quentin, G., “Measurement of the periodicity of internal surfaces by ultrasonic testing,” *Journal of Physics D: Applied Physics*, vol. 15, no. 10, pp. 1835–1841, 1982.

[101] de Billy, M., Cohen-Tnoudji, F., Jungman, A., and Quentin, G., “The possibility of assigning a signature to rough surfaces using ultrasonic backscattering diagrams,” *IEEE Transactions on Sonics and Ultrasonics*, vol. SU-23, no. 5, pp. 356–363, 1976.

[102] Declercq, N. F., Degrieck, J., Briers, R., and Leroy, O., "Diffraction of homogeneous and inhomogeneous plane waves on a doubly corrugated liquid/solid interface," *Ultrasonics*, vol. 43, pp. 605–618, 2005.

[103] Jungman, A., Cohen-Ténoudji, F., and Quentin, G., "Diffraction experiments in ultrasonic spectroscopy: preliminary results on the characterization of periodic or quasi-periodic surfaces," in *Ultrasonics International 1977 Conference Proceedings*, (Guilford), pp. 385–396, IPC Sci. Tech., 1977.

[104] Mampaert, K., Nagy, P., Leroy, O., Adler, L., Jungman, A., and Quentin, G., "On the origin of the anomalies in the reflected ultrasonic spectra from periodic surfaces," *Journal of the Acoustical Society of America*, vol. 86, no. 1, pp. 429–431, 1989.

[105] Blessing, G., Eitzen, D., Ryan, H., and Slotwinski, J., "Surface micrometrology using ultrasound," in *Proceedings of IEEE 1990 Ultrasonics Symposium*, pp. 1047–1052, 1990.

[106] de Billy, M., Adler, L., and Quentin, G., "Measurements of backscattered leaky lamb waves in plates," *Journal of the Acoustical Society of America*, vol. 75, no. 3, pp. 998–1001, 1984.

[107] Tamir, T. and Bertoni, H., "Lateral displacement of optical beams at multilayered and periodic structures," *Journal of the Optical Society of America*, vol. 61, no. 10, pp. 1397–1413, 1971.

[108] Lamkanfi, E., Declercq, N. F., Paepegem, W. V., and Degrieck, J., "Finite element analysis of transmission of leaky rayleigh waves at the extremity of a fluid-loaded thick plate," *Journal of Applied Physics*, vol. 101, p. 114907, 2007.

[109] Declercq, N. F., Teklu, A., Breazeale, M. A., Briers, R., Leroy, O., Degrieck, J., and Shkerdin, G. N., "Study of the scattering of leaky rayleigh waves at the extremity of a fluid loaded thick plate," *Journal of Applied Physics*, vol. 96, no. 10, pp. 5836–5840, 2004.

[110] Declercq, N. F., Degrieck, J., and Leroy, O., "The double-sided ultrasonic beam displacement," *Applied Physics Letters*, vol. 85, no. 18, pp. 4234–4236, 2004.

[111] Meegan, G., Hamilton, M., Il'inskii, Y. A., and Zabolotskaya, E., "Nonlinear stoneley and scholte waves," *Journal of the Acoustical Society of America*, vol. 106, no. 4, pp. 1712–1723, 1999.

[112] Miyashita, T., "Sonic crystals and sonic wave-guides," *Measurement Science and Technology*, vol. 16, pp. R47–R63, 2005.

[113] Kushwaha, M., Halevi, P., Dobrzynski, L., and Djafari-Rouhani, B., "Acoustic band structure of periodic elastic composites," *Physical Review Letters*, vol. 71, no. 13, pp. 2022–2025, 1993.

[114] Sánchez-Pérez, J., Caballero, D., Mártinez-Sala, R., Rubio, C., Sánchez-Dehesa, J., Meseguer, F., Llinares, J., and Gálvez, F., "Sound attenuation by a two-dimensional array of rigid cylinders," *Physical Review Letters*, vol. 80, no. 24, pp. 5325–5328, 1998.

[115] Laude, V., Wilm, M., Benchabane, S., and Khelif, A., "Full band gap for surface acoustic waves in a piezoelectric phononic crystal," *Physical Review E*, vol. 71, p. 036607, 2005.

[116] Thomas, E. L., Gorishnyy, T., and Maldovan, M., "Phononics: Colloidal crystals go hypersonic," *Nature Materials*, vol. 5, pp. 773–774, 2006.

[117] Vasseur, J., Deymier, P., Frantziskonis, G., Hong, G., Djafari-Rouhani, B., and Dobrzynski, L., "Experimental evidence for the existence of absolute acoustic band gaps in two-dimensional periodic composite media," *Journal of Physics: Condensed Matter*, vol. 10, pp. 6051–6064, 1998.

[118] Wilm, M., Khelif, A., Ballandras, S., Laude, V., and Djafari-Rouhani, B., "Out-of-plane propagation of elastic waves in two-dimensional phononic band-gap materials," *Physical Review E*, vol. 67, p. 065602, 2003.

[119] Shin, Y., Oh, S., and Coker, S., "Classical vibrational modes in phononic lattices: theory and experiment," *Zeitschrift fur Kristallographie*, vol. 220, pp. 765–809, 2005.

[120] Cheng, W., Wang, J., Jonas, U., Fytas, G., and Stefanou, N., "Observation and tuning of hypersonic bandgaps in colloidal crystals," *Nature Materials*, vol. 5, pp. 820–826, 2006.

[121] Kushwaha, M., "Stop-bands for periodic metallic rods: Sculptures that can filter the noise," *Applied Physics Letters*, vol. 70, no. 24, pp. 3218–3220, 1997.

[122] Lee, C.-S., Kim, J.-E., Park, H. Y., Chang, K., and Lim, H., "Essential role of impedance in the formation of acoustic band gaps," *Journal of Applied Physics*, vol. 87, no. 4, pp. 1593–1596, 2000.

[123] Uris, A., Rubio, C., Estelles, H., Sanchez-Perez, J. V., Martinez-Sala, R., and Llinares, J., "Design of lightweight multilayer partitions based on sonic crystals," *Applied Physics Letters*, vol. 79, no. 26, pp. 4453–4454, 2001.

[124] Manzanares-Martinez, B., Sanchez-Dehesa, J., Hakansson, A., Cervera, F., and Ramos-Mendieta, F., "Experimental evidence of omnidirectional elastic bandgap in finite one-dimensional phononic systems," *Applied Physics Letters*, vol. 85, no. 1, pp. 154–156, 2004.

[125] Meseguer, F., Holgado, M., Caballero, D., Benaches, N., Sanchez-Dehesa, J., Lopez, C., and llinares, J., "Rayleigh-wave attenuation by a semi-infinite two-dimensional elastic band-gap crystal," *Physical Review B*, vol. 59, no. 19, pp. 12169–12172, 1999.

[126] de Espinosa, F. M., Jimenez, E., and Torres, M., "Ultrasonic band gap in a periodic two-dimensional composite," *Physical Review Letters*, vol. 80, no. 6, pp. 1208–1211, 1998.

[127] Vasseur, J., Djafari-Rouhani, B., Dobrzynski, L., Kushwaha, M., and Halevi, P., "Complete acoustic band gaps in periodic fibre reinforced composite materials: the carbon/epoxy composite and some metallic systems," *Journal of Physics: Condensed Matter*, vol. 6, pp. 8759–8770, 1994.

[128] Liu, Z., Zhang, X., Mao, Y., Zhu, Y., Yang, Z., Chan, C., and Sheng, P., "Locally resonant sonic materials," *Science*, vol. 289, pp. 1734–1736, 2000.

[129] Chandra, H., Deymier, P., and Vasseur, J., "Elastic wave propagation along waveguides in three-dimensional phononic crystals," *Physical Review B*, vol. 70, p. 054302, 2004.

[130] Khelif, A., Choujaa, A., Benchabane, S., Djafari-Rouhani, B., and Laude, V., "Guiding and bending of acoustic waves in highly confined phononic crystal waveguides," *Applied Physics Letters*, vol. 84, no. 22, pp. 4400–4402, 2004.

[131] Goffaux, C., Maseri, F., Vasseur, J., Djafari-Rouhani, B., , and Lambin, P., "Measurements and calculations of the sound attenuation by a phononic band gap structure suitable for an insulating partition application," *Applied Physics Letters*, vol. 83, no. 2, pp. 281–283, 2003.

[132] Kushwaha, M. and Halevi, P., "Band gap engineering in periodic elastic composites," *Applied Physics Letters*, vol. 64, no. 9, pp. 1085–1087, 1994.

[133] Maldovan, M. and Thomas, E. L., "Simultaneous localization of photons and phonons in two-dimensional periodic structures," *Applied Physics Letters*, vol. 88, p. 251907, 2006.

[134] Kokkonen, K., Kaivola, M., Benchabane, S., Khelif, A., and Laude, V., "Scattering of surface acoustic waves by a phononic crystal revealed by heterodyne interferometry," *Applied Physics Letters*, vol. 91, p. 083517, 2007.

[135] Hsiao, F.-L., Khelif, A., Moubchir, H., Choujaa, A., Chen, C.-C., and Laude, V., "Complete band gaps and deaf bands of triangular and honeycomb water-steel phononic crystals," *Journal of Applied Physics*, vol. 101, p. 044903, 2007.

[136] Khelif, A., Choujaa, A., Djafari-Rouhani, B., Wilm, M., Ballandras, S., and Laude, V., "Trapping and guiding of acoustic waves by defect modes in a full-band-gap ultrasonic crystal," *Physical Review B*, vol. 68, p. 214301, 2003.

[137] Vasseur, J., Deymier, P., Chennai, B., Djafari-Rouhani, B., Dobrzynski, L., and Prevost, D., "Experimental and theoretical evidence for the existence of absolute acoustic band gaps in two-dimensional solid phononic crystals," *Physical Review Letters*, vol. 86, no. 14, pp. 3012–3015, 2001.

[138] Yang, S., Page, J., Liu, Z., Cowan, M., Chan, C., and Sheng, P., "Ultrasound tunneling through 3d phononic crystals," *Physical Review Letters*, vol. 88, no. 10, p. 104301, 2002.